Faculty of Science and Engineering
Department of Petroleum Engineering

Numerical simulations of fluid flow through a single rough walled fracture

Armin Hosseinian

This thesis is presented for the Degree of
Doctor of Philosophy of
Curtin University of Technology

March 2011

Declaration

To the best of my knowledge and belief this thesis contains no material previously published by any other person except where due acknowledgment has been made. This thesis contains no material which has been accepted for the award of any other degree or diploma in any university.

Name: Armin Hosseinian

Signature: *Date: 01/03/2011*

Abstract

The morphological properties of rock fractures may have a significant influence on their hydromechanical behaviour. Fracture surface roughness could change the fluid flow regime from laminar to turbulent, while it causes the flow properties to deviate from cubic law for smooth channels due to a change in fracture equivalent hydraulic aperture. Different empirical (including the well known Joint Roughness Coefficient, JRC) and statistical methods have been proposed for surface roughness characterisation in an attempt to link them to the hydromechanical behaviour of fractures.

This thesis aims to investigate the potential for assessment of fluid behaviour by studying its surface geometrical properties. D_{R1} and D_{R2}, the 2D and 3D roughness parameters developed recently using Riemannian geometry, were used to correlate fracture geometry to its flow behaviour. Also, the 2D Riemannian isotropy parameter (I_{R2}) was used to correlate surface roughness anisotropy with directionality in fluid flow behaviour along different directions.

Numerical simulations in both 2D and 3D were performed assuming the laminar flow regime using FLUENT software. This assumption is, to a large extent, acceptable for situations where the height to length ratios of a fracture is very small. 2D analysis of synthetic profiles with different geometries demonstrated how a change in profile roughness can affect flow response, for example, the pressure drop. JRC flow channels developed in this work as combinations of pairs of JRC profiles were simulated numerically. The analysis results indicated that channels with a similar JRC average for the upper and lower walls but a different JRC profile number responded differently when they were subjected to fluid flow. Therefore, assuming special fluid properties, correlations developed using the pressure drop of a fracture can be estimated by its analogy to JRC flow channels.

3D simulations of a corrugated plane were performed assuming different asperity height distributions, for fluid travelling along different directions with respect to surface geometry and at different shear displacements. No asperity contact and failure is assumed in the analysis performed in this work. D_{R2} analysis results of the corrugated plane indicated how fluid flow could be related to surface geometry. For instance, it was observed that the pressure drop was maximised along the direction of maximum roughness and reduced to its minimum along a

perpendicular direction which shows anisotropy in fluid flow behaviour. Significant changes in pressure drop due to shear offset indicated the importance of fracture wall displacements with respect to each other. A detailed analysis of one synthetically generated surface, and also five surfaces with identical statistical parameters except their correlation distances being different, further confirmed the above concepts. This was followed by analysing a real rock like fracture which was studied elsewhere for fracture shear tests in the lab. Simulation of this surface was performed with particular interest in identifying the locations where the velocity magnitude reduced to nearly zero after the fracture was subjected to a shear offset corresponding to maximum shear stress. These areas were found to be very similar to the locations of asperity degradations as observed through lab experiments. The roughness analysis of the surface was in agreement with the correlation found between the mechanical and hydraulic behaviour of the surface.

The results of this research demonstrate how detailed analysis of surface geometry could provide valuable information with respect to surface flow behaviour. Detailed discussions and interpretations of the results will be presented and various conclusions will be made.

Acknowledgements

I would like to express my gratitude to all those who gave me the possibility to complete this thesis.

I owe my deepest gratitude to my supervisor, Associate Professor Vamegh Rasouli, for his professional supervision and supports. His precious guidelines enabled me to comprehend and to develop this fantastic research topic.

It is my pleasure to thank Professor Brian Evans, the head of the Department of Petroleum Engineering, for his honour of supports during my study.

I would like to thank my associate supervisor, Dr.Ranjeeth Utikar, for his valuable guidance for numerical simulations using FLUENT.

I would like to express my gratitude to Mr. Faez for his continuous encouragement during the course of my studies.

I am grateful to Mr.Bahman Mozayani, Ms. Fakhereh Veshkini, Ms. Eve Rice, and all their families who supported me thoroughly during my stay in Australia.

I am indebted to many of my friends, especially Mr. Asadi, Mr. Younessi, and Mr. Chamani, current PhD students of the Department of Petroleum Engineering, who we shared our knowledge and I experienced implausible times with them.

To

My great father, who is supportive to me in all manners and his brilliant advices always show me bright way of life.

My incredible mother, who always gives me love unconditionally and I will never forget her patience and kindness.

My lovely sister, Sarvin, who is worth than everything for me and I will be grateful for all her kindness forever.

Contents

Page

List of Figures

Page

List of Tables

Nomenclature

ρ	Fluid density (Kg/m^3)
ν	Kinematic viscosity (m^2/s)
μ	Fluid viscosity (Kg/ms)
V	Fluid Velocity (m/s)
Q	Volumetric flow rate (m^3/s)
ΔP	Pressure drop (Pa)
Le	Real profile length
L	Projected profile length
CL	Correlation length
δ	Relative roughness
λ	Wavelength
λ'	Half a Wavelength
σ	Log normal distribution
k	Fracture permeability
K_H	Hydraulic conductivity
Δu	Shear displacement
K	Roughness
h	Aperture
h_{m}	Mean aperture
h_{H}	Hydraulic aperture
$(h_{\mathrm{H}}/h_{\mathrm{m}})^3$	Normalised fracture permeability
JRC	Joint Roughness Coefficient
d_{mc}	Minimum closure distance in JRC flow channels
$h_{\mathrm{m}}^{\mathrm{n}}$	Normalised mean aperture
$h_{\mathrm{H}}^{\mathrm{n}}$	Normalised hydraulic aperture
D_{R1}	1D Riemannian roughness parameter
D_{R2}	2D Riemannian roughness parameter
I_{R2}	Isotropy in roughness determination
UHC	Unit Hydraulic Cell

1 Fluid flow analysis in a single channel

The hydraulic mechanism of rock fractures can be considered an important aspect in many engineering fields such as petroleum and mining. In particular, the petroleum engineering production from a fractured reservoir is strongly related to the arrangement of a network of natural fractures. However, in contrary to a smooth channel, the two walls in rock fractures are typically rough and this has a great impact on the fluid flow through the fracture. Therefore, a proper study of fluid flow in rock fractures requires a coupling of the fluid mechanics with rock mechanics. Most of the developed models used for rock fractures employ the fundamental concept of fluid flow in a smooth channel, which is referred to as a 'parallel plane' model in the literature. Therefore, in this Chapter, after a brief review of the fluid flow in a smooth channel, the importance of fracture surface morphology on flow response of fluid will be discussed and the need for further study regaridng this concept will be highlighted. The rest of this Chapter summarises the outline, objectives and significance of this research work and the thesis structure.

1.1 Fluid flow in smooth channels

A study of the fluid flow in a smooth channel comprising two parallel plates is perhaps the simplest flow scenario in a single channel. The flow equations for this scenario can be obtained from the general Navier-Stokes equations (Kleinstreuer, 1997).The parallel plane flow is categorised as Couette flow and Poiseuille flow. The Poiseuille flow can be produced by a pressure gradient, in which the top and lower walls of the channel are fixed (i.e. zero average velocity). In contrast, the Couette flow occurs when two parallel plates have a relative motion with the pure shear flow produced by a constant pressure field. Figure 1.1 shows the velocity profiles (streamlines) corresponding to Couette and Poiseuille flows in a smooth channel, respectively. From this figure, it can be seen that the velocity profile in Poiseuille flow is parabolic, whereas for the Couette flow, it is dissimilar. Considering that during the flow of fluid in natural rock fractures the two walls are not in motion, we will only consider Poiseuille equations in this thesis. This is discussed in the next subsection.

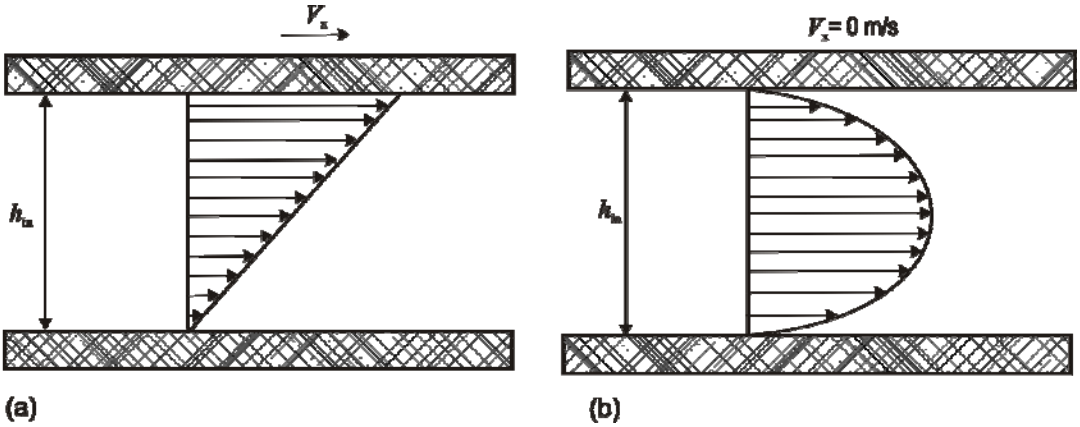

Figure 1.1 Velocity profiles for (a) Couette, and (b) Poiseuille flow in a smooth channel

1.1.1 Parallel plane flow and Cubic Law

We assume a Newtonian fluid which is laminar, incompressible, isothermal, single phase, viscous, unsteady and parabolic. These assumptions, without the gravity effect, will reduce the Navier-Stokes equation to the simple form of

$$\rho \frac{\partial V}{\partial t} = -\frac{\partial P}{\partial x} + \mu \frac{\partial^2 V}{\partial x^2} \tag{1.1}$$

where, ρ is the fluid density, V is the velocity, P is the pressure with x and y components, and μ is the fluid viscosity.

The left term in equation 1.1 is the nonlinear convective inertia force which represents the acceleration component of fluid motion. The presence of this term in a steady state flow can be described as the fluid velocity of particles which can be changed or accelerated because of the fluid tendency to move to a position with a different velocity. Equating the inertia term to zero means that fluid particles are moving in pure translation with a constant velocity, which is a result of zero acceleration for these particles. This results in a flow which follows straight path lines (i.e. streamlines), in which the dependency of each particle can only be on coordinates perpendicular to the direction of the flow (Constantinescu, 1995) and is referred to as 'parallel' flow.

Discarding the inertia or acceleration term, equation 1.1 reduces to

$$\frac{\partial P}{\partial x} = \mu \frac{\partial^2 V_x}{\partial y^2} \tag{1.2}$$

where, V_x is the fluid velocity in x direction.

The no slip boundary condition is applied for Poiseuille flow in a non-porous medium, in which V_x= 0 for both y=0 and y=h (see Figure 1.1). Applying these boundary conditions, equation 1.2 reduces to a parabolic velocity profile in the form of

$$V_x = -\frac{1}{2\mu}\frac{dp}{dx}y(h-y) \tag{1.3}$$

Equation 1.3 shows that velocity is only a function of fluid viscosity and the pressure gradient. The maximum parabolic velocity in Poiseuille flow takes place at the middle of the flow channel (see Figure 1.1). By substituting $y=h/2$ in equation 1.3, the maximum velocity as occurs at the centre of the channel (see Figure 1.1 (a)), is obtained as

$$\overline{V}_x = -\frac{h^2}{8\mu}\frac{dp}{dx}. \tag{1.4}$$

Also, the average velocity in x direction ($\overline{V}_x$) is derived as the ratio of volumetric flow rate in the x direction (Q_x), and the separation distance of the parallel plates of the channel or plate opening (h), i.e.

$$\overline{V}_x = \frac{Q_x}{wh} \tag{1.5}$$

where w is the width of the parallel plate channel. For a parallel plate channel with a unit width (w=1)

$$\overline{V}_x = \frac{Q_x}{h}. \tag{1.6}$$

Replacing Q_x from

$$Q_x = w\int_0^h V_x dy \tag{1.7}$$

and V_x from Equation 1.3 into Equation 1.6, the average velocity in the x direction for a parallel plate with a unit width is obtained as

$$\overline{V}_x = -\frac{h^2}{12\mu}\frac{dp}{dx}. \tag{1.8}$$

As the continuity equation is applied in Poiseuille flow (i.e. Q_x is constant), the pressure gradient must be constant and is defined as a linear function of x (Constantinescu, 1995), corresponding to Figure 1.1, i.e.

$$-\frac{dp}{dx} = \frac{P_1 - P_2}{L}. \tag{1.9}$$

In this equation, L is the length of the parallel plate channel in the x direction, and P_1 and P_2 are the uniform pressures into two opposite cross sections in the parallel plate channel.

From equations 1.6 and 1.8, the volumetric flow rate of a parallel plate channel with a unit width (w=1) can be derived as

$$Q_x = -\frac{h^3}{12\mu}\frac{dp}{dx}. \tag{1.10}$$

Equation 1.10 is well known as 'Cubic Law' and is vastly used in studying fluid flow through smooth parallel plate channels with aperture h. According to cubic law, the flow rate is proportional to the aperture cubed, with the velocity profile of flow between the two smooth walls being parabolic.

Cubic law is a fundamental equation used largely for fluid flow analysis in channels and pipes. This equation has also been applied by many people (for example, Zimmerman, 1996) to study fluid flow in a single natural fracture. However, as the walls of rock fractures are usually rough, modifications have been proposed to account for the effect of surface morphology. In the following subsection, a brief introduction to the effect of surface roughness and its effect on fluid flow will be given. A detailed review of literature relevant to rock fractures will be given in the next Chapter.

1.2 Effect of surface morphology on fluid flow

The great impact of morphology of the channel (or fracture in this study) through which the fluid flows have been discussed and studied by many researchers (Brown, 1987; Brown, 1989; Brown *et al.*, 1995; Enru, 2005; Ge, 1997; Neuzil and Tracy, 1981; Patir and Cheng, 1978; Tsang, 1984; Zimmerman and Bodvarsson1996; Zimmerman and Yeo, 2000). The surface irregularity (roughness) can be defined as the surface height distribution or the shape of the surfaces (Olson and Barton, 2001). Brady and Brown (2004) defined roughness as 'a measure of the inherent surface unevenness and waviness'. To realise the complexity associated with characterising roughness, it is perhaps useful to note a statement by Thomas (1999): "roughness seems to be such a property, with the added difficulty that it is not always so easy to define as a concept".

An immediate influence that surface irregularities may cause to flow characteristics is the change of fluid regime, i.e. from laminar to turbulent, as schematically shown in Figure 1.2. From this figure, one would expect regularly layered

streamlines of fluid passing through a smooth channel, whereas the flow streamlines deviate from being parallel as the channel walls become rough.

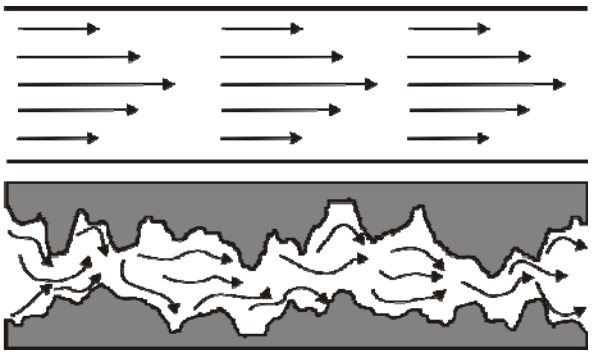

Figure 1.2 Streamlines in a smooth (Top) and a rough walled channel (Bottom)

The presence of surface roughness also causes a deviation from cubic law as introduced in the previous section for smooth walled channels. In rough channels, or rock fractures in our study, apertures are distributed irregularly and they are not constant along the profile geometry. This makes it difficult to assign a proper single value as the aperture of the channel (h) into a cubic law equation. This is significantly important as the aperture appears with a power of three in the cubic law equation (see equation 1.10). Figure 1.3 (a) shows that for a synthetic triangular profile, the mid distance between the top and bottom wall, or mean aperture (h_m), can be replaced with h in the cubic law, this is not true for real fractures as can be seen from Figure 1.3 (b). Several attempts have been made to introduce an appropriate value for the equivalent opening of a rough channel to be used in cubic law. This is while the appropriateness of using cubic law for fluid flow study of real fractures is still debatable.

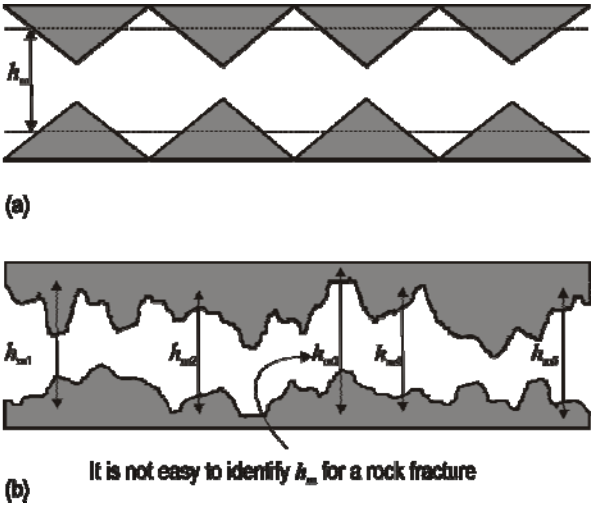

Figure 1.3 Mean aperture concept (h_m) (a) synthetic and (b) and rock fracture

Witherspoon *et al.* (1980) investigated the validity of cubic law for fluid flow in a deformable rock fracture experimentally. They reported an apparent reduction in flow due to a deviation from the parallel plane model. To account for this effect, they proposed a correction factor in the cubic law equation. Accordingly, they concluded that their modified cubic law held true for open or closed fractures in which the normal stress was below 20 MPa and was independent of rock types. Tsang and Witherspoon (1983) developed a single fracture represented by a collection of voids and the closure of the fractures resulted in deformation of these voids. Their purpose was to understand the effect of normal stress on fluid flow through a single fracture. They suggested using an equivalent version of cubic law by replacing the weighted average, $<h^3>$, with the single value of the fracture, h. They summarised that in cooperating the roughness into fluid flow study on deformable rock fractures under stress, the parallel plane was inadequate. Neuzil and Tracy (1981) modelled a real fracture as a combination of a number of parallel plates and therefore modified the cubic law equation by proposing a log of normal aperture frequency distribution for fractures.

Brown (1987) proposed applying the concept of the mean value of the aperture (mean aperture) into the cubic law based on his numerical studies. According to his results, when the surface walls were separated by one standard deviation, the modified cubic law underestimated the flow rate from about 40% to 60%. The concept of mean aperture has also been used to estimate flow characteristics such as transmissitivity of rock fractures (Brown, 1987; Patir and Cheng, 1978; Zimmerman *et al.*, 1991). However, as it shown in Figure 1.3, estimating the mean aperture for real rock fractures is not straightforward.

The Reynolds equation was employed as an alternative to cubic law by Brown (1987), Patir and Cheng (1978), and Zimmerman and Bodvarsson (1996) to analyse the fluid flow in rock fractures where the aperture varies only in the direction of the applied pressure gradient. They also suggested substituting the hydraulic aperture h_H with opening h in the Reynolds equation. “The hydraulic aperture is defined as the equivalent parallel plate aperture which would permit a given volumetric flow rate under an assigned pressure gradient”, as stated by Federico (1998).

The results reported by these investigators suggest the need for modification of the cubic law for its application in the study of real fractures. Also, in most of these studies, laminar flow is assumed for studying fluid flow.

The assumption of laminar flow has been widely used by people for fluid flow study in various applications, and in particular in fractured reservoirs (Sarkar, 2002). This assumption can capture to a large extent the effect of large scale roughness or tortuosity of fractures. However, when the effect of small scale roughness is significant, for example in the case of fluid flow around a wellbore, a turbulent flow regime is to be applied into the models. In this work, the objective is to simulate large scale roughness and therefore a laminar flow assumption has been adopted in all models.

To simply investigate the validity of this assumption, we recall the Reynold's number as

$$\mathrm{Re} = \frac{\rho V L}{\mu} = \frac{Q \rho L}{\mu A}. \tag{1.1}$$

While a wide range of Reynold's numbers have been proposed for transition between laminar to turbulent flow in rock fractures (Bear, 1988; Sarkar *et al.*, 2004), assumption of a Reynold's number of unity is found to be for applications concerned with petroleum engineering, i.e. fluid flow through fractures reservoirs. For a flow channel with a unit width, or for a 2D geometry, the area (A) is identical to the fracture height (h). Therefore the above equation can be rearranged as

$$\frac{h}{L} = \frac{Q \rho}{\mu}. \tag{1.2}$$

From this equation, assuming water with ρ=1000 kg/m^3 and μ=0.001 cp, the ratio of height to length of the fracture at the transition flow regime will be $h/L = 0.1$. When this ratio is less than 0.1, it indicates that the flow regime is likely to be laminar. In reservoir engineering applications, the viscosity of the oil as the hydrocarbon is much less than water (i.e. $h/L << 0.1$), and therefore assuming that water is the most critical and conservative case in the above calculations. This implies that the assumption of laminar flow, when the ratio of *h/L* is small, is reasonable. This is the basic assumption for all simulations carried out in this study.

In addition to the mean aperture and hydraulic aperture parameters in fluid flow analysis of rock fractures, other statistical parameters, such as fractals and empirical methods, and mainly the joint roughness coefficient (JRC) have been proposed to consider the effect of surface roughness. In this research, an attempt is made to use a recently developed parameter for roughness characterisation in the fluid flow analysis of rock fractures. D_{R1} and D_{R2} are the 2D and 3D Riemannian roughness parameters recently proposed by Rasouli (2002) and Rasouli and Harrison (2010), which allow an

investigation of the roughness of linear profiles and fracture surfaces, respectively. Also, I_{R2} is the isotropy parameter which will be used for studying the anisotropy in roughness determination. These parameters will be introduced briefly in Chapters 2 and 5 respectively.

1.3 Objective of this thesis

According to the problems briefly introduced in the above sections, the objectives of this PhD thesis can be summarised as below.

1) Identify the strengths and shortcomings of the available techniques and methods for fluid analysis of rock fractures through a comprehensive review of the literature.
2) Simulate a number of synthetic profiles numerically to obtain a correlation for pressure drop estimation as a function of profile geometry and fluid properties. FLUENT software will be used for the numerical simulations in this study.
3) Develop JRC flow channels as combinations of pairs of JRC profiles and simulate them to study responses to fluid flow and develop correlations between flow properties and JRC.
4) Find correlations between D_{R1} and fluid flow properties by simulating real fracture profiles.
5) Investigate the correlation between fluid flow behavior of 2D fractures and profile roughness (i.e. D_{R1}). This includes synthetic and real rock profiles.
6) Perform 3D numerical simulations of a corrugated plane, as well as statistically generated rock fractures to study the change in surface roughness on fluid flow behavior. This is followed by an analysis of a real rock like fracture. The anisotropy and the effect of shear displacement of fractures on fluid flow response will be investigated for all these surfaces. The effect of stresses is not included in this work and therefore no asperity failure is considered.
7) Calculate the Riemannian roughness and anisotropy parameters (D_{R2} and I_{R2}) for surfaces simulated earlier to investigate any correlation between surface geometrical properties and fluid flow behavior.

1.4 Significant of this research

Fluid flow in a rough fracture is a problem which has been the subject of many theoretical, computational, and experimental investigations and is as yet far from being thoroughly understood. Mathematically, it would be desirable to have a clearer understanding of the conditions under which the governing Navier-Stokes equations can be replaced by simpler and more tractable governing equations such as stokes equations (creeping flow) or the Reynolds lubrication equation.

Before studying a complex network of fractures, it is logical to understand how fluid flows through a single rough-walled rock fracture. This has been studied by a number of researchers before, as mentioned in Sections 1.1 and 1.2. However, in all of these works, the effect of roughness of fracture surfaces has been taken into account in fluid flow formulae using simple parameters such as JRC or statistical parameters. These parameters are unable to adequately incorporate the effect of fracture geometry into fluid flow behaviour.

The use of FLUENT software in this work in both 2D and 3D simulations is in fact, one of a few attempts made for the simulation of real rock fractures. The simulation results obtained in this research will highlight the capabilities of this software for the analysis of real rock fractures. The hydraulic aperture back calculated from FLUENT considers the real cross section against the fluid path and thus the correlations developed for synthetic profiles have a high level of high accuracy.

The extensive simulation and modelling of JRC flow channels carried out in this work using FLUENT will indicate why enough care must be practiced when this approach is used for the roughness characterisation of real rock profiles and their use in fluid flow analysis of rock fractures. This is also an attempt made for the first time.

In this thesis, an attempt is made to investigate the correlation between newly developed roughness and isotropy parameters in both 2D and 3D (Rasouli, 2002 and Rasouli and Harrison, 2010) in fluid flow formulae for real fractures. These roughness parameters are believed to be better representatives of surface roughness for real rock fractures. In particular, the 3D simulations and roughness calculations carried out in Chapter 5 indicate how extracting geometrical properties of a fracture surface enables us to understand fluid flow behaviour of the surface. This includes information on the directional dependency of fluid flow when it travels along different directions, the effect of small and large scale roughness, and the influence of shear displacement on flow response.

The above are all innovative concepts which are going to be practiced for the first time in this research work and the results are expected to advance the fundamental science in this subject.

1.5 Thesis structure

Based on the objectives of this work, this thesis is structured in different Chapters which are explained briefly below.

In Chapter 2, different approaches and models proposed for the fluid flow analysis in rock fractures will be reviewed. In particular, the use of the Joint Roughness Coefficient (JRC) and statistical parameters in fluid flow analysis of real fractures will be discussed. Also, a brief review of the new roughness parameter (D_{R1}) is given.

An introduction to the Computational Fluid Dynamics code (CFD) which is used by FLUENT software in fluid flow analysis of channels will be covered at the beginning of Chapter 3. The output results of the simulation of some synthetic profiles using FLUENT will be given in this Chapter. This will be followed by the development of a new correlation for synthetic profiles using which the hydraulic aperture will be estimated. Pressure drop can thus be estimated from profile geometrical properties and fluid characteristics. These formulae include D_{R1} which accounts for the effect of surface morphology.

In Chapter 4, a detailed analysis of JRC flow channels using FLUENT will be reported. The digitised elevation data of JRC profiles will be used to build JRC flow channels as a combination of two similar or dissimilar profiles. Correlations developed between D_{R1} and pressure drops of JRC profiles will be given. The usefulness of the JRC approach used for pressure drop estimation of real fractures will be shown at the end of this Chapter.

3D simulations of a corrugated plane, as well as a number of statistically generated surfaces, will be reported in Chapter 5. Here, the roughness and isotropy parameters corresponding to these surfaces will be calculated and correlations between surface morphology and fluid flow behaviour will be investigated. The results of a real rock like fracture will be presented and the fluid flow results will be compared with the lab shear test experiments carried out on this fracture elsewhere.

In Chapter 6, the conclusions and recommendation from this PhD thesis will be presented.

Chapter 1: **Flow analysis of fluid in a single channel**

A brief review of fluid flow in smooth channels and the importance of surface morphology on flow response of rough fractures are presented.

Chapter 2: **Fluid flow in rock fractures**

- A review of existing literature regarding fluid flow studies of rough fracture surfaces.
- A brief introduction of roughness characterisation methods including JRC, statistical methods and D_{R1}, 1D Riemannian roughness parameter.
- Analytical solutions of equivalent hydraulic aperture for channels with synthetic geometries are reviewed and correlated with the profile's D_{R1}.

Chapter 3: **Pressure drop estimation for 2D synthetic fractures**

- A brief introduction to FLUENT software used for fluid flow simulations.
- Synthetic channels with symmetric and asymmetric triangular geometries are simulated and hydraulic behaviour with respect to a channel's geometrical properties is investigated.
- Correlations are developed between geometrical and fluid parameters of a unit hydraulic cell (UHC) based on flow simulations of several geometries. The analysis is based on specific fluid properties. The correlations can be used to estimate the pressure drop of a real rough fracture assuming the profile has a combination of a number of UHCs.

Chapter 4: **Fluid flow response of JRC exemplar profiles**

JRC flow channels are developed as combinations of pairs of JRC exemplars and simulations of these channels are carried out using FLUENT. Correlations are developed assuming a specific set of fluid properties which estimates the fracture pressure drop based on average channel JRC.

Chapter 5: **3D fluid flow simulations of rough rock fractures**

3D simulations of a corrugated plane plus a number of statistically generated surfaces will be presented. The effect of roughness and isotropy parameters on fluid flow characteristics corresponding to these surfaces will be studied. The 3D simulation results of a number of statistically generated surfaces and a real rock like fracture will be presented. The directionality of fluid flow when it travels along different orientations, the effect of a fracture's small and large scale roughness and the shear displacement effect on flow response of the fracture will be studied.

Chapter 6: **Conclusion and future work**

References

Figure 1.4 Structure of the thesis.

2 Fluid flow in rock fractures

In the previous Chapter, the importance of fracture surface morphology on fluid flow characteristics was briefly reviewed. In this study, fluid flow analysis of a single fracture in 2D and 3D will be considered. This fundamental is required to understand the fluid flow behavior in complex fracture network geometries, such as in naturally fractured reservoirs.

In this Chapter, different models proposed for fluid flow analysis in rough rock fractures are briefly reviewed. In particular, the use of the joint roughness coefficient (JRC) and statistical parameters in fluid flow analysis of real fractures will be covered. Analytical formulae developed for synthetic profiles will be introduced and their applications to study real rock fractures will be assessed. This will be followed by an introduction to roughness parameter (D_{R1}) which is used for characterisation of roughness of 2D profiles. Analogous to this parameter, the 3D roughness and isotropy parameters will be introduced briefly in Chapter 5, where a 3D simulation of rough fractures will be presented.

2.1 Modeling fluid flow in rough fractures

The existing models which study the fluid flow in rough fractures are briefly reviewed in this section. These are explained in four classes of mechanical and numerical models, statistical methods and the well known joint roughness coefficient (JRC).

2.1.1 Mechanical models

Perhaps one of the first attempts in studying fluid flow through rough fractures was made by Lomize (1951), who conducted experimental works using parallel glass plates with rough surfaces.

Tsang (1984) investigated the effect of path tortuosity and connectivity on fluid flow rate through a single rough fracture. He presented 2D dimensional electrical resistors for flow paths and used different resistances in terms of the inverse of the fracture aperture cubed. His results indicated that a decrease in the flow rate (caused by

the effect of path tortuosity) was dependent on the roughness characteristics of the fracture. Accordingly, the larger effect of tortuosity was in small aperture distribution. He also concluded that small apertures manipulated the permeability of the fracture which had a great effect on tortuosity.

Assuming laminar flow in a rock fracture, a simple approach to model fluid flow characteristics such as transmissivity or permeability can be achieved by employing cubic law coupled with Darcy's law (Brown, 1987; Jaeger *et al.*, 2007; Zimmerman and Yeo, 2000; Zimmerman and Bodvarsson, 1996). The use of cubic law for real rock fractures has been examined by many researchers.

Cubic law was validated experimentally by Witherspoon *et al.* (1980) for laminar flow of fluids through open fractures consisting of parallel planar plates. They introduced a simplified form of the cubic law by deriving the following equation:

$$Q/\Delta h_{\mathrm{Hyd}} = \frac{C}{f}(h)^3 \tag{2.1}$$

in which Q is the flow rate (m^3/s), Δh_{Hyd} is the difference in hydraulic head (m), C is a constant that depends on the flow geometry and flow rate, h is the fracture aperture assumed to be planar planes, and f is a fracture surface characteristic factor which is constant and varies between 1.04 and 1.65, where f=1 corresponds to a smooth channel. They reported that since the flow rate was proportional to h^3, a slight change in aperture can significantly influence flow behavior. In their model, it was assumed the planar surfaces representing the two walls of the fracture remained parallel and thus were not in contact at any point.

The lubrication theory has been used by Zimmerman *et al.* (1991) to study the permeability of rough-walled rock fractures. They studied an idealised model of fracture geometry, in which the roughness followed a sinusoidal variation. This study concluded that in order for the lubrication approximation to be valid, the fracture walls should be smooth over lengths in the order of one standard deviation of the aperture, which is a much less restrictive condition than had previously been thought (e.g. Brown, 1987).

Zimmerman and Bodvarsson (1996) studied and quantified various geometric and kinematics conditions that were necessary in order for the Navier-Stokes equations to be replaced by a more tractable lubrication or Hele-Shaw equations. They found that the reduced Reynolds number, R_e^*, which is defined as

$$R_e^* = \rho V_{ave} h^2 / \mu\lambda << 1, \tag{2.2}$$

needed to be much less than one in order for the lubrication equation for a smooth channel to be valid. In this equation ρ is the fluid density (kg/m^3), V_{ave} is the average velocity along the fracture (m/s), h is the parallel plane opening (m), μ is the fluid viscosity (kg/ms), and λ is the characteristic length of the channel in the direction of the flow (m). The above assumption is reasonably valid in the case of real rock fractures, as the ratio of h/λ is usually much less than one. Several similar studies have been undertaken to evaluate the validity of Reynolds equation in rock fracture applications (Brown, 1987; Sisavath *et al.*, 2003; Zimmerman *et al.*, 1991; Zimmerman and Bodvarsson, 1996).

Ge (1997) studied fluid flow through sinusoidal fracture geometries with an amplitude of $h_m\delta$, as shown in Figure 2.1. The fracture wavelength is λ with its mean aperture being h_m. The results of his study are given in Figure 2.2 and indicate the normalised pressure gradient in x direction, $(\Delta p)h_m^3/12\mu Q_x$, varies periodically along the fracture and it increases as fracture relative roughness, δ, becomes larger (i.e. increasing $h_m\delta/\lambda$ in Figure 2.2). This conclusion is contrary to the results expected from cubic law which predict a constant pressure gradient according to the assumption of a constant fracture opening along the x direction.

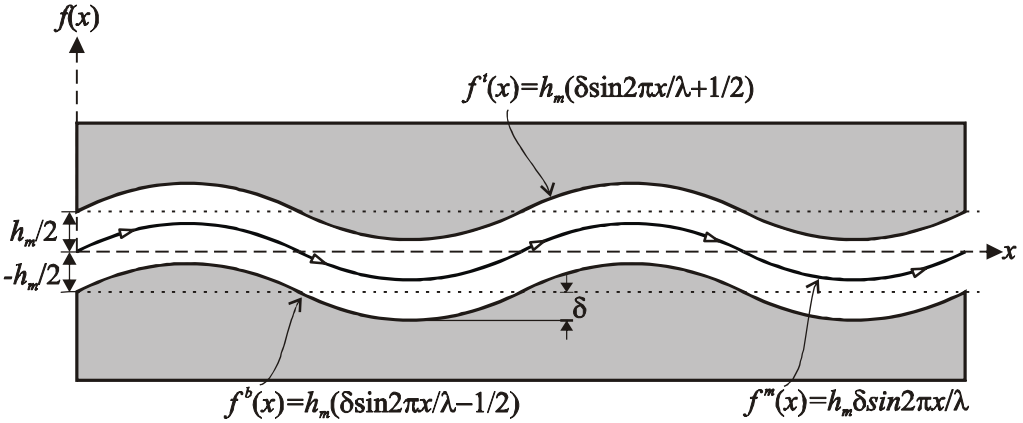

Figure 2.1 Fluid flow in a fracture with sinusoidal surface geometry (After Ge, 1997).

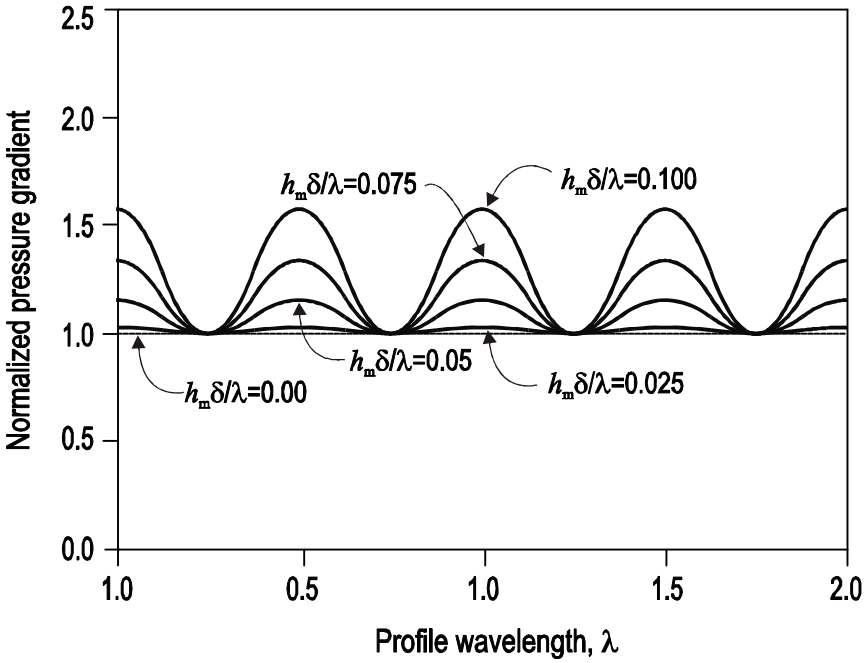

Figure 2.2 Normalised pressure gradient in a sinusoidal fracture with respect to roughness and in x direction (After Ge, 1997).

Oron and Berkowitz (1998) did a fluid flow study of fractures in an impermeable rock. For a section of a fracture, shown in Figure 2.3, they defined a geometric aspect ratio parameter as

$$\delta_G \equiv B / L , \tag{2.3}$$

where, B is a half-aperture, L is the distance between the inlet and outlet along the fracture geometry, and δ_G is the geometric aspect ratio. They found the local cubic law was an adequate first-approximation of the flow, when $\delta_G{}^2 \leq 1$ and the local relative roughness parameter, δ, was much less than unity. This led them to conclude that in cubic law, the aperture should be measured as an average over a distance, L, normal to the mean trend of the walls.

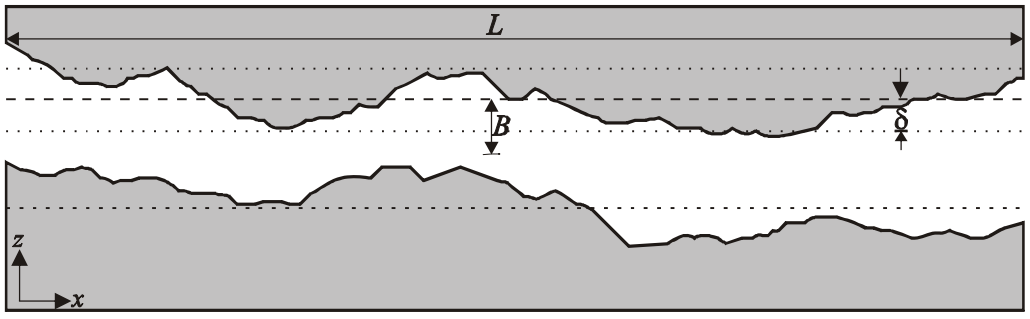

Figure 2.3 A self affine fracture cross section, δ=0.1. (After Oron and Berkowitz, 1998).

Yeo and Ge (2005) examined the applicability of the Reynolds equation in fluid flow analysis by studying a fracture with sinusoidal wall geometry, as shown in Figure 2.4. In this Figure, it can be seen that the aperture varies along the profile.

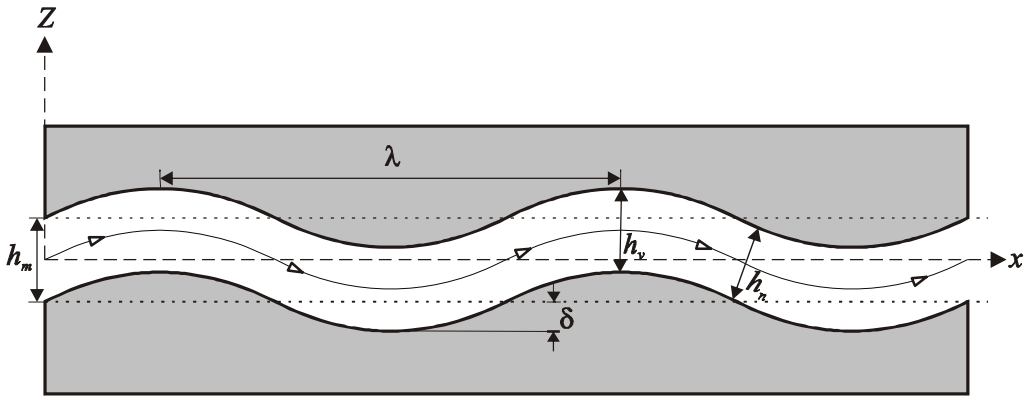

Figure 2.4 A sinusoidal flow channel with true aperture (h_n), vertical aperture (h_v), mean aperture (h_m) and amplitude (λ) (After Yeo and Ge, 2005).

Proposing parameter

$$(h_m / \lambda).(\delta / \lambda) \tag{2.4}$$

in which, λ is the amplitude of oscillated fracture roughness, h_m/λ represents roughness, and δ/λ is a measure of tortuosity, they found Reynolds equation to be applicable in rock fractures when $(h_m/\lambda)/(\delta/\lambda)<0.01$. They also reported that the presence of roughness, and neglecting the tortuosity and true aperture, are reasons for overestimation of flow when the Reynolds equation in Darcy flow is being used.

2.1.2 Numerical models

Brown (1987) simulated the laminar flow between rough surfaces numerically using the finite-difference method. His simulation was based on the Reynolds equation as a particular form of Naiver-Stokes equations with the objective of developing an expression which explicitly accounts for surface roughness. From the results of his studies, he stated that, "the parallel plane model can be considered only as a qualitative description of flow though real fractures".

Using a finite difference code, Thompson and Brown (1991) solved the Reynolds equation for different generated 3D fracture geometries to investigate the effect of surface roughness anisotropy on fluid flow. Their results showed the existence of a relationship between the flow rate and contact areas due to a reduced fracture opening.

Yeo *et al.* (1998), using experiments and finite element analysis solved Reynolds equation to investigate the effect of shear displacement on natural sandstone fractures. They used radial and unidirectional flow with a different shear displacement of 0, 1, and

2 mm in their experimental study. They showed that by increasing shear displacement the fluid flow anisotropy could change. Their studies also showed that the permeability was less in the direction parallel to shear displacement than the direction of transverse to the shear displacement.

Jing (2003) reviewed the applied numerical modeling in rock mechanics applications. He described the Discrete Element Method (DEM) as a powerful numerical modelling tool due to its flexibility to handle a moderately large number of fractures, for purely mechanical problems.

The effects of fracture roughness and aperture on the hydraulic and mechanical properties of fractured rock masses have also been investigated by Enru (2005). His work further highlights the difficulty in quantifying parameters which control the fluid flow from seismic data. He found that hydraulic aperture primarily controlled the fluid flow and that the mechanical aperture (arithmetic average of aperture distributions) was a key parameter to describe the fracture compliances which determined the elastic response of fractured rock masses.

Sarkar *et al.* (2004) studied fluid flow through fractures using numerical simulations and addressed the challenging issue of characterising hydraulic properties of fractures. They used Computational Fluid Dynamics (CFD) code, available in commercial software FLUENT, using a finite-volume based discretisation scheme. They applied steady-state, viscous, laminar flow simulations for a Newtonian fluid in both 2D and 3D fracture models. According to their results, for hydraulic characterisation purposes, fluid flow in fractures can be sufficiently modelled using both Stokes and Navier-Stokes equations for flows with a Reynolds number of up to approximately 100. They also concluded that numerical solutions of either Stokes or Navier-Stokes equations could be used to model the slow flow of viscous and Newtonian fluids (e.g. oil and water) in subsurface fractures. According to their investigations, "for complicated 3D fracture geometries, or for complex 2D or 3D fracture networks, flow simulation may be the only way to estimate the true equivalent hydraulic aperture of the fractured medium".

In another study by Sarkar (2002), he studied the fluid flow in fractures using a finite difference approach, and analysed the effects of fracture properties (e.g. fracture geometry) on flow and its effect on flow paths at a micro scale. His approach was similar to the discrete fracture network (DFN) models for studying the fluid flow through fractures, with a non-porous rock matrix surrounded by an impermeable

surface. He employed the Stokes equation and the ERFLAC simulator and examined his computation by different case studies on dissimilar reservoirs, each with a flow path distinction. He reported permeability values only for those directions along which the actual transmission of fluid through the rock occurred. Accordingly, he suggested permeability was inversely proportional to the complexity of the flow path. He also concluded that permeability was a strong function of the ease of flow through a fracture.

FLUENT simulation was also applied by Nazridoust *et al.* (2006), to analyse flow conditions through fracture sections for different flow rates. They studied the accuracy of parallel plane models to estimate pressure drops through the fractures. On the basis of the CFD simulation data, they developed a new expression for the friction factor for flow through fractures for a Reynolds number (Re) much less than 10 as

$$f_{\mathrm{F}} = \frac{123}{R_e}\left(1 + 0.12R_e^{\,0.687}\right), \tag{2.5}$$

$$R_e = \frac{Q}{\upsilon} \tag{2.6}$$

where, f_{F} is the fracture friction coefficient, R_{e} is the Reynolds number, which is constant at every section of the fracture and defined as the ratio of the flow rate per unit width (Q), and the fluid kinematic viscosity (υ). This study showed that the pressure drop was dominated by the smallest aperture passages of the fracture. They also stated that the parallel plane flow model with the use of an appropriate effective fracture aperture and inclusion of the tortuosity factor (θ) could provide reasonable estimates for pressure drops in the fracture.

A recent study on laminar, single phase flow along the fracture was carried out by Crandall *et al.* (2010a) for permeable Berea sandstone using FLUENT software. Their study was based on the fracture profiles which were similar to Brownian fractal structures. Accordingly, they developed an equation to estimate the friction factor by applying the tortuosity factor (θ_T), as defined by Nazirdoust *etal.* (2006), and Tsang (1984).Their equation is

$$f = \frac{123}{R_{\mathrm{e}}}\frac{\left(1 + 0.12R_{\mathrm{e}}^{\,0.687}\right)}{1 + 61.5(1+\theta)\left(1 + 0.12R_{\mathrm{e}}^{\,0.687}\right)kh_D / \overline{H}^3} \tag{2.7}$$

$$\theta_{\mathrm{T}} = \frac{L_{\mathrm{e}}}{L} - 1 \tag{2.8}$$

where, θ_T is the tortuosity factor , L_e is the distance between inlet and outlet boundary (i.e. profile length) , L is the fracture length, h_D is the formation height from Darcy's law, k is the matrix permeability of fracture (i.e. k=0 for impermeable rock fracture), and $\overline{H}$ is the effective fracture aperture .Their study indicated that the occurrence of largest pressure drops is in smallest apertures along a fracture.

Schmittbuhl *et al.* (2008) modelled the viscous flow through a fracture by approaching a finite difference scheme of the Stokes equation (i.e. Low Reynolds number) with a lubrication approximation. They also carried out experimental measurements of the flux through the fracture of a mixture of glycerol and water with a different average fracture aperture and compared the results of these methods. In this study, the fracture hydraulic conductivity was computed as

$$K_H = \mu Q / \Delta P , \tag{2.9}$$

where, μ is viscosity, Q is the flow rate, and ΔP is the pressure gradients. Also, with holding cubic law at a large scale for fracture aperture, the hydraulic conductivity was expressed as

$$K_H = h_m^3 / 12 , \tag{2.10}$$

where, h_m is the mechanical (mean) aperture. In this study, the concept of critical mechanical aperture (h_m^c) was proposed as being the smallest mechanical aperture. The plot of hydraulic conductivity, as obtained from equations 2.9 and 2.10, is given in Figure 2.5. This figure shows a significant departure from cubic law at a small closure of the fracture in which $h_m \approx h_m^c$. The results also indicated that in viscous flow with a sufficiently open fracture, the influence on the flow through its aperture and hydraulic conductivity was significantly controlled only by long wavelengths of the fracture morphology.

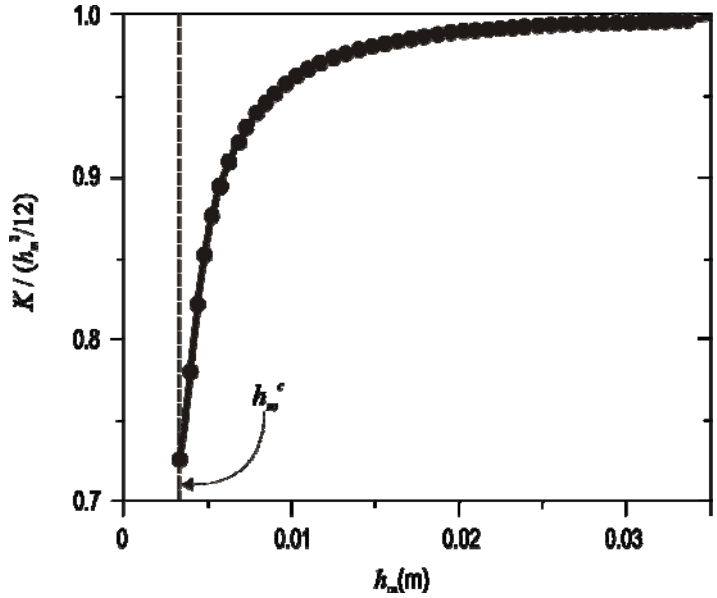

Figure 2.5 Hydraulic conductivity, K, versus mechanical aperture h_m. The vertical dashed line indicates the aperture at rigid contact h_m^c (After Schmittbuhl *et al.*, 2008).

Koyama *et al.* (2008) applied the finite element method (FEM) to study the hydro mechanical behaviour of fluid flow due to shearing of the fracture and particle transport for 2D fracture geometry. Their numerical simulation was based on solving both the Navier–Stokes and the Reynolds equation and comparing those results to demonstrate the degree of validity of the Reynolds equation. The results obtained for different hydraulic pressures of 1, 10, 100 Pa and 1 Pa and shear displacements of 0 and 2 mm indicated similar results where the maximum velocity occurred at the centre of the fracture. However, they observed some deviation of maximum velocity from the centre line when the Navier–Stokes equation was used. They interpreted this as being due to a sudden change in the fracture geometry (i.e. difference in wall roughness). The results shown in Figure 2.6 indicated that the Reynolds equation overestimated the total flow rate in which the velocity profile was assumed to be parabolic by five to 10 percent.

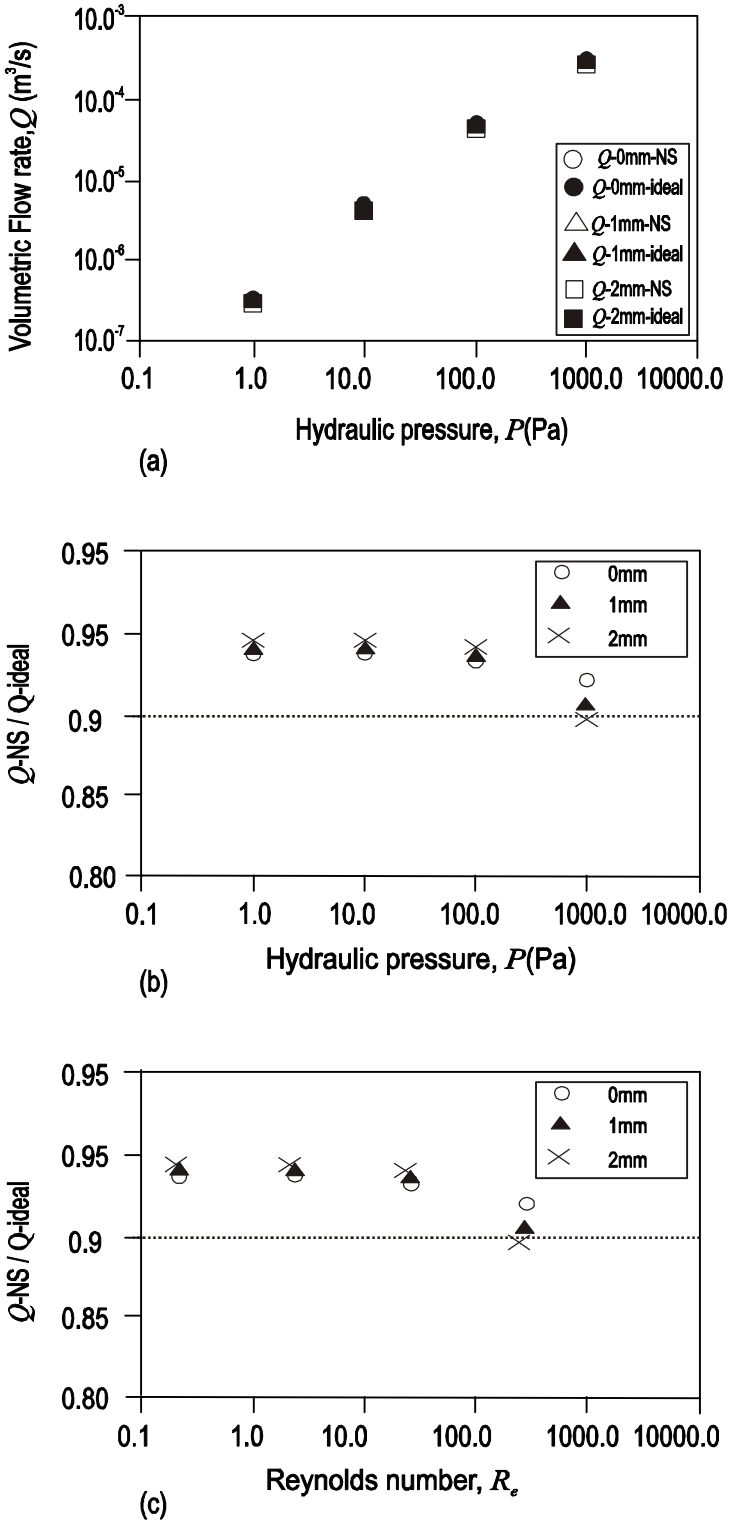

Figure 2.6 Flow simulation results for different shear displacements from NS: Navier-Stokes equation, and ideal: Reynolds equation (After Koyama *et al.*, 2008).

Nemoto *et al.* (2009) presented experimental and bi-directional flow simulations to measure the contact area and study the anisotropic flow behaviour in granite fractures with varied shear displacements at normal stresses of up to approximately 100MPa. Their study was based on the Watanabe *et al.* (2008) study for artificially generated

granite tensile fractures. The observed results showed that a less tortuous flow path in the perpendicular direction was due to the distribution of the contacting asperities. They defined the permeability ratio, k_r, as

$$k_r = \frac{k_{\mathrm{Pr}}}{k_{\mathrm{Pa}}} \quad , \tag{2.11}$$

Where, k_{Pr} and k_{Pa} are the permeabilities in the directions perpendicular and parallel to shear displacement, correspondingly.

According to the results plotted in Figure 2.7, they obtained significant permeability in the direction perpendicular to the shear displacement. They also showed that permeability decreased as a result of increasing the normal stress.

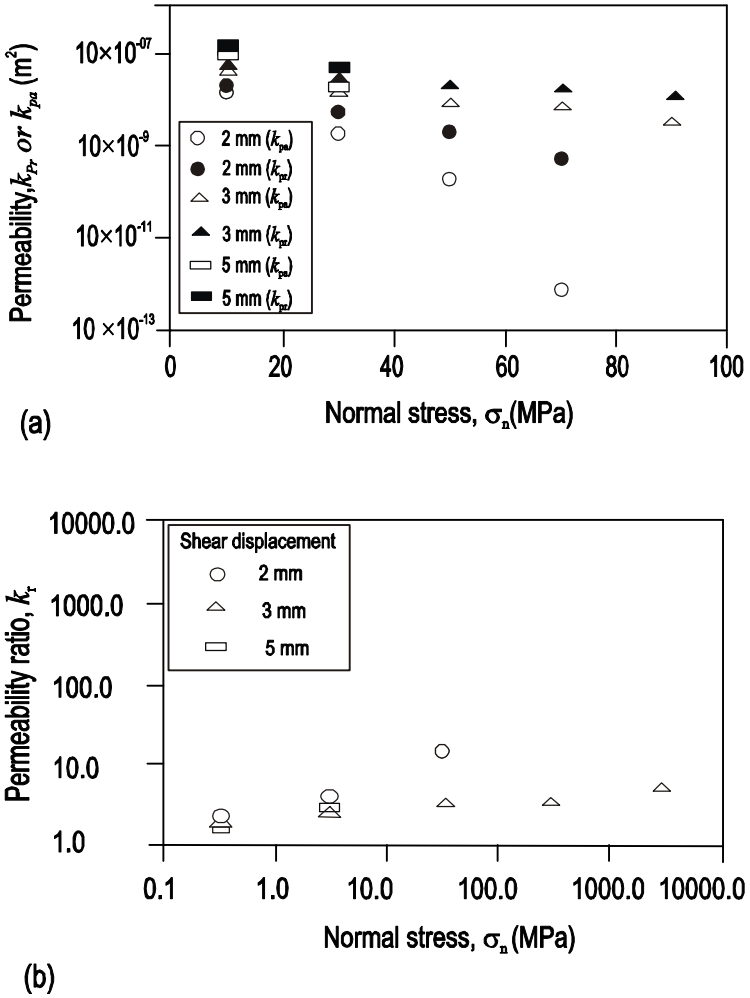

Figure 2.7 Estimated permeability based on the numerical results (a) different direction to the shear displacement and (b) permeability ratio (After Nemoto *et al.*, 2009).

Using the finite element method (FEM) and laboratory experiments, Koyama *et al.* (2009) considered the effect of shear displacement on aperture distribution and transmissivity under different normal stresses and normal stiffness conditions. They introduced a special algorithm for treatment of the contact areas with a zero-aperture

which captured the tortuous flow fields and channelling effects under normal stress and stiffness conditions during shearing, which is important for particle transport simulations in fractures. Their results indicated that the Reynolds equation can be used for all stages of shear displacement and the hydraulic properties can be back calculated from the Reynolds equation.

Kristinof *et al.* (2010) simulated air and water flow through a granite block with a single fracture, using both numerical and experimental approaches to consider the effect of in situ stresses on fluid flow. They employed triaxial loading experiments and cubic law in their studies. Their results showed a different trend for pressure in the fracture itself and the block adjacent to it.

Petchsingto and Karpyn (2009) employed CFD to investigate single-phase flow dynamics in an impermeable rough fracture using the high-resolution X-ray computed tomography images for a Berea sandstone core. They compared the 3D FLUENT simulation results for a rough fracture with a smooth parallel plane which had the similar mean aperture of the rough fracture. Their simulation results indicated a non-uniform decrease for pressure profiles in a real fracture compared to a uniform change of pressure in a parallel plane model. They described this phenomenon as a result of the existence of flow barriers in rough fractures caused by asperities. According to Figure 2.8, they concluded that a similar hydraulic aperture for a parallel plane and real fracture showed a similar pressure drop, in contrast to when a similar mean aperture is used.

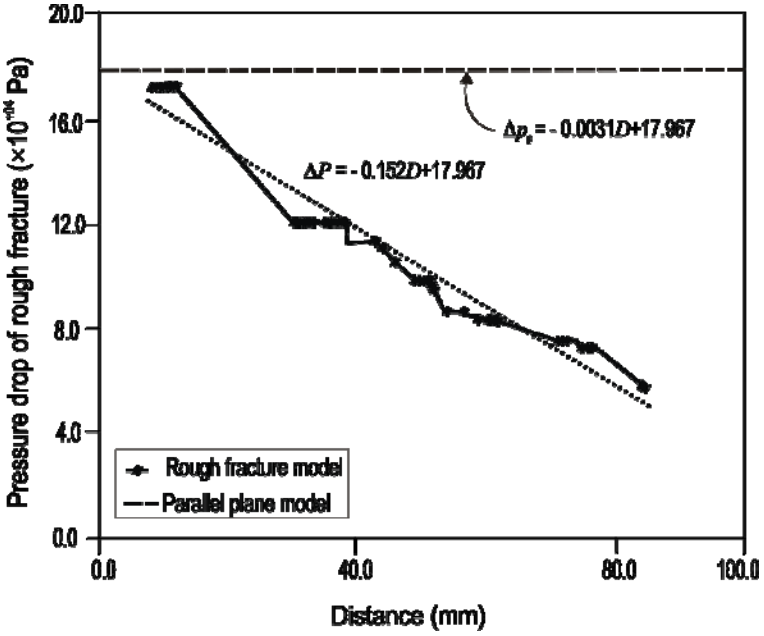

Figure 2.8 Pressure drop of a real rough fracture compare to a parallel plane model (After Petchsingto and Karpyn, 2009).

Sarifzadeh *et al.* (2009) used the FLUENT software to study the effect of roughness on velocity fields through rough fractures. They simulated the turbulent flow through an artificial 3D rock fracture using a different range of velocities between 0.01 to 1 m/s. They normalised the average velocity by dividing it by the inlet velocity. Their simulation results for a different range of Reynolds numbers from 4.5 to 450 indicated a non-linear disparity for static pressure. They also observed that the acceleration results from inertial effect could occur from a fluid flow convergence-divergence effect and could occur at sharp corners of the fracture in which the aperture changed suddenly. Their results also showed that by increasing the Reynolds number corresponding to the inlet velocity, the normalised velocity decreased if the normalised aperture was increased.

2.1.3 Statistical and Geo-statistical models

Since fracture roughness can be expressed as the ratio between the arithmetic mean h_m and standard deviation of the aperture in a non-dimensional form (Zimmerman *et al.*, 1991), statistical and geo-statistical methods have been employed to analyse the aperture variation in rock fractures.

Neuzil and Tracy (1981) proposed a fluid flow model in a fracture in which the fracture was presented by a set of parallel plane openings with different apertures, as shown in Figure 2.9. They derived a modified Poiseuille equation by employing an aperture frequency distribution, $f(h_V)$, as

$$Q_f = LJ\frac{\gamma}{12\mu}\int_0^\infty {h_V}^3 f(h_V)dh_V \,, \tag{2.11}$$

where Q_f is the flux through fracture (m^3/s), L is the total length of the fracture normal to flow (m), J is the gradient of piezometric head (dimensionless), γ is the specific weight of water, ρg, (kg/m^2s^2), and h_V is the vertical fracture aperture.

Consequently, they approximated $f(h_V)$ by a log normal density function and derived the following equation in relation to the standard deviation (σ):

$$Q_f = LJ\frac{\gamma}{12\mu}[l]^3 \exp\left(3\zeta + 9(\sigma^2/2)\right). \tag{2.12}$$

In this equation, $[l]$ is the unit length, ζ is the log normal distribution parameter (dimensionless), and σ is also the log normal distribution parameter (which corresponds to the simple poiseuille equation if it is zero. They also defined the mean aperture in their proposed model as

$$h_{\mathrm{m}} = [l]\exp\left(\zeta + (\sigma^2/2)\right). \tag{2.13}$$

According to the modified Poiseuille equation, they suggested that the flow in a fracture could be predicted as long as the distribution parameters (i.e. ζ and σ) were known. They also concluded that flow was affected by the largest apertures due to the proportionality between flow and the cubic power of aperture.

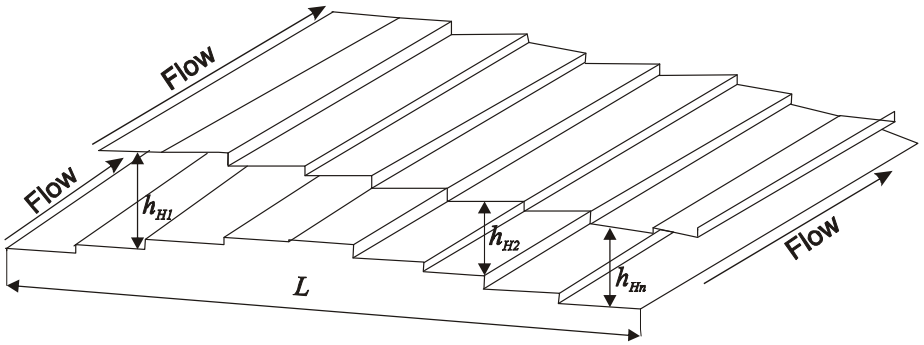

Figure 2.9 Schematic of a fracture model (After Neuzil and Tracy, 1981).

Early attempts to find a correlation between hydraulic aperture (h_{H}) and mean aperture (h_{m}) were done by Lomize (1951) based on experimental studies. He introduced a normalised permeability parameter as

$$\left(h_{\mathrm{H}}/h_{\mathrm{m}}\right)^3 = \frac{1}{1+17\left(2\,h_{\mathrm{m}}/\sigma\right)^{1.5}}, \tag{2.14}$$

with σ being the standard deviation of fracture apertures.

A similar correlation was suggested by Patier and Cheng (1978) which carried the assumption that the fracture asperities had a Gaussian height distribution. This is in the form of

$$(h_{\mathrm{H}}/h_{\mathrm{m}})^3 = 1 - 0.9e^{-0.56(h_{\mathrm{m}}/\sigma)}. \tag{2.15}$$

A fractal dimension (D_{f}) has been used by number of researchers to consider the effect of fracture surface roughness in fluid flow analysis. For example, Brown (1987) reported that the fractal dimension of fractures he examined numerically changed from two to 2.5, which covered a wide range of roughness. His study was based on a local surface height with a Gaussian random variable distribution having a standard deviation σ. His studies indicated that in general the larger the fractal dimension, the higher the hydraulic aperture (h_{H}). Plotting the results of simulations for fractures with different fractal dimensions, as shown in Figure 2.10, he concluded that the normalised

permeability $(h_H/h_m)^3$ at small standardised mean apertures (h_m/σ) showed noticeable deviations from cubic law.

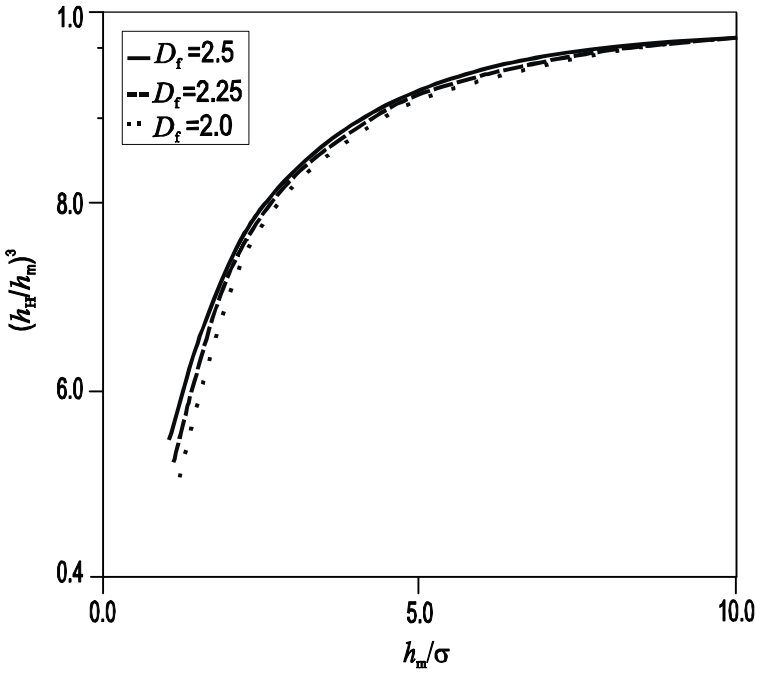

Figure 2.10 Comparison of hydraulic aperture, h_H, with the mean aperture, h_m (Brown, 1978).

In a similar attempt, Zimmerman *et al.* (1991) proposed the following equation which relates normalised permeability to h_m/σ for a fracture with sinusoidal geometry:

$$(h_H/h_m)^3 = 1 - 1.5(\sigma/h_m)^2 . \tag{2.16}$$

Similar studies carried out by Enru (2005) resulted in a nonlinear relationship between normalised permeability and the ratio of σ/h_m:

$$(h_H/h_m)^3 = (1 + (\sigma/h_m)^2)^{-3/2} . \tag{2.17}$$

Renshaw (1995) derived a nonlinear relationship between hydraulic and mechanical aperture (mean aperture) in a fracture whose aperture distribution obeyed a log normal distribution. The correlation is in the form of

$$(h_H/h_m) = \exp(-\sigma_B^2/2) \tag{2.18}$$

$$(h_m/\sigma_b) = \frac{\exp(\sigma_B^2/2)}{\{\exp(\sigma_B^2/2)[\exp(\sigma_B^2/2) - 1]\}^{1/2}} , \tag{2.19}$$

where, σ_B^2 and σ_b^2 are the variance of the log aperture and the fracture aperture distribution, respectively.

In equations 2.18 and 2.19, σ_B is calculated using the equation for variance of log normal distribution which is derived as

$$\sigma_B = \left(e^{\sigma^2} - 1\right) e^{2\bar{B}+\sigma^2} \tag{2.20}$$

where, σ is the variance and $\bar{B}$ is the mean value of normal distribution for apertures, respectively.

Figure 2.11 compares the results obtained from equations 2.15, 2.16, 2.17, and 2.18 with the latter correlation proposed by Renshaw (1995). A close agreement between different proposed models is seen from this figure.

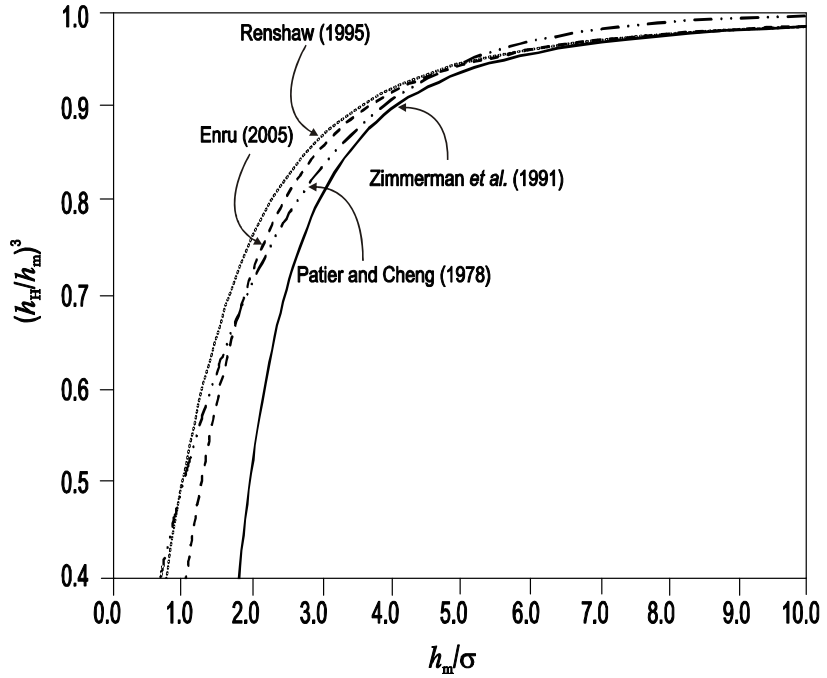

Figure 2.11 Normalised permeability of a fracture as a function of standard deviation of roughness, proposed by different authors.

Using a similar approach to previously mentioned studies, Ge (1997) developed equations for laminar fluid flow through a channel whose geometry is shown in Figure 2.12. The lower wall of the channel is flat, whereas the upper wall has a symmetric triangular geometry with an asperity angle of θ. Assuming that cubic law holds, he proposed the following correlation:

$$(h_H/h_m)^3 = \frac{(\delta/h_{in})^2}{(\delta/2h_{in})^4}\left[\frac{2\cos\theta}{\cos\alpha/2(1+\cos\theta)}\right]^3 \tag{2.21}$$

$$(h_m/\sigma) = 2\sqrt{3}\left(\frac{h_{in}}{\delta} + \frac{1}{2}\right). \tag{2.22}$$

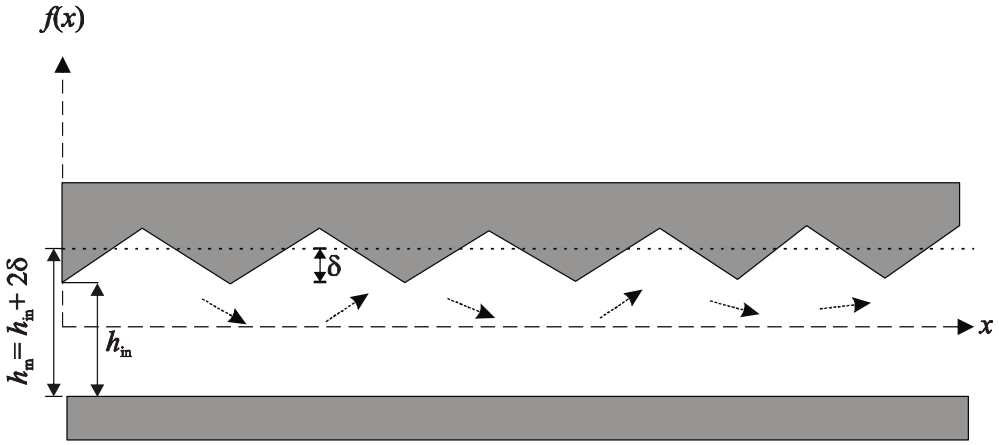

Figure 2.12 Nonparallel planar fracture geometry with opening h_{in} and asperity height, 2δ (After Ge, 1997).

Figure 2.13 shows the results obtained by Ge (1997). From this, he concluded that the absolute error in permeability increased by increasing the inclination angle of the asperity. He suggested the error in the permeability estimation was small for nearly parallel surfaces, but increased rapidly as a result of increasing the asperity inclination angle.

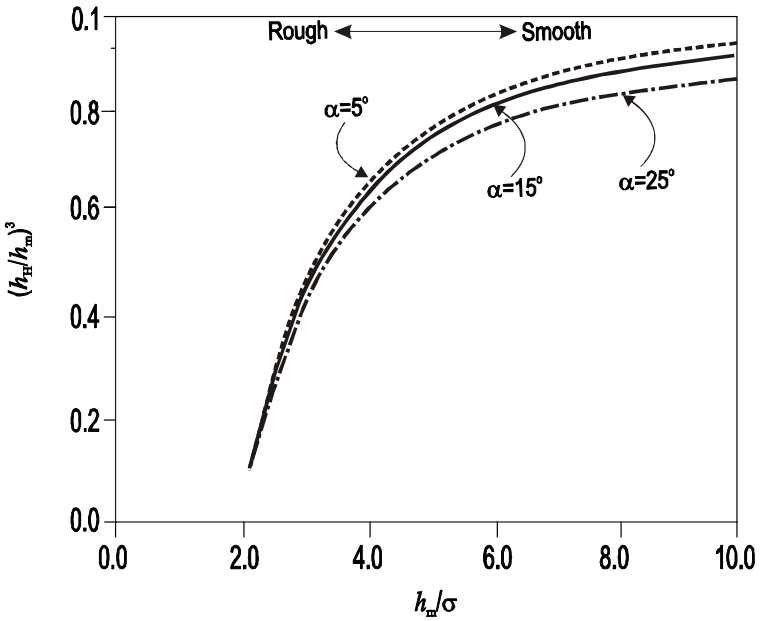

Figure 2.13 Normalised permeability as a function of standard deviation of roughness and the inclination angle of the upper surface (After Ge, 1997).

2.1.4 Joint Roughness Coefficient (JRC)

The joint roughness coefficient (JRC) proposed by Barton and Choubey (1977), is perhaps the most commonly used parameter for quantifying fracture surface roughness. Based on their extensive lab experiments, they proposed 10 typical rock profiles with different roughness and waviness as being representative of real rock fracture geometries. The considered ten profiles, ordered from smoothest to the roughest, were assigned different JRC values ranging from 1 to 20. By undertaking a visual comparison of a real fracture surface, a profile with closest geometry to the fracture should be chosen and assigned the same JRC value to the real fracture surface. The exemplar JRC profiles are shown in Figure 2.14. JRC has been correlated to the mechanical and hydraulic properties of rock fractures. For this reason, and also the simple application of this approach, JRC has been widely used in different rock engineering applications to study the hydro-mechanical properties of fractures, even though it is well known that JRC is a subjective method which suffers from a number of other deficiencies (Rasouli, 2003).

Following their experimental analysis, Barton and Choubey (1977) obtained the JRC values by back-calculation from the shear strength of fracture (τ) as

$$JRC = \frac{\lambda \tan(\tau/\sigma_{\mathrm{n}}) - \phi_{\mathrm{b}}}{\log_{10}^{(JCS/\sigma_{\mathrm{n}})}} \ , \tag{2.23}$$

where, σ_{n} is the effective normal stress, JCS is the joint wall compressive strength, λ is the maximum amplitude for a measured profile length (L_{e}), and ϕ_{b} is the basic function angle which is obtained from residual shear tests on a flat un-weathered rock surface.

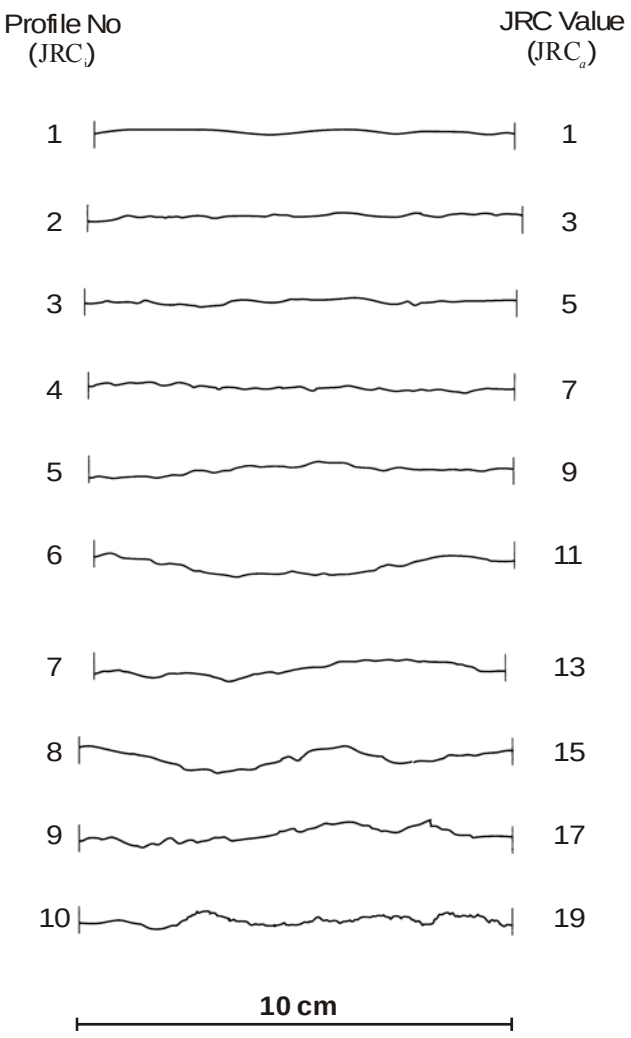

Figure 2.14 JRC exemplar profiles (After Barton and Choubey, 1977).

Barton *et al.* (1985) performed an experimental analysis on the fluid flow coupled with the shear-flow behaviour of rock fractures and compared their results with data used by other researchers (see Figure 2.15). From this study, they proposed the following correlation between mechanical aperture (h_m), and hydraulic aperture, or theoretical parallel plate analogy (h_H) in relation to JRC:

$$h_H = \frac{JRC^{2.5}}{\left(h_m / h_H\right)^2} \tag{2.24}$$

or

$$h_H = \frac{{h_m}^2}{JRC^{2.5}}.$$

In equation 2.24, h_m and h_H are expressed in μm. It should be noted that this equation is only valid for $h_m \geq h_H$. From this equation, and as seen from Figure 2.16, as

fracture surface becomes rougher, the difference between the mechanical and hydraulic aperture increases (i.e. larger h_m / h_H ratios). Also, the ratio of h_m / h_H even for smooth natural joints is likely to be higher than 1.0, which is believed to be due to the influence of the roughness and the tortuosity of the flow channel which causes an increase in the head losses.

Figure 2.15 also shows that even for very rough profiles, the influence of roughness and tortuosity decreases as the fracture opens and the ratio of h_m/h_H approaches 1.0 (Barton, 1982). During shearing of a fracture, equation 2.24 only applies to pre-peak regions corresponding to a maximum shear displacement, $u_{sp.}$ Further studies regarding this concept were also carried out by Barton and de Quadros (1997), and Olson and Barton (2001).

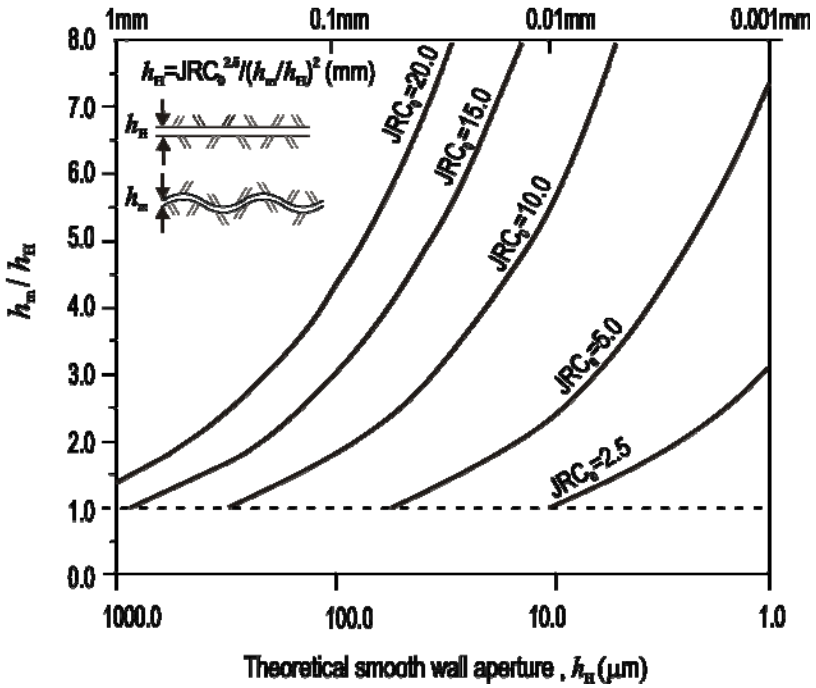

Figure 2.15 Relationship between fracture wall aperture and h_m/h_H as a function of JRC data (After Barton, 1982).

The latter researchers extended the application of Equation 2.24 to a post peak region where the shear displacement was larger than approximately 0.75 u_{sp}. In this situation, the profile had undergone some failure and roughness of the profile was expected to be reduced. They therefore suggested that instead of the original profile JRC, the mobilised JRC denoted as JRC_{mob} should be utilised and accordingly proposed the following correlation for the post peak phase:

$$h_{\mathrm{H}} = \left(\frac{h_{\mathrm{m}}}{h_{\mathrm{H}}}\right) JRC_{\mathrm{mob}}^{2} \,. \tag{2.25}$$

Figure 2.16 gives an example output plot of equations 2.24 and 2.25. The starting point of the shear test is shown by (o), which depends on an initial assumed mechanical aperture (h_{m0}). The boundary between pre-peak and peak shear strength is shown by (•).

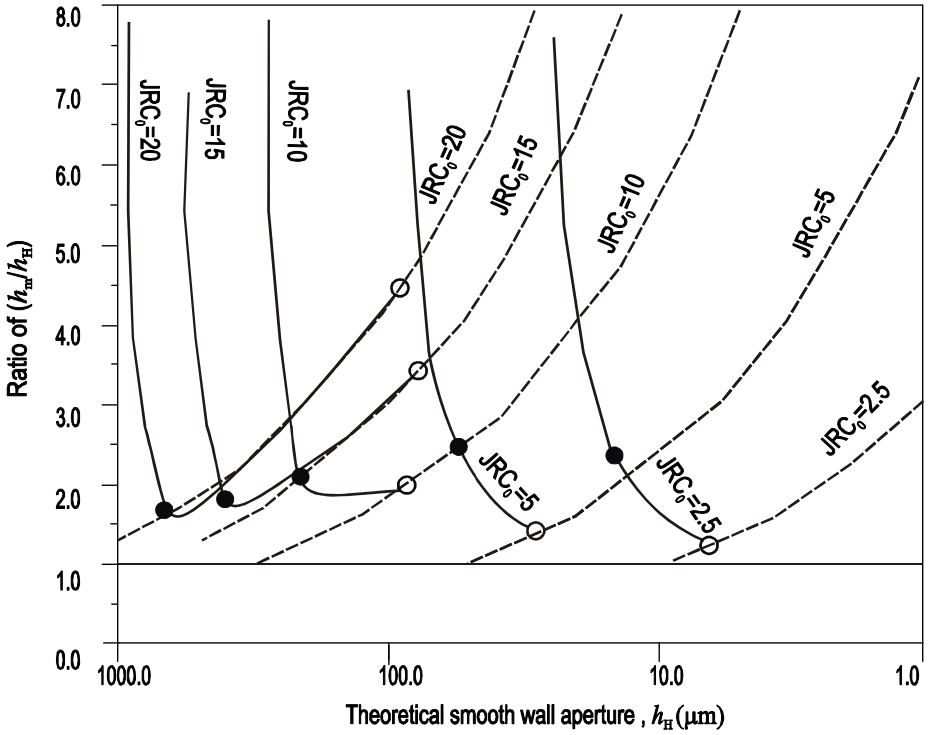

Figure 2.16 Hydraulic aperture, h_{H}, versus ratio for both normal loading/unloading, $h_{\mathrm{m}}/h_{\mathrm{H}}$ (Olson and Barton, 2001).

Through their laboratory experiments, Barton and de Quadros (1997) introduced relative hydraulic roughness ($K/2h_{\mathrm{m}}$), similar to that originally proposed by Louis (1969) to develop the isotropic coefficient of hydraulic conductivity (K_{H}) as

$$K_{\mathrm{H}} = \frac{g{h_{\mathrm{H}}}^{2}}{12\nu}\frac{1}{C} \tag{2.26}$$

where

$$C = a + b(K/2h_{\mathrm{m}})^{1.5} \,. \tag{2.27}$$

In the above equations, K is the difference between the highest peak and the lowest valley of the physical wall roughness, C is the hydraulic roughness coefficient, g is the gravity (m/s^2), h_m is the joint mechanical aperture (m), v is the coefficient of

kinematic viscosity of the fluid (m^2/s), and a and b are the constants of the equation. Also,

$$h_m \geq 15.15\ K \text{ or } K/2h_m \leq 0.033 \tag{2.28}$$

Figure 2.17 shows the relationship between the relative roughness and the roughness coefficient, as proposed by different people. This figure shows that the validity of the above developed equation is when $K/2h_m \leq 0.033$, in which case when the roughness coefficient, C, tends towards unity.

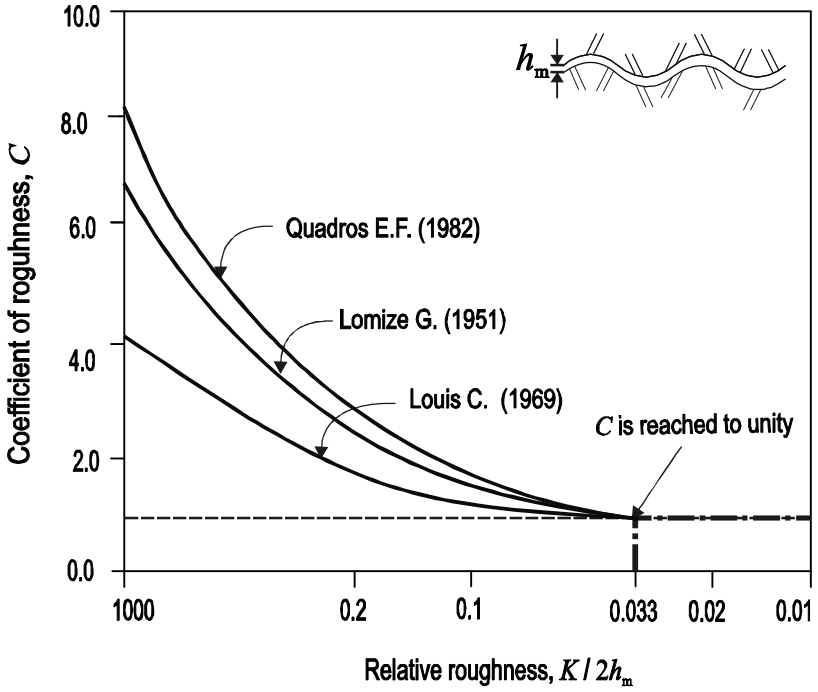

Figure 2.17 Coefficient of roughness (C) versus relative roughness $K/2h_m$ (After Barton and Quadros, 1997).

On further investigation, Barton and de Quadros (1997) correlated the relative hydraulic roughness to JRC through the correlation below:

$$\frac{K}{2h_m} = \frac{JRC^{3.5}L}{800h_m^{\ 2}}. \tag{2.29}$$

In this equation, L (mm) is the measured profile length. According to their observations, assuming the upholding of cubic law, this correlation is valid for low values of $K/2h_m$ for flow in joints with correlated and uncorrelated rock surfaces.

Scesi and Gattinoni (2007) proposed relationships to estimate the hydraulic conductivity tensor in order to study water flow in fractured rock masses. They derived different hydraulic conductivity equations, based on the relative roughness (δ/D_h) which was initially proposed by Louis (1967) in relation to the JRC from Equation 2.24,

proposed by Barton *et al.* (1985). Their derived equations are for a profile geometry shown in Figure 2.18 for different fluid flow conditions (i.e. laminar, inertia and turbulent). Here, D_h is the hydraulic diameter of the non-circular channel (i.e. K per twice the h_m in rock fractures).

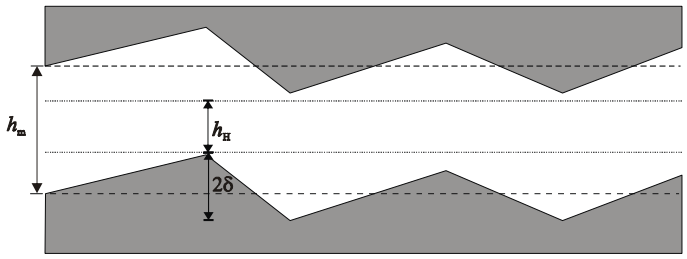

Figure 2.18 Fracture geometry used by Scesi and Gattinoni (2007).

The plot of mechanical aperture (h_m), versus hydraulic conductivity (K_H) shown in Figure 2.19 indicates a reduction in hydraulic conductivity as a result of increasing JRC, or profile roughness for inertia flow. That is, the general expectation from laminar flow passing through a rough channel. In that situation, fluid is moving through the tortuous pathways. However, profile roughness is less influential at large aperture values in laminar flows. Therefore, Scesi and Gattinoni (2007) proposed the use of a following simplified equation for Poiseuille flow through fracture planes to estimate hydraulic aperture as

$$K_{H\mathrm{i}} = g h_{\mathrm{Hi}}^{\ 2} / 12\nu \ , \tag{2.30}$$

where, subscript i refers to i_{th} fracture.

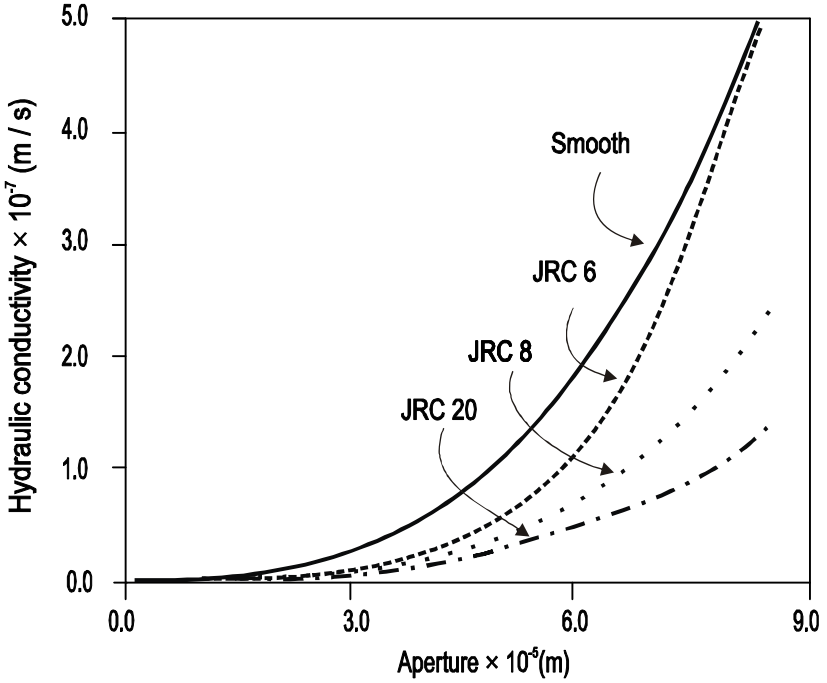

Figure 2.19 Hydraulic conductivity as a function of aperture and JRC for non-parallel laminar conditions (After Scesi and Gattinoni, 2007).

They also showed the range of validity of their equations by plotting the mechanical aperture (h_m) versus JRC which is shown in Figure 2.20.

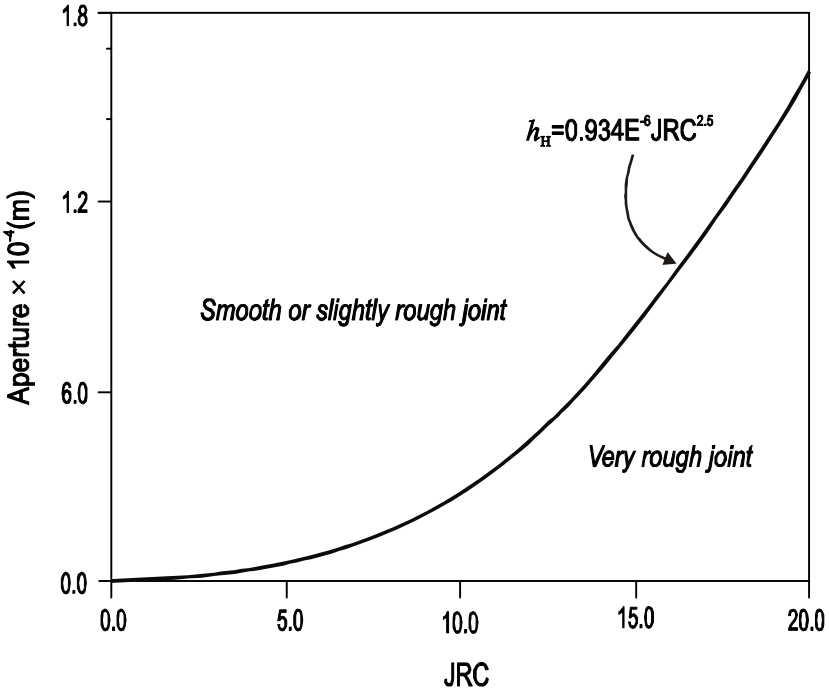

Figure 2.20 Fracture aperture as a function of JRC (After Scesi and Gattinoni, 2007).

According to Figure 2.20, they obtained a maximum aperture for each series of JRCs where the effect of roughness was considerable in the laminar flow regime. Their

results indicated that the maximum aperture for JRC = 2, 4, 6 (i.e. with not very marked asperities) was roughly 10^{-4} m, for JRC = 8, 10, 12, 14, (i.e. intermediate roughness) was between 10^{-4} and 10^{-3} m, and for JRC = 16, 18, 20 (with high roughness) was around10^{-3} m.

Giacomini *et al.* (2008) studied steady-state flows in a porous medium using the 3D FEM code ABAQUS and compared their numerical study results with mechanical shear stress tests proposed originally by an earlier study. They applied Darcy's law for a saturated porous rock and developed a model based on the cubic law to investigate the flow anisotropy through a natural joint. They also used JRC and Z_2 proposed by Tse and Cruden (1979) to estimate the micro scale roughness and the hydraulic aperture (i.e. equation 2.24) for each element of their numerical model. Their results indicated higher values of isotropic distribution of flow obtained from numerical models and the Reynolds equation compared to experimental results. However, they reported the overestimation of flow rate values by Reynolds equation by two orders of magnitude compared to their numerical model.

Using CFD with three dimensional meshes, Crandall *et al.* (2010b) examined the relation of macroscopic roughness parameters JRC and fractal (D_f) with the effective flow through the fractures in Berea sandstone. They recorded the pressure drop from the simulation and estimated the h_H by back calculating from the cubic law. Their CFD simulation for water flow and low Reynolds number flow (i.e. Re<1), indicated that fractures with a higher JRC and D_f showed tortuous pathways and 35 times smaller transmissivity compared to the smaller JRC and D_f. According to Figure 2.21, they reported a linear relationship between JRC and transmissivity.

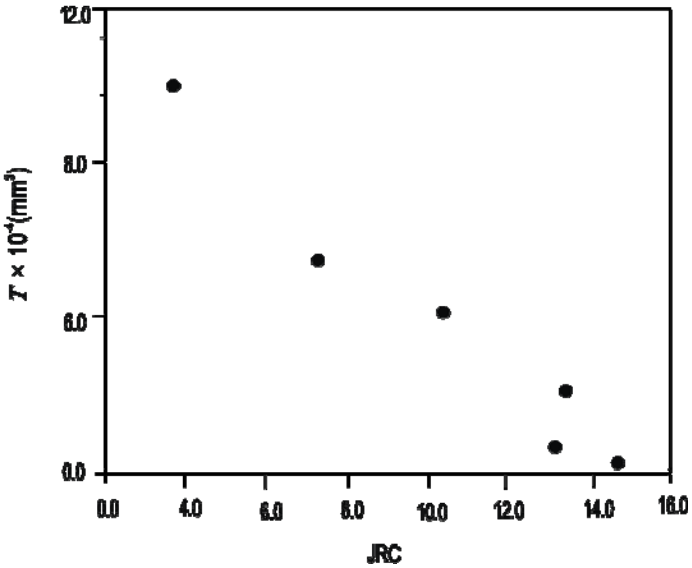

Figure 2.21 Transmissivity, T, versus JRC (After Crandall *et al.* 2010b).

They also showed that the hydraulic aperture (h_H) could be approximated by the average vertical distance between each segment of the top and bottom surface of the fracture, h_V, (i.e. vertical aperture) which is in contrast for rougher fractures with higher JRC's due to the effect of roughness on fluid resistance properties. Their results presented as normalised hydraulic aperture and this is shown in Figure 2.22.

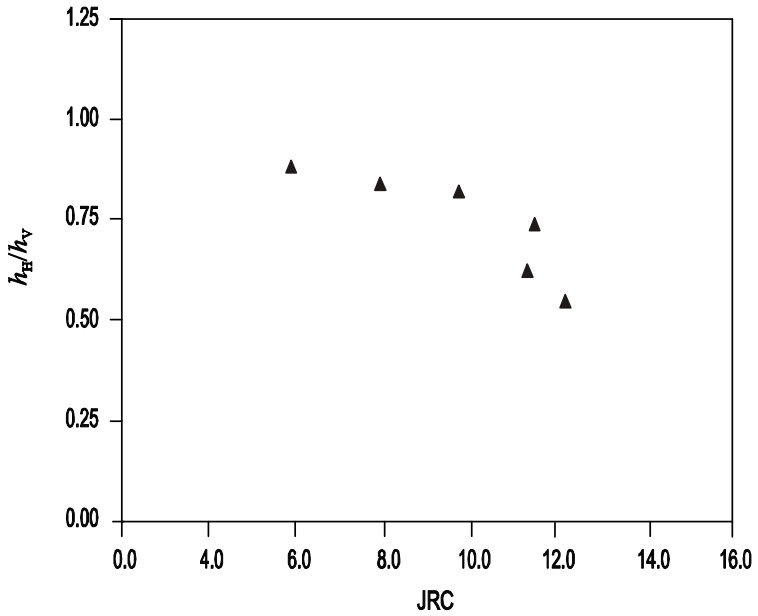

Figure 2.22 Normalized h_H versus JRC (Crandall *et al.*, 2010b).

The above literature indicates that JRC has been extensively used to consider the effect of surface morphology in the hydraulic response of fractures. However, the subjective nature of JRC for quantitative characterisation of roughness remains debatable. This is perhaps the reason for attempts being made to propose an objective statistical parameter for roughness determination after JRC proposed, some of which were presented in subsection 2.1.3.

In this research, a new roughness parameter recently developed using Riemannian geometry (Rasouli and Harrison, 2010) in fluid flow studies of rough profiles will be used. In the next subsection, a brief review of Riemannian dispersion parameters as a new roughness measurement parameter is given.

2.1.5 Riemannian roughness parameter, D_{R1}

The idea of characterising the roughness of a rough fracture based on the distribution of deviation angles from a smooth plate was firstly introduced by Barton (1971). Fecker and Rengers (1971), through their practical measurements using a

compass mounted on a smooth plate, also found that as the base plate (sampling scale) increased, the scatter of the measurements decreased. Therefore, statistical analysis of deviation angles is in fact an approach that can quantify surface roughness and, for example, the standard deviation of angles of the plate measured at different scales and at different orientations could lead to a parameter for characterising roughness at different scales and orientations. This brief explanation indicates two important properties in roughness measurement: scale dependency and anisotropy.

By extracting unit normal vectors from a surface, Rasouli and Harrison (2010) analysed these vectors statistically to characterise surface roughness. In the simple case of a linear profile, introducing a hypothetical connected pin sampling device, the unit normal vectors to the profile can be extracted at different scales and on a random sampling basis. This is shown in Figure 2.23.

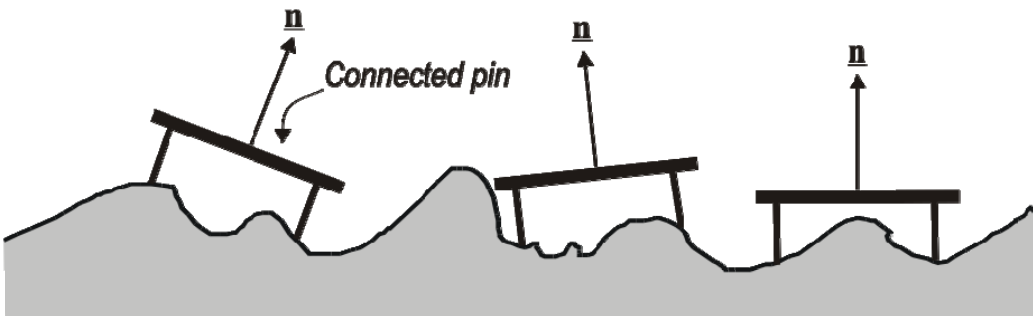

Figure 2.23 Profile sampling technique using a connected pin (Rasouli and Harrison, 2010).

Rasouli and Harrison (2010) argued these normal vectors were all located on a periphery of a unit circle, i.e. these vectors were circular data and therefore statistical analysis of such data was to be carried out in Riemannian space, rather than in Euclidean space, as is a common approach. A simple difficulty with Euclidean geometry is that, for example, the mean of two unit vectors (0.0, 1.0) and (1.0, 0.0) is (0.50, 0.50), which corresponds to a point located inside the circle, while the original data are points located on the circle. This means that Euclidean geometry does not take into account the shape of the data distribution.

As shown in Figure 2.24, the transfer of 2D Euclidean data in Riemannian space is obtained by unwrapping the circle. In this 1D space, the data are points located on a line called the principal chart, with their coordinates being defined by the distance from a point defined in this line. For the two vectors mentioned above, the corresponding coordinates in Riemannian space are points with lengths of 0 and $\pi/2$, i.e. the curved length on the circle. The simplest 2D geometry in Euclidean space is a unit circle and its

correspondence in Riemannian space is a 1D line. All statistical analysis of vectors (including data mean and variance) can now be performed in 1D Riemannian space. For the two example vectors, the mean value is $\pi/4$. Once the calculations are completed, the data can be transferred back to the Euclidean space, i.e. corresponding to the unit circle. In this case for example, the mean of the data will be located on the unit circle. In the above simple example, the mean vector as is transferred back to the circle shows point (0.50, 0.50) but this time it is located on the circle. In other words, for the case of linear profiles, the data can be considered as their angles with respect to a datum axis. In the example here, the representations of the two vectors in Riemannian space are 0 and $\pi/2$, corresponding to the angle identifying vectors (0.0, 1.0) and (1.0, 0.0).

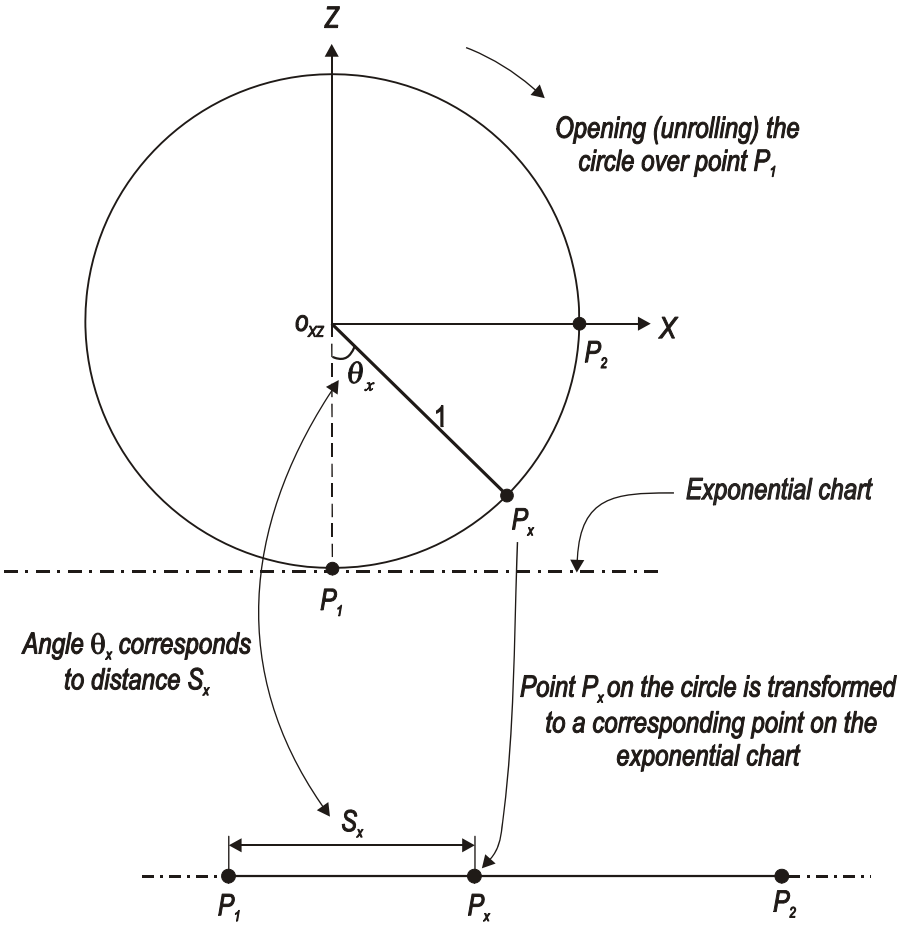

Figure 2.24 Riemannian representation of a 2D unit vector in Euclidean space (Rasouli and Harrison, 2010).

Similar to what was explained for a 2D linear profile above, the unit vectors extracted from a rock surface using a hypothetical sampling device will be located on the surface of a unit sphere. The Riemannian representation of a unit sphere is a 2D plane. Transformation of data from a unit sphere to its corresponding Riemannian space

is not straightforward and requires complicated mathematical computations. The reader is referred to Rasouli and Harrison (2010) for a detailed discussion on this.

For linear profiles, Rasouli and Harrison (2010) proposed the 1D Riemannian dispersion parameter (D_{R1}) corresponding to the standard deviation of unit normal vectors calculated on the principal chart as a measure of profile roughness. The larger the D_{R1}, the rougher the profile will be.

For a synthetic symmetric triangular profile shown in Figure 2.25,

$$D_{R1} = \theta = \tan^{-1}(2K/\lambda). \tag{2.31}$$

which shows that for such a profile the base angle (represented in radians) of the profile is the measure of roughness in Riemannian space. D_{R1} changes between 0 and $\pi/2$ but in real rock profiles the base angle is less likely to be greater than about 10 degrees (i.e. 0.175).

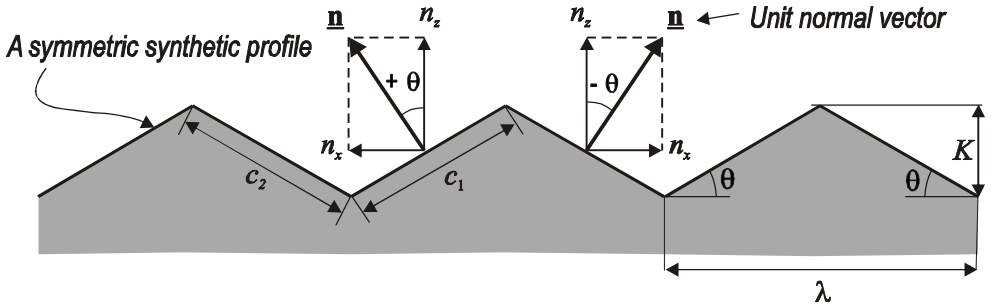

Figure 2.25 Unit normal vectors to a symmetric synthetic profile (Rasouli and Harrison, 2010).

In Figure 2.26, an asymmetric synthetic triangular profile is shown. The geometry of this profile is identified using two angles θ_1 and θ_2 corresponding to chords c_1 and c_2, respectively. For such a profile D_{R1} is obtained as

$$D_{R1} = \left[K_1(\theta_1 - \bar{\theta})^2 + \frac{c_2}{c_1} K_1(\theta_2 - \bar{\theta})^2 \right]^{1/2} + \left(K_1(\theta_1) + \frac{c_2}{c_1} K_1(\theta_2) \right) \tag{2.32}$$

where

$$c_1 = \left(\lambda_1^{\,2} + h^2\right)^{1/2}, c_2 = \left(\lambda_2^{\,2} + h^2\right)^{1/2}, K_1 = c_1/(c_1 + c_2). \tag{2.33}$$

As the symmetry ratio (λ_1/λ_2) increases towards unity ($\lambda_1 \rightarrow \lambda_2 = \lambda$), it can be seen that equation 2.32 approaches equation 2.33, i.e. roughness of a symmetric triangular profile.

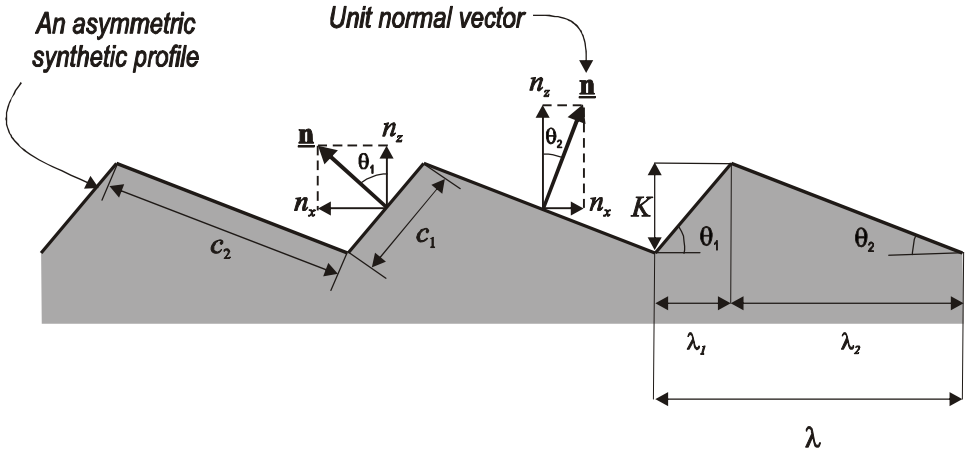

Figure 2.26 Unit normal vectors to an asymmetric synthetic profile (Rasouli and Harrison, 2010).

For a sinusoidal profile in the general form of $z = \delta \sin bx$, with amplitude 2δ and wavelength $\lambda = 2\pi/b$ (or aspect ratio δ/λ), as shown in Figure 2.27, calculations of D_{R1} results in

$$D_{R1} = \left(S_{R1}^2\right)^{1/2} = \left[\frac{2}{3}\left(\tan^{-1}\left(2\pi\delta/\lambda\right)\right)^3\right]^{1/2} = \left(\frac{2}{3}\right)^{1/2}\left[\tan^{-1}\left(2\pi\delta/\lambda\right)\right]^{3/2}, \qquad (2.34)$$

which indicates that profile roughness increases as the wavelength (λ) decreases or amplitude (2δ) increases, but not as a linear proportion. From this equation, the maximum value of roughness is 1.6074. By comparing this equation to equation 2.31, it can be found that geometrically, a sinusoidal profile shows a larger range of roughness values than a synthetic symmetric profile. This is because the maximum deviation of normals on a sinusoidal profile is larger than on the corresponding symmetric profile (Rasouli and Harisson, 2010).

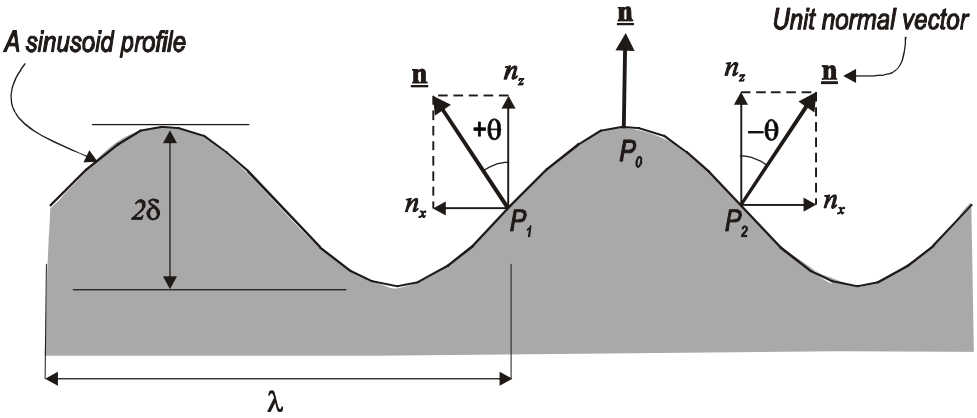

Figure 2.27 Unit normal vectors to a sinusoidal profile (Rasouli and Harisson, 2010).

2.2 Hydraulic aperture estimation for synthetic profiles

Analytical formulae have been proposed to estimate hydraulic aperture (h_H) for profiles with synthetic geometries. A review of these analytical solutions will assist in understanding the effect of geometrical properties of a rough channel on fluid flow. Some researchers have suggested simulating real rock fractures with synthetic channels and used similar formulae to estimate hydraulic aperture and pressure drop along the profile (Elswoorth and Goodman, 1986; Zimmerman *et al.*, 1991). Hence, in this section a brief review of analytical solutions proposed for flow channels with sinusoidal and triangular wall geometries are given.

2.1.6 Series and parallel flow

The direction of fluid flow through a fracture can be considered either parallel or perpendicular to the aperture variation. These are referred to as series and parallel flows (Bear, 1988; Federico, 1998; Zimmerman and Bodvarsson, 1996) respectively, as shown in Figure 2.28. From this figure, it is easy to see the effect of surface morphology or roughness is more important in series flow compared to parallel flow. Therefore, in this work, only the formulae for series flow will be given as this is also more likely to occur in natural fractures.

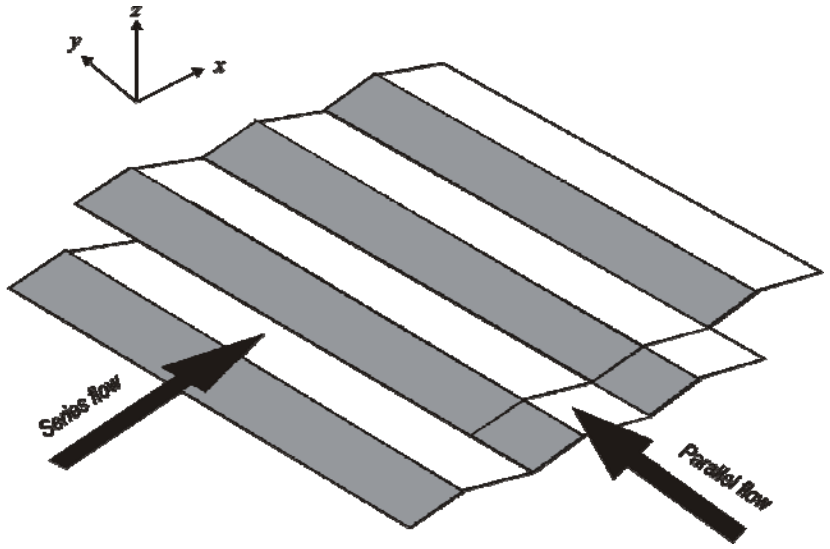

Figure 2.28 Parallel and series flow.

In series flow, the total pressure (ΔP) in a channel with length L can be assumed as the summation of pressure in N discrete segments with individual length L_i. Each segment contains constant aperture h_i and the total fracture width (w) (Bear, 1988). Thus

$$\Delta P = \sum_{i=1}^{N} \Delta P_i \,. \tag{2.34}$$

Assuming the applied pressure gradient between the inlet and outlet being $\left|\overline{\nabla P}\right| = \left(P(0) - P(L)\right)/L$, the flow rate in each segment, which is equal to the total flow rate in the case of series flow, is obtained as (Federico, 1998):

$$Q = \frac{w\left|\overline{\nabla P}\right|}{12\mu}\left\langle h^{-3}\right\rangle^{-1} \quad , \tag{2.35}$$

where $\langle\ \rangle$ denotes the average aperture of the rough profile which will be replaced in the cubic law. In comparison, the flow rate for parallel flow is obtained as

$$Q = \frac{w\left|\overline{\nabla P}\right|}{12\mu}\left\langle h^{3}\right\rangle \,. \tag{2.36}$$

In the above equations $\left\langle h^{-3}\right\rangle^{-1}$ and $\left\langle h^{3}\right\rangle$ determine the hydraulic aperture for series and parallel flows, respectively. The hydraulic aperture in series and parallel flow is also referred to as the harmonic and arithmetic mean, respectively (Zimmerman and Bodvarsson, 1996).

It is also well known that the actual effective conductivity is bounded between the series flow (as the lower limit) and the parallel flow (as the upper limit). In real cases, a mixture of these two occurs and therefore Zimmerman *et al.* (1991) proposed the use of the geometric mean (h_g) of the conductivities as

$$h_g^3 = \sqrt{\left\langle h^{-3}\right\rangle^{-1} \times \left\langle h^{3}\right\rangle} \,. \tag{2.37}$$

2.1.7 Sinusoidal profiles

Letalleur *et al.* (2002) developed an analytical model to study the effects of lubricant film flow where the fluid is assumed it is undergoing pressure while sheared between two parallel sinusoidal wavy surfaces in a sliding motion. Figure 2.29 shows the geometry of the profile with the bottom and top surface velocities of U_1 and U_2, respectively. We refer to this geometry as a non-mate channel as there is a half wavelength phase difference between the two wall geometries. In contrast, the mate geometry is the one with both walls being parallel to each other. Also, it is assumed that there is no contact between asperities of upper and lower walls.

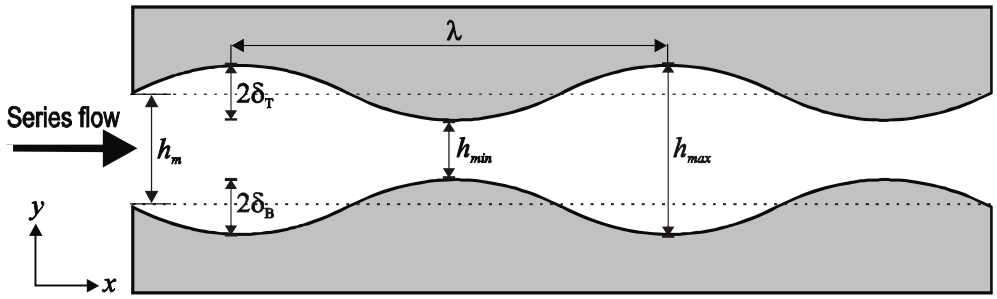

Figure 2.29 Geometry of a sinusoidal surface (After Letalleur *et al.*, 2002).

The aperture field, $h(x)$ is obtained as the area between the top and bottom wall of the fracture, i.e.

$$h(x) = h_2(x) - h_1(x), \tag{2.38}$$

where $h_1(x)$ and $h_2(x)$ are the geometry equation of the bottom and top surfaces, respectively. This was proposed by Letalleur (2002) as

$$h_i(x,t) = h_{i0} + \sqrt{2}\sigma_i \sin\left(\frac{2\pi}{\lambda}(x - U_{ix}t) + \varphi_i\right), \tag{2.39}$$

Where, h_{i0} is the mean planes of surface i, φ_i is the surface phase (i.e. amount of shear displacement) at initial time t_0, and σ is the root mean square (r.m.s) roughness of each surface. The r.m.s roughness (σ) is similar for both top and bottom surfaces and can be defined in relation to its relative roughness (i.e. δ_t or δ_b, in Figure 2.30) as $\sigma_i^2 = \delta_i^2/2$ with δ_i being the relative roughness for each top and bottom surface.

In Poiseuille flow, which is the flow type appropriate for our studies (see Section 1.1.1), the walls remain static and therefore $U_1 = U_2 = 0$. Considering this assumption, equations 2.38 and 2.39 lead to

$$h(x) = h_m + \delta_T \sin\left(\frac{2\pi}{\lambda}(x) + \varphi_2\right) - \delta_B \sin\left(\frac{2\pi}{\lambda}(x) + \varphi_1\right). \tag{2.40}$$

In this equation, h_m is the mean distance between the two surfaces.

Also for a non-mate sinusoidal geometry, as shown in Figure 2.30, for the lower and upper wall of fracture $\varphi_1 = 0$ and $\varphi_2 = 2\pi n/\lambda$, respectively. Here, n is the shear offset of the lower wall with respect to the upper wall, which changes between 0 and λ. Hence, φ_2 has a range between 0 and 2π. Considering this and performing some mathematical calculations (see Letalleur *et al.*, 2002 for details), the aperture field equation for a non-mate sinusoidal profile is obtained as

$$h(x) = h_{\mathrm{m}}\left[1 + \frac{2\delta_{\mathrm{T}}}{h_{\mathrm{m}}}\sin(\frac{\pi n}{\lambda})\sin(\frac{2\pi x}{\lambda} + \frac{\pi n}{\lambda} - \frac{\pi}{2})\right]. \tag{2.41}$$

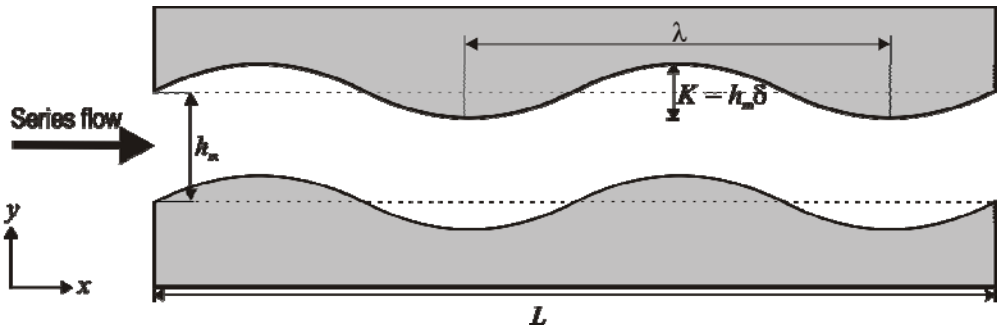

Figure 2.30 Geometry of a non-mate sinusoidal surface.

It is to be noted that in equation 2.41 the term $2\delta_{\mathrm{T}}$is twice the relative roughness of the top surface (or bottom surface) and is sometimes referred to as roughness (K).

The hydraulic aperture term, is estimated as

$$\left\langle h^{-3}\right\rangle = \frac{1}{2\pi}\int_0^{2\pi} \frac{1}{h_m{}^3\left[1 + \frac{K}{h_{\mathrm{m}}}\sin(\frac{\pi n}{\lambda})\sin(\frac{2\pi x}{\lambda} + \frac{\pi n}{\lambda} - \frac{\pi}{2})\right]^3} dx\,. \tag{2.42}$$

The solution of this integral is trivial and requires use of the Sommerfeld integrals (Constantinescu, 1995). The details of this can be found in (Maday, 2002) and results in

$$\left\langle h^{-3}\right\rangle = \frac{1 + (C^2/2)}{h_{\mathrm{m}}^3\left(1 - C^2\right)^{5/2}} \tag{2.43}$$

and

$$\left\langle h^{-3}\right\rangle^{-1} = h_{\mathrm{m}}^3\frac{\left(1 - C^2\right)^{5/2}}{1 + (C^2/2)}\,, \tag{2.44}$$

where C is a constant parameter and in this case

$$C = \frac{K}{h_{\mathrm{m}}}\sin\left(\frac{\pi n}{\lambda}\right). \tag{2.45}$$

Assuming K=$h_{\mathrm{m}}\delta$ for a sinusoidal profile (figure 2.30) with constant aperture (Zimmerman *et al.*, 1991) in which δ is the relative roughness for the top or bottom surface, equation 2.44 can be rewritten in the form of

$$\left\langle h^{-3}\right\rangle^{-1} = h_{\mathrm{m}}^3\frac{\left[1 - \delta^2\sin^2\left(\frac{\pi n}{\lambda}\right)\right]^{5/2}}{1 + \left[\frac{\delta^2}{2}\sin^2\left(\frac{\pi n}{\lambda}\right)\right]}. \tag{2.46}$$

Equation 2.46 allows calculation of hydraulic aperture at any relative shear displacement between the two walls of a sinusoidal shaped profile to be made. This equation indicates that for a mate channel geometry (i.e. n=0) $\left\langle h^{-3}\right\rangle^{-1}=h_m^3$, the hydraulic aperture is equivalent to the mean aperture, as expected. For n=λ/2, the geometry shown in Figure 2. 31 will be changed to the geometry shown in Figure 2.30 (i.e. a non-mate channel) with its hydraulic aperture being

$$\left\langle h^{-3}\right\rangle^{-1}=h_{\mathrm{m}}^3\frac{\left(1-\delta^2\right)^{5/2}}{1+\left(\delta^2/2\right)}. \tag{2.47}$$

It is noted that in deriving this equation, the effect of profile wavelength (λ) has been neglected due to the assumption of the gradual aperture variations, i.e., $h/\lambda << 1$. This is why in equation 2.47 profile wavelength does not appear. Equation 2.47 indicates that the hydraulic aperture in the series is less than the mean aperture, h_m.

The roughness value, δ, *can* be linked to Riemannian roughness parameter (D_{R1}) introduced in Subsection 2.1.5 as

$$\delta=\frac{\lambda\tan^{2/3}\left(D_{R1}\times\sqrt{1.5}\right)}{2\pi}, \tag{2.48}$$

and therefore the hydraulic aperture in terms of D_{R1} for series flow can be written as (from equations 2.46)

$$\left\langle h^{-3}\right\rangle^{-1}=h_m^3\frac{\left[1-\left[\frac{\lambda^2\tan^{4/3}\left(D_{R1}\times\sqrt{1.5}\right)}{4\pi^2}\right]\sin^2\left(\frac{\pi n}{\lambda}\right)\right]^{5/2}}{1+\left[\left(\frac{\lambda^2\tan^{4/3}\left(D_{R1}\times\sqrt{1.5}\right)}{8\pi^2}\right)\sin^2\left(\frac{\pi n}{\lambda}\right)\right]} \tag{2.49}$$

or in the special case of a mate channel geometry (i.e. a shear offset of n=λ/2), similar to equation 2.47 as

$$\left\langle h^{-3}\right\rangle^{-1}=h_m^3\frac{\left[1-\frac{\lambda^2\tan^{4/3}\left(D_{R1}\times\sqrt{1.5}\right)}{4\pi^2}\right]^{5/2}}{1+\left[\frac{\lambda^2\tan^{4/3}\left(D_{R1}\times\sqrt{1.5}\right)}{8\pi^2}\right]}. \tag{2.50}$$

In Figure 2.31, the hydraulic aperture versus relative profile roughness (δ) calculated from equations 2.47 and 2.50 is shown. To show the effect of changing profile roughness, in this plot a maximum aperture (the distance between the two peaks of upper and lower profile) of h_{max}=2 was assumed and for different values of roughness

the mean aperture (h_m) was calculated as $h_m = h_{max} - 2\delta = 2 - 2\delta$. It should be noted that the plot, shown in Figure 2.31, is based on an estimation of the hydraulic aperture by applying the different mean aperture (h_m), as changing the relative roughness causes changes in the mean aperture (i.e. mean aperture increases by increasing the relative roughness). Also, the profile wavelength (λ) is two in this example; however, as mentioned earlier, its effect is negligible in these calculations considering that the ratio of profile height to wavelength is high. For comparison purposes, the plot of D_{R1} versus hydraulic aperture is also shown in this figure. The results show a close agreement between the results of the two approaches, indicating applicability of D_{R1} in representing profile roughness effects in the hydraulic analysis of channels. However, for real rock profiles, it is more appropriate to use D_{R1} in characterising fracture roughness and hence it is a preferred parameter for use.

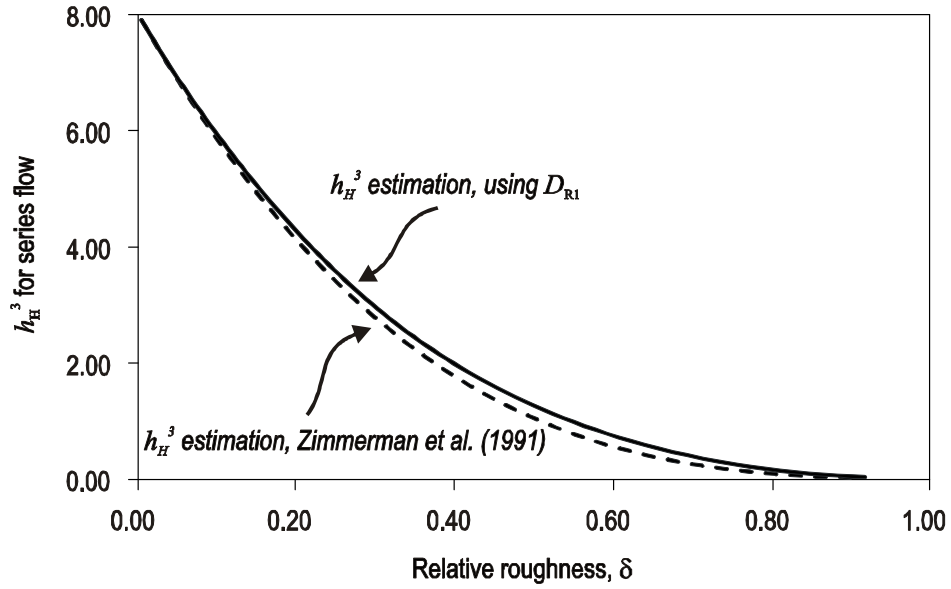

Figure 2.31 Hydraulic aperture of a sinusoidal channel as a function of roughness.

2.1.8 Symmetric triangular profiles

Similar to the sinusoidal channels discussed in the previous subsection, analytical solutions can be developed to estimate hydraulic aperture in a fluid channel with symmetric triangular geometry walls. This is discussed here.

In an early attempt, Elsworth and Goodman (1986) studied the effect of shear offset and normal closure on the hydraulic aperture and conductivity of rock joints by employing different profile geometries. They considered sinusoidal and triangular profile geometries as an approximate for observation of natural joints which was applied in both non-tortuous and tortuous flow under laminar and turbulent flow

conditions. According to their study, they developed expressions to estimate hydraulic aperture under different geometry profiles. However, the proposed expression for non-mate triangular profile (Figure 2.32) was applicable for parallel flow. For the purpose of this research, an equation is being developed to estimate hydraulic aperture for such a profile in a series flow based on the proposed expression by the Elsworth and Goodman (1986) study. The developed equation will then be applied to estimate the hydraulic aperture within a unit cell corresponding to a half wavelength of a symmetric triangular shaped channel later in this subsection. In that regard, the fluid is assumed to travel from left to right, and parallel to the aperture variation (i.e. series flow).

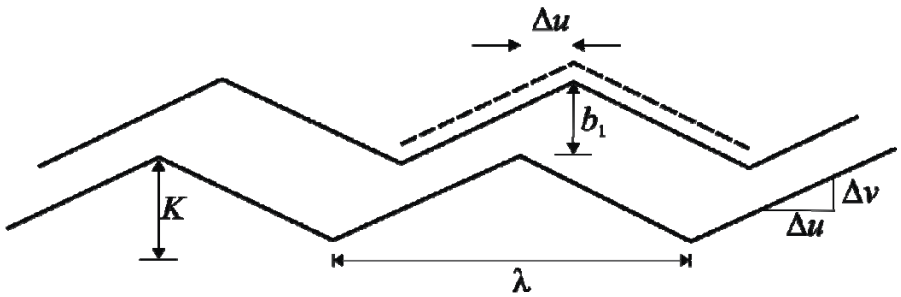

Figure 2.32 Triangular geometry profile (After Elsworth and Goodman, 1986).

In Figure 2.32, b_1 is the vertical displacement of the top surface for a mate or non-mate saw tooth profile. That parameter can be considered as the mean aperture (h_m) for a mate saw tooth profile (Elsworth and Goodman, 1986). Accordingly, equation 2.51 can be used to quantify the hydraulic aperture in series for a mate saw-tooth profile:

$$\left\langle h^m \right\rangle = \frac{\Delta u}{\lambda \Delta v (m-1)} \left[\frac{1}{(h_m - \Delta v)^{m-1}} - \frac{1}{(h_m + \Delta v)^{m-1}} \right] + 4\left(\frac{1}{2} - \frac{\Delta u}{\lambda} \right) \left[\frac{1}{(h_m - \Delta v)^{m}} - \frac{1}{(h_m + \Delta v)^{m}} \right] \tag{2.51}$$

where, Δu and Δv are the shear and normal displacement respectively, m is an arbitrary exponent (indicate the flow behavior) which is considered as three for laminar flow, h_m is the mean aperture, and λ is the wavelength of the triangular profile.

The term Δu is assumed to be equal to $\lambda/2$ in which the top wall is shearing above the bottom wall, which indicates a non-mate saw tooth profile.

The normal displacement, Δv, can be applied into Equation 2.51 for a non-mate saw tooth profile in the term of

$$\Delta v = \frac{2 \Delta u K}{\lambda} \tag{2.52}$$

or

$$\Delta v = K \tag{2.53}$$

The mean aperture also, can be define as (Zimmerman *et al.*, 1991)

$$h_m = K + h_{\min} \tag{2.54}$$

Accordingly, Equation 2.51 can be reduced to

$$\left\langle h^{-3} \right\rangle^{-1} = \frac{(d_m^2 - 3\sigma^2)^2}{d_m} \tag{2.55}$$

Where, σ is the standard deviation of the height distribution and can be defined for a saw tooth profile as $K / 2\sqrt{3}$ (Zimmerman *et al.*, 1991).

It should be noted that equation 2.55 can be used to estimate the hydraulic aperture in series flow for a unit hydraulic cell (UHC) with the wavelength of λ/2. To compare the estimated hydraulic aperture for triangular and sinusoidal profiles, the plot of hydraulic aperture versus roughness estimated from equations 2.47 and 2.55 is shown in Figure 2.33. Similar to the plot for sinusoidal profiles (Figure 2.31) a profile wavelength of 2, with h_{max}=2 was used in this example. The results indicate a reduction in hydraulic aperture as a result of increasing profile roughness, as expected. For comparison purposes, in this figure, the results for a corresponding sinusoidal profile (given in Figure 2.30) for a fixed mean aperture (h_m=2) are also shown. That is because the effect of roughness and profile geometry on hydraulic aperture will be considered for different profile geometry types (i.e. sinusoidal and triangular). The results indicate that the hydraulic aperture for a flow channel with sinusoidal shaped walls is less than that of a symmetric triangular channel. This can be interpreted due to the larger real length of a sinusoidal profile compared to a triangular profile, which causes a larger pressure drop and therefore lesser hydraulic conductivity. D_{R1} is a useful statistical indicator for such a small difference, as it analyses the unit normal vectors extracted from a profile, which indirectly relates to the real profile length. Therefore, for real rock fracture profiles with a much more complicated geometry, it is believed that D_{R1} would be a more appropriate parameter for use in hydraulic calculations. This is discussed in further detail in the next two Chapters.

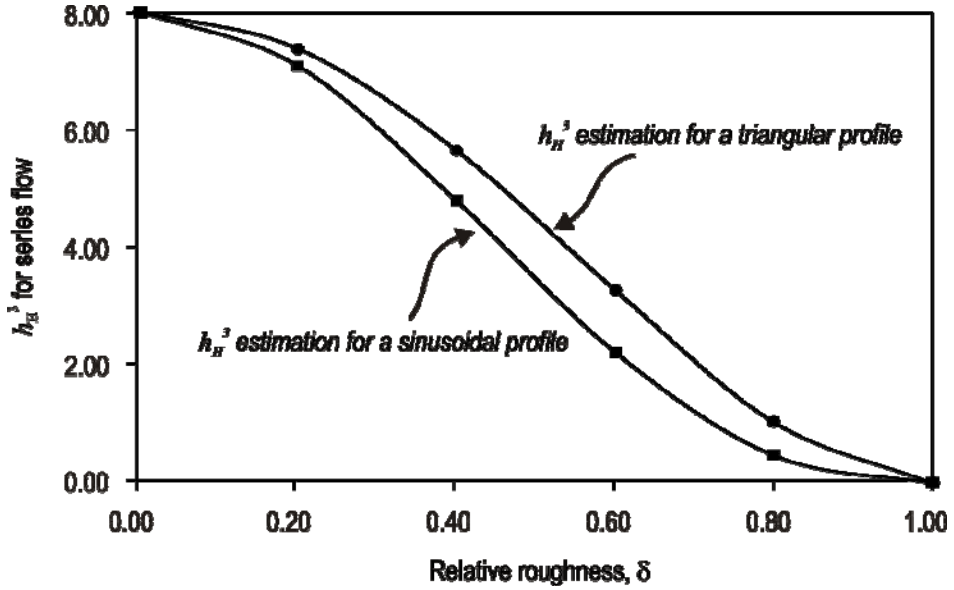

Figure 2.33 Hydraulic aperture versus roughness in channels with fixed mean aperture (h_m) for symmetric triangular and sinusoidal geometries.

2.3 Summary

The first part of this Chapter presented a review of the roughness effect on fluid flow study through rock fractures. Different methods of integrating roughness in flow analysis were discussed. A new statistical parameter (D_{R1}) was introduced for characterisation of profile roughness. In the next step, the analytical solutions for hydraulic aperture estimation of sinusoidal synthetic channels were presented. Similar formulae were extracted for channels with synthetic symmetric triangular channels. D_{R1} was integrated in these equations and was shown to be able to represent channel hydraulic property changes with respect to its geometry. In the next Chapter, fluid flow simulation results for synthetic 2D channels will be presented.

3 Pressure drop estimation for 2D synthetic fractures

In the previous Chapter, the importance of fracture geometry, or its roughness, on the fluid flow behaviour was discussed and existing approaches to study this effect were presented. In this Chapter, the results of the simulation of synthetic profiles, including symmetric and asymmetric triangular profiles using Computational Fluid Dynamics (CFD) code are presented. A brief introduction to CFD and its simulation software, known as FLUENT, will be given in the first section of this Chapter. Based on the CFD simulation analysis, correlations were developed where it was possible to predict the pressure drop. Pressure drop in these synthetic profiles were also linked with the new roughness parameter, D_{R1}, and the results presented. The correlations will be applied to estimate pressure drop along rock fracture profiles.

It should be noted that, in this study, the range of profile apertures were chosen to be between 0.01 cm and 1 cm. This is within the range of fracture apertures observed in naturally fractured reservoirs, based on the extracted data from the image log (Bahrami *et al.*, 2008) as shown in Figure 3.1.

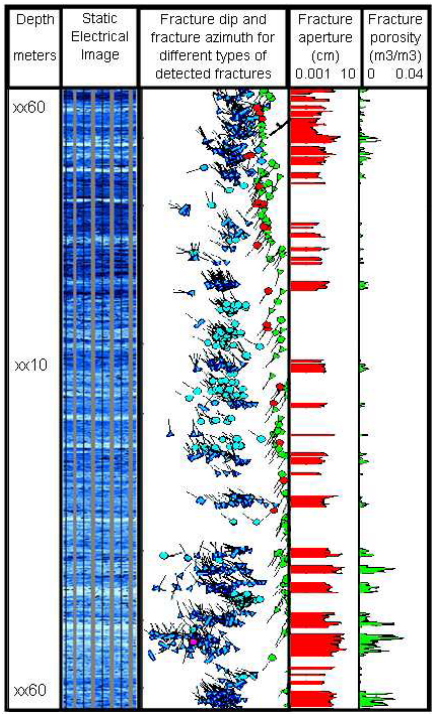

Figure 3.1 Fracture aperture distribution in a section of a hydrocarbon reservoir (Bahrami, *et al.* 2008).

3.1 Computational Fluid Dynamics (CFD)

CFD has been used for solving flow problems numerically in a wide range of engineering applications. FLUENT uses the finite element method to simulate fluid flow for compressible and incompressible fluids with capabilities that consider laminar and turbulent, steady-state, or transient fluid flow problems. The conservation equations for mass and momentum are solved in FLUENT to determine the fluid flow properties such as pressure drop or velocity magnitude for all kind of fluid flows. The flow simulation in FLUENT is performed using the generated mesh and employing different numerical solvers. Those settings and solvers used in this research will be described. The mesh generation uses Gambit software.

For the purpose of this study, the flow in a fracture is assumed to be laminar, incompressible, isothermal and in a steady-state regime and for a viscous Newtonian fluid (Zimmerman and Bodvarsson, 1996).

FLUENT software employs two different solver technologies: pressure based and density based. In this study incompressible flow is studied and the pressure based solver is used in all cases.

In FLUENT, both single-precision and double-precision versions of FLUENT versions are available. Using double-precision solver, (2ddp) is applied for some applications such as a thin pipe with a long length, or for geometries with a high aspect-ratio of grids which need sufficient transformation of boundary information. The floating point number in double-precision solver is representative of 64 bits of memory.

To run a case in FLUENT, the mesh is imported and appropriate mesh scale and settings should be applied. The material and boundary conditions can then be set. There is a data base for different kinds of materials, where the physical properties of materials are stored and can be called upon. The main material properties are density, and viscosity.

There are a wide range of boundary conditions (BC) available in FLUENT to simulate fluid flow. The boundary condition should be created in Gambit when the mesh is generated. However, it is possible to change the boundary conditions in FLUENT if necessary. Some of the boundary types used in this study are velocity inlet, mass flow inlet and pressure outlet.

The velocity inlet boundary condition is proposed for incompressible flows and is used to define the flow velocity within all relevant scalar properties of the flow at the flow inlet. This kind of BC is used when the inlet velocity is known.

The simulation is then performed until the mass flow rate between the inlet and outlet boundary conditions becomes theoretically identical to satisfy continuity equations. Accordingly, the flow rate along the geometry is constant and the velocity in each segment of geometry is calculated by FLUENT to have a consistent flow rate. The boundary condition at the inlet is considered as the velocity inlet in the analysis carried out in this Chapter. However, the mass flow inlet is another possibility that could be used when the effect of fracture geometry is studied. This is what is used for the simulations of JRC flow channels in the next Chapter and also in the case of 3D simulations of rock fractures.

The pressure outlet is the boundary condition needed for all models in this study required to specify the static (gauge) pressure at the outlet boundary. The gauge pressure is assumed to be zero in order to estimate the inlet and outlet pressures and then calculate the pressure drop. The pressure is also estimated using the SIMPLE algorithm (Semi-Implicit Method for Pressure-Linked Equations).

In FLUENT, a different discretisation scheme for the convection terms of each governing equation is available. In this study, the second order upwind scheme is used for more accuracy and also to avoid the errors which may be caused based on the mesh shape and also to handle the large computational effort required in fine mesh grids. The reader is referred to the FLUENT manual for further information on various simulation aspects of this software (Fluent Inc., 2005).

In the next section, applications of FLUENT in the simulation of fluid flow in synthetic profiles will be described.

3.2 Symmetric triangular profiles

Figure 3.2 shows fluid channels with their wall geometry as a symmetric triangular profile. To be consistent, the fluid channel shown in Figure 3.2 (a) will be referred to as a ‘mate’ fluid channel. In this geometry, there is no shear offset of the lower wall with respect to the upper wall. Similarly, Figure 3.2 (b) shows a ’non-mate‘ fluid channel with a lower wall shear offset of a half wavelength relative to the upper wall.

In Figure 3.2, K is the asperity height, h_{in} is the opening (or aperture), h_H is the hydraulic aperture (or equivalent aperture) and θ is the asperity angle. λ and L_e are the projected (i.e. boundary length) and real profile lengths, respectively, which are related to each other as

$$L_e = 2\left[(K)^2 + \left(\frac{\lambda}{2}\right)^2\right]^{0.5} \tag{3.1}$$

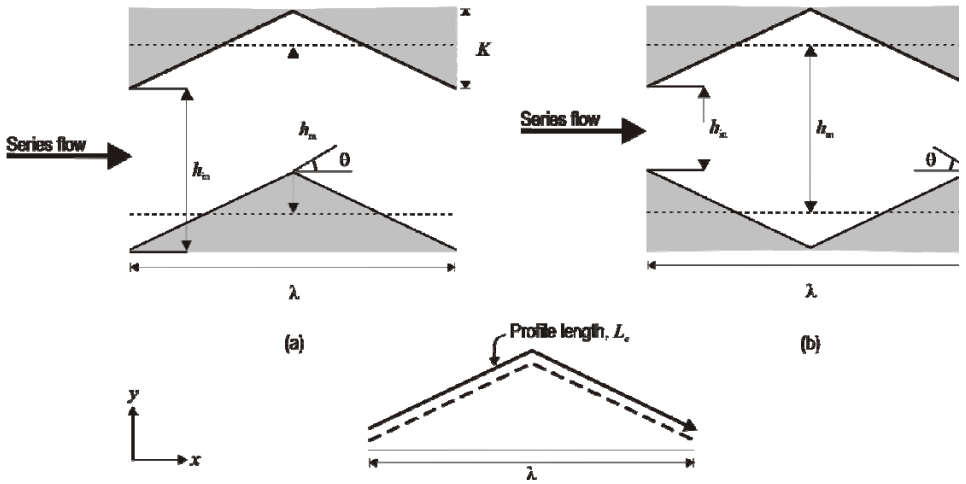

Figure 3.2 Geometry of a (a) mate and a (b) non-mate symmetric triangular fluid channel.

Several profiles, similar to those shown in Figure 3.2, were subjected to a fluid flow analysis using FLUENT software to determine pressure drops and perform sensitivity analyses on different geometrical and fluid properties. The 'velocity inlet' and 'pressure outlet' were considered as the two left and right boundaries with stationary walls in all models. In all simulations, the laminar fluid flow was applied from the left to the right side of the geometry profile (i.e. from velocity inlet BC to pressure outlet BC). The reason to choose laminar flow is that the water flow in reservoirs can be considered as laminar and it is more important in narrow fractures (Sarkar, 2002). In all profiles, a constant length of λ=10 cm was used for consistency purposes and profile roughness was changed by choosing different L_e, corresponding to a different asperity height (K).

At this stage, and because the purpose of this study is to investigate the effect of profile geometry on pressure drop, water with a density of 998.1 kg/m^3 is considered as the fluid flowing through the profile. The hydraulic input data used for the analysis of both profile geometries are given in Table 3.1.

Table 3.1 FLUENT input data for simulation of symmetric profiles

Velocity (m/s×10^{-3})	Volumetric flow rate (m^3/s×10^{-7})	Fluid	Viscosity (Pa.s×10^{-3})
1, 50, 400	1 , 50 , 400	Water	1

The results of FLUENT simulations are given for mate and non-mate fluid channels in the subsections below, respectively.

3.2.1 Mate flow channels

Sensitivity analyses were carried out to investigate the effect of profile geometry on pressure drop and the results are summarised below.

Profile length (L_e)

Fluid channels with a constant opening of h=0.01 cm were chosen and FLUENT simulations were carried out. The simulations were repeated for different fluid velocities but as an example, the results are presented for a fluid velocity of 0.001 m/s. The results for other velocities show a similar trend. As plotted in Figure 3.3, the simulation results indicate that pressure drop increases as profile length becomes larger. This is equivalent to an increase in profile height, as the projected lengths of profiles are constant (L=10 cm). Using the pressure drop obtained from simulation hydraulic aperture, (h_H) was estimated for each profile length from cubic law (equation 1.10) and the results are also shown in Figure 3.3. It is important to note that for mate profiles, the profile length (L_e) is to be used in the cubic law equation, as the laminar flow sees the whole profile length. It is noted that the hydraulic aperture reduces as a result of an increase in profile length.

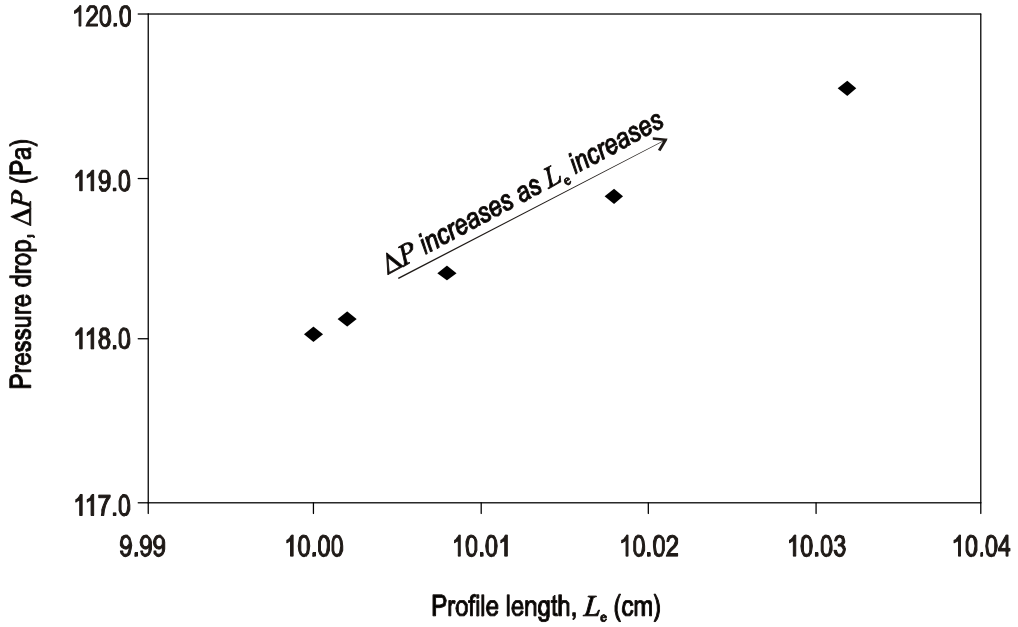

Figure 3.3 Flow simulation results for mate symmetric triangular channels with different profile length (L_e).

The simulation results showed that for mate profiles, the pressure drop was similar for all profiles with equal lengths (L_e). This means that profiles with a different number of asperities but a similar total profile length (this requires profiles to have different asperity heights) behaved similarly.

As an example, Figure 3.4 shows the contours of total pressure and velocity magnitude for a profile with four asperities. The results of Figure 3.4 indicate that the total pressure, as expected, reduces as fluid moves toward the channel outlet. As the flow regime is laminar, velocity profile is parabolic: it is maximum at the centre of the channel and reduces to its lowest value at the two walls.

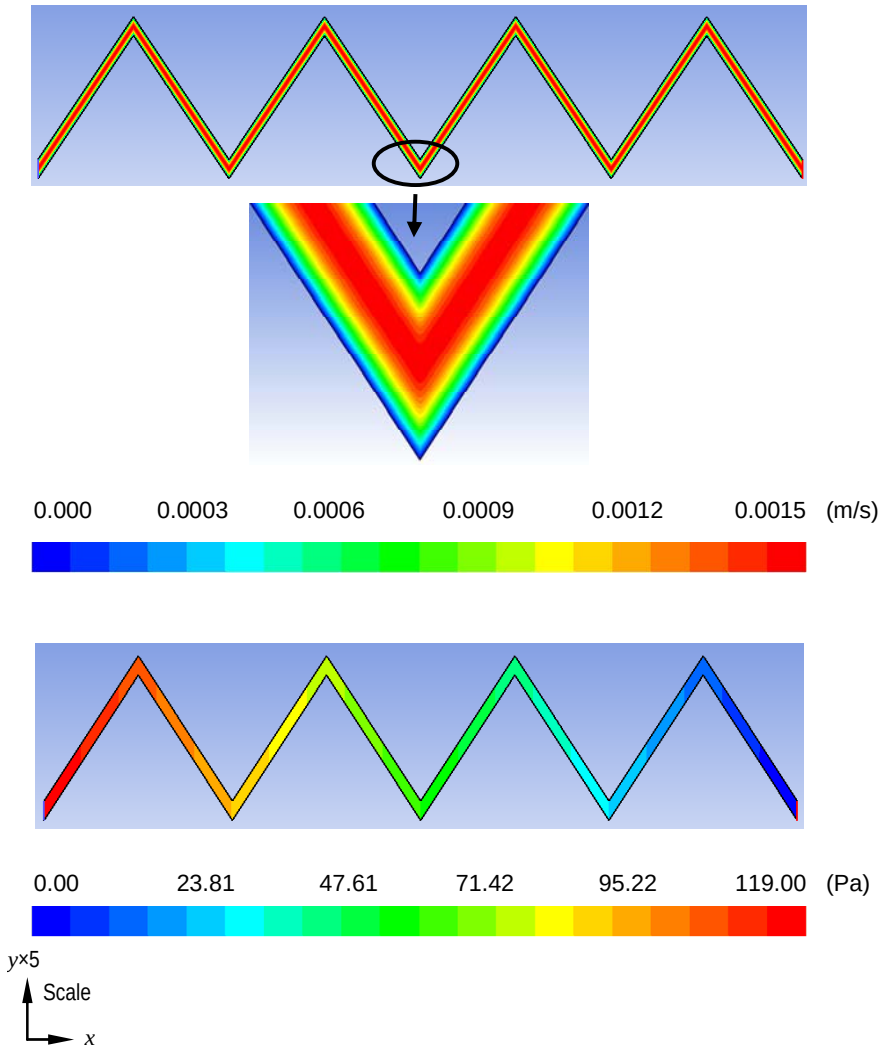

Figure 3.4 Contours of (Top) velocity magnitude and (Bottom) total pressure for a mate symmetric triangular profile.

Opening

Figure 3.5 shows the results of the sensitivity analysis of pressure drop with respect to the fluid channel opening (h_{in}) for a mate triangular profile with single asperity. The results of this figure show that, considering all other parameters are constant, pressure drop reduces as a result of the increasing profile inlet opening, which is in agreement with cubic law. The hydraulic aperture was then estimated using cubic law for each profile and the results are also presented in Figure 3.5, which show an increase as the profile opening becomes larger. As shown in this figure, h_H is equivalent to the opening h_{in} for different mate fluid channels and therefore calculation of pressure drop for these profiles is less cumbersome. However, it will be shown in the next subsection that this is not the case for non-mate profiles.

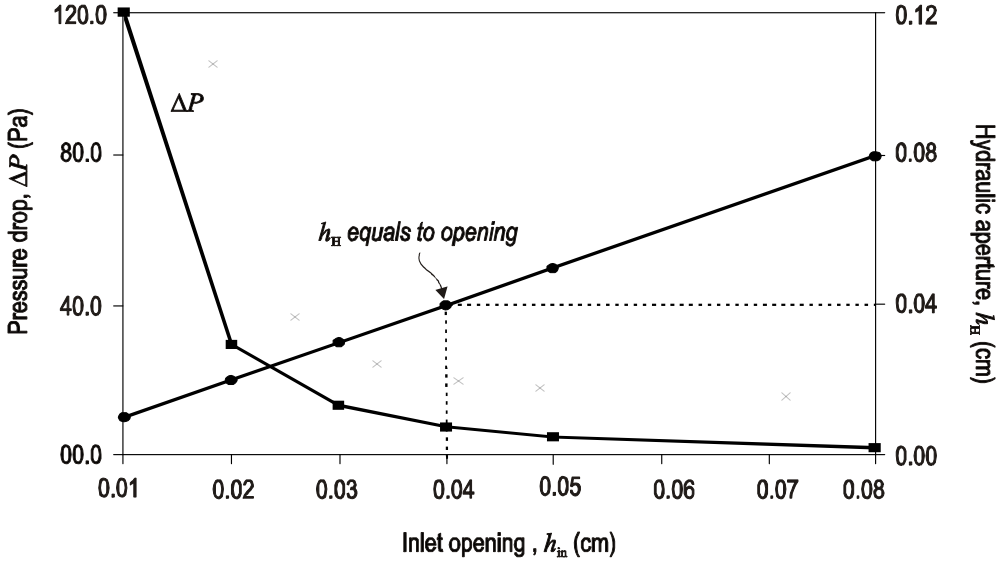

Figure 3.5 Flow simulation results for mate symmetric triangular channels with different inlet openings (h_{in}).

3.2.2 Non-mate flow channels

Fluid flow analysis of a non-mate profile whose geometry is shown in Figure 3.2 (b) is not as simple as the mate profile discussed in the previous subsection. This is because the opening of a non-mate profile changes along the profile and is not constant. Therefore, contrary to the results shown for a mate profile in Figure 3.6, the hydraulic aperture is not equivalent to the profile opening. In this study, correlations are developed from several FLUENT simulation runs using an estimation of the equivalent hydraulic aperture of a non-mate symmetric profile. Figure 3.6 shows the example output contours of total pressure drop and velocity magnitude from a FLUENT simulation for a trianglur profile with real length, asperity height, and an opening of 10

cm, 0.10 cm, and 0.05 cm, respectively. The inlet velocity in this study was chosen to be 0.001 m/s. The results indicate how fluid pressure drops as the fluid moves towards the outlet boundary and that velocity is maximised where the channel throat is the least. In the following section, the results of a sensitivity analysis on different geometrical and hydraulic properties for non-mate symmetric profiles will be given.

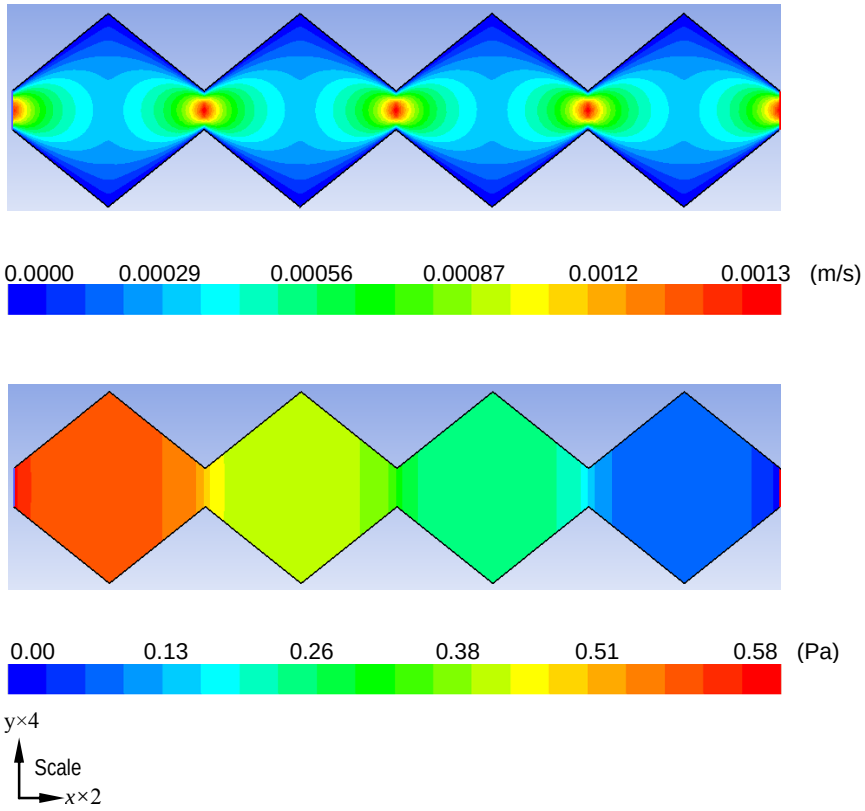

Figure 3.6 Contours of (a): velocity magnitude, m/s and (b): total pressure (Pa), for a non-mate symmetric triangular profile.

Profile length (L_e)

The results of pressure drop for non-mate profiles with a different real length (L_e) are given in Figure 3.7. Considering the constancy of all other parameters, and assuming that maximum opening along the profile is not constant, pressure drop decreases as profile length becomes longer. This is due to the fact that with larger asperities fluid faces a larger area to travel along the channel when the maximum opening (h_{max}) is not fixed. However, if the maximum opening is fixed, a reverse trend is expected (i.e. pressure drop increases as profile length increases). This is because with larger profile lengths, the asperities will be larger and hence fluid faces a more reduced throat along the channel. This reduced width causes larger pressure drops.

The results shown in Figure 3.7 are for a fluid velocity of 0.001 m/s, inlet opening of 0.01 cm and the volumetric flow rate of $1\times10^{-0.7}$ m^3/s. This figure also shows that for profiles with a larger number of asperities, but the same real length (i.e. lesser profile asperity height), pressure drop increases. This is because with larger asperities fluid faces more reduced throat along the channel. This reduced width is the reason for larger pressure drops for a higher number of asperities.

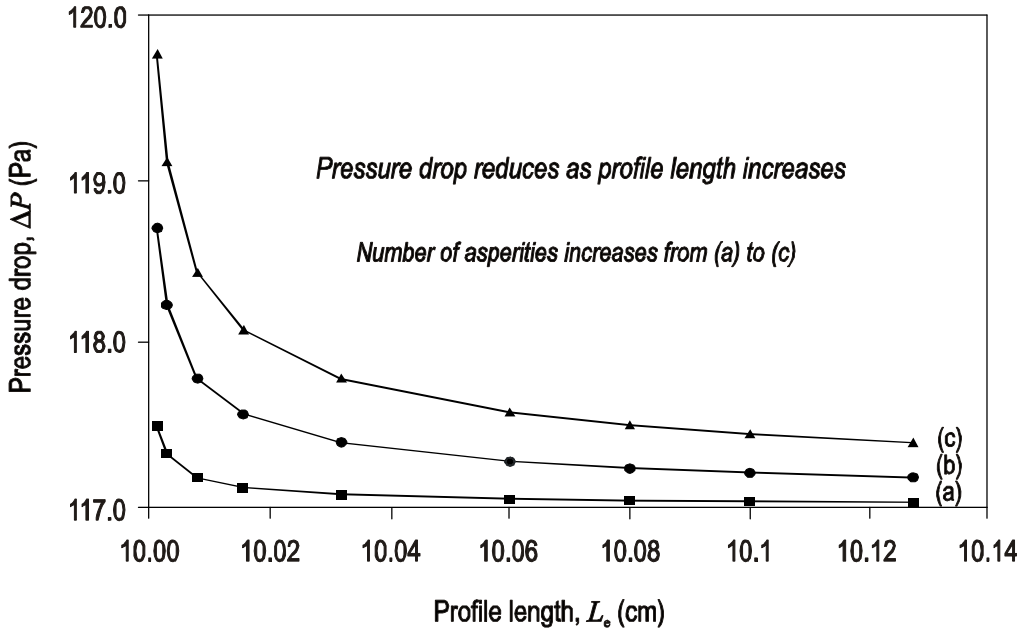

Figure 3.7 Simulation results of pressure drop for symmetric profiles with different real profile lengths (L_e) for (a) one, (b) four, and (c) eight number of asperities.

Back calculation of hydraulic aperture from simulation results using the cubic law equation indicates that h_H increases as L_e increases and this increase is more severe for profiles with a larger number of asperities (see Figure 3.8).

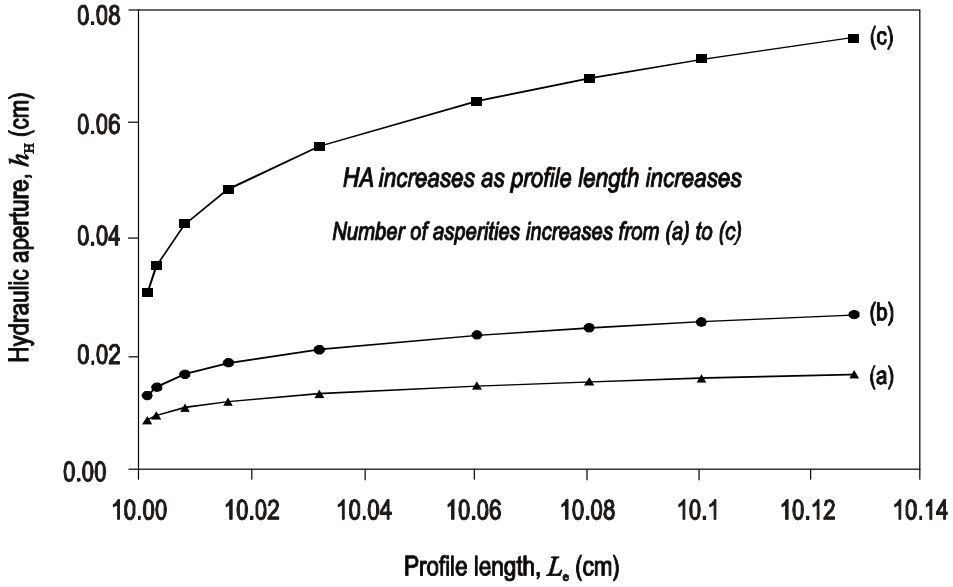

Figure 3.8 Hydraulic aperture for non-mate symmetric profiles with different profile length (L_e) for (a) one, (b) four, and (c) eight number of asperities.

Opening

By increasing the fluid channel opening and keeping all other parameters constant, this will result in a pressure drop reduction, as shown in Figure 3.9 for a non-mate symmetric triangular profile with single asperity. This is simply because the fluid has a wider area to pass through if the opening is larger. Back calculation of h_H from simulation results and using the cubic law equation indicates that h_H increases as inlet channel opening (h_{in}) increases but the relation is not linear as was the case for a mate profile (see Figure 3.6). This relationship becomes more difficult to predict once other parameters such as fluid velocity or asperity height are changed.

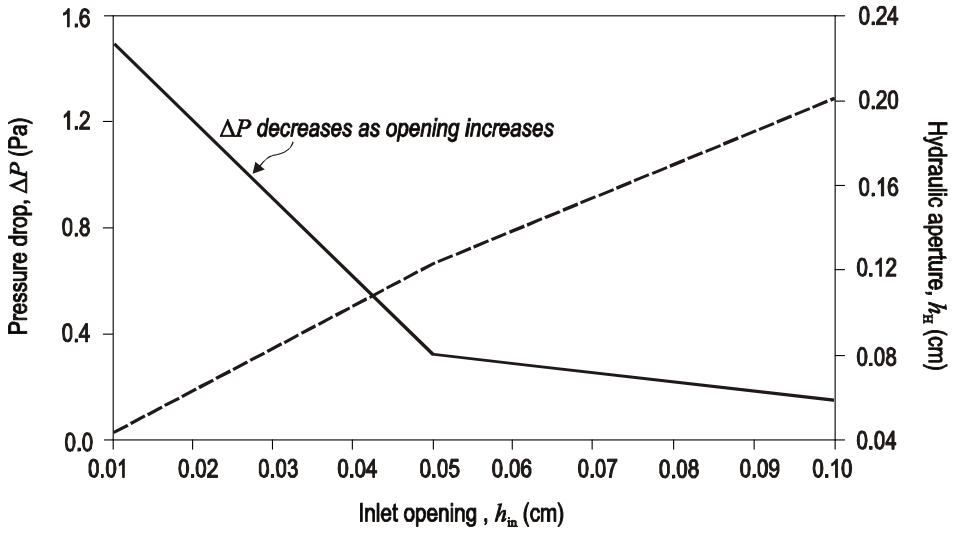

Figure 3.9 Pressure drop for non-mate symmetric profiles with different inlet openings (h_{in}).

Fluid velocity

Figure 3.10 shows the effect of changing fluid velocity on pressure drop from a FLUENT simulation and hydraulic aperture back calculated from the cubic law formula, for example, a channel with an asperity height (K) of 0.02 cm, four asperities, and different openings of 0.01, 0.05 and 0.1 cm. This figure indicates that by increasing fluid velocity, h_H reduces. More interestingly, as the fluid velocity becomes very large, h_H tends toward the channel opening (h) itself, i.e. identical to a channel with two flat walls. This is due to the fact that at large velocities the fluid does not see the profile geometry and tends to pass along a straight path directly from the inlet to the outlet through the centre part of the channel.

The results of Figure 3.10 show that as velocity increases, pressure drop increases too. Here, only the pressure drop for an opening of 0.01 cm is shown as an example but the pressure drop for a non-mate profile with a different inlet opening shows the same trend. Increasing velocity reduces both L_e and h_H but the effect of h_H is larger according to the cubic law equation and hence the pressure drop shows an increase.

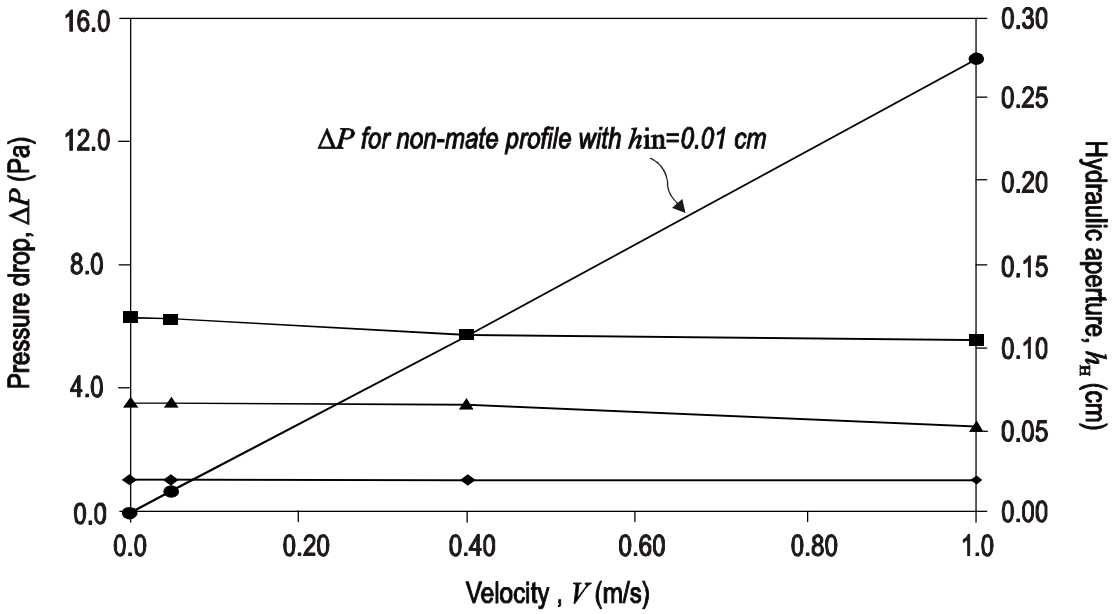

Figure 3.10 Pressure drop and h_H for non-mate symmetric profiles with different fluid velocities.

Asperity height (roughness)

The effect of asperity height (K) on pressure drop was simulated in FLUENT by changing this parameter while other variables were kept constant. Another major assumption is the variable maximum opening (h_{max}). Increasing the roughness also indicates an increasing of the profile length (L_e). The results of such an analysis are shown in Figure 3.11 which indicates that as asperity height or profile roughness increases pressure drop reduces, which is because there is a wider area for fluid to pass through the channel. For such simple profile geometries a change in K corresponds directly to changing asperity angle θ, or roughness parameter D_{R1} as explained in Section 2.15 of Chapter 2. Therefore, a similar trend is observed in Figure 3.11 between pressure drop and D_{R1}, i.e. as D_{R1} increases, pressure drop reduces. Hence, D_{R1} can be applied to a fluid flow analysis of rock fractures as a parameter to estimate the profile length. This aspect will be considered in the next Chapter.

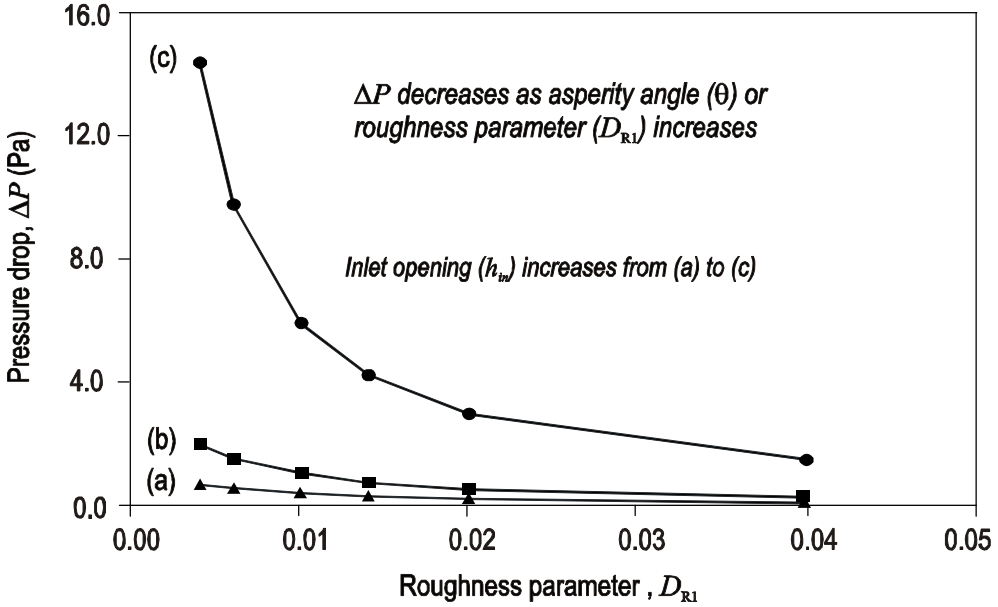

Figure 3.11 Effect of roughness parameter (D_{R1}) on pressure drop in a symmetric non-mate fluid channel for (a) h_{in}=0.01 cm , (b) h_{in} =0.05 cm , and (c) h_{in} =0.1 cm.

As mentioned earlier for non-mate profiles, due to its geometry the hydraulic aperture (h_H) is a function of different parameters and needs to be estimated in order to calculate pressure drop. In the following subsection, a correlation is developed based on the simulation of several channels with a half wavelength which allows an estimation of h_H to be made using more complicated geometries. Before representing the results, the analytical solutions developed for such simple geometry, similar to what was presented in Chapter 2 for sinusoidal profiles, will be developed in the next section.

3.3 Analytical analysis of a unit hydraulic channel (UHC)

Similar to the sinusoidal channels discussed in Section 2.1.7, analytical solutions can be developed to estimate hydraulic aperture in a fluid channel with symmetric triangular geometry walls. This is discussed here.

A unit hydraulic cell (UHC) corresponding to a half wavelength of a symmetric triangular shaped channel is shown in Figure 3.12. It is assumed the fluid flows from left to right.

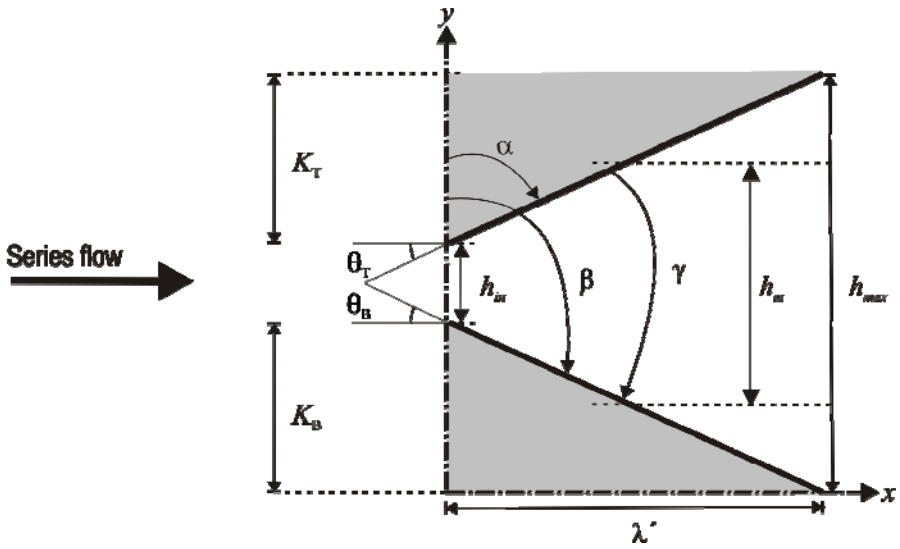

Figure 3.12 Geometry of a unit hydraulic cell (UHC).

From this figure, the following relations are held between profile roughness of the top and bottom walls (K_T, K_B), length (λ'), and minimum and maximum distances between the two walls (i.e. h_{in} and h_{max}):

$$h_{\max} = h_{in} + K_T + K_B \tag{3.2}$$

$$h_m = h_{in} + \left(\frac{K_T + K_B}{2} \right). \tag{3.3}$$

In Figure 3.12, the position of the top and bottom walls can be determined using their angles with respect to the y axis (i.e. α and β, respectively). In this figure, the angle between the two walls is shown as γ.

The standard deviation of the height distribution for such a profile can be estimated as (Zimmerman *et al.*, 1991)

$$\sigma = \frac{h_{\max} - h_{in}}{2\sqrt{3}} = \frac{K_T + K_B}{2\sqrt{3}}, \tag{3.4}$$

which leads to

$$K_T + K_B = 2\sqrt{3}\sigma . \tag{3.5}$$

The equations representing the bottom and top wall geometries of this synthetic channel can be written in the forms of

$$h_B(x) = \frac{K_B}{\lambda'} x - h_{in} \tag{3.6}$$

and

$$h_T(x) = \frac{K_T}{\lambda'} x . \tag{3.7}$$

Accordingly, the aperture field is calculated as

$$h(x) = h_T(x) - h_B(x) = \frac{1}{\lambda'}\left(K_T - K_B\right)x + h_{in} . \tag{3.8}$$

As discussed in Chapter 2 and similar to a sinusoidal profile, the hydraulic aperture in a series flow for half a wavelength of this channel is estimated as

$$\left\langle h^{-3} \right\rangle = \frac{1}{\lambda'} \int_0^{\lambda} \frac{1}{h^3(x)} dx . \tag{3.9}$$

Substituting $h(x)$ from Equation 3.8 in this equation leads to

$$\left\langle h^{-3} \right\rangle = \frac{1}{\lambda'} \left[- \frac{\lambda'}{4\left(k_T + K_B\right)\left(h_{in} + \frac{2\left(K_T + K_B\right)}{\lambda'} x \right)^2} \right]_0^{\lambda} . \tag{3.10}$$

Replacing h_{in} from Equation 3.3 and simplifying this equation it reduces finally to

$$\left\langle h^{-3} \right\rangle^{-1} = \frac{1}{h_m} \left(h_m^2 - \left(\frac{K_T + K_B}{2} \right)^2 \right)^2 \tag{3.11}$$

or

$$\left\langle h^{-3} \right\rangle^{-1} = \frac{1}{h_m} (h_m^2 - 3\sigma^2)^2 . \tag{3.12}$$

For a channel geometry with identical slopes (i.e. K_T=K_B=K) equations 3.11 and 3.12 are simplified to

$$\left\langle h^{-3} \right\rangle^{-1} = \frac{(h_m^2 - K^2)^2}{h_m} = \frac{(h_m^2 - 3\sigma^2)^2}{h_m} . \tag{3.13}$$

This equation is what was originally proposed by Zimmerman *et al.* (1991).

It can be shown that theoretically, the hydraulic aperture would be identical if the fluid travels from right to left as in Figure 3.12, i.e. the pressure drops are expected to be directionally independent.

Equation 3.11 can be written in terms of angles α, β and γ shown in Figure 3.12. From this figure

$$K_T = \frac{\lambda'}{\tan\alpha} , \tag{3.14}$$

$$K_B = \frac{\lambda'}{\tan\beta}, \tag{3.15}$$

$$\gamma = \beta - \alpha . \tag{3.16}$$

Substituting Equations 3.14 and 3.15 in Equation 3.11 results in

$$\left\langle h^{-3} \right\rangle^{-1} = \frac{1}{h_m}\left(h_m^2 - \frac{\lambda'^2}{4}\left(\cot\alpha + \cot\beta\right)^2 \right)^2 . \tag{3.17}$$

In order to investigate the effect of changes in channel geometry on hydraulic behaviour, in Figure 3.13 the variation of hydraulic aperture with respect to angle between the two walls (γ) is plotted. In this figure, the top and bottom walls are located symmetrically about the *x* axis. In this example, a UHC with λ'=1 cm and h_m=0.01 cm was assumed for illustration purposes. The results of this figure show how hydraulic aperture increases as the channel walls deviate from each other.

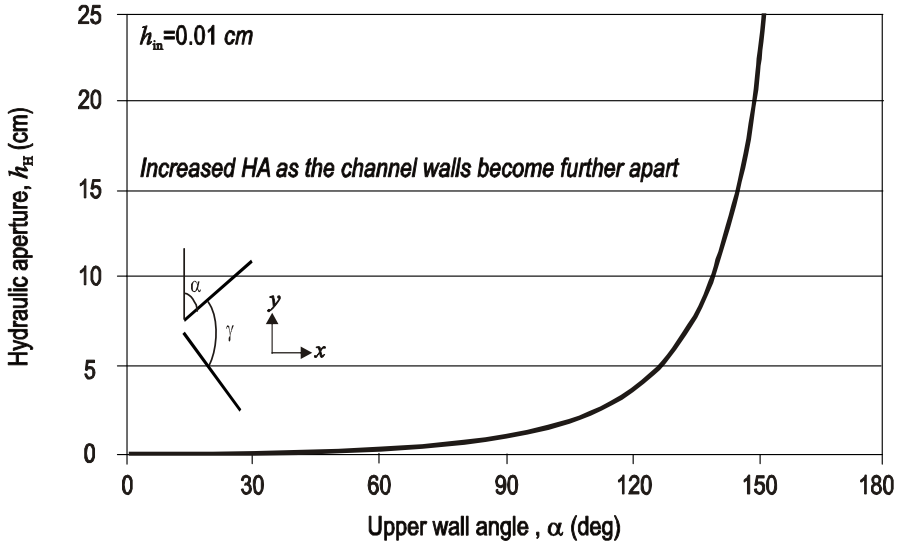

Figure 3.13 Hydraulic aperture as a function of wall distances.

Equation 3.11 can be rewritten in terms of the UHC minimum opening, i.e. the inlet opening ($h_{\min}$) as

$$\left\langle h^{-3} \right\rangle^{-1} = \frac{1}{h_{\min} + K}\left(\left(h_{\min} + K\right)^2 - K^2 \right)^2 , \tag{3.18}$$

where, $K = \left(K_T + K_B\right)/2$.

The maximum opening (i.e. at the UHC outlet) is a function of h_{in} and can be simply calculated as

$$h_{\max} = h_{in} + 2K = h_{in} + 2\lambda'\cot\alpha . \tag{3.19}$$

Figure 3.14 shows the plot of h_H/h_m as a function of h_{in}/h_{max}. The results of this figure indicate that hydraulic aperture increases as the UHC inlet opening becomes larger, however, it approaches the mechanical aperture when h_{in} becomes very large and thus the ratio of h_{in}/h_{max} gets close to unity. It is important to note that this result is independent of the size of the top or bottom wall (or say, K) and is only dependent upon the ratio of the h_{in}/h_{max}. While this result may be acceptable to some extent, it is important to note that the analytical equations developed here do not consider the flow properties but only look at the geometry of the UHC. For example, the flow rate is an important factor which can significantly influence the results. For a constant flow rate, increasing the ratio of h_{in}/h_{max} is expected to cause an increase in hydraulic aperture, however, beyond a certain limit this trend may reverse and does not approach the mechanical aperture. This indicates why conducting an appropriate fluid flow analysis where hydraulic parameters are also integrated with geometrical properties of the channel is required.

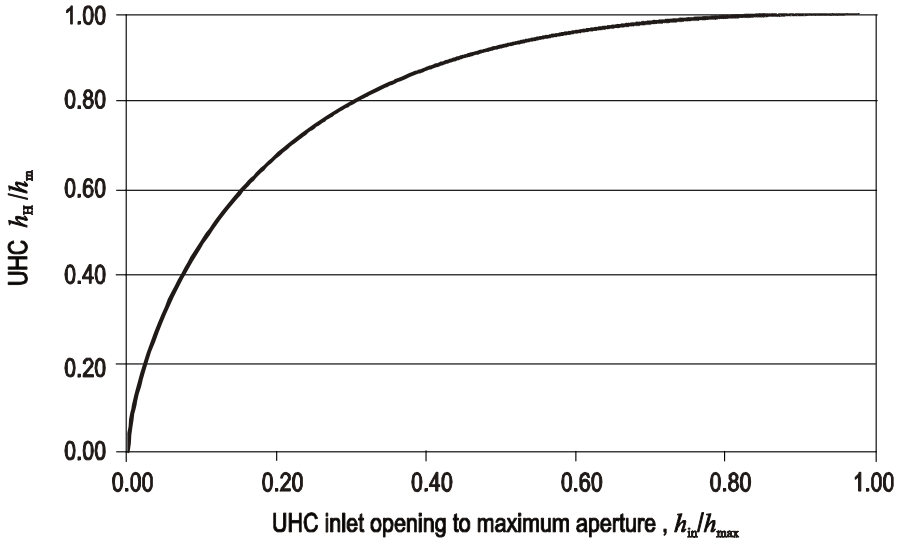

Figure 3.14 Hydraulic aperture as a function of channel geometry.

In order to take the effect of channel orientation into account, the UHC length along different directions needs to be included in equation 3.17. This could be simply assumed as the length of the line corresponding to angle $\alpha+\gamma/2$ or $\beta-\gamma/2$, depending on the UHC orientation, which is equivalent to

$$l=\frac{\lambda'}{\sin(\alpha+\gamma/2)}. \tag{3.20}$$

A similar approach was used by Sarkar *et al.* (2004) to estimate pressure drop for smooth channels aligned along different orientations.

From equation 3.20, the pressure drop changes are a direct function of length *l* and the hydraulic aperture changes inversely with respect to λ. Therefore, the modified hydraulic aperture, where the effect of UHC orientation is also taken into account, can be expressed as

$$\left\langle h^{-3}\right\rangle^{-1}=\left[\frac{1}{h_{\mathrm{m}}}\left(h_{\mathrm{m}}^{2}-\frac{\lambda'^{2}}{4}\left(\cot\alpha+\cot\beta\right)^{2}\right)^{2}\right]\frac{\sin\left(\alpha+\gamma/2\right)}{\lambda'}. \tag{3.21}$$

This equation indicates that hydraulic aperture changes as a function of angle α, or UHC orientation and its maximum occurs at angle $\alpha=90^{\circ}-\gamma/2$, i.e. when the UHC is symmetric about the *x* axis, corresponding to a minimum length for the UHC (i.e. λ').

In Figure 3.15, the plot of hydraulic aperture changes corresponding to UHCs with a different angle between the two walls and different orientations are shown. As an example, this plot is for a minimum aperture of h_{in}=0.01cm. In this figure, the loci of maximum hydraulic aperture corresponding to UHCs oriented along different directions are shown.

It is important to note that in these calculations the gravity effect is not considered and the results obtained here correspond to a change in UHC geometry only.

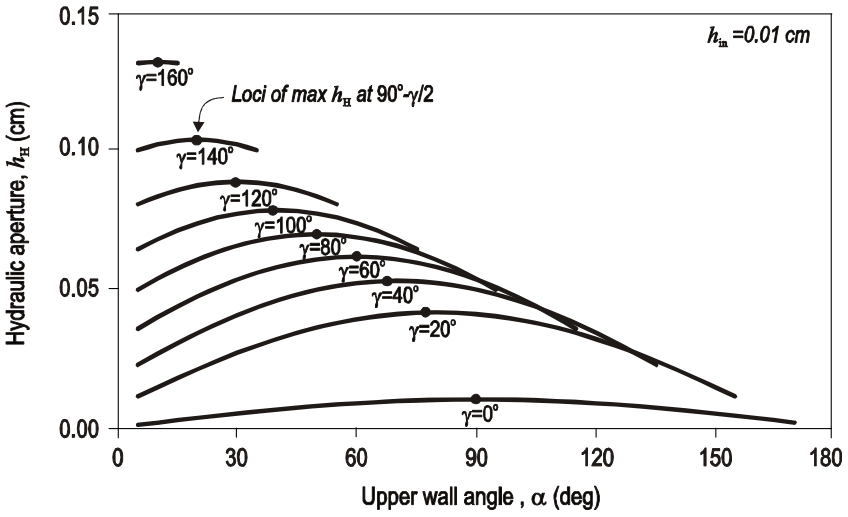

Figure 3.15 Hydraulic aperture as a function of channel orientation.

In Figure 3.16, the simulation results performed using FLUENT for a UHC with a different range of angle γ when angle α changes between 25° and 130 ° are compared with those obtained using the analytical solutions of Figure 3.15 with a constant $Q=1\times10^{-07}$ m^3/s for all models. This figure shows a close agreement between the two approaches. From this figure, a lesser discrepancy is expected between the results of the

two approaches when γ is less than 80 deg, and when angle α is enough large, i.e. the channel aperture is not large. This is due to the fact that the given constant flow rate becomes ineffective for large channel apertures. This demonstrates that the analytical formulae developed above can be used with a reasonable accuracy for the purpose of studying real rock fractures, assuming that a real fracture is a combination of several discrete UHC.

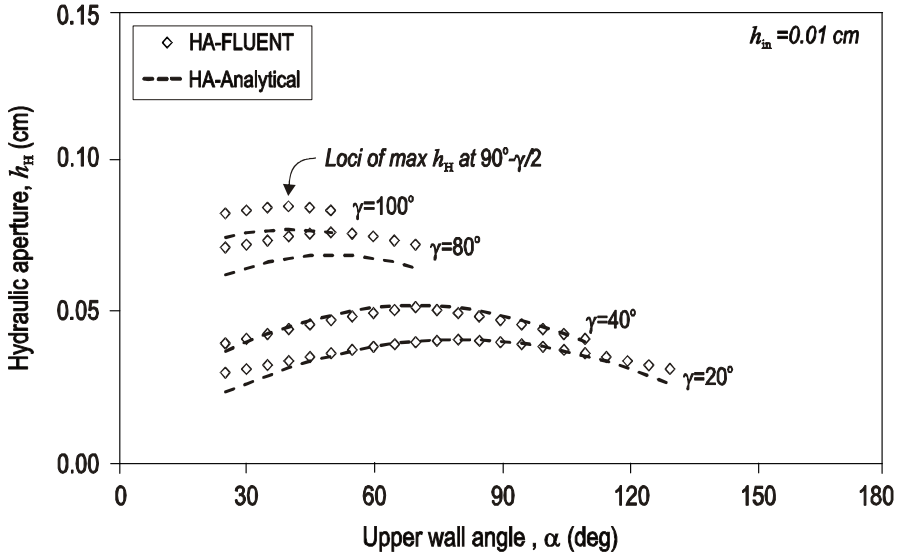

Figure 3.16 Simulation results for a UHC.

3.4 FLUENT simulation of a UHC

In this section, the simulation result of UHCs with different geometries will be presented. The results are used to develop correlations between hydraulic apertures and UHC geometrical parameters.

Figure 3.17 shows the generated mesh using Gambit for a UHC with h_{in}=0.01 cm, and $\gamma=30^o$ (i.e.$\alpha=120^o$). The use of high density quad mesh using different interval counts for each profile ensures a high accuracy for the results obtained from FLUENT. The contours of velocity magnitude and total pressure from FLUENT simulation corresponding to this UHC are shown in Figure 3.18. Water was used in this simulation and a constant mass flow rate of 9.982×10^{-5} kg/s was applied for modelling. The results indicate how fluid pressure drops as the fluid moves towards the outlet boundary and that velocity is maximised where the channel throat is the least.

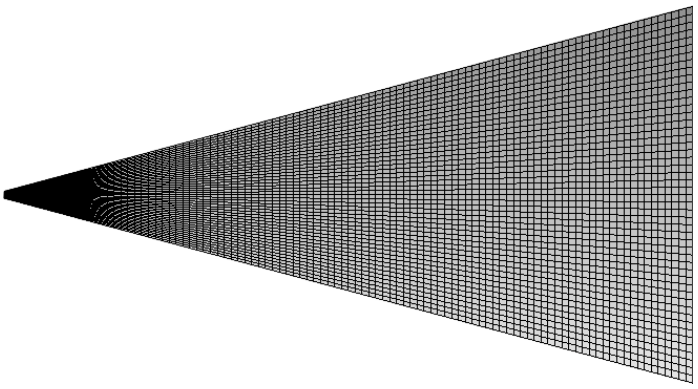

Figure 3.17 The generated quad mesh in Gambit for UHC with h_{in}=0.01 cm.

Below, the FLUENT simulation results for UHCs corresponding to angle α which indicates the loci of maximum for the different angle γ (i.e. 90^o-γ/2) are outlined.

In Figures 3.19 and 3.20, the hydraulic apertures back calculated from cubic law are shown for UHC with the different angle γ. Figure 3.19 shows the results for h_{in} between 0.01 and 0.05 cm where, for illustration purposes, the results correspond to h_{in} between 0.1 and 3 cm and are plotted in Figure 3.20. This figure shows that in general, hydraulic aperture approaches h_{in} with γ=0, i.e. smooth channel with opening h_{in}. However, when h_{in} is greater than 0.1 cm this is no longer the case: the hydraulic aperture at γ=0 is less than h_{in}. This is due to the fact that the flow rate is the same for all models and therefore at longer inlet sizes, the fluid velocity becomes very small and therefore, the fluid flow becomes less independent of channel geometry.

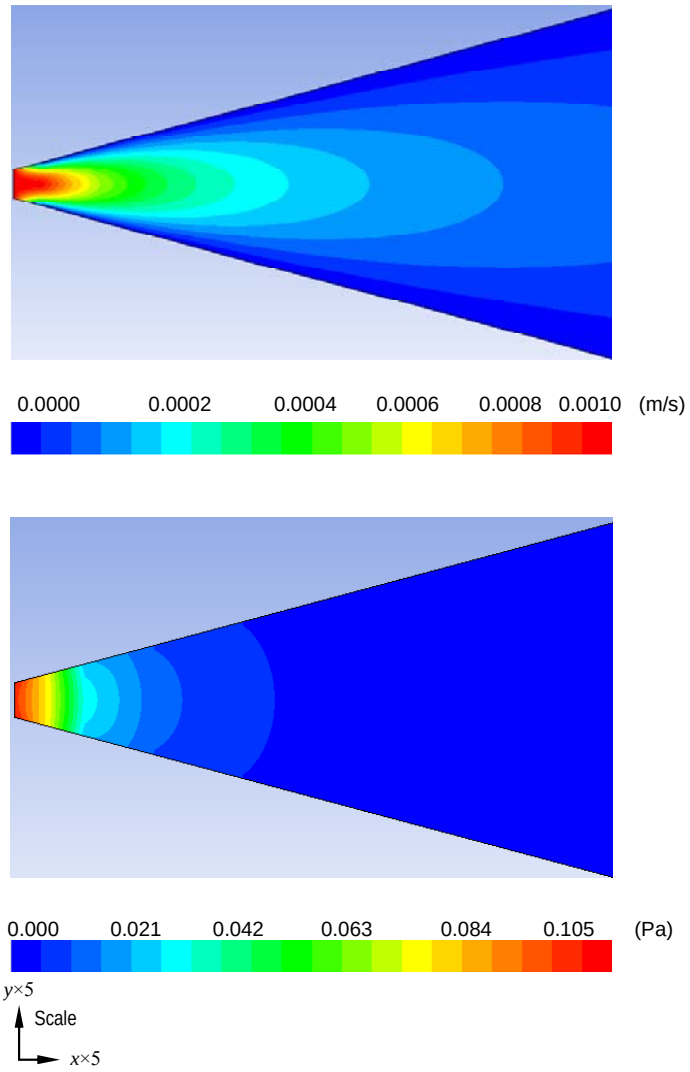

Figure 3.18 Contours of (Top): velocity magnitude, m/s and (Bottom): total pressure (Pa), h_{in}=0.01 cm.

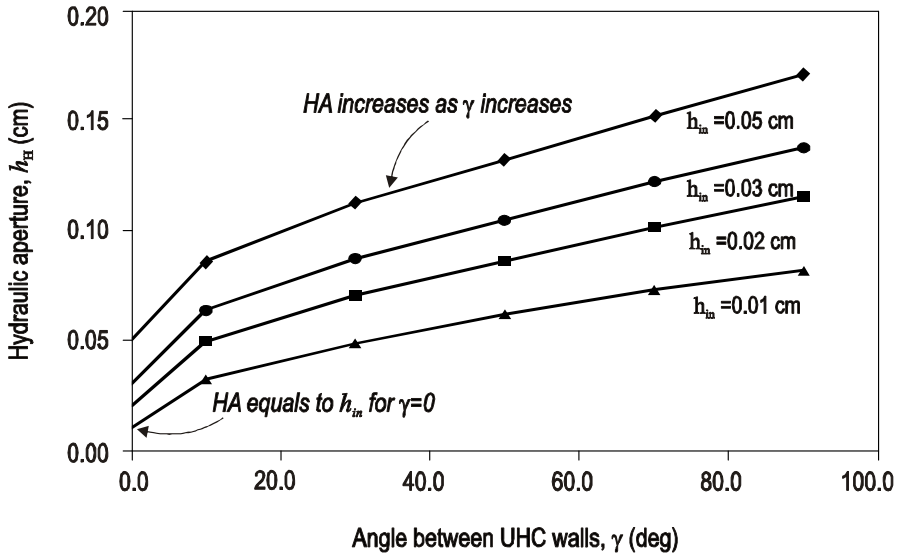

Figure 3.19 Simulation results of hydraulic aperture for a unit hydraulic cell (UHC) with different h_{in} less than 0.05 cm.

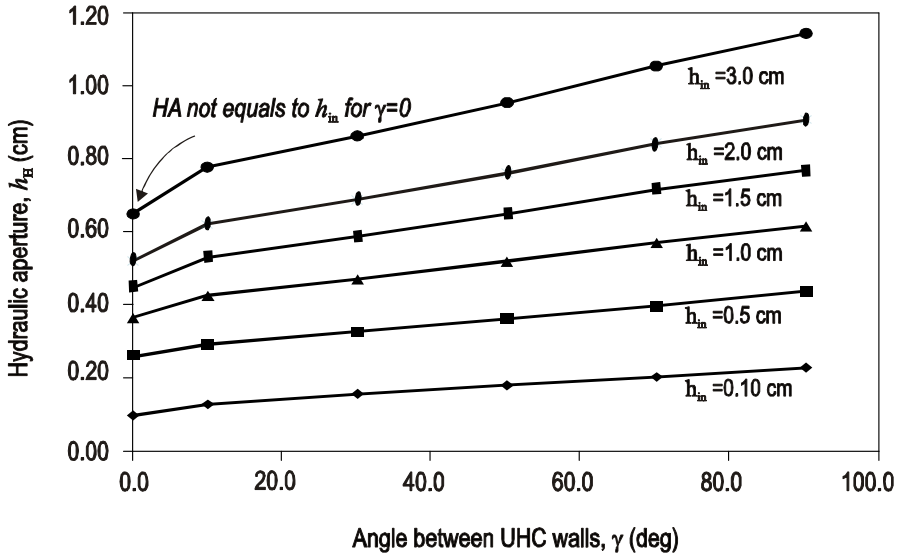

Figure 3.20 Simulation results of hydraulic aperture for a unit hydraulic cell (UHC) with h_{in} between 0.1 and 3.0 cm.

The FLUENT output for contours of total pressure of UHC with h_{in}=0.5 cm, and γ=30^o are shown in Figure 3.21. This figure indicates that the larger pressures occur at the corners of the model.

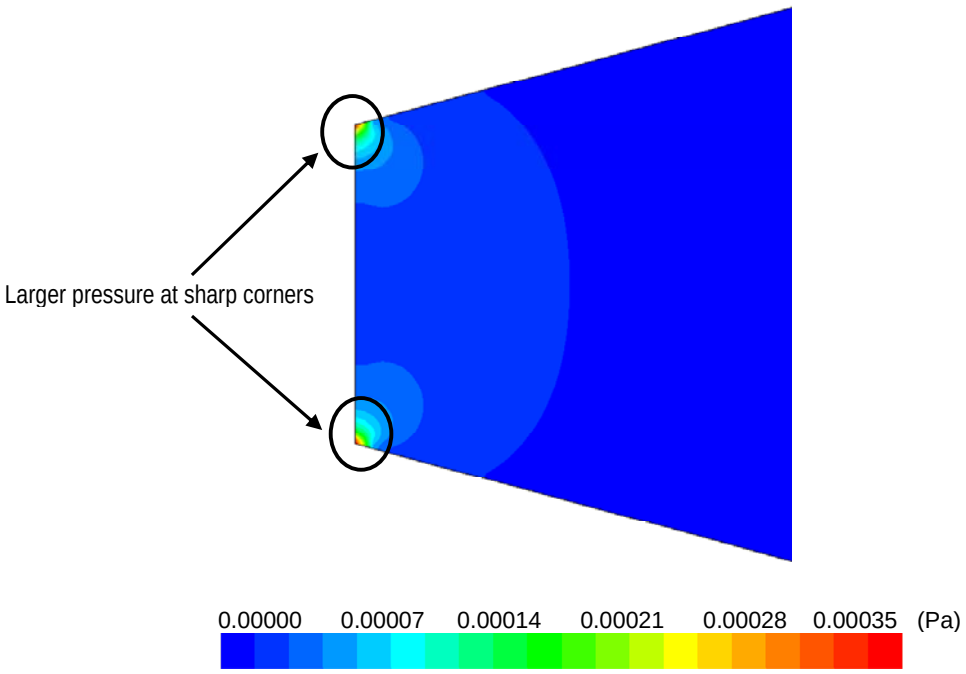

Figure 3.21 Contours of total pressure (Pa) for a unit hydraulic cell (UHC) with h_{in} = 0.5 cm.

3.4.1 Developed Correlation

Using multi-variable regression techniques, the relationship between hydraulic aperture of the UHC as a function of inlet opening (h_{in}) and the angle between UHC walls (γ) can be written as

$$h_H = C_1 + C_2 \gamma^{C_3} \tag{3.22}$$

Where coefficients C_1, C_2 and C_3 are

$$\begin{aligned} C_1 &= h_{in} \\ C_2 &= 0.0184 h_{in}^{0.2309} \qquad \text{for } h_{in} < 0.10\text{cm} \\ C_3 &= 0.771 h_{in} + 0.5386 \end{aligned} \tag{3.23}$$

and

$$\begin{aligned} C_1 &= 0.3622 h_{in}^{0.554} \\ C_2 &= 0.0036 h_{in} + 0.0043 \qquad \text{for } h_{in} \geq 0.10\text{cm}. \\ C_3 &= 0.0196 h_{in} + 0.74 \end{aligned} \tag{3.24}$$

In these equations, h_{in} is in cm and γ is in degrees. It is also important to note that these correlations are developed for a UHC with a length of 1 cm and based on a constant flow rate of Q=1×10^{-7} m^3/s.

Having estimated hydraulic aperture from correlation 3.22, the pressure drop $\Delta P_{(\lambda'=1cm)}$ can be calculated for a UHC as

$$\Delta P = F_L \Delta P_{(\lambda'=1cm)} \tag{3.24}$$

or

$$\Delta P = F_L \frac{0.12 \mu \lambda' Q}{(0.01 h_{H(\lambda'=1cm)})^3} \tag{3.25}$$

where, μ (Pa.s) is the viscosity, λ' (cm) is the UHC projected length, Q (m^3/s) is the volumetric flow rate , and h_H (cm) is the equivalent hydraulic aperture. In equation 3.25, F_L is the length correction factor, as the developed correlation was based on the analysis of profiles with λ'=1 cm. F_L is estimated as (see Figure 3.22)

$$F_L = \frac{\lambda'}{\mathrm{Sin}(\alpha)} = \frac{\lambda'}{\mathrm{Cos}(\gamma/2)}. \tag{3.26}$$

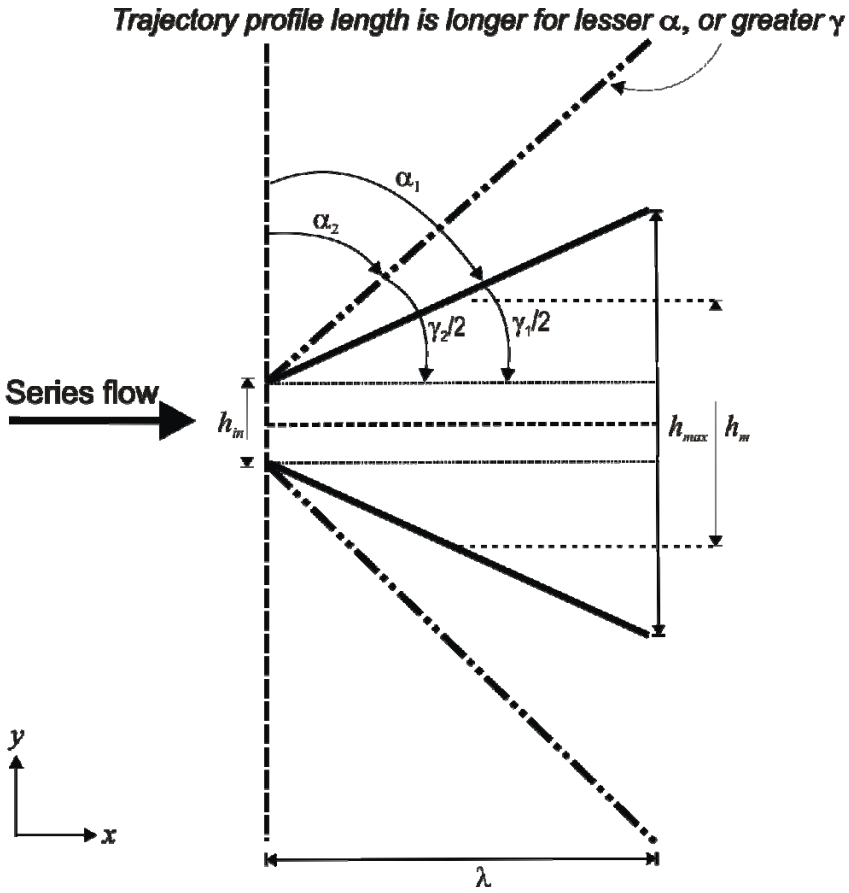

Figure 3.22 Comparison of geometry of two UHCs.

To assess the validity of the developed correlation, the pressure drops for a number of profiles with different geometries were calculated using equations 3.25 and the results compared against those obtained using the FLUENT simulation.

In Figure 3.23, the geometry of two synthetically generated flow channels are shown. The asperity height of the upper and lower walls was generated based on a linear random generation of numbers. The channel can be considered as a combination of 18 UHCs connected in the series. The channel pressure drop can be obtained as the sum of the pressure drop in each UHC. Therefore, the hydraulic aperture corresponding to each UHC was estimated from correlations 3.22 and 3.25, from which pressure drop corresponding to each UHC was calculated from the cubic law equation and then the total pressure drop was obtained. The results are shown for both flow channels in Table 3.2. Each flow channel was separately subjected to the FLUENT analysis and the pressure drops obtained from the simulation are also given in Table 3.2. This table shows a very close agreement between the results obtained from the two approaches with less than 10% error. This demonstrates the applicability of the developed correlation for a good estimation of pressure drop in a 2D channel.

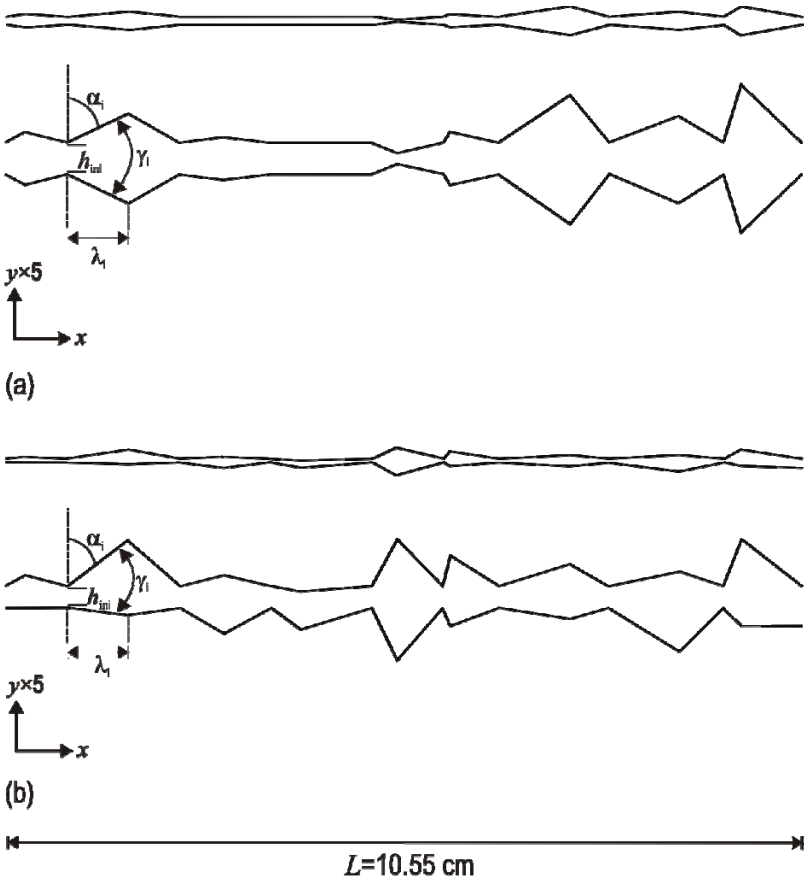

Figure 3.23 Two synthetically generated flow channels.

Table 3.2 Pressure drop calculated from developed correlations and estimated from simulation.

Geometry profile	ΔP-FLUENT (Pa)	ΔP-Correlation (Pa)	Error (%)
Symmetric (Figure 3.23-a)	0.107	0.096	9.81
Asymmetric (Figure 3.23-b)	0.053	0.058	8.61

3.5 Summary

In this Chapter, a wide range of synthetic triangular profiles were subjected to fluid flow simulations using FLUENT software. Both mate and non-mate geometries were studied and the effect of a number of asperities and asymmetric profiles were investigated. Analytical calculations for a unit hydraulic cell were developed from which the equivalent hydraulic aperture can be estimated. It was discussed why the fluid parameters were needed to be included for hydraulic aperture estimation and therefore correlations were developed based on simulations of a wide range of UHC geometries for a particular set of fluid parameters. The developed correlation applied to the analysis

of two generated flow channels and comparison of the results with those obtained from direct FLUENT simulation demonstrated the applicability of the correlations.

In the next Chapter, JRC flow channels developed from JRC profiles will be subjected to the fluid flow simulations of FLUENT and correlations will be derived for estimation of flow properties of real 2D rock fracture.

4 Fluid flow response of JRC exemplar profiles

Numerical and analytical studies of fluid flow for synthetic channels (i.e. sinusoidal and triangular) were carried out in the last two Chapters. In this Chapter, to incorporate the effect of profile roughness in hydraulic behaviour of fractured rock masses, the joint roughness coefficient (JRC) proposed by Barton and Chobey (1977) is used (see Section 2.1.4).

In this Chapter, JRC flow channels are developed and subjected to fluid analysis using FLUENT software. Correlations will be derived based on simulation results of which fluid flow parameters of 2D fractures can be estimated.

4.1 Fluid flow analysis of single JRC flow channels

JRC has been correlated to the mechanical and hydraulic properties of rock fractures (e.g. Barton *et al.*, 1985). For this reason, and also the simple application of this approach, JRC has been widely used in different rock engineering applications to study the hydro-mechanical properties of fractures, even though it is well known that JRC is a subjective method and suffers from a number of deficiencies (Hosseinian *et al.*, 2010a; Liu and Sterling, 1990; Rasouli and Harrison, 2001). In real applications one should estimate the JRC of the top and bottom walls of a fracture and then use equation (2.24), to obtain estimation for hydraulic aperture (h_H) of the fracture. The hydraulic aperture is then replaced with opening h in the cubic law equation for smooth channels to estimate the pressure drop along a fracture (see Subsection 1.1.1).

There are two immediate difficulties associated with the above and similar approaches can be pointed out. The first issue is related to the subjective nature of JRC assessment as discussed earlier: different JRC values may be assigned to a rock profile by different people, which leads to different results for the fluid response of a fracture. To partly overcome this problem, the statistical parameters of rock profiles have been correlated to JRCs which allows a more objective assessment of roughness of rock surfaces to be made. This is discussed in detail in the next section and a new correlation

developed between JRC and the newly proposed roughness parameter (D_{R1}) will be presented.

The second difficulty in using the above approach is related to averaging JRC values of the top and bottom walls of the fracture. To explain this issue, four synthetically generated fractures are shown in Figure 4.1. The top and bottom walls of these fractures are profiles taken from JRC exemplars. Each fracture is referred to as JRC_{ij} where i and j are indices indicating the top and bottom wall of the JRC profile number. As seen from Figure 4.1, fractures shown in Figure 4.1(a) and 4.1 (b) are made up from JRC profiles number 5 and 9 but their position has been changed. This is the same for fractures in Figures 4.1 (c) and 4.1 (d) where JRC profiles six and eight constitute the top and bottom walls of these two channels. For each fracture, the JRC value corresponding to the top and bottom wall is also given in Figure 4.1. An important point is that for all these fractures the average JRC is similar and equivalent to JRC_a=13. From Figure 4.1, one can immediately see a large difference between geometry of these fractures while their averaged JRC is similar.

The above simple example shows a potentially large error in estimating fracture hydraulic parameters due to the averaging of JRC of the top and bottom walls of a fracture without considering the geometry and position of each wall individually. The importance of this becomes clearer if it is noted that 100 fractures with combinations of JRC profiles could be generated and in some cases the average JRC of five fractures may be similar (for instance JRC_a = 11 represents five flow channels of JRC_{210}, JRC_{39}, JRC_{48}, JRC_{57} and JRC_{66}). However, the fluid flow properties corresponding to the averaged roughness parameter may also be useful in obtaining a mean expected response of the fracture.

The study presented here was initiated as a result of the above findings and therefore JRC flow channels were developed with a combination of pairs of JRC profiles. These generated fractures were subjected to numerical analysis of fluid flow using FLUENT software. This is discussed in the following sections.

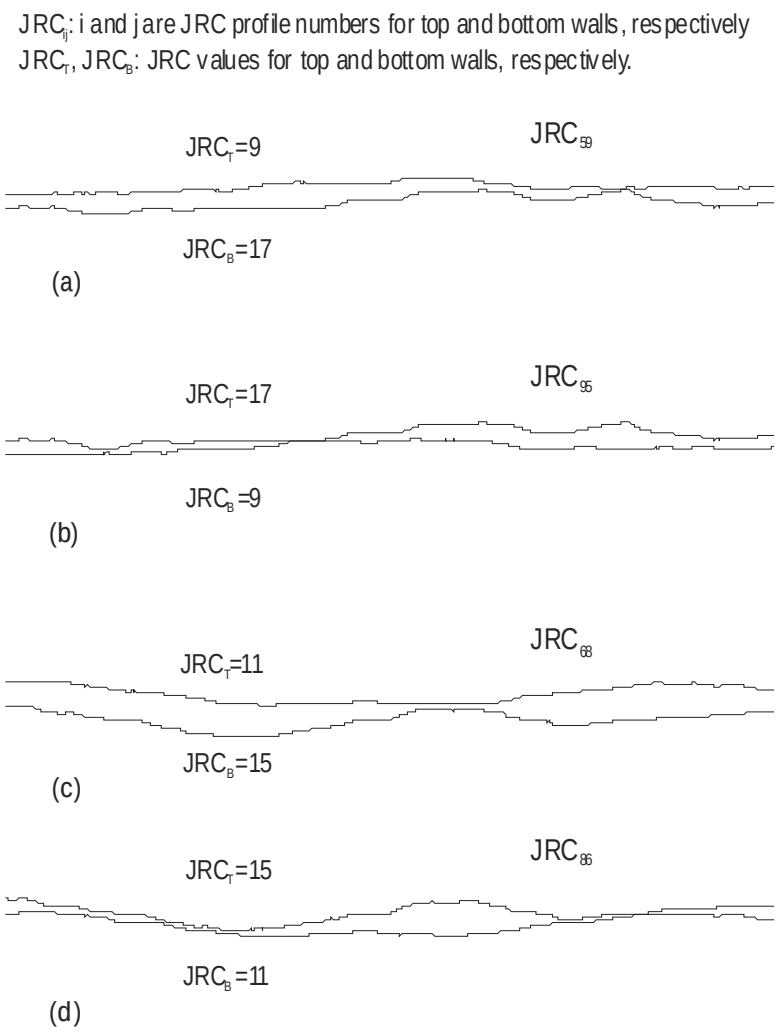

Figure 4.1 Four generated JRC flow channels with JRC_T (Top wall) and JRC_B (Bottom wall).

4.2 Development of JRC flow channels

In this study, bearing in mind that JRCs are meant to represent the range of real rock surface geometries, a detailed analysis of JRC profiles with respect to fluid flow was carried out. For this purpose, JRC flow channels were developed where the top and bottom wall of each channel was taken to be one of the 10 JRC exemplars (see Figure 2.14). The digital elevation of JRC profiles was extracted from the scan of printed images of the ten profiles at high resolution (Rasouli, 2002).

Examples of JRC channels showed in Figure 4.1, where channel JRC_{ij} represents a fracture whose top and bottom walls are JRC profiles i and j, respectively. Considering 10 JRC profiles, a total of 100 JRC flow channels can be generated. It is

important to note that, as per the discussion in the previous section and from Figure 4.1, the fluid flow response of flow channel JRC_{ij} is not necessarily similar to that of JRC_{ji}.

The 2D analysis of fluid flow requires no contact between the top and bottom wall at any point along the fracture length. In this study, in order to retain the consistency throughout the fluid analysis of different JRC flow channels a constant minimum closure distance (d_{mc}) was assumed for all 100 flow channels. This allows for a disregard of the influence of minimum throat size on fluid flow behaviour and allows an investigation of the effect of channel geometry only. In Figure 4.2, d_{mc} is shown for a typical JRC flow channel. However, to investigate the effect of the minimum closure on flow response, the analyses were performed for three different d_{mc} of 0.01, 0.05 and 0.1cm, respectively: this is thought to be comparable with real rock fractures and the results corresponded to lesser d_{mc} which indicated they were highly affected by reduced opening size. Therefore 300 flow channels were analysed in total. It is important to note that for flow channels of $JRC_{ii,}$ where the top and bottom walls are identical, it can be seen that in most cases a large departure from one wall is required to satisfy the condition of $d_{mc}>0$ (Hosseinian *et al.*, 2010a) . This is more intense in the case of JRC profiles which contain steep lag intervals and therefore it was found that within the d_{mc} range of 0.01 to 0.1cm inclusion of the results of these profiles is inappropriate. This will not have an impact on the correlations developed here, as statistically reduction of 100 cases to 90 will not result in a loss of general data trend.

The average JRC value corresponding to a JRC flow channel (JRC_a) is the average of the JRC value corresponding to the top and bottom wall. However, as also noted in the previous section, several channels may have similar JRC_a depending on the JRC values of the top and bottom wall (for example flow channels JRC_{59} and JRC_{68} shown in Figure 4.1).

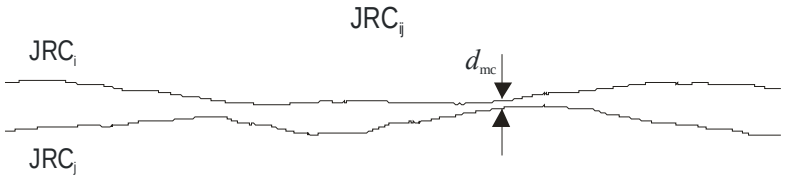

Figure 4.2 A typical JRC flow channel with minimum closure distance, h_{min}.

The aim of this chapter is to analyse a large range of flow channels based on a combination of JRC profiles corresponding to real fractures and thus obtain correlations

between fracture mechanical and hydraulic parameters. Analysis of these simulated fractures will be conducted numerically using FLUENT software.

4.3 Correlation between JRC and D_{R1}

The subjective nature of the JRC approach in characterising surface roughness was mentioned in Section 4.1. This was discussed to be important when JRC is used to estimate fracture hydro-mechanical properties. To partly overcome this difficulty several attempts have been made to correlate JRC with some statistical parameters. For example, Tse and Cruden (1979) investigated the relationship between different statistical parameters and JRC values. They found that the values of root mean square (RMS) slope (Z_2) is correlated with JRC and therefore presented the following correlation for estimation of JRC of real rocks:

$$\mathrm{JRC} = 32.2 + 32.47 \log Z_2 \tag{4.1}$$

In the above equations Z_2 is defined as

$$Z_2 = \left[\frac{1}{L} \int_0^L \left(\frac{dz}{dx} \right)^2 dx \right]^{0.5} \tag{4.2}$$

where L is the sampling length.

Considering the potential advantages of D_{R1} as explained in Section 2.1.5 as a quantitative measure of roughness, an attempt is made in this study to correlate this parameter with JRC: this will allow an indirect estimation of JRC of a rock profile from its D_{R1} value. Accordingly, D_{R1} corresponding to 10 exemplar JRC profiles were estimated at a very small sampling size and the results are shown in Figure 4.3. This figure shows that, in general, D_{R1} increases as JRC becomes larger, although this trend is not consistently followed from one JRC profile to the next larger profile: for example D_{R1} reduces from JRC = 15 to JRC = 17. From Figure 4.3 it is also seen that JRC = 19 shows a larger D_{R1} compared to other profiles. Discarding the point corresponding to JRC = 19, the following linear correlation fits the data best

$$D_{R1} = 0.0069\mathrm{JRC} + 0.1172 \tag{4.3}$$

or

$$\mathrm{JRC} = \frac{\left(D_{R1} - 0.1172\right)}{0.0069} \tag{4.4}$$

The results of Z_2 and D_{R1} estimated for some rock fractures will be compared in Section 4.6. However, it is important to mention that depending on the range of roughness of real rocks, D_{R1} can be up-scaled to be representative of larger Mahalanobis distances (Rasouli and Harrison, 2010) but this requires further research which is not the subject of this work.

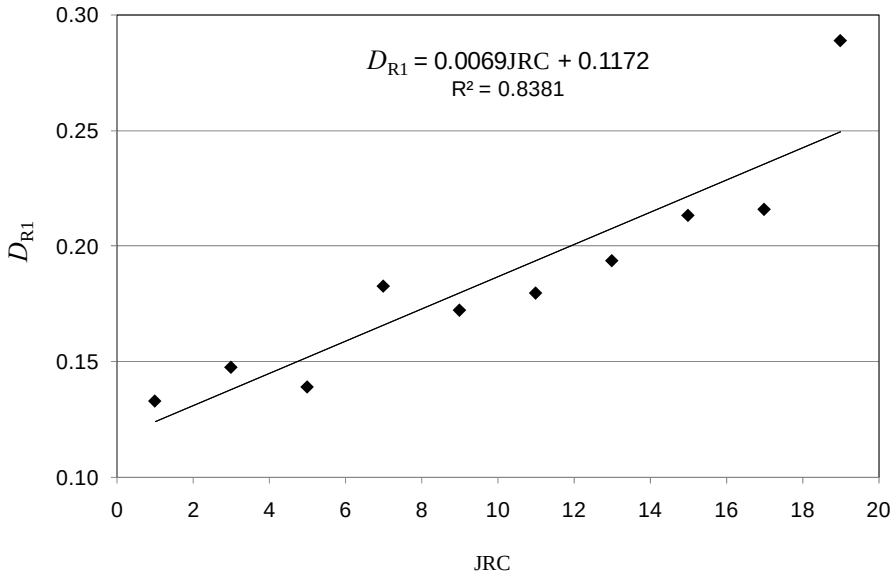

Figure 4.3 Correlation between JRC and Riemannian roughness parameter D_{R1}.

Based on the detailed discussions given in the two previous sections, similar JRC average values for a fracture could be obtained as a result of different combinations of JRC profiles forming the top and bottom walls of the fracture. Therefore, to obtain a more representative correlation for estimating JRC with its particular applications in fluid flow analysis, we calculated D_{R1} for different profiles with a 20 cm length as being the combined length of the top and bottom walls corresponding to each JRC flow channel. As for each channel, changing the position of the top and bottom walls did not change the roughness of the combined profile. A total of 55 profiles with a length of 20 cm were generated. Each combined profile represented an average JRC value. These profiles represented a range of geometry of rock fractures and therefore their average was expected to be a more appropriate value for use in the fluid flow analysis of rock fractures. As an example, Figure 4.4 shows a combined JRC profile produced from the JRC96 flow channel. The average JRC for this profile is $JRC_a = 14$.

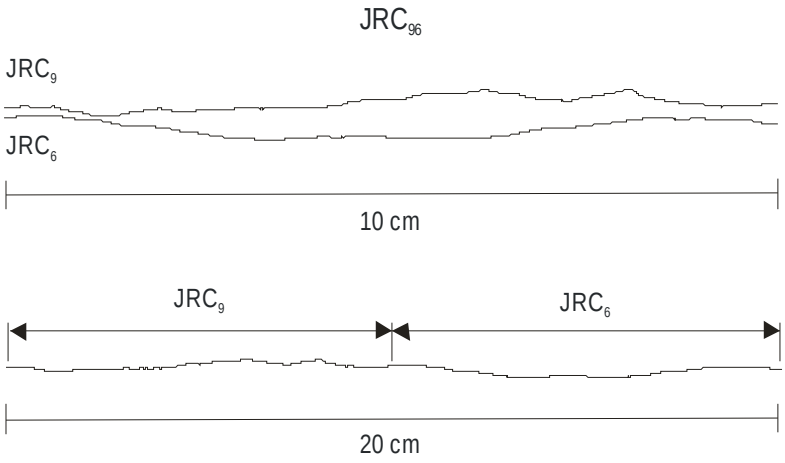

Figure 4.4 A combined JRC profile.

All 55 combined JRC profiles were subjected to D_{R1} analysis. The plot of D_{R1} versus average JRC value corresponding to each profile is shown in Figure 4.5. This figure shows an increasing trend for D_{R1} as JRC increases. Also, Figure 4.5 demonstrates how fractures with similar averaged JRC values may differ in their roughness and therefore a range of roughness is expected for an averaged JRC value. For example, as can be found from Figure 4.5, D_{R1} changes between 0.1806 and 0.2238 for JRC=10 depending on which combination of JRC profiles form the top and bottom walls of the fracture. In this example, the minimum JRC_a belongs to combined profile JRC_{38} with JRC_{110} being the roughest channel. A linear correlation between D_{R1} and JRCa is obtained in the form of 55 combined JRC profiles were subjected to D_{R1} analysis. The plot of D_{R1} versus average JRC value corresponding to each profile is shown in Figure 4.5. This figure shows an increasing trend for D_{R1} as JRC increases. Also, Figure 4.5 demonstrates how fractures with similar averaged JRC values may differ in their roughness and therefore a range of roughness is expected for an averaged JRC value. For example, as can be found from Figure 4.5, D_{R1} changes between 0.1806 and 0.2238 for JRC=10 depending on which combination of JRC profiles form the top and bottom walls of the fracture. In this example, the minimum JRC_a belongs to combined profile JRC_{38} with JRC_{110} being the roughest channel. A linear correlation between D_{R1} and JRC_a is obtained in the form of

$$D_{R1} = 0.0071 JRC_a + 0.1185, \tag{4.5}$$

or

$$JRC_a = \frac{(D_{R1} - 0.1185)}{0.0071} \tag{4.6}$$

From Figure 4.5 the upper and lower bounds for JRC_a variation could be defined as below:

$$JRC_a(LL) = \frac{(D_{R1} - 0.1072)}{0.0064} \tag{4.7}$$

and

$$JRC_a(UL) = \frac{(D_{R1} - 0.1230)}{0.0101} \tag{4.8}$$

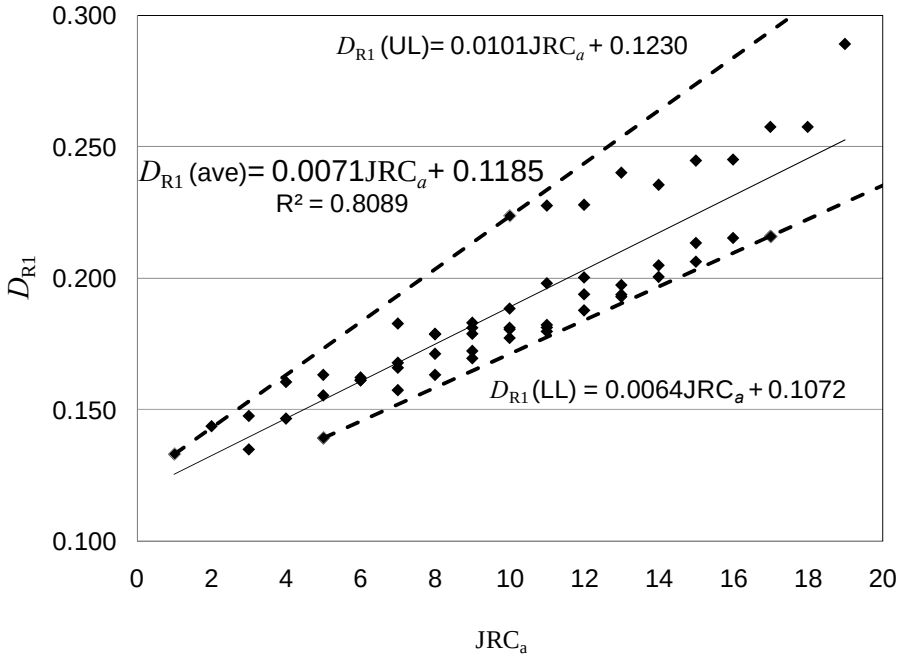

Figure 4.5 D_{R1} for combined JRC profiles.

The mean JRC estimated from Equation 4.6 provides close results to that of Equation 4.4, but gives a window within which the JRC may change. The above analysis shows a wide range for JRC_a depending on the roughness of the two walls of the fractures and therefore it is more appropriate to assign a range, instead of a unique number, within which the JRC_a varies. This range of JRC_a can be used for fluid flow analysis which in turn determines a possible range for flow parameters, for example mean hydraulic aperture or fracture pressure drops. This will be discussed in section seven where applications for some real rock profiles are given.

As explained above, a proposition will be made to estimate JRC_a for a fracture from D_{R1} corresponding to combined length of the two walls, but not as an average of JRC corresponding to each wall, which is common practice. The results of our analysis indicate that JRC_a, estimated from the proposed approach here, provides slightly larger

values for JRC of the fracture and that is a better parameter when it is linked with hydraulic parameters of the fractures.

4.4 Fluid flow simulation using FLUENT

All JRC flow channels were subjected to fluid flow analysis to obtain a representative range for flow response of real rock fractures. The analysis carried out for three minimum closure distances (d_{mc}) of 0.01, 0.05 and 0.10cm. The simulations were performed numerically using FLUENT software.

Table 4.1 shows the parameters used for simulations of JRC flow channels, similar to those properties used for synthetic geometries in the previous Chapters.

Table 4.1 FLUENT input data for simulations of JRC flow channels

Boundary Conditions:	
Inlet	Mass flow inlet
Outlet	Pressure outlet
Fluid:	Water
Density (kg/m^3)	998.2
Viscosity (kg/ms)	0.001
Volumetric flow rate (m^3/s)	1×10^{-7}

In order to perform all simulations consistently and efficiently in terms of running time, journal files were written in a text user interface (TUI) format for both Gambit and FLUENT. A journal file contains a series of TUI commands written in a text file using a text editor or generated by FLUENT as a transcript of the commands given to FLUENT. Using journal files is very useful when a series of similar simulations need to be executed, as it provides a shortcut (FLUENT inc., 2005).

Figure 4.6 shows an example of generated mesh using Gambit for one JRC flow channel. The use of high density quad meshes (a total of 5000 nodes along the profile length and 25 nodes across the profile) ensures a high accuracy for the results obtained from FLUENT.

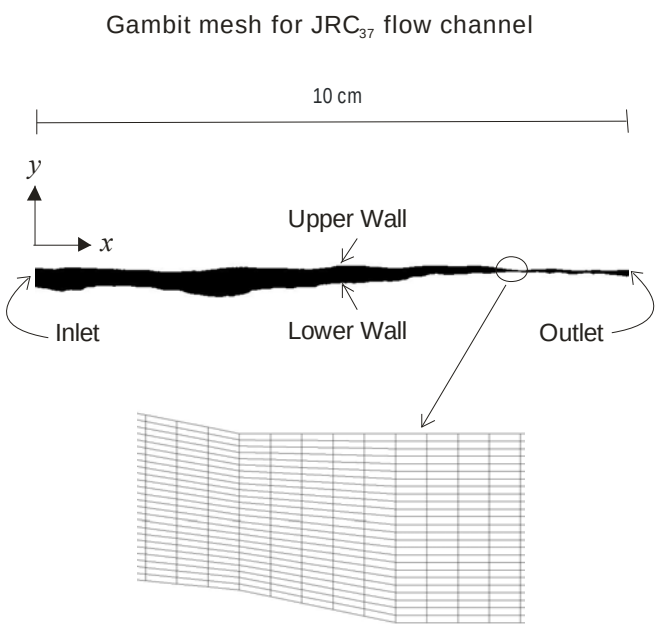

Figure 4.6 An example output of Gambit mesh for JRC37 flow channel.

All meshes were imported to FLUENT and subjected to fluid flow analysis. Various hydraulic properties can be presented graphically in FLUENT including pressure and velocity contours. As an example, the contours of total pressure and average velocity magnitude corresponding to JRC_{37} are shown in Figure 4.7. Figure 4.7 (a) shows how total pressure reduces as the fluid moves to the right, i.e. from channel inlet towards the outlet. The total pressure changes from a maximum of 1.43 Pa at the inlet to a minimum of 0 Pa when it arrives at the channel outlet: i.e. a total pressure drop of 1.43 Pa. The small range of pressure values are due to a small value of flow rate assumed for the simulations. This is unimportant in this study as the main objective of this work is to compare the response of different JRC flow channels. However, one may normalise the pressure values by dividing them by pressure drop of a smooth channel with its opening being equivalent to the minimum closure distance (d_{mc}) of the given JRC flow channel. Considering that the length of all JRC flow channels are identical (i.e. 10cm) and for a unit width, the pressure drop corresponding to three d_{mc} of 0.01, 0.05 and 0.1cm would be obtained from equation 1.10 as 120, 0.96 and 0.12 Pa, respectively.

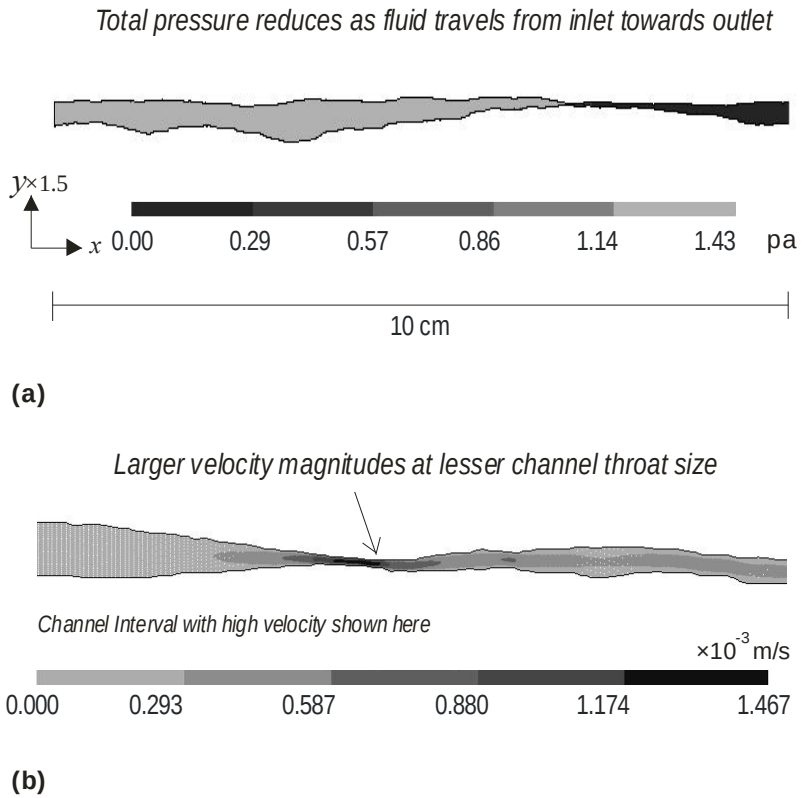

Figure 4.7 An example contours of total pressure and (b) velocity magnitude for JRC flow channel JRC37 with h_{min}=0.01cm.

In Figure 4.7 (b) the contours of velocity magnitude shown for a small interval of this fracture, where the maximum velocity occurs, indicates a variation range between 0 and 0.001467 m/s. As expected, it can be seen that larger velocities occur at lower openings along the channel with its maximum being at the point where the opening is equal to d_{mc}, i.e. the lowest opening along the fracture. Also, considering the flow is laminar with a hyperbolic velocity profile, it is clear that getting closer to channel walls makes the velocity reduce and finally become zero.

4.5 Data analysis of JRC flow channels

In this section, the results of fluid flow analysis of JRC flow channels performed using FLUENT are presented. However, in order to interpret the results given here, it is important to note that in this study we have considered a constant minimum closure distance (d_{mc}) for all JRC flow channels. This was done to discard the significant impact of the maximum reduction in channel size on flow response and to allow an investigation of the effect of channel roughness on flow response. Therefore, it is expected, that as the JRC flow channel walls become rougher, i.e. larger JRC_a, the

mechanical aperture of the channel increases, which in general results in a smaller pressure drop or average fluid velocity, assuming that the flow rate is constant. In other words, in presented JRC flow channels the maximum distance between the two walls is not constant and changes based on the assumed d_{mc}.

The pressure drop for JRC flow channels was extracted directly from FLUENT simulations. This data was used to estimate the hydraulic aperture (h_H) from back analysis of the cubic law given in equation 3.

As an example, Figure 4.8 shows the results of mechanical aperture calculated for JRC flow channels. In this example, the minimum closure distance is d_{mc}=0.01cm. As seen from this figure, h_m increases as JRC_a become larger. The power correlation fitted to the data in Figure 10 allows estimating h_m from JRC_a. A window shown in Figure 4.8 determines the range of data variation for mechanical aperture. The mechanical aperture can also be estimated from the ratio A/L (A is the area between the two walls of the fracture and L is fracture length) (Hosseinian *et al.*, 2010b).

Similar trends were observed for two other cases with d_{mc}=0.05cm and d_{mc}=0.1cm, where mechanical aperture increases with d_{mc}. Therefore, the following correlations were developed based on the normalised aperture (i.e. the aperture divided by the d_{mc}):

$$h_m^n = 1 + \frac{0.05}{d_{mc}} JRC_a^{0.52} \tag{4.9}$$

$$h_m^n \left(\begin{matrix} UL \\ LL \end{matrix} \right) = h_m^n \pm \frac{0.10}{d_{mc}} \tag{4.10}$$

where $h_m^n \left(\begin{matrix} UL \\ LL \end{matrix} \right)$ gives the upper and lower limits for change in mechanical aperture.

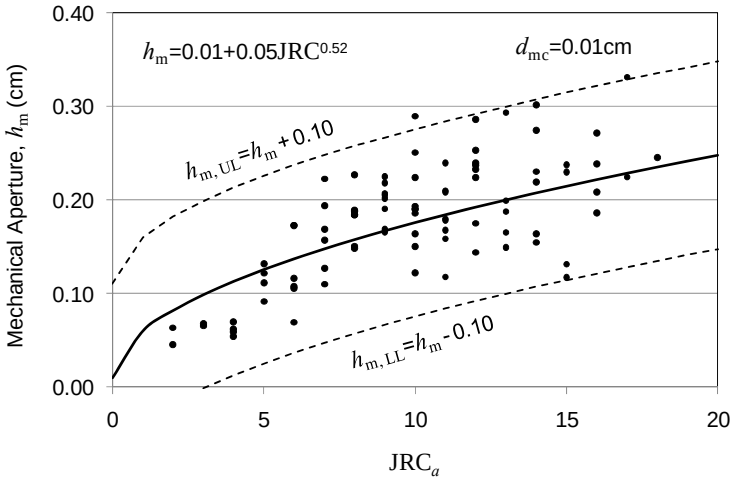

Figure 4.8 Mechanical aperture for JRC flow channels with h_{min}=0.01cm.

An increase in d_{mc} is expected to increase the hydraulic aperture but with a different trend to that of the mechanical aperture. Figure 4.9 shows the plots of hydraulic aperture versus JRC_a corresponding to three d_{mc} of 0.01, 0.05, and 0.1cm, respectively. The power correlations fitted to the data are shown in Figure 4.9. It can also be seen from this figure that the data varies within a window of ±0.012 to ±0.03 and to ±0.04 from Figure 4.9(a) to 4.9(c).

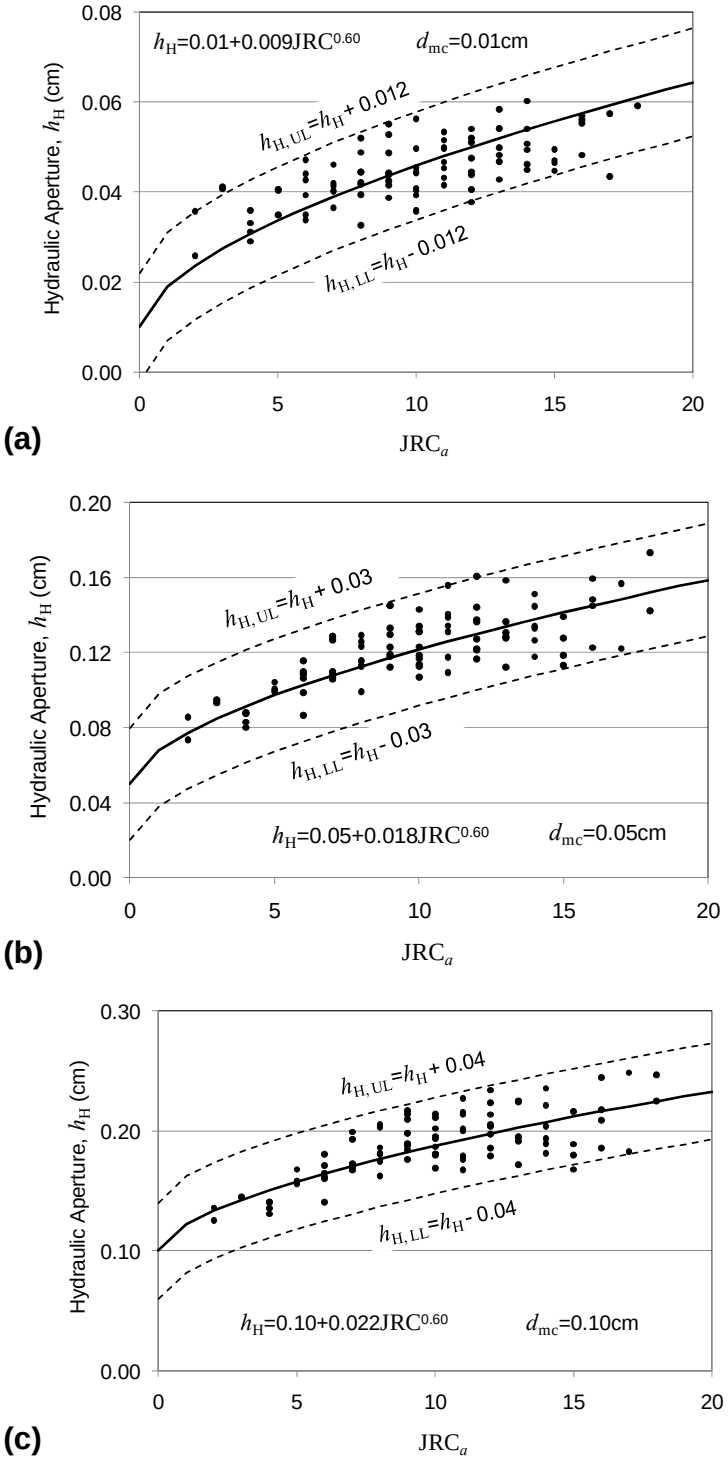

Figure 4.9 Hydraulic aperture for JRC flow channels with different h_{min}.

From the correlations obtained in Figure 4.9, the following correlation was developed for h_H^n as a function of JRC_a and d_{mc}:

$$h_H^n = 1 + \frac{0.06}{d_{mc}^{0.58}} JRC_a^{0.60} \tag{4.11}$$

with data being distributed in a window of

$$h_H^n \left(\begin{matrix} UL \\ LL \end{matrix} \right) = h_H^n \pm \left(\frac{0.13}{d_{mc}^{0.50}} \right) \tag{4.12}$$

In the above equations d_{mc} is in cm. Equation 4.11 shows that regardless of the roughness of the JRC flow channel, if d_{mc} becomes very large the normalised hydraulic aperture approaches to unity, i.e. hydraulic aperture will be equivalent to d_{mc}.

A plot of h_m versus h_H shown in Figure 4.10 shows a gradual increase in h_H as h_m increases. This figure shows the results corresponding to d_{mc} = 0.01 cm, however, similar trends were observed for two other cases where d_{mc} is equal to 0.05 cm and 0.10 cm. Accordingly, the power correlation below was derived between normalised mechanical and hydraulic aperture:

$$h_H^n = \frac{1.77}{d_{mc}^{0.35}} h_m^{0.87 d_{mc}^{0.2}} \tag{4.13}$$

A variation window similar to equation 4.12 was found to be appropriate for Figure 4.10, which shows the range of changes of h_H as a function of h_m.

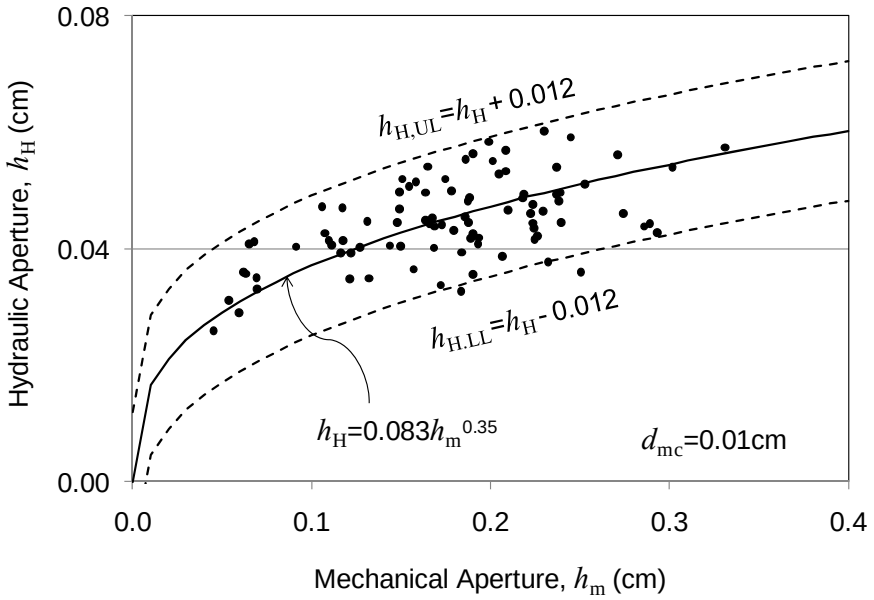

Figure 4.10 Mechanical aperture for JRC flow channels with h_{min}=0.01cm.

Figure 4.11 presents the plots of $(h_H/h_m)^3$ versus JRC_a for different flow channels.

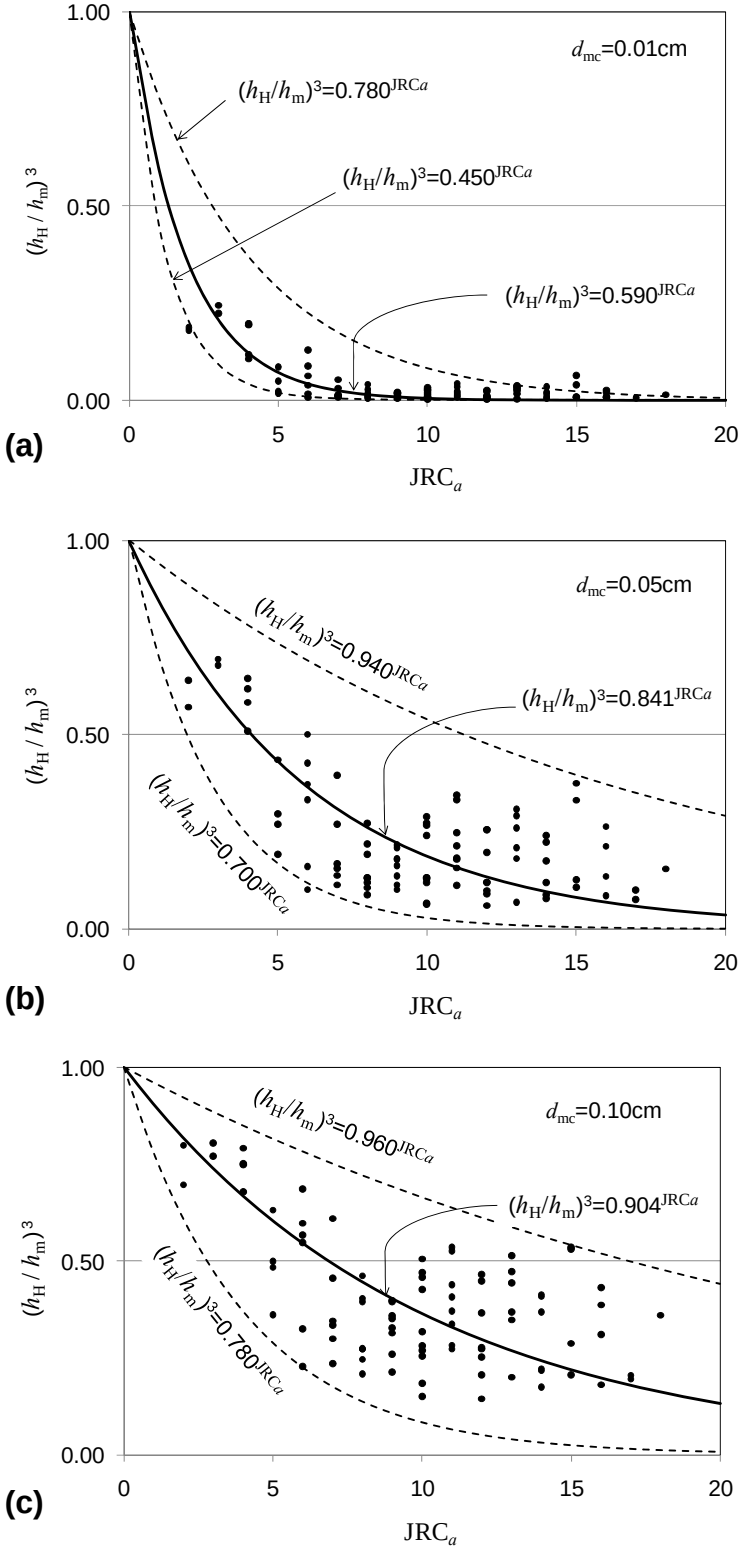

Figure 4.11 Permeability of JRC flow channels with different h_{min}.

The results indicate that larger channel roughness leads to smaller hydraulic conductivity. Also, in comparing Figures 4.11 (a) to 4.11 (c), the larger the d_{mc} the

larger the channel permeability. The best fit to the data is shown in Figure 4.11 including the window in which data distributes. Generalising the results obtained from this figure, a correlation between JRC flow channel permeability as a function of JRC_a and d_{mc} is obtained in the form of

$$\left(\frac{h_H}{h_m}\right)^3 = \left(1 - 0.03 d_{mc}^{-0.565}\right)^{JRC_a} \tag{4.14}$$

As this equation shows, and is seen from Figure 4.11, permeability reduces significantly when d_{mc} get closer to zero and approaches unity for very large values of d_{mc} regardless of the channel roughness.

For real rocks, JRC_a can be estimated in relation to D_{R1} from equation 4.6, in order to obtain permeability through Equation 4.14.

A plot of permeability as a function of h_m/σ, where σ is the standard deviation corresponding to JRC_a can also be produced (Zimmerman *et al.*, 1991). Figure 4.12 shows such a plot for three different d_{mc}. This plot shows how a range of data distribution increases as d_{mc} or h_m increases. In general, permeability increases as the ratio of h_m/σ becomes larger but this is more consistent for d_{mc} = 0.10cm compared to two other smaller openings and for ratios of h_m/σ greater than approximately 3. The results presented here are similar to those reported by other researchers as discussed in Section 2.1.3 (see Figure 2.11 in Chapter 2).

From Figure 4.12, a correlation between permeability of JRC flow channels and h_m/σ is obtained as

$$\left(\frac{h_H}{h_m}\right)^3 = 1 - 2.25\left(\frac{\sigma}{h_m}\right) \tag{4.15}$$

where the data changes within a window with a lower limit of

$$\left(\frac{h_H}{h_m}\right)^3_{LL} = 1 - \left(\frac{\sigma}{h_m}\right) \tag{4.16}$$

and an upper limit of

$$\left(\frac{h_H}{h_m}\right)^3_{UL} = 1 - 3.70\left(\frac{\sigma}{h_m}\right) \tag{4.17}$$

From equations 4.15 to 4.17, it can be seen that as h_m/σ becomes larger, the channel roughness reduces and therefore permeability increases.

For very large values of h_m/σ the permeability approaches unity (i.e. $h_H=h_m$), which corresponds to a smooth channel. On the other hand, as roughness increases, the deviation between hydraulic and mechanical aperture increases.

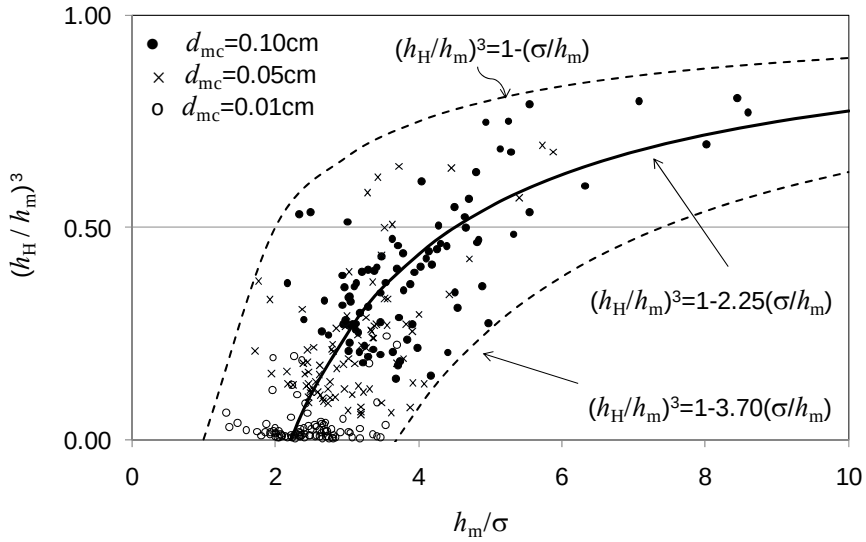

Figure 4.12 Permeability of JRC flow channels with different h_{min} as a function of h_m/σ .

In Figure 4.13 (a), the results of average velocity magnitude (V_n) for JRC flow channels are plotted. The velocity values are normalised with respect to the velocity of a smooth channel with an opening of d_{mc}. As seen from this figure, channels with larger JRC_a show a lesser V_n because the average area of the channel subjected to the flow is larger. Similarly, Figure 4.13 (a) shows the larger the $d_{mc,}$ the higher the average velocity. Correlations between V_n and JRC_a corresponding to three minimum closure distances are given in Figure 4.13, which can be used as a guide. Similar interpretations can be made from Figure 4.13 (b) where the plot of V_n versus h_m/σ is presented. A larger velocity is expected as d_{mc} increases and also a larger roughness for the flow channel (i.e. lesser h_m/σ) results in a lesser V_n.

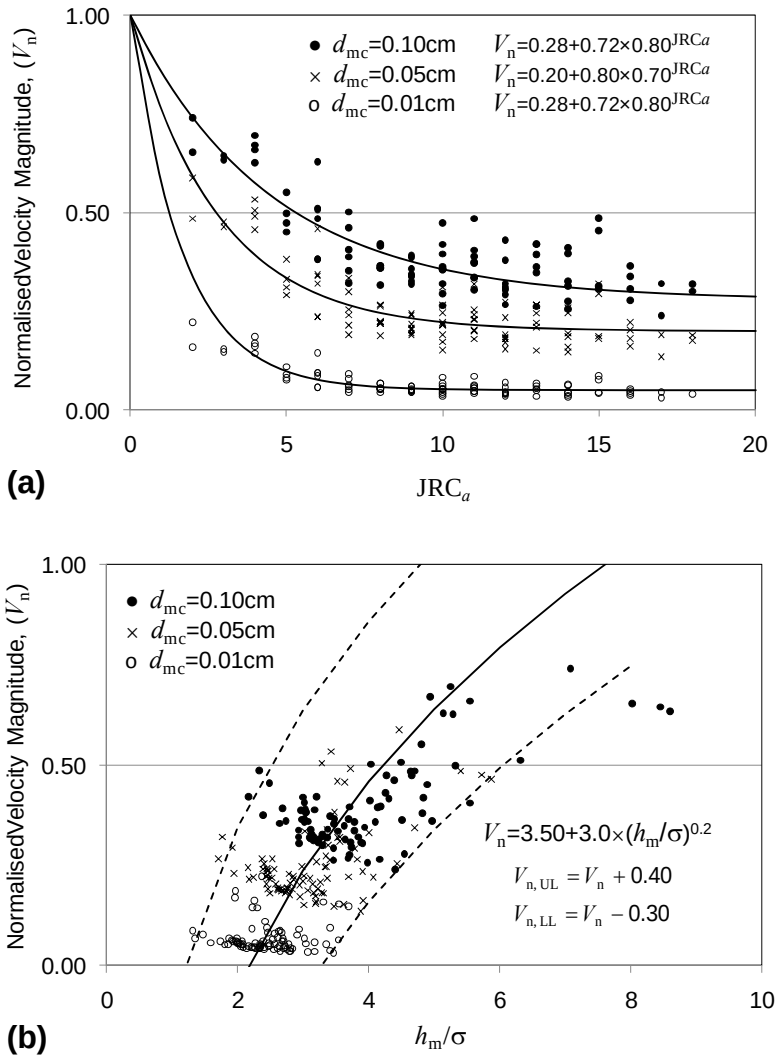

Figure 4.13 Normalised velocity magnitude versus (a) JRC_a and (b) h_m/σ for JRC flow channels with different h_{min}.

The results of normalised pressure drop (ΔP_n) for JRC flow channels are plotted in Figure 4.14 for data corresponding to channels having a d_{mc} = 0.10 cm, with a larger range of values compared to the other two channel openings. This figure shows a reduction in pressure drop as the average JRC of the channel increases: this is due to the fact that the d_{mc} is constant in all cases but the two walls depart further away from each other. Also, a variation range of between approximately +0.10 and -0.05 is observed for pressure drop changes.

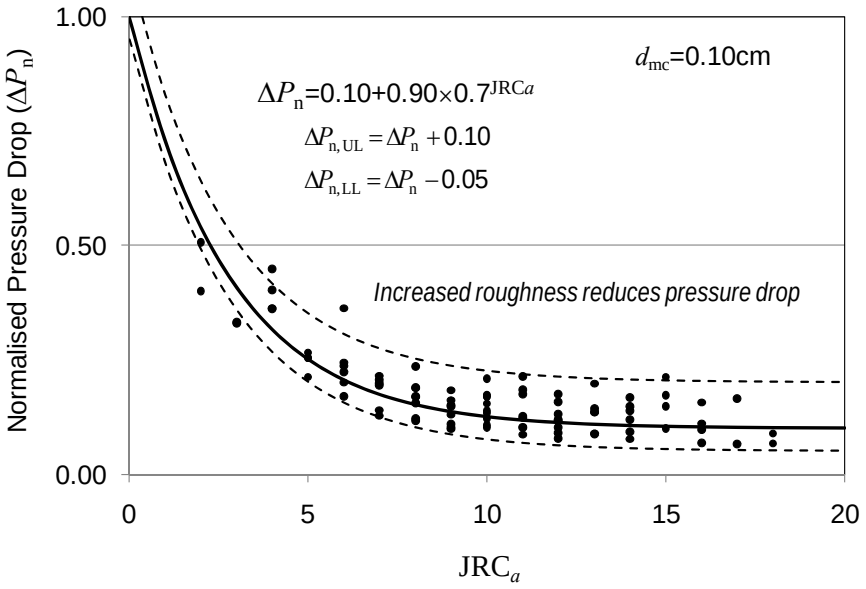

Figure 4.14 Normalised pressure drop versus JRC$_a$ for JRC flow channels with h_{min}=0.10 cm.

A similar trend was observed for JRC flow channels with a d_{mc} = 0.01 cm and 0.05 cm and accordingly, the following correlation was developed between pressure drop and JRC$_a$ as a function of d_{mc}:

$$\Delta P_n = d_{mc} + (1 - d_{mc})\left(1 - 0.15 d_{mc}^{-0.32}\right)^{JRC_a}, \tag{4.18}$$

where pressure drop changes within a window of

$$\begin{aligned} \Delta P_{n,UL} &= \Delta P_n + d_{mc} \\ \Delta P_{n,LL} &= \Delta P_n - \frac{d_{mc}}{2} \end{aligned} \tag{4.19}$$

In this equation, d_{mc} is in cm. Equation 4.18 indicates that, regardless of the roughness of the flow channel, pressure drop increases significantly when d_{mc} becomes very small, but approaches unity if d_{mc} increases largely: the latter corresponds to the pressure drop of a smooth channel with opening d_{mc}. As can be seen, equation 4.18 satisfies the limit conditions (i.e. ΔP approaches infinity if d_{mc} tends towards zero) and appears to give a good estimation of the pressure drop of rock fractures. This will be assessed in Section 4.6, where applications of this correlation in some rock fractures are presented.

Several similar correlations could be developed between various geometrical and hydraulic parameters of JRC flow channels depending on the particular application required. However, the results of JRC flow channels show how it may be possible to

obtain a more generalised flow response of real rock surfaces by analysing a large range of simulated fractures.

Using the developed correlations above, it is possible to estimate the average JRC_a values of the fracture walls using correlations 4.1 or 4.6 from corresponding Z_2 or D_{R1} values. Then, the hydraulic aperture can be calculated from equation 4.11 and pressure drop can be estimated through equation 4.18.

It is important to note the input parameters used (see Table 4.1) to derive these correlations. If a fracture is analysed with properties different to those used here, the flow parameters should be modified accordingly.

The developed correlations will be applied to the analysis of several real rock fractures in the next section.

4.6 Analysis of rock fractures

In order to examine the range of applications of the developed correlations in the previous section, several real rock fractures with a wide range of average roughness were studied using these correlations. Here the results corresponding to nine fractures taken from a granite block are presented and compared with those obtained from direct simulation of these fractures using FLUENT software.

In order to demonstrate the applicability of the correlations developed here, an attempt was made to extract 2D profiles with a wide range of roughness along different directions across the granite block. The geometry of nine fractures (F1 to F9) used for this study is shown in Figure 4.15.

The length of all fractures was taken to be 10 cm, similar to the JRC flow channels. The minimum closure distance (d_{mc}) was different for these fractures (ranging from 0.03 to 0.10 cm). A selection of smaller d_{mc} was found to be inappropriate for illustration purposes as, in this situation the fracture response would be significantly affected by a sudden reduction of the fracture opening.

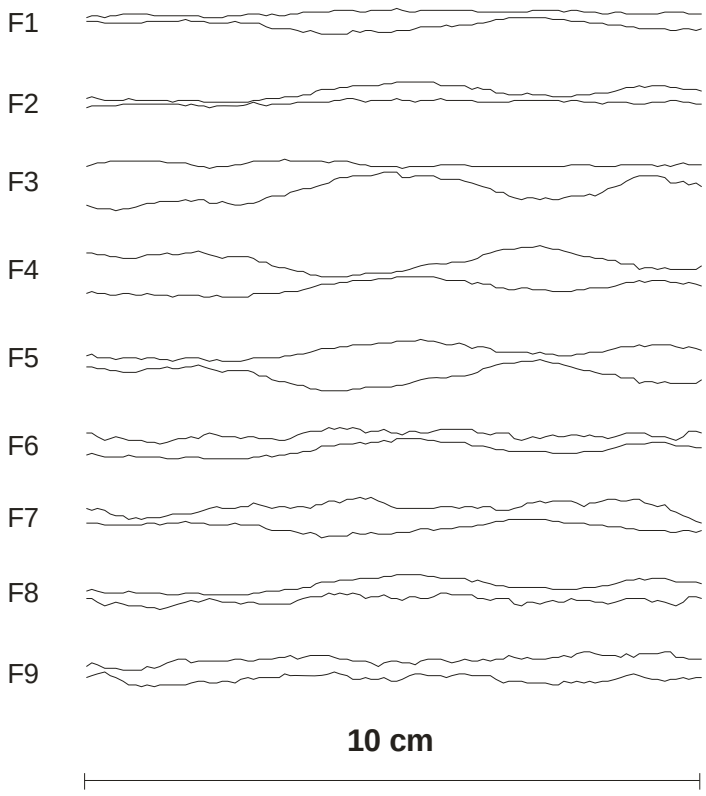

Figure 4.15 Geometry of nine rock fractures F1 to F9 used for fluid analysis.

In Table 4.2, d_{mc}, together with statistical parameters Z_2 and D_{R1} introduced in Section 4, are estimated for these fractures and shown. It is interesting to note that fracture F5 and F6 have a similar roughness (i.e. D_{R1}) but their d_{mc} is different: it is 0.10 and 0.07 for fracture F5 and F6, respectively. The data in Table 4.2 was used to estimate JRC_a for these fractures from Equation 4.1 and 4.6, respectively, and these values are also shown in Table 4.2 and plotted in Figure 4.16. From this figure, it appears that for these fractures D_{R1} generally overestimates JRC_a compared to those obtained from Z_2.

Table 4.2 Roughness parameters calculated for nine rock fractures F1 to F9

Fracture	d_{mc}	D_{R1}	**JRC_a (from D_{R1})**	**JRC_a (from Z_2)**
F1	0.054	0.1652	6.58	5.06
F2	0.034	0.1700	7.25	5.55
F3	0.076	0.2271	15.30	9.08
F4	0.073	0.2290	15.56	10.36
F5	0.102	0.2352	16.43	10.36
F6	0.071	0.2347	16.37	11.48
F7	0.077	0.2458	17.93	11.04
F8	0.071	0.2500	18.52	11.48
F9	0.067	0.2612	20.00	13.63

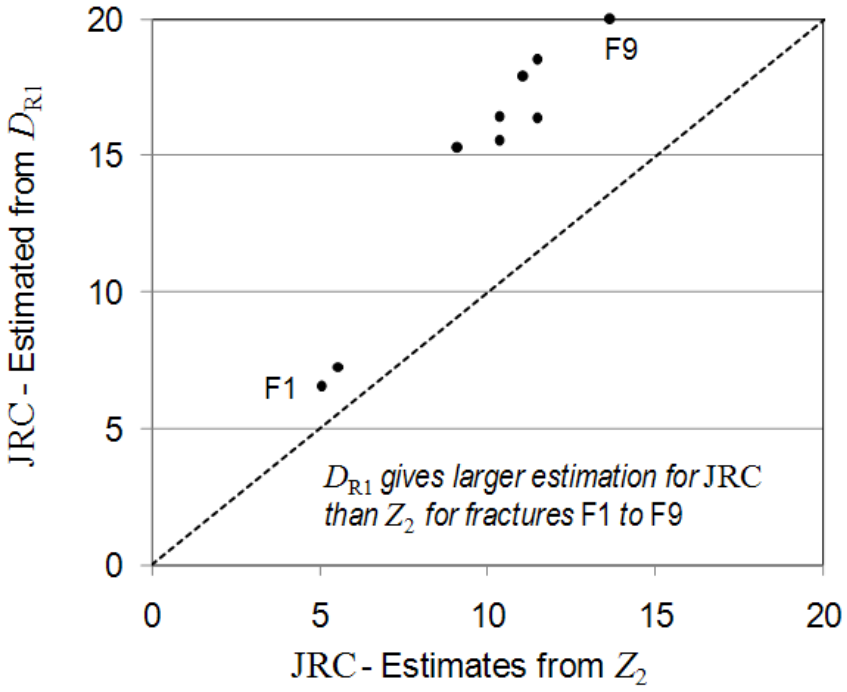

Figure 4.16 Roughness assessment for fractures F1 to F9.

Fractures F1 to F9 were subjected to FLUENT analysis and correlations were also developed in the previous section and applied to estimate their flow parameters. In Figure 4.17 (a), the normalised mechanical apertures (h_m^n) for these fractures estimated through correlation 4.9 is compared against those obtained from FLUENT simulations. Similarly, Figure 4.17(b) shows hydraulic apertures (h_H^n) corresponding to fractures estimated from correlation 4.11 and simulations. In Figure 4.17, the upper and lower limits for apertures obtained from correlations 4.10 and 4.12, respectively, are marked. This figure indicates a very good agreement between the results obtained through the developed correlations and simulation, as most of the data is distributed alongside the line with a 45° slope and is within the expected limits.

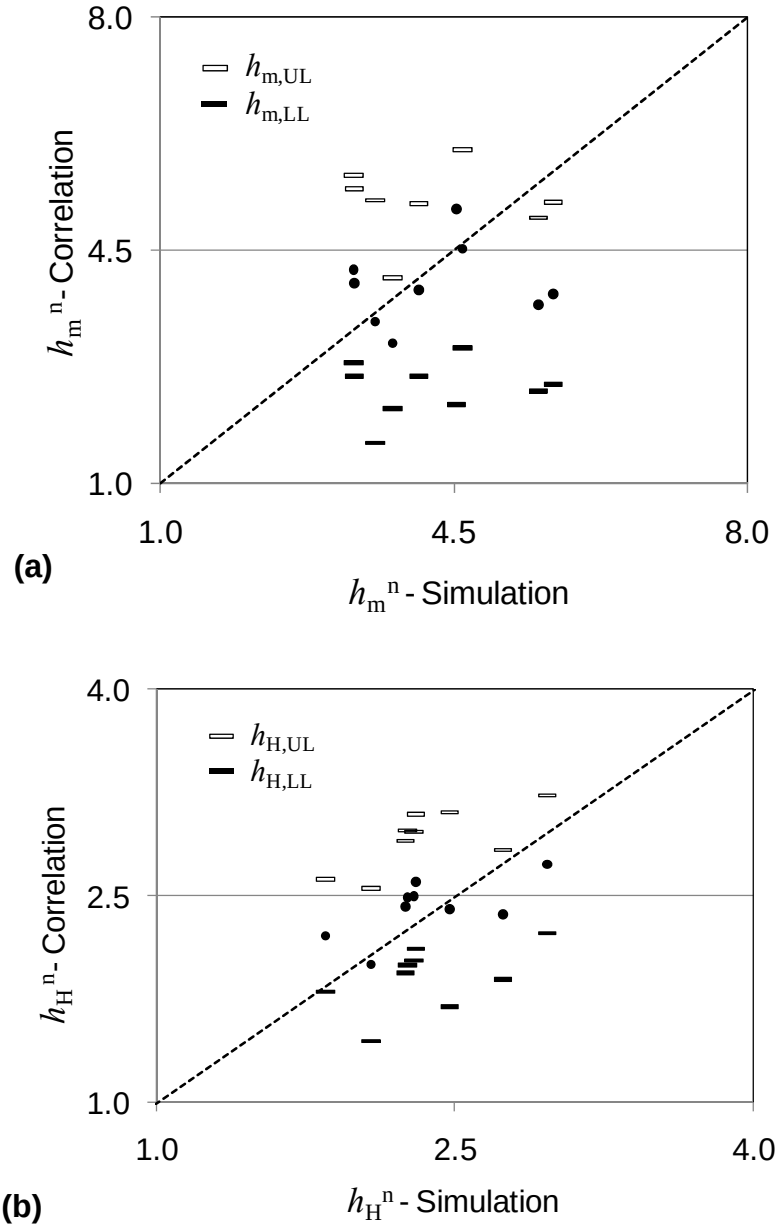

Figure 4.17 Comparison of normalised (a) Mechanical and (b) hydraulic aperture for fractures F1 to F9 obtained from developed correlations and simulation.

Figure 4.18 presents the results of normalised pressure drop for fractures F1 to F9 obtained from the simulation and correlation 4.18. The expected limits for data variation estimated from correlation 4.19 are marked in Figure 4.18. This figure shows a good prediction made by the developed correlation for fracture pressure drop based on the JRC flow channels.

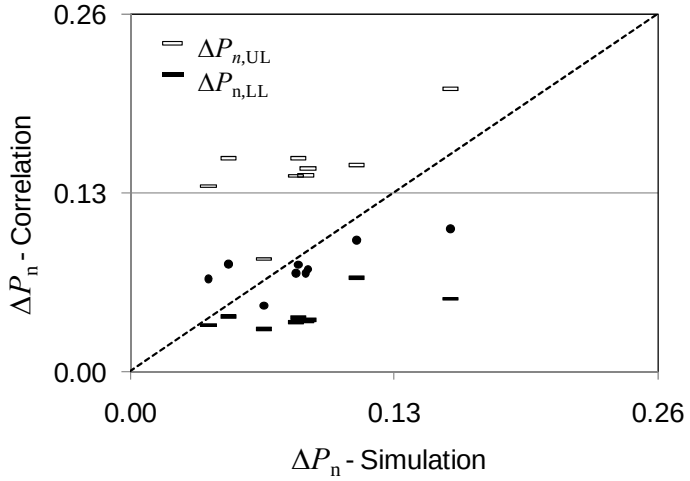

Figure 4.18 Comparison of normalised pressure drop for fractures F1 to F9 obtained from developed correlations and simulation.

The results of Figures 4.17 and 4.18 demonstrate the applications of developed correlations based on JRC flow channels to estimate hydraulic parameters of rough rock fractures. In Figure 4.19, the normalised mechanical (h_m) and hydraulic (h_H) apertures estimated for given fractures are plotted against their roughness parameter D_{R1}. From this figure, it can be seen that generally both mechanical and hydraulic apertures increase from fracture F1 to F9, i.e. as fractures become rougher. Correspondingly, the pressure drop reduces as we move from fracture F1 to F9, as depicted in Figure 4.20. In Figure 4.20, it is interesting to note that fracture F5 indicates a larger pressure drop than F6 although their roughness is identical. Looking at the geometry of these two fractures, it is seen that in Figure 4.15 fracture F5 experiences a large reduction in its opening which results in a larger aperture and hence pressure drop.

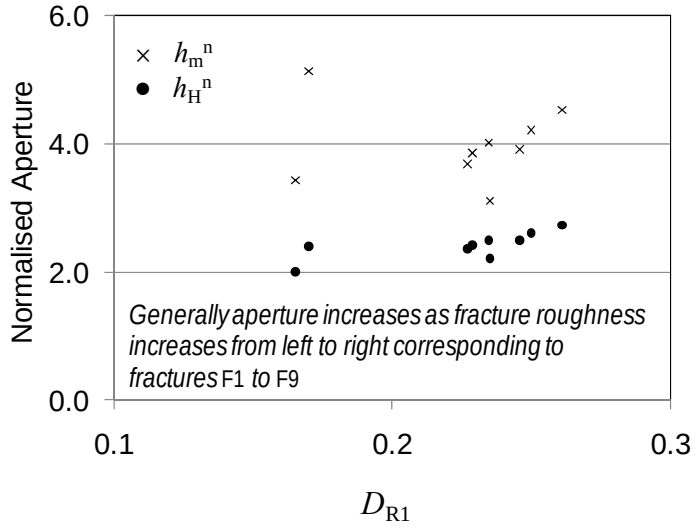

Figure 4.19 Normalised mechanical and hydraulic aperture versus D_{R1} for rock fractures F1 to F9.

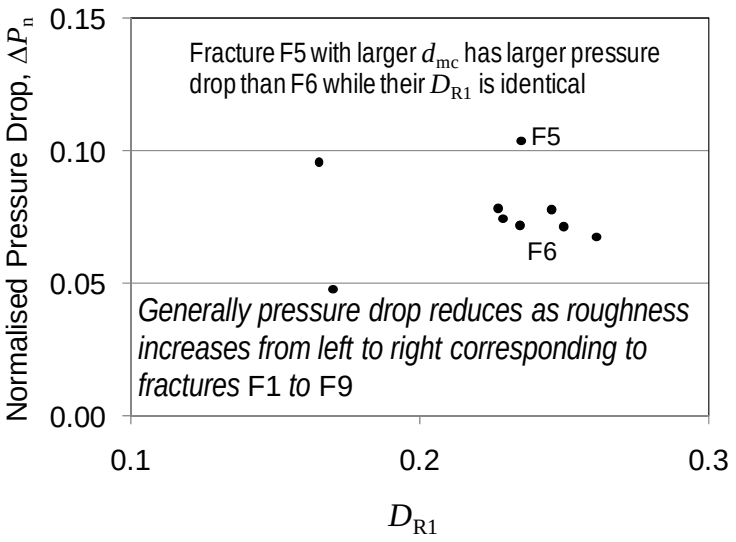

Figure 4.20 Normalised pressure drop versus D_{R1} for rock fractures F1 to F9.

In Figure 4.21, the plot of fracture permeability is shown with respect to D_{R1}. From this figure, it is expected that in general fracture permeability reduces from F1 to F9 due to a lesser area being exposed to fluid flow when the fracture becomes rougher. This figure indicates a larger permeability for fracture F5 than F6. This is due to the fact that fracture F5 has a larger d_{mc} compared to F6 (see Table 4.2) which results in a larger transmissivity.

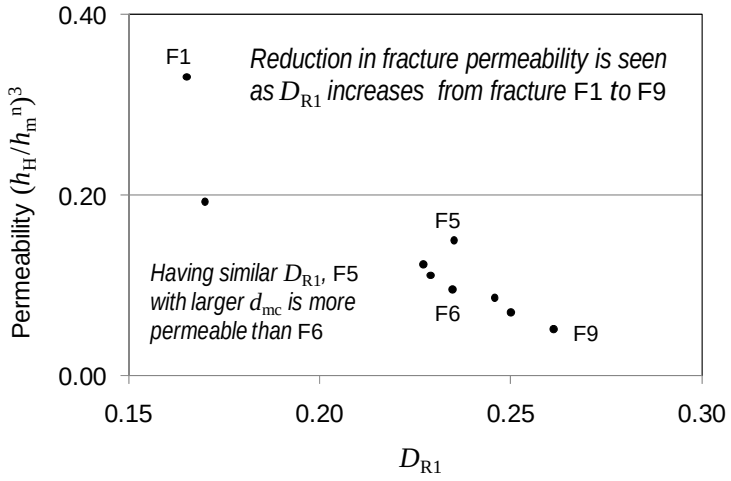

Figure 4.21 Permeability versus D_{R1} for rock fractures F1 to F9.

The above discussions and conclusions demonstrate the capability of developed correlations in considering different factors (e.g. minimum closure distance, roughness, etc) in order to estimate the hydraulic parameters of fractures. Further investigations are currently being carried out to expand such applications.

4.7 Summary

In this Chapter, through simple examples, it was shown how different flow channels with different geometries could have a similar averaged roughness value (or JRC). It was also illustrated how changing the position of the top and bottom walls of a fracture could lead to a different fracture geometry and thus different flow responses, while averaged roughness was identical in both cases.

The analysis of combined JRC profiles resulted in a more generalised correlation between averaged JRC_a and roughness parameter D_{R1}. By having D_{R1} for a real rock fracture, this correlation could be used to estimate average JRC_a. The results indicated how wide the range of JRC_a could be depending on which combination of JRC profiles were presented as the top and bottom wall of the fracture.

From the analysis of JRC flow channels, various correlations between channel geometrical and hydraulic properties were developed. In order to only investigate the roughness effect, the minimum closure distance for the channels was kept to be constant. The results showed how pressure drop reduced as average JRC_a increased and this corresponded to an increase in fracture mechanical and hydraulic apertures.

When comparing the results obtained for the nine real fractures from developed correlations and direct simulation using FLUENT software, the applicability of the proposed formulae was demonstrated to a large extent. Further research is ongoing to study additional real fractures.

Having established a number of fundamental concepts of fluid flow in 2D rough fractures, the next Chapter will discuss 3D simulations of rock fractures and the results will be presented.

5 3D fluid flow simulations of rough rock fractures

In previous Chapters, the analysis of fluid flow in 2D rock profiles was discussed. While various concepts related to the effect of fracture geometry on fluid flow response of the channel could be demonstrated using 2D analysis, the appropriate approach is to carry out simulations in 3D. In this Chapter, the advantages of 3D over 2D simulations of fluid flow will be briefly explained. The 2D version of Riemannian roughness parameter, which is used to investigate the correlation between surface roughness and fluid flow response, will be introduced. The results of 3D simulations of a corrugated plane, some randomly generated surfaces, and real fracture surfaces will also be presented and discussed.

5.1 3D versus 2D analysis

In Chapter 2, a comprehensive review of different 2D models developed for fluid flow analysis of rock fractures were presented. Some of these models were correlated with JRC to encapsulate the effect of surface roughness in the fluid flow response of fractures. The use of 2D models is very useful in terms of demonstrating the effect of various surface geometrical properties on fluid flow in rough fractures. However, in real situations, a correct approach to study fluid flow is by the models developed in 3D. The main difficulty in using 2D models that fluid stops flowing when the aperture becomes zero, whereas in real situations it is very likely that fluid travels along parallel sections to a given direction. Studying fluid flow anisotropy also requires 3D simulations.

Some researchers have tried to simulate and analyse fluid flow in rock fractures in 3D (e.g. Giacomini *et al.*, 2008; Komaya *et al.*, 2008; Komaya *et al.*, 2009; Kulatilake, 2008). However, only a few of these studies have used FLUENT for their modelling (Crandal *et al.*, 2010a; Crandal *et al.*, 2010b; Nazridoust *et al.*, 2006; Petchsingto and Karpyn, 2009; Sarkar *et al.*, 2004). Considering the capabilities of FLUENT for fluid flow simulations, as discussed in the case of linear profiles in Chapters 3 and 4, in this Chapter the 3D version of FLUENT for analysis of a number of generated and real rock

fractures will be used. In particular, the objective of this work is to investigate the relationship between surface roughness and the fluid flow response of fractures.

Commonly, to produce a 3D contour map of a surface, a number of closely spaced traces are made, using an on-line digital computer connected to a roughness measuring instrument, or by using a Stereoscan electron microscope (Dagnall, 1980). Representation of a surface as a combination of several linear profiles is an indirect approach in the determination of surface properties, for example its roughness determination, and the parameters describing surface properties are called pseudo-bi-dimensional parameters (Belem *et al.*, 2000). Instead, an appropriate approach for investigating surface properties is the kind performed in a direct way (in-plane analysis). For example, in terms of roughness determination of a fracture surface, the first attempt was made by Fecker and Rengers (1971) who used a geological compass with a number of differently sized back plates to investigate the range in orientations of a rough surface at different scales. Belem *et al.* (2000) analysed fracture surface roughness using both direct and indirect methods, and with reference to the mechanical properties of the surface. As a result, they concluded that the results obtained from the indirect methods underestimated the characteristics of the surface. Therefore, considering the significant influence of roughness of fluid flow response of rock fractures, it would be appropriate to use a direct approach to correlate fracture geometry, or roughness, to its fluid flow behaviour. Hence, in this work, the 2D version of Riemannian roughness parameter (D_{R2}) will be used to investigate relationships between fluid flow and geometry of rough fractures. In the next section, a brief introduction to D_{R2} is given.

5.2 2D Riemannian roughness parameters

In order to extract the distribution of unit normal vectors to a surface, analogy to a connected pin device was used for linear profiles (see Figure 2.23), Rasouli (2002) proposed the use of an equilateral tripod (see Figure 5.1.a) for sampling a surface randomly. It was expected that as the tripod size increased, the data dispersion reduced, as was also suggested by Fecker and Rengers (1971): this is known as the scale dependency in roughness assessments. As shown in Figure 1.b, the tripod size can be defined as the radius of the circumcircle to the tripod. Tripod orientation (θ) is given by the angle from the X axis, as shown in this figure. By random sampling at different tripod orientations, roughness anisotropy can be studied in a direct way. From Figure

5.1.b, it can be seen that tripod orientations of θ and $\theta + 120^{o}$ (i.e. 0° and 120°, or 10° and 130°, and so on) are identical. This means that by sampling a surface using an equilateral tripod, the analysis only needs to be performed at orientations between zero and 120°. This means that in-plane analysis using an equilateral tripod involves less sampling than linear profiling. In Figure 5.1.c, the relation between different geometrical parameters of a tripod is given.

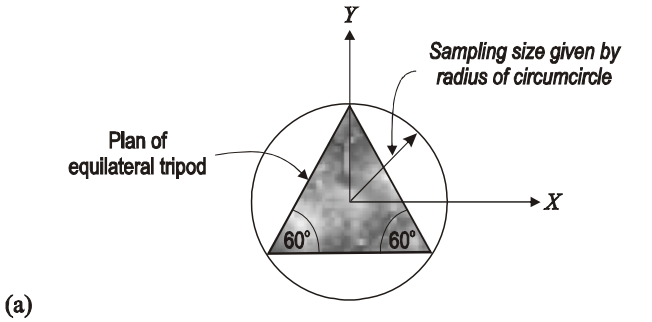

(a)

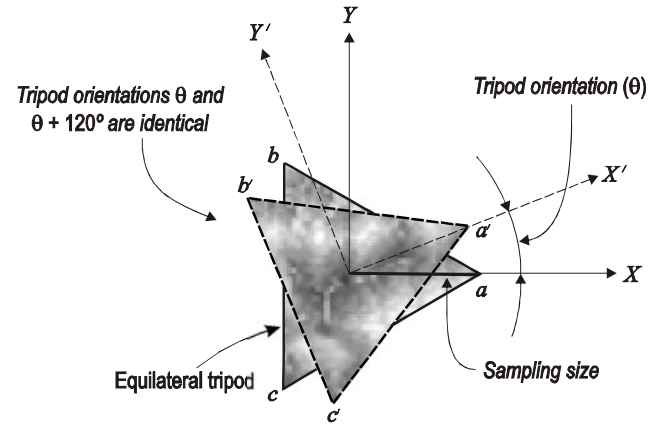

(b)

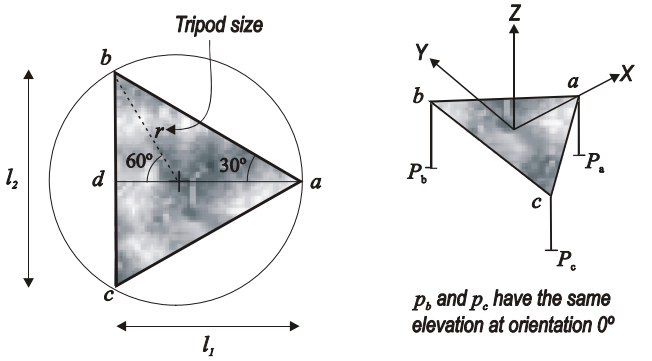

$$r = (2/3)\, l_1 = 0.67\, l_1$$

$$l_1 = (3/2)\, r = 1.5\, r$$

$$l_2 = 2\, r \sin 60^{o} = 1.732\, r$$

(c)

Figure 5.1 Geometry of an equilateral tripod used for rock surfaces sampling.

The extracted unit normal vectors at a specific sampling size define points located on the surface of a unit hemisphere. There are spherical data (corresponding to circular data in 2D case) whose statistical analysis requires their transformation into Riemannian space in order to consider the curved length between data. The Riemannian space for 3D Euclidean data is a 2D plane where the points in 3D are unwrapped into this plane. Statistical analysis of data is performed in this plane and the results are transferred back into the surface of the unit sphere. The Riemannian statistical parameters include data mean and variance, Mahalanobis distances and the Riemannian orientation (or variance-covariance) matrix. The orientation matrix provides valuable information about data dispersion. The nonzero eigen values of the orientation matrix (e_1 and e_2) are related to the unit Mahalanobis distance of data, and are an indication of data dispersion. For two sets of data, the smaller the eigen values, the more concentrated will be the data, or in this work, the smoother the surface roughness will be. Therefore, Rasouli (2002) proposed the mean of e_1 and e_2 as a measure of dispersion of data and called this the 2D Riemannian dispersion (D_{R2})

$$D_{R2} = \frac{e_1 + e_2}{2}. \tag{1}$$

Parameters e_1 and e_2 are in fact the size of diagonals of a 2D ellipse in 2D Riemannian space: the larger the size of the ellipse, the more dispersed the data. Similarly, the ratio of the two eigen values (e_2/e_1) indicates the anisotropy of the data, or in this study the anisotropy in surface roughness. The closer this ratio is to unity, the more isotropic is the distribution. Thus, this ratio was proposed as a means of measuring the isotropy of a data set, or anisotropy in roughness determination, i.e.

$$I_{R2} = \frac{e_2}{e_1}. \tag{2}$$

In the subsequent sections, FLUENT software is used for 3D fluid flow simulations of a simple corrugated plane, some generated surfaces and real rock surfaces. Riemannian roughness and anisotropy parameters will be used to correlate fluid flow properties with surface geometry parameters.

5.3 Fluid flow analysis of a corrugated flow channel

A corrugated plane, representing either the top or bottom face of a fluid channel, shown in Figure 5.2 is the simplest surface geometry which was used in this study. The aspect ratio (K/λ) of the surface is 0.1, which is thought to be comparable with that of real rock surfaces. From Figure 5.2, it appears that this surface has orthogonal principal directions of roughness (corresponding to X and Y directions). Similar to a synthetic symmetric triangular profile (see Section 3.2), both mate and non-mate geometries can be considered for this flow channel depending on the shear displacement of the top face with respect to the bottom face. The influence of roughness, fluid flow direction and shear displacement of the two faces on fluid flow parameters will be analysed and discussed in the following subsections.

It is to be noted that similar fluid parameters to those used for 2D cases will be used in all 3D models in this Chapter to allow comparison of the results where possible. Here, a corrugated plane has a length and width of 6 cm with an aperture of 0.2 cm (Figure 5.3). A mass flow inlet and pressure outlet was used for the 3D simulations of the corrugated channel in FLUENT (see Figure 5.3) with a constant flow rate of 1×10^{-7} m^3/s. The simulation results, as well as the roughness analysis of the corrugated plane, are presented in the following subsections.

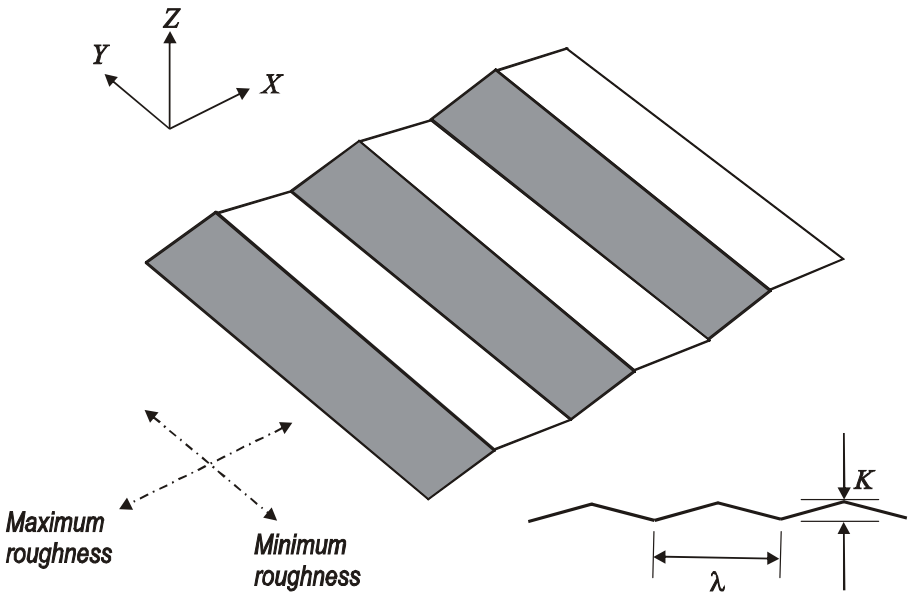

Figure 5.2 A corrugated plane with orthogonal preferred orientations of roughness.

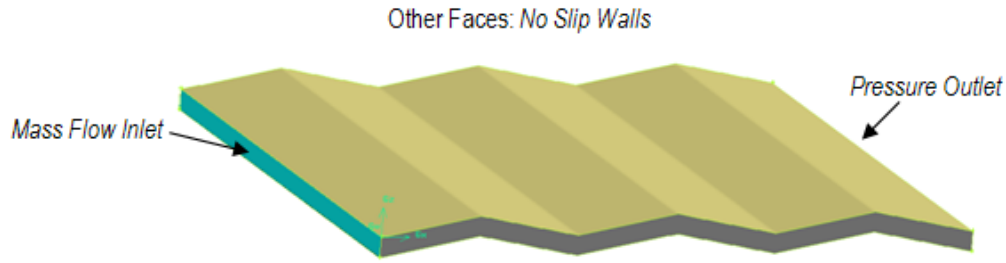

Figure 5.3 A corrugated flow channel used for fluid flow simulations using FLUENT.

5.3.1 Effect of surface roughness

A mate and non-mate corrugated flow channels were subjected to FLUENT simulations. The aperture in the case of the mate channel was assumed to be 0.2 cm: which is the minimum distance between the two faces in the case of a non-mate channel. Figure 5.4 shows the contours of pressure drop and velocity magnitudes for the mate channel.

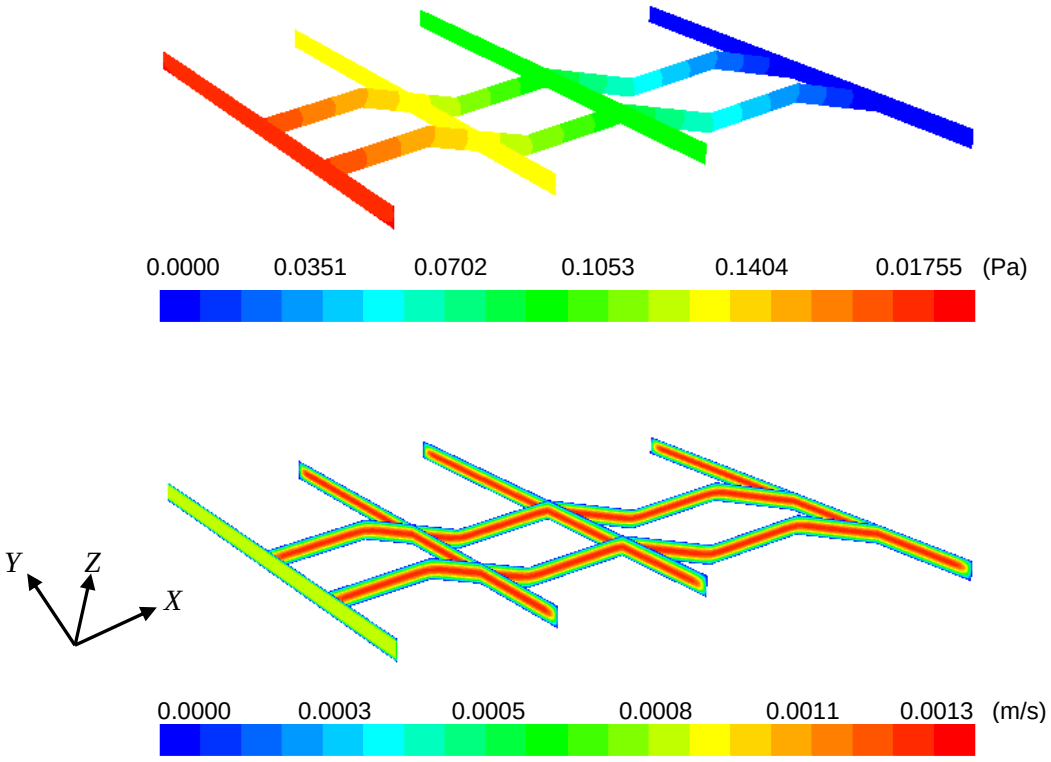

Figure 5.4 Contours of total pressure (Top) and velocity magnitude for a mate corrugated flow channel.

Similar plots for the non-mate channel are shown in Figure 5.5. The results indicate how pressure reduces as fluid travels from inlet to outlet. Also, the laminar assumption for the flow regime is the reason for having a parabolic velocity profile where the maximum velocity occurs at the centre of the channel and reduces to zero

when it approaches the surface walls. For non-mate channel, the largest velocity occurs where the aperture is minimised.

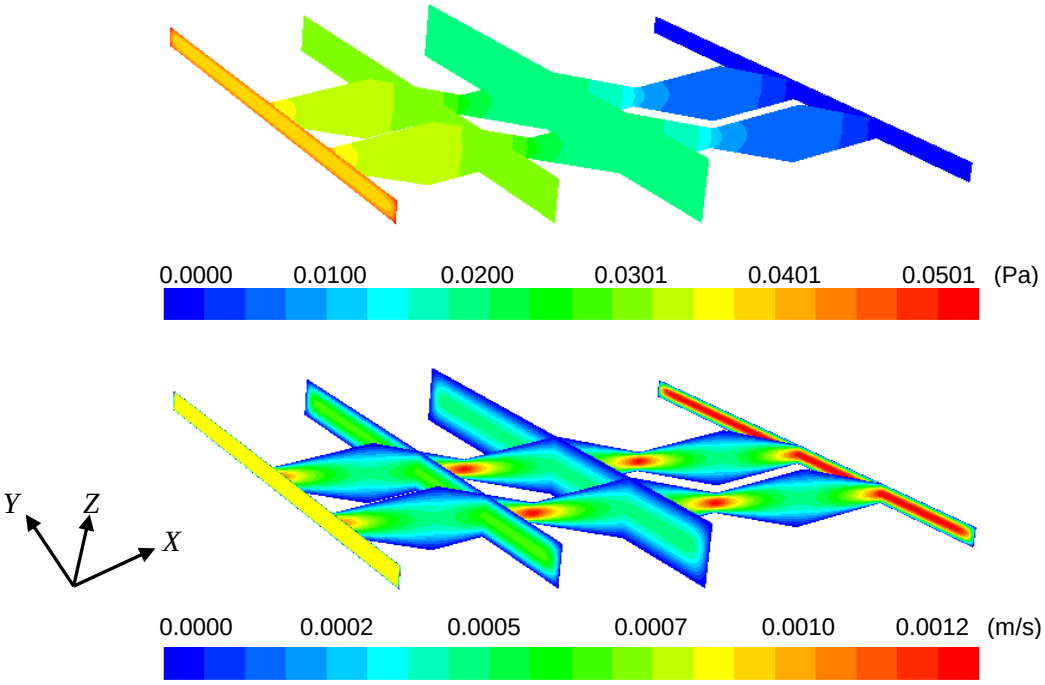

Figure 5.5 Contours of total pressure (Top) and velocity magnitude for a non-mate corrugated flow channel.

5.3.2 Anisotropy in fluid flow behaviour

As shown in the previous section, fluid flow response is influenced by surface roughness. This means that in real situations, fluid flow is directionally dependent while surface roughness is anisotropic (Rasouli and Harrison, 2000). However, the scale dependency in roughness determination, as explained in Section 2.1.5 and also in Section 5.2, results in different roughness values for a surface at different sampling sizes. To investigate this, analysis of fluid flow for a corrugated channel along different directions was performed. Due to the symmetric geometry of this surface, the analysis needs to be carried out for angles between 0° and 90°.

Figure 5.6 shows corrugated flow channels with different orientations, indicated by the angle of crest line with respect to the *Y* axis. Also, the analyses were done for both mate and non-mate surfaces with a wavelength of 2.0 cm. Figures 5.7 and 5.8 show the results of pressure drops calculated when fluid is travelling along different directions for mate and non-mate corrugated channels, respectively. The results indicate how pressure drop reduces when fluid flows parallel (along the *Y* direction) in

comparison with flow in a series (i.e. along the *X* axis). This is due to a smaller length of surface against the fluid in 90° than 0°. Also, the lesser the surface height distribution (i.e. roughness), the lesser the pressure drop as can be seen from these figures. The range of pressure drops for a mate channel (Figure 5.7) is larger than that of a non-mate channel (Figure 5.8) as the hydraulic aperture is larger for the latter surface geometry.

These results indicate the relationship between surface morphology and fluid flow behaviour. The direction of extreme roughness values are easily understood for this surface, however, this is trivial for the case of real fracture surfaces and hence, the use of statistical parameters which objectively identifies roughness is essential.

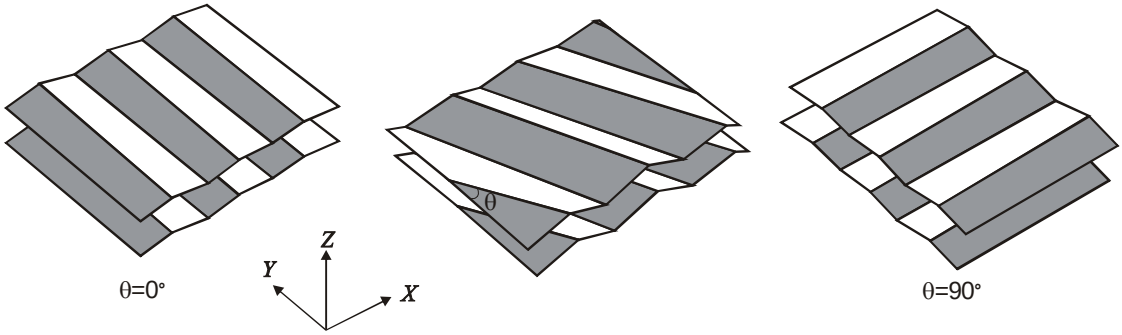

Figure 5.6 Geometry of corrugated flow channels with different orientations.

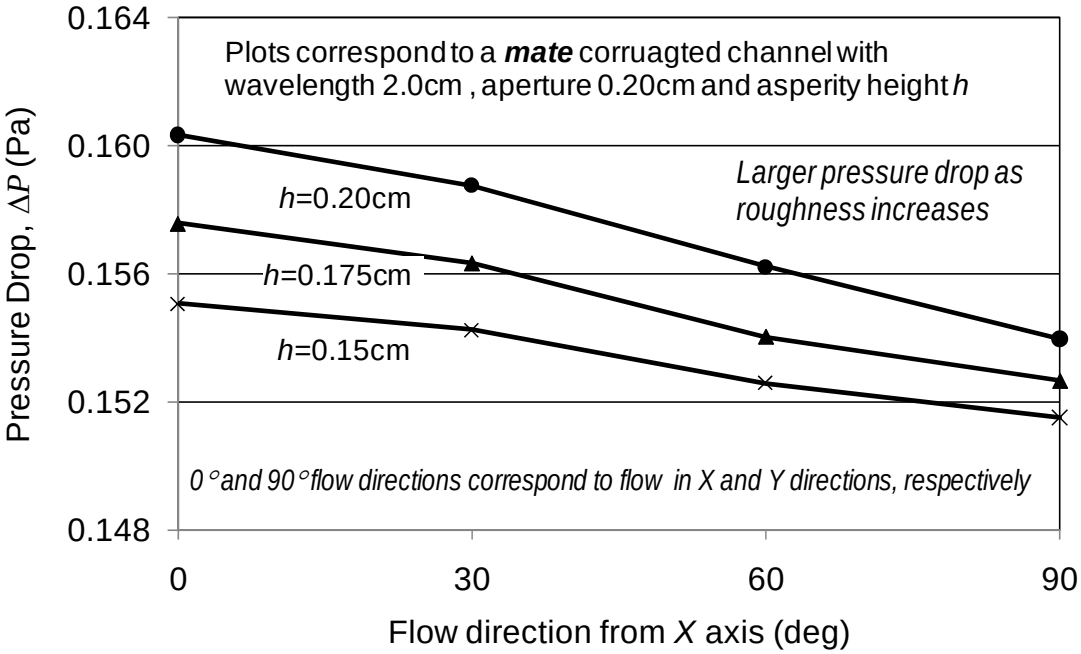

Figure 5.7 Pressure drops for a mate corrugated channel when fluid flows along different orientations.

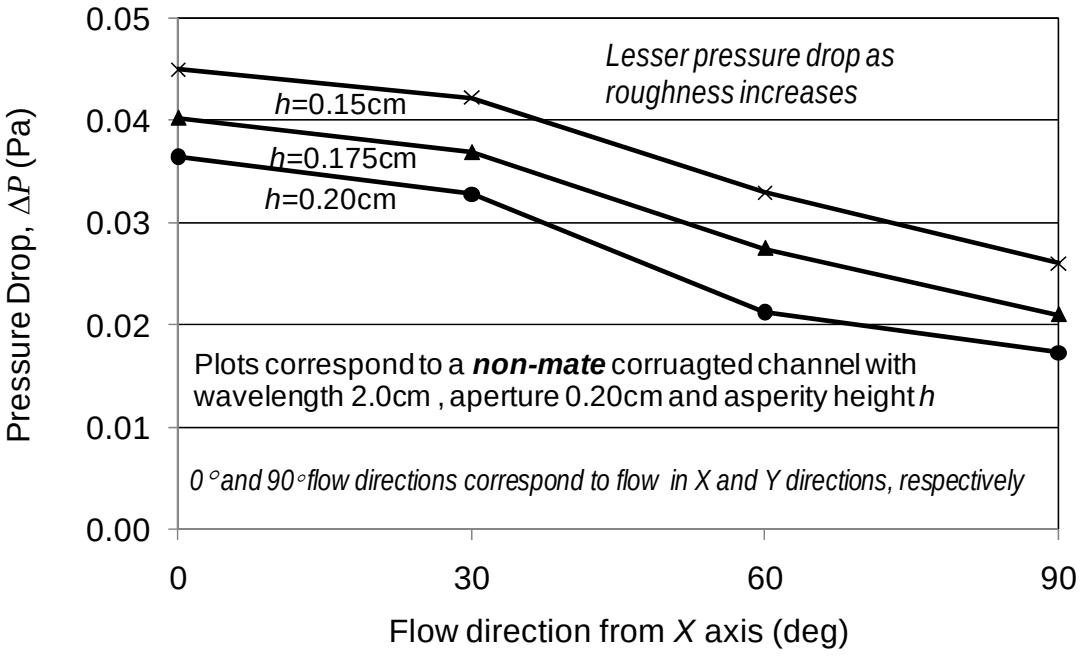

Figure 5.8 Pressure drops for a non-mate corrugated channel when fluid flows along different orientations.

5.3.3 Shear offset

In the previous subsection, the presented results corresponded to mate and non-mate corrugated channel geometries. In real situations, shearing of two sides of the fracture walls is very likely to happen, for example in a reservoir. For example, reservoir depletion or injection, as occurs in a produced reservoir, could result in shear displacements due to a change in effective in-situ stresses. Even a small shear displacement, can change the fracture fluid flow behavior significantly. To indicate this, here, a corrugated flow channel for which the upper wall has been sheared with respect to the lower wall is simulated. Geometries with different amounts of shear offset are studied for comparison purposes. Also, no failure or contact of fracture asperities are considered in these analyses, as the objective is mainly to investigate surface flow response due to shear displacements. As can be easily recognised from Figure 5.6, shear offset of half wavelength of the top wall changes the corrugated channel from a mate to a non-mate geometry and vice versa.

In Figures 5.9 and 5.10, the pressure drop as a function of shear offset is given for the corrugated flow channel with an aperture of 0.20 cm when fluid travels along the *X* and *Y* directions, respectively. In both figures zero and half wavelength (here 1.0 cm) shear displacement corresponds to mate and non-mate flow channels, respectively. The results of Figure 5.9 show that pressure drop increases due to fracture shear offset and it is higher when asperity height is larger. This is in fact due to a larger length of fracture

being subjected to fluid as the two walls move with respect to each other. In this figure, it can be seen that when shear offset gets close to fracture half wavelength, i.e. 1.0 cm, the pressure drop tends to infinity as for this special geometry, the fracture becomes a non-mate channel with zero aperture at integer numbers of channel half wavelength. Contrary to this, when fluid flows along the *Y* axis direction, increased shear offsets correspond to reduced pressure drops and the larger the surface roughness, the less the pressure drop. The results of Figure 5.9 may appear to be misleading in the first instance, however, reduced pressure drops as shear offset and asperity height increase is due to increased hydraulic aperture.

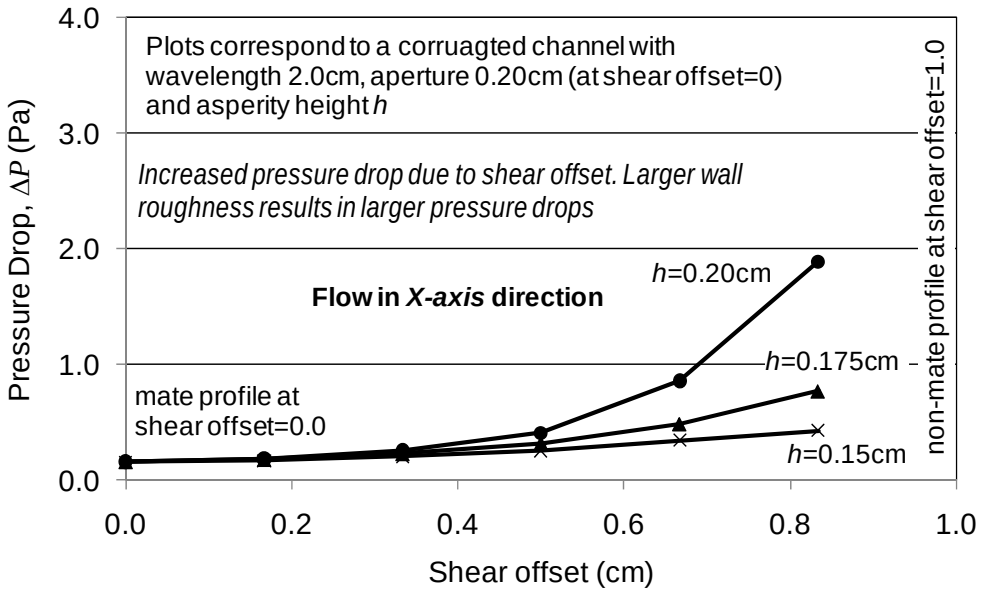

Figure 5.9 Pressure drop of corrugated channel at different shear offsets (flow in *X* axis).

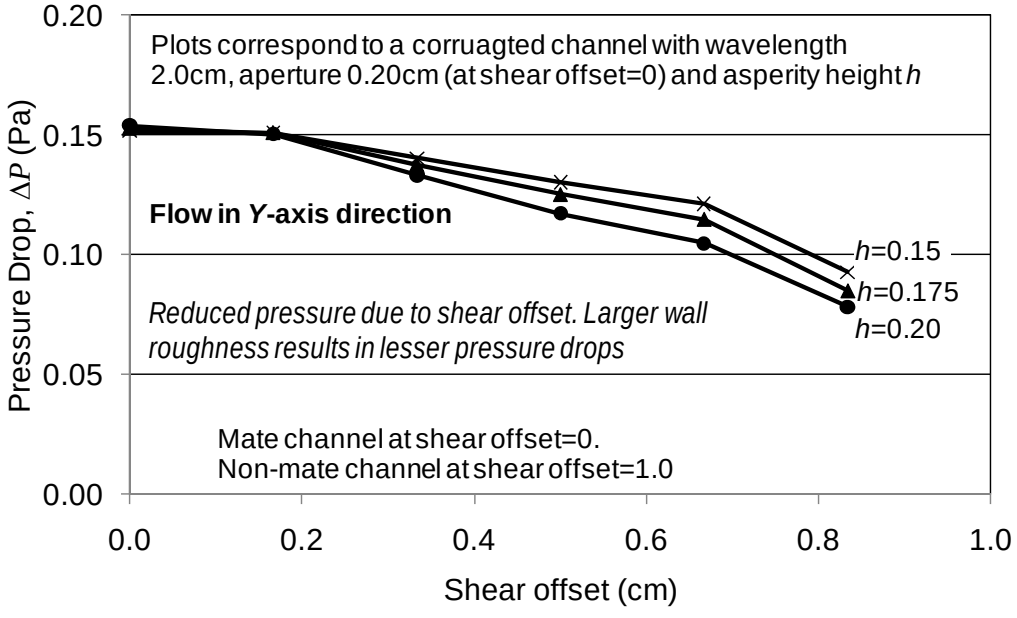

Figure 5.10 Pressure drop of corrugated channel at different shear offsets (flow in *Y* axis).

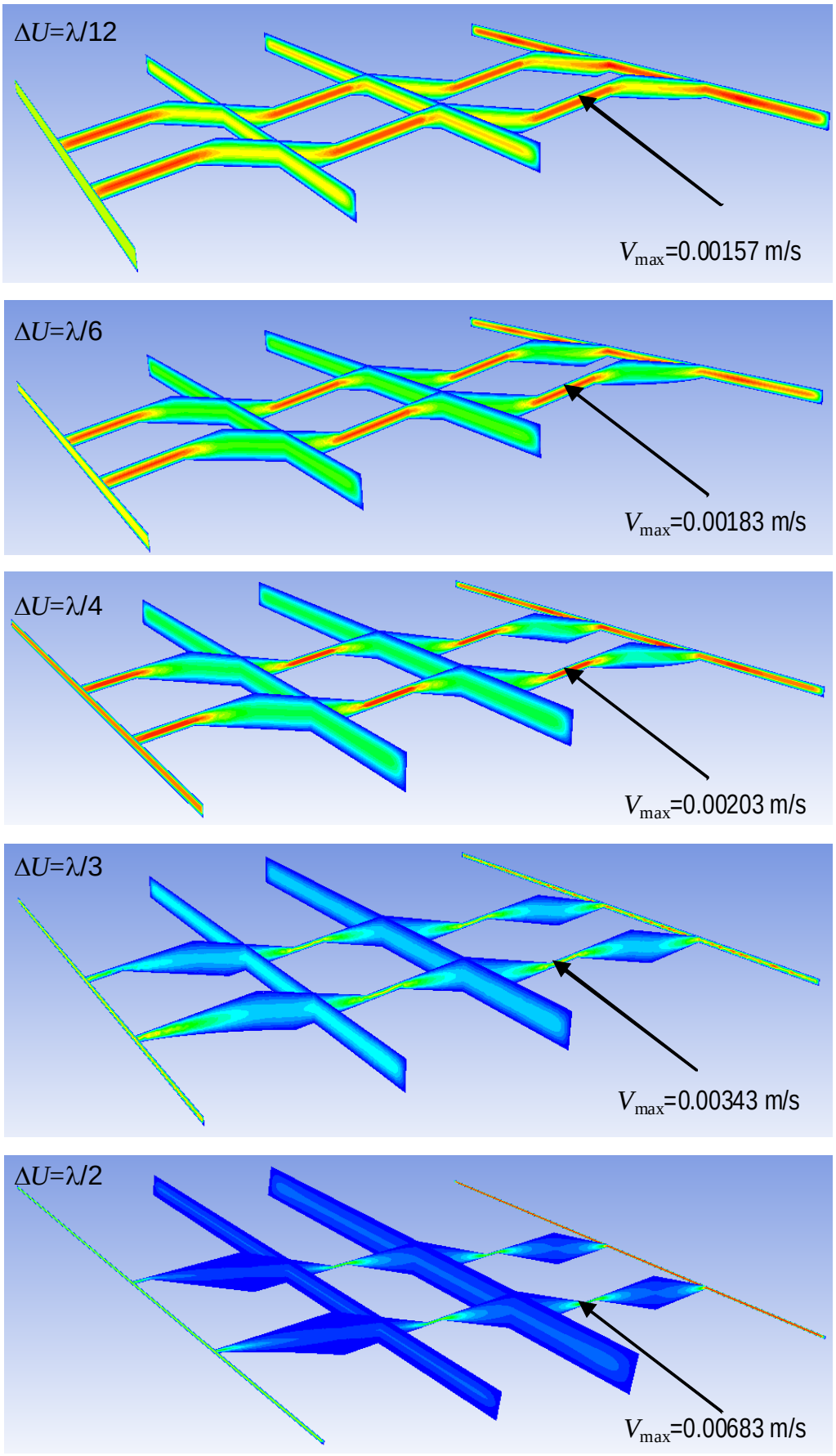

Figure 5.11 Velocity magnitude of a corrugated channel at different shear offsets (fluid flow from left to right).

In Figure 5.11, the plots of velocity magnitudes for the corrugate plane when fluid travels along the X direction from left to right are shown for different shear displacements (ΔU) changing from $\lambda/12$ to $\lambda/2$, where λ is the wavelength of the corrugated plane. The results show how velocity profiles change as a result of fracture shear offset. Also, the maximum velocity (V_{max}) increases as shear offset becomes larger and its maximum occurs for non-mate geometry.

The above results indicate how surface geometry changes and the location of channel walls with respect to each other could significantly influence fluid flow response of the corrugated plane. In the next subsection, the result of roughness analysis of this surface is presented to investigate this concept further.

5.3.4 Correlation between roughness and flow parameters

From Figure 5.6 it can be noted that vertical cross sections of a corrugated plane along different directions define different asymmetric linear profiles with different aspect ratios (l_1/l_2) as discussed in Section 2.1.5. Therefore, using an indirect approach for analysis of a corrugated plane, D_{R1} can be estimated for this surface corresponding to profile geometry along different directions. Such results, presented by Rasouli (2002), are shown in Figure 5.12, which shows orthogonal directions for roughness of the corrugated plane: the maximum roughness is along the X direction whereas the surface appears to be completely smooth (D_{R1}=0) along the Y direction. The surface roughness changes smoothly from a minimum to maximum roughness direction.

A similar interpretation is expected to be obtained from a direct approach of surface characterisation, i.e. in-plane analysis using tripod sampling and Riemannian statistical methods, as presented in Section 5.2. Figure 5.13 shows the results of a Riemannian analysis of the corrugated surface. In this figure, D_{R2} corresponding to normal vectors extracted at different tripod sizes along orientation zero (i.e. X direction) is calculated. At this orientation, two legs of the tripod will be always touching similar surface elevations whereas the third leg will deviate along the X-Z plane, representing surface roughness at a given scale. However, when the tripod size is identical to an integer number times the wavelength of the corrugated plane (these are 1.34, 2.67, 5.34, etc as shown in Figure 5.13) all three legs have similar height coordinates regardless of the location of the tripod. In this situation, the normal vector to tripod would be always perpendicular to the X-Y plane, representing a smooth surface and as seen from Figure

5.12, D_{R2} is zero at these scales. From this figure it is also noted that, in general, roughness reduces as scale increases.

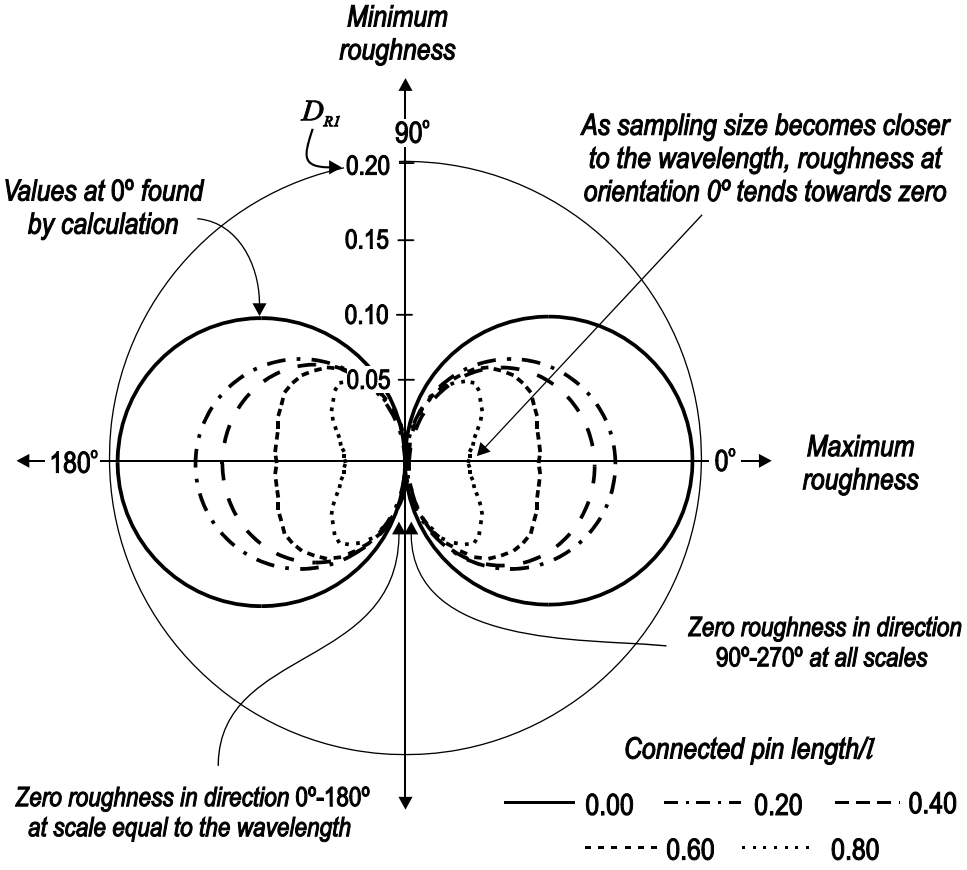

Figure 5.12 Linear profiling analysis of a corrugated plane (Rasouli, 2004).

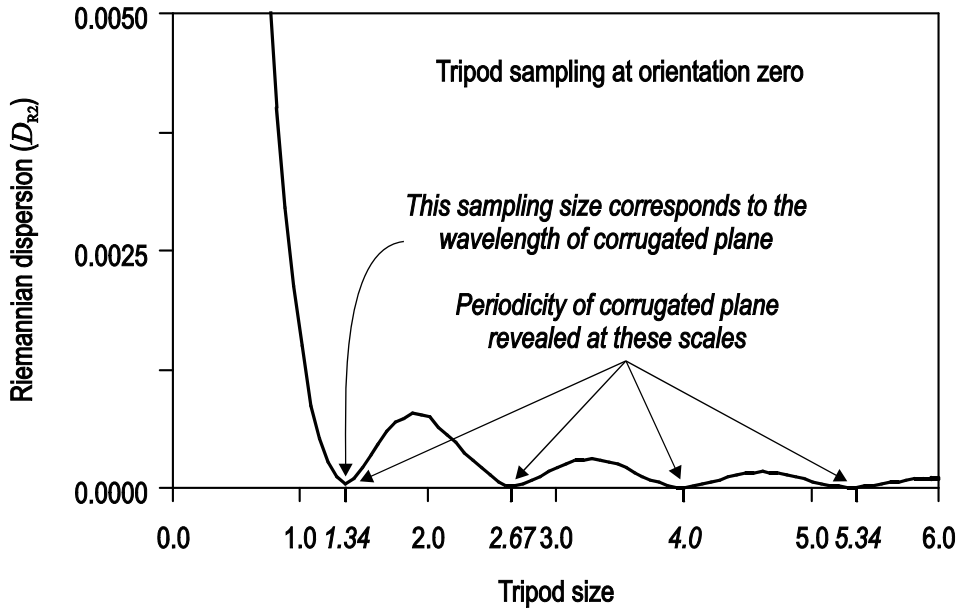

Figure 5.13 In-plane roughness analysis of corrugated plane at orientation zero (Rasouli, 2002).

To show the anisotropy in the geometry of a corrugated plane, in Figure 5.14 the I_{R2} values are calculated corresponding to different orientations for the tripod and at three different scales. In general, lesser anisotropy is seen at larger scales, as noted from this figure, and is due to a reduced variation of normal vectors at larger sampling sizes. Zero isotropy at orientations of 0°, 60° and 120° is due to the fact that tripod geometry would be identical at these tripod locations for a corrugated plane and as explained earlier, at these orientations the tripod only deviates within the *X*-*Z* plane with zero changes in the *X*-*Y* plane.

The roughness analysis presented here indicates how the periodicity of the corrugated plane can be recovered by finding the direction along which I_{R2} reduces to zero for all scales. In real rocks this may not be seen very clearly, but a similar approach can be applied. Having recovered the surface geometrical properties, it could be possible to obtain information about the fluid flow behaviour of the surface. This will be discussed further in the next sections by analysing a few generated surfaces whose statistical parameters are known.

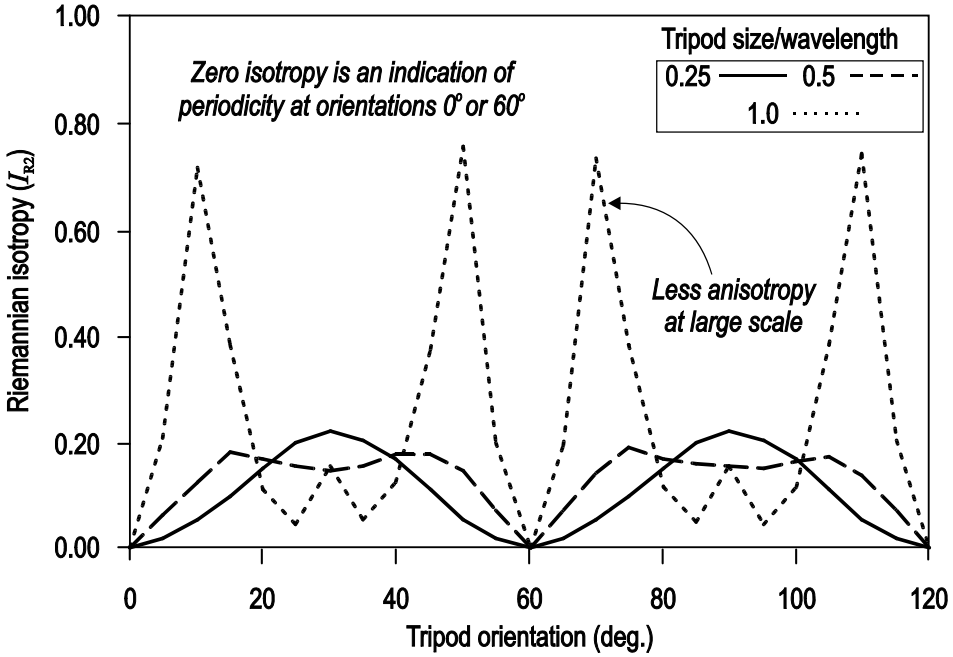

Figure 5.14 Anisotropy of a corrugated plane geometry (Rasouli, 2002).

5.4 Simulations of generated fracture surfaces

The analysis of a corrugated flow channel, as presented in the previous section, showed how surface geometry could influence the flow response of a surface. In this section, a similar analysis will be conducted on synthetic flow channels whose geometries are generated with different statistical parameters.

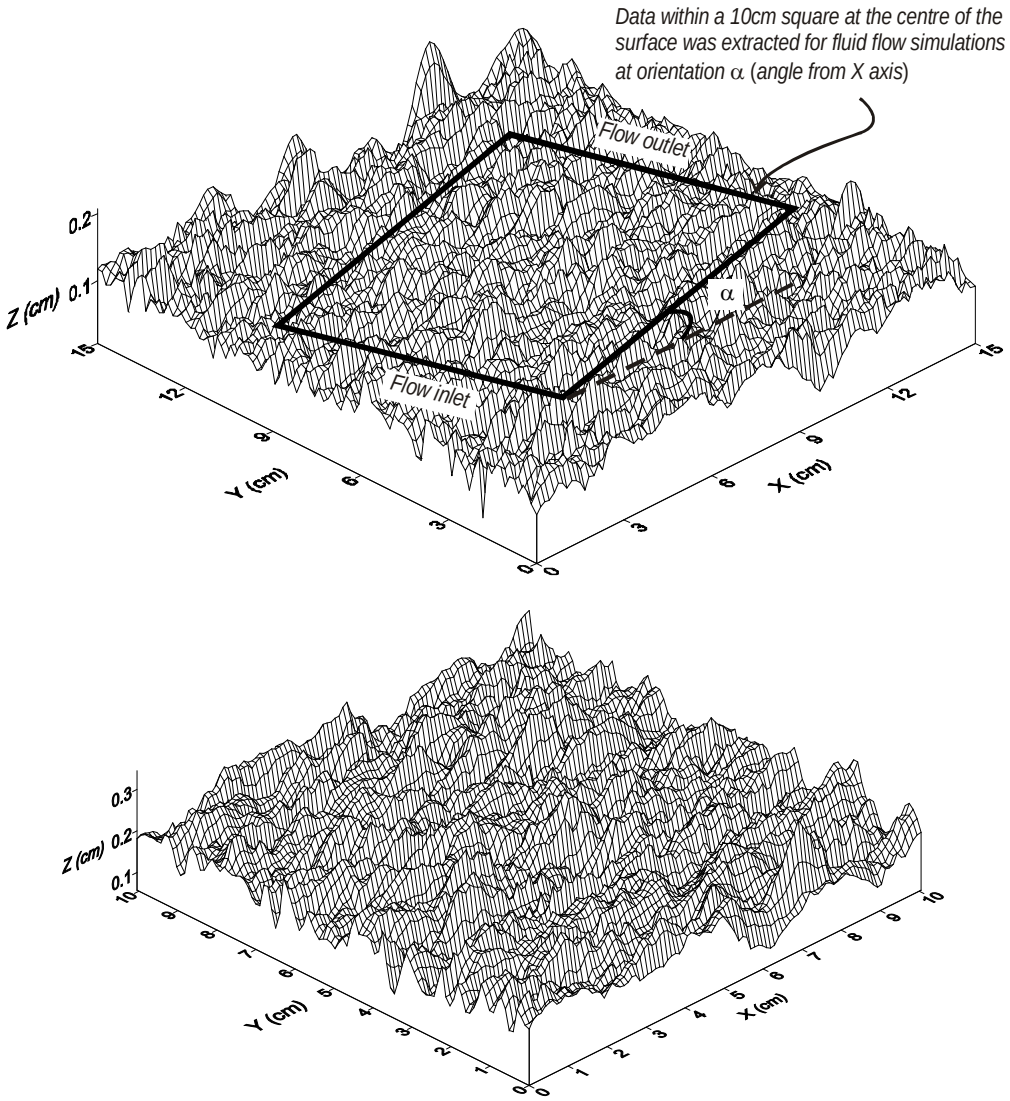

Figure 5.15 Geometry of a randomly generated surface for directional fluid flow simulations (top); and extracted geometry at direction zero (α=0).

A random surface generation algorithm using Gaussian statistics was used in this work to generate rough surfaces with different geometries. This is based on the method introduced by Garcia (1984), where an uncorrelated distribution of surface points using a random number generator (i.e. white noise) is convolved with a Gaussian filter to achieve correlation. This convolution was performed using the discrete Fast Fourier Transform (FFT) algorithm as used in MATLAB.

As the objective of this study is to simulate the effect of large scale roughness, i.e. fracture tortuosity on fluid flow behaviour, surfaces with different roughness and waviness were generated. Similar to the corrugated channel, the effect of surface roughness and tortuosity, surface anisotropy and shear offset were studied.

Figure 5.15 (top) shows the geometry of a synthetic surface generated for fluid flow analysis. The surface has an equal length and width of 15 cm in both *X* and *Y*

directions, respectively. The asperity height distribution ranges between 0 and 0.2 cm, with a correlation distance of 1.0 cm used for surface generation. The data was generated with a preferred deviation along *Y* axis, i.e. 90° direction.

Assuming an identical surface, a flow channel was created when two surfaces were considered with a predefined aperture. This aperture was set to 0.11 cm in this study to ensure that after shearing the upper wall along the lower wall, they did not come into contact with each other. However, a zero aperture was allowed at some points between the two surfaces. The channel inlet and outlet could be identified simply when the fluid flowed along the *X* or *Y* directions. However, it is trivial to determine these flow boundaries when the fluid flows along any other direction. Therefore, for practical purposes we extracted data from part of this surface which was located inside a square placed at the centre of this surface with different orientations (α) and analysed corresponding channels to simulate fluid flow in different directions. The size of the square chosen was 10 cm, as shown in Figure 5.15 (bottom). As can be seen, part of the data would be missed when data is extracted corresponding to different orientations, however, our comparative analysis indicated that this had a minor effect and would not cause significant changes to the fluid flow results. Figure 5.15 (bottom), shows, as an example, the extracted data at direction zero (α=0).

Fluid flow simulations were carried out using FLUENT for this synthetic channel. Figure 5.16 shows the total pressure and velocity magnitudes for this channel for a fluid flowing along the *X* direction and at zero shear offset. The results shown in this figure belong to a *Z* plane (0.2 cm) and therefore, the white areas are the locations where this plane does not have any intersection with fracture walls. The velocity magnitude changes significantly for this fracture at different points depending on the distance between the two walls at different locations. Figure 5.17 is the plot of velocity magnitudes when the fluid travels along the *Y* axis direction. When fluid flows in *Y*-direction fluid particles are moving perpendicularly to the peaks and valley of the generated rough surface (Figure 5.15). The velocity legends of Figures 5.16 and 5.17 show that the maximum velocity is higher for the case of flow in *Y*-direction (0.0012 m/s) compared to the *X*-direction (0.0011 m/s), this contradicts what is stated in the last paragraph on page 117. The same thing is observed if one compares the maximum velocity values in Figure 5.18 and 5.19, i.e. $V_{X,max}$=0.0022 m/s is less than $V_{Y,max}$ =0.0026 m/s.

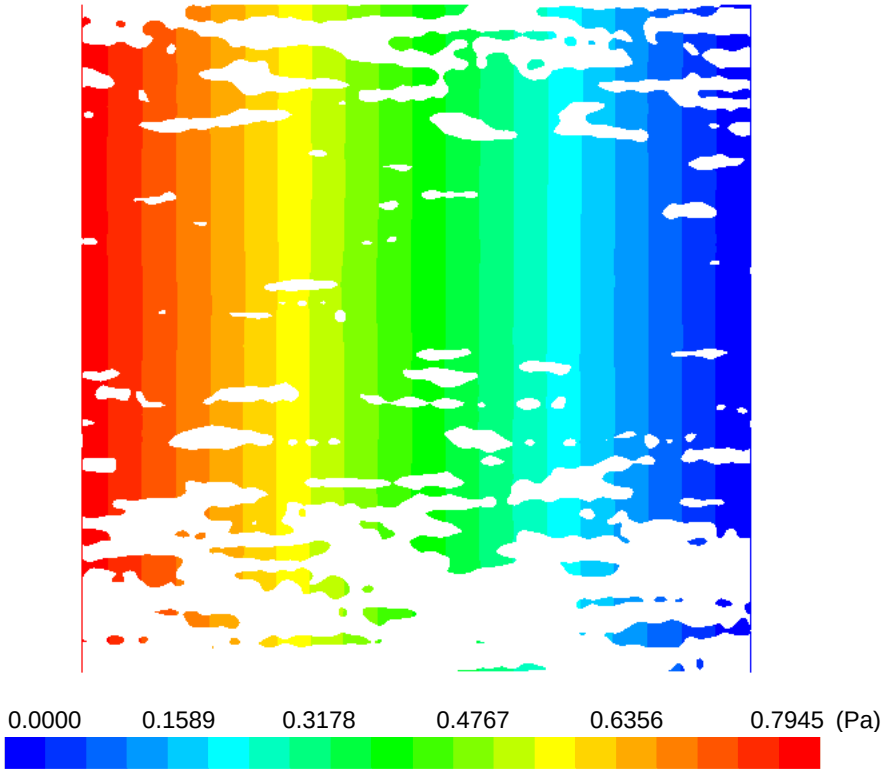

Figure 5.16 Top view of contours of total pressure (top) and velocity magnitude for synthetic channel at zero shear offset: fluid flow in X axis direction.

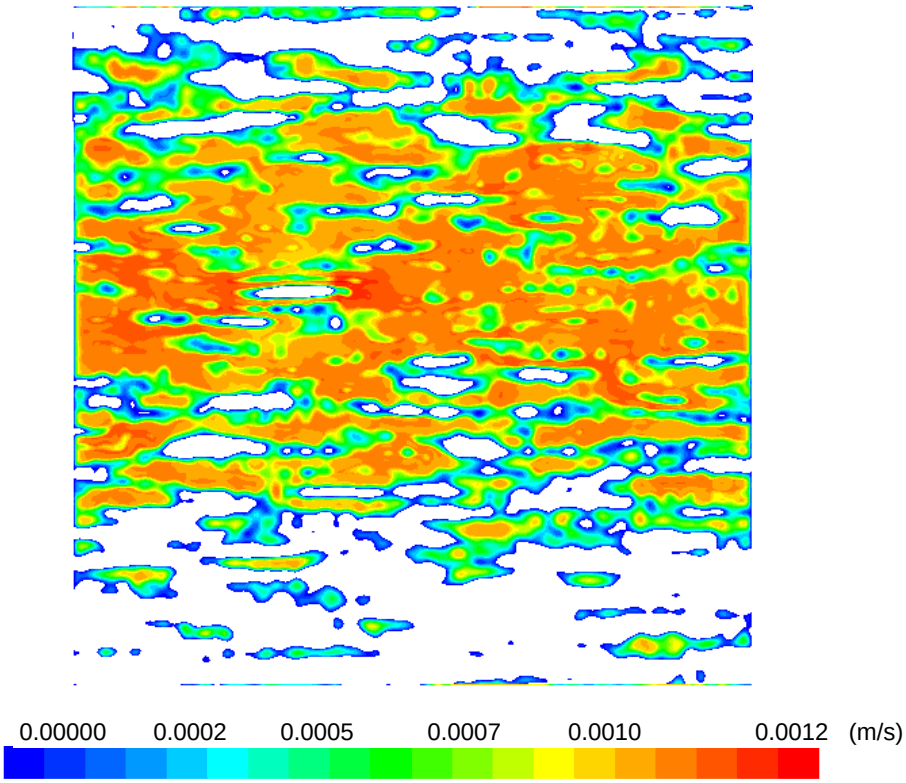

Figure 5.17 Top view of contours of velocity magnitude for synthetic channel at zero shear offset: fluid flow in Y axis direction.

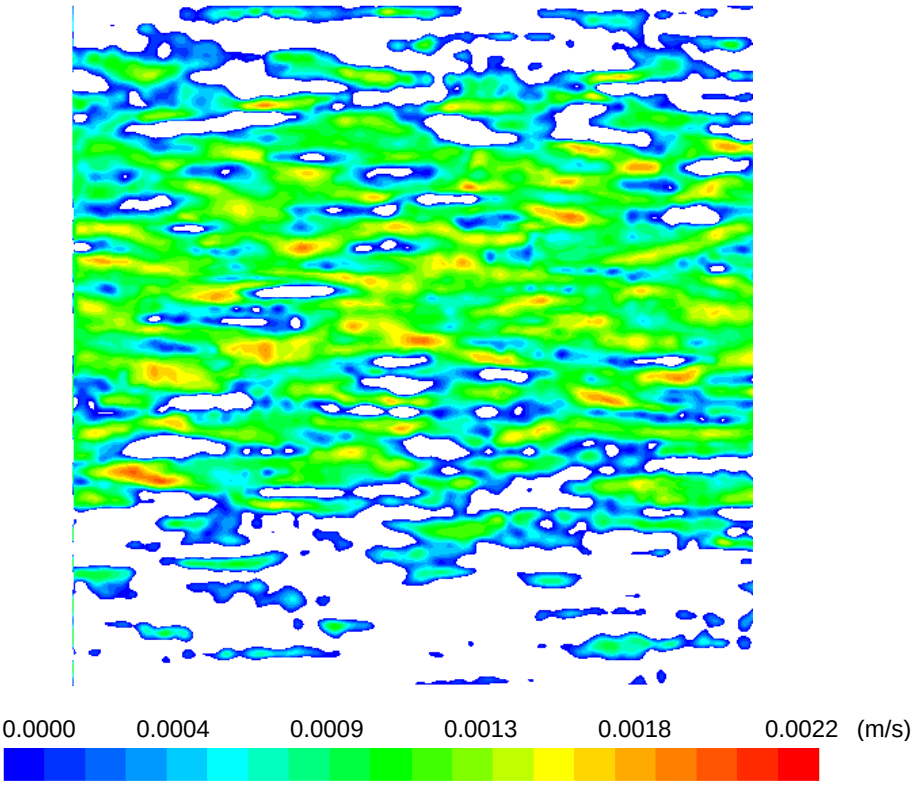

Figure 5.18 Top view of sheared synthetic channel (ΔU=0.6 cm) where at several point aperture reduces to zero: Fluid flow in X axis direction.

The results of velocity magnitudes for this surface corresponding to a *X*-*Y* plane when a shear offset of 0.60 cm is taken place are shown in Figures 5.18 and 5.19 for flow in *X* and *Y* directions, respectively. In this situation, the upper surface is translated 0.6 cm along the *X* axis with respect to the lower surface while the aperture is 0.11 cm. In comparing Figures 5.16 and 5.17, it can be seen how shear offset and flow direction can significantly change the flow behaviour of the fracture. The velocity magnitude changes across the plane section (shown in Figures 5.18 and 5.19) indicate how the velocity may reduce to zero at some point along this section as the aperture reduces to zero. In this situation, the fluid changes its direction and flows around this point. The results indicate how, as a result of fracture shearing, the fracture aperture may vary from one point to another and this causes a large impact on fluid flow response of the surface (for instance fluid velocity).

The results of flow simulations along different orientations are given in Figure 5.20. In this example, the shear offset is zero, i.e. a mate channel with a constant opening of 0.11 cm at different points. From this figure an increased pressure drop is noted as the fluid flow direction changes from a *X* to *Y* direction. Also, the larger the fracture height distribution (i.e. roughness), the higher the pressure drops.

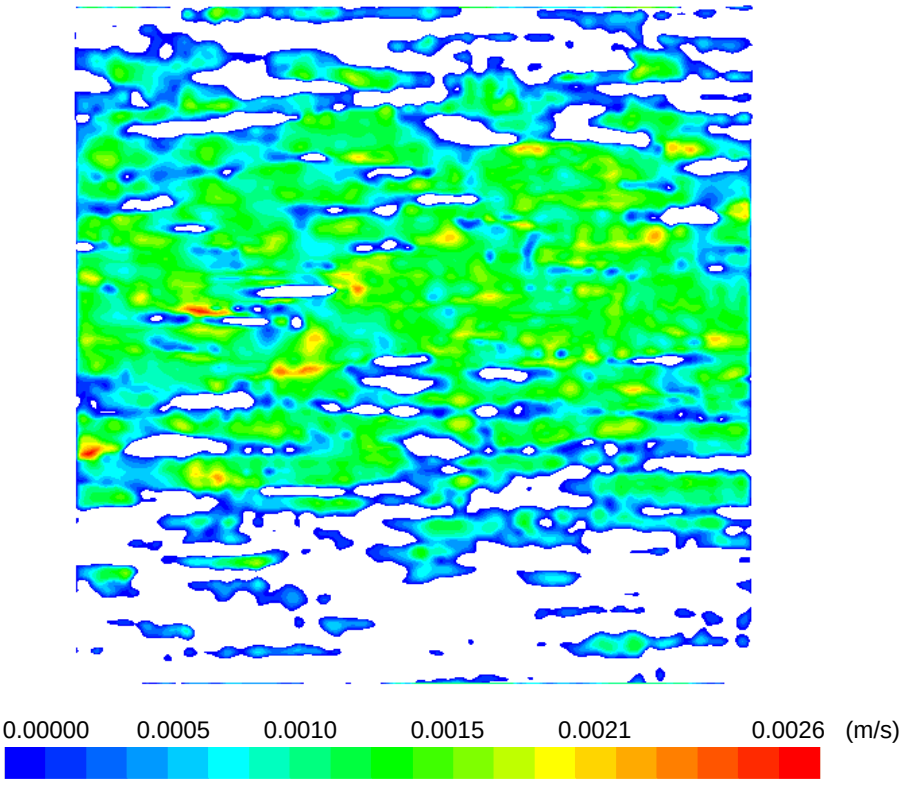

Figure 5.19 Top view of sheared synthetic channel (ΔU=0.6 cm) where at several point aperture reduces to zero: fluid flow in *Y* axis direction.

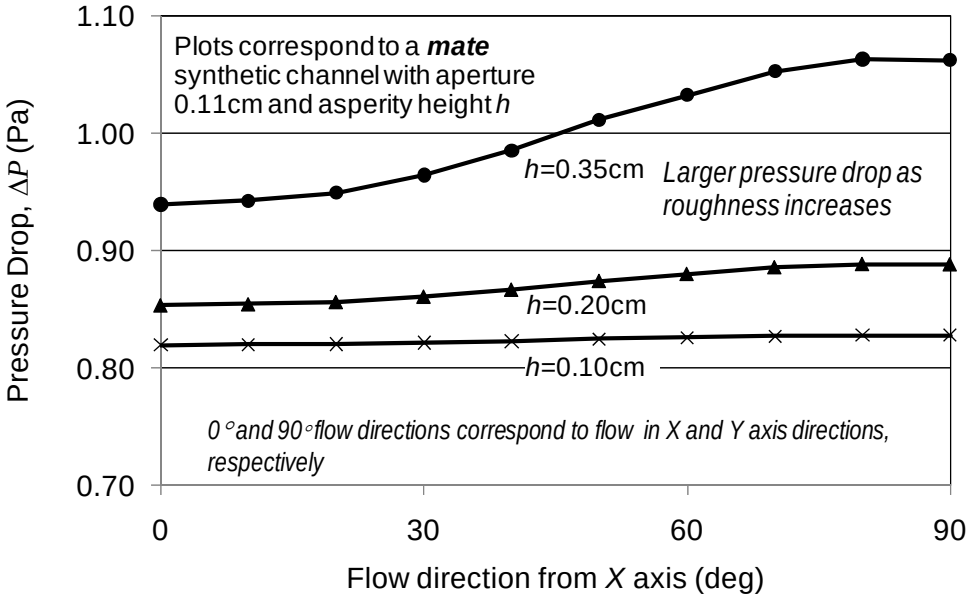

Figure 5.20 Pressure drops of synthetic channel for fluid flow along different directions (shear offset=0).

Figure 5.21 presents the results of flow simulations for the synthetic channel when one wall is sheared with respect to the other wall. In this example, the fracture height distribution changes between 0.0 and 0.2 cm. The results are also given for two cases where fluid flows along the *X* and *Y* axis, respectively. From this figure, it can be seen how pressure drop is a function of shear offset and also flow direction.

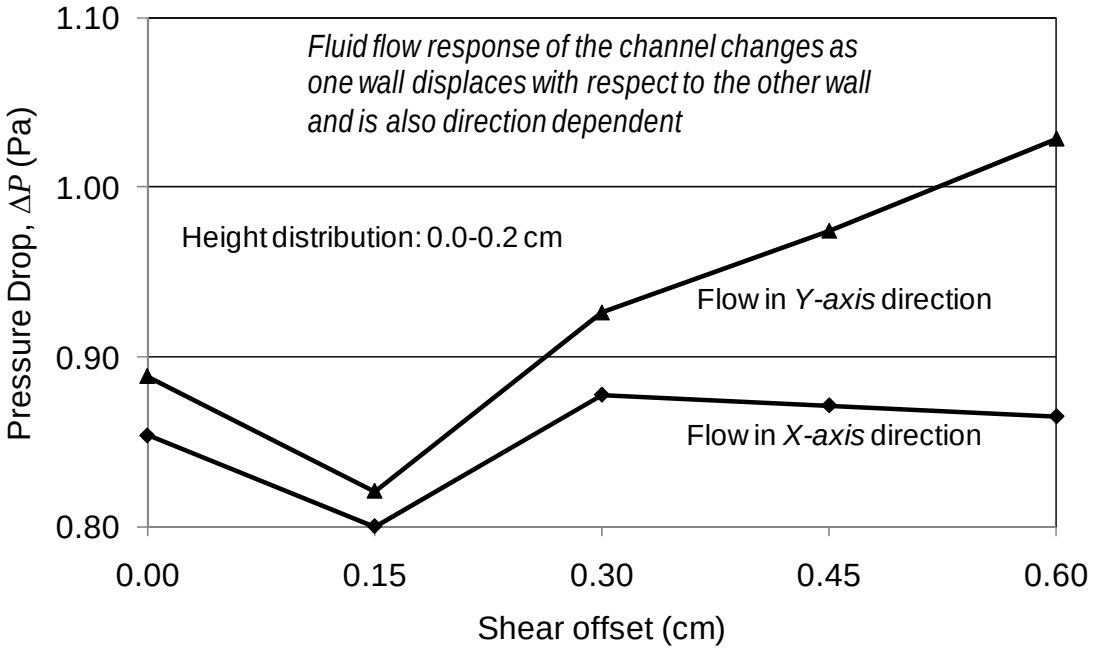

Figure 5.21 Pressure drop changes of a synthetic channel due to shear offset when fluid flows along two perpendicular directions.

In order to investigate the relationship between fracture roughness and flow response for the synthetic channel simulated here, D_{R2} analysis was carried out. Tripod sampling of the surface (see Figure 5.15, bottom), as explained in Section 5.2, was performed at different scales and along different orientations and D_{R2} was calculated in each case. D_{R2} showed minor differences with respect to different directions and reduced as tripod size increased. The results shown in Figure 5.22 indicate that roughness of surfaces becomes substantially zero at scales larger than approximately 2.5 cm.

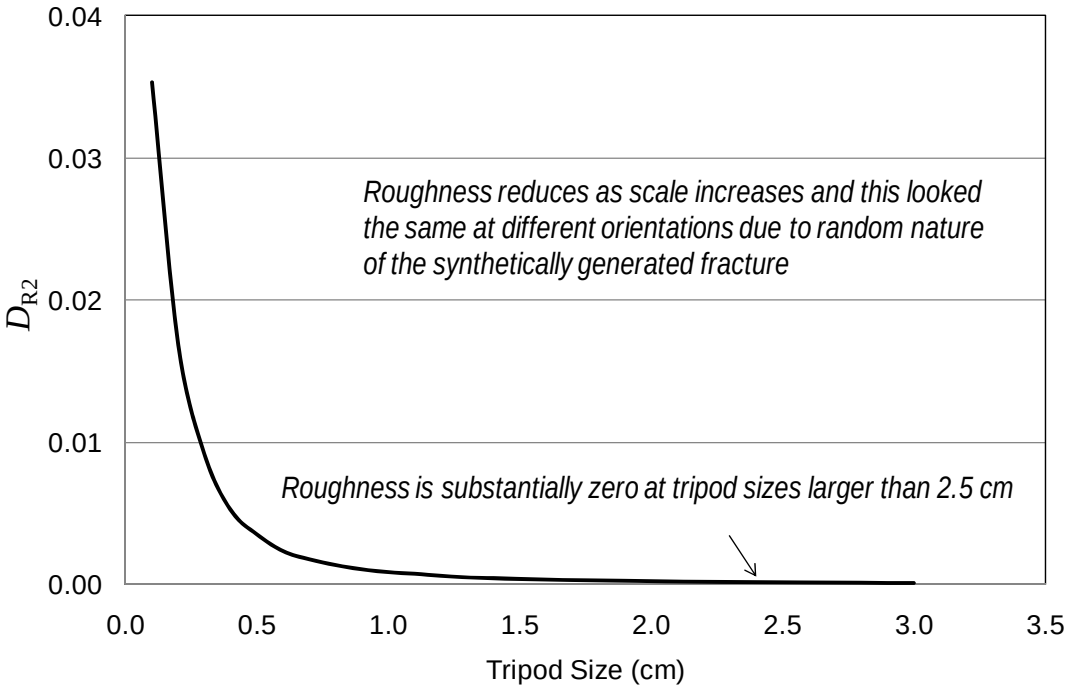

Figure 5.22 Roughness parameter D_{R2} calculated for synthetic surface.

In Figure 5.23, the results of D_{R2} calculated at different tripod orientations are presented corresponding to range of tripod sizes of 0.1 to 1.0 cm. From this figure, it is shown how roughness of surface changes with scale and orientation. For example, at a scale of 0.1 cm for tripod size, the largest roughness appears to occur at orientations of 0 and 90 degrees. As scale becomes larger, surface roughness becomes less anisotropic and also smaller.

The results of roughness analysis for the synthetic surface are given in Figure 5.24 in a rose diagram representation format. For presentation purposes, the results are shown in four diagrams, each representing the D_{R2} values at different orientations corresponding to six scales. It should be noted that due to the nature of tripod sampling, the results for 0° to 120° repeats for orientations of 120° to 240° and as well as 240° to

360°. The results of this figure show again how roughness changes as scale increases from 0.1 to 2.4 cm and that roughness is directionally dependent.

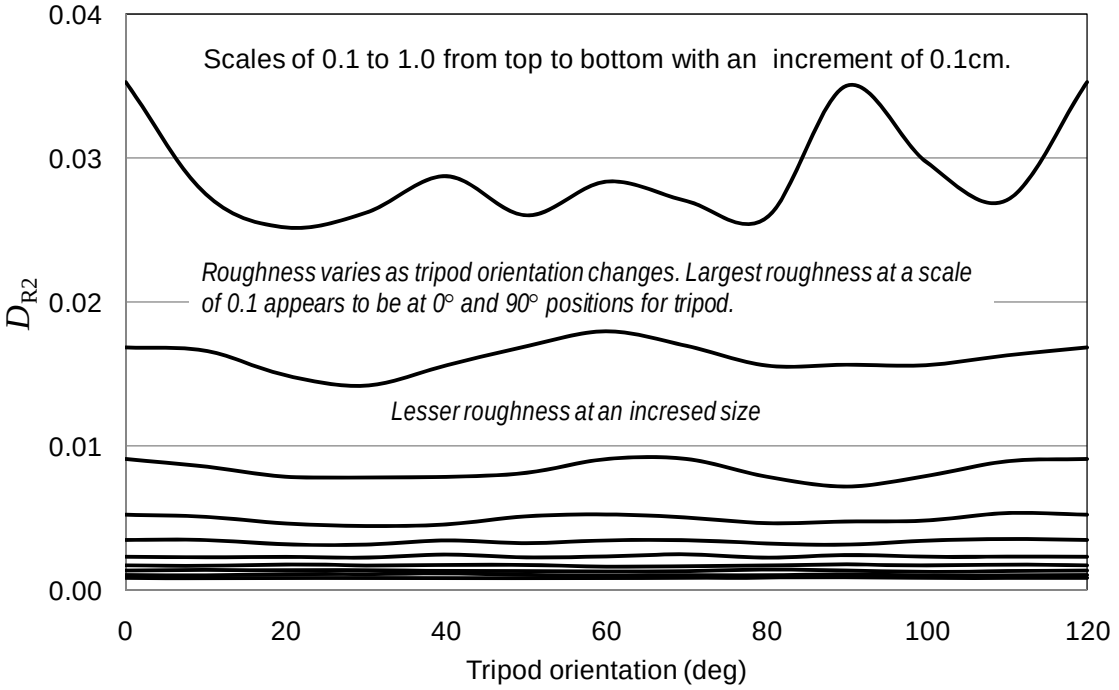

Figure 5.23 D_{R2} calculated for synthetic surface at different orientations and scales.

Recalling the discussion given in Subsection 5.3.4 for the roughness of the corrugated plane, in order to investigate the existence of any small or large scale roughness in a preferred direction for the generated synthetic surface we calculated the isotropy parameter I_{R2} for this surface. In Figure 5.25, the results of such analyses are shown in a rose diagram form corresponding to different scales and orientations for tripod sampling. In this figure, similar to the results of D_{R2} (see Figure 5.24), the values corresponding to 120° to 240° and 240° to 360° are identical to 0° to 120°. The scales change from 0.1 to 2.4 cm in Figure 5.24 from the highest top to the bottom plot. The values of I_{R2} increase from 0.0 to 1.0 from the centre of plot to its perimeter: i.e. less anisotropy as we move away from the centre. The results of this figure indicate that I_{R2} is a directionally dependent parameter itself but in general, at larger scales it becomes less variable at different orientations and its dispersion reduces due to less variation in the normal vectors to the surface.

A different representation of the results of Figure 5.25 is shown in Figure 5.26 where I_{R2} is plotted versus sampling orientation for different tripod scales. Besides conclusions made from Figure 5.25, the most interesting observation from Figure 5.26 is the fact that a general reduction in I_{R2} values is dominant at orientations of 30° and 90° for most given scales. Similarly, the largest values for I_{R2} as seen from this figure occur at 0 and 60 degrees for tripod orientations. Comparing this conclusion with Figure 5.14 for the corrugated plane, it indicates that this surface is most likely periodic along the *Y* axis direction (note that minimum I_{R2} values for the corrugated plane observed at 0 and 60 degrees, when the plane was periodic along the *X* axis). As mentioned earlier, the synthetic surface was generated with a preferred angle of 90° and this confirms the results obtained here. It should be noted that a clear reduction to zero, as observed for the corrugated plane, is not expected for a randomly generated or real fracture but having relatively small values for I_{R2} and along different directions can be a strong indication of surface periodicity.

The above results are comparable to fluid flow response of the synthetic channel. Having periodicity along the *Y* axis direction it is expected to have a larger surface against the fluid flowing in this direction (or correspondingly larger pressure drops) with a tendency to reduce as the fluid direction changes to the *X* axis. This is indeed in agreement with the simulation results presented in Figures 5.20 and 5.21 for this surface. This analysis shows the potential correlations between fracture morphology and its flow response.

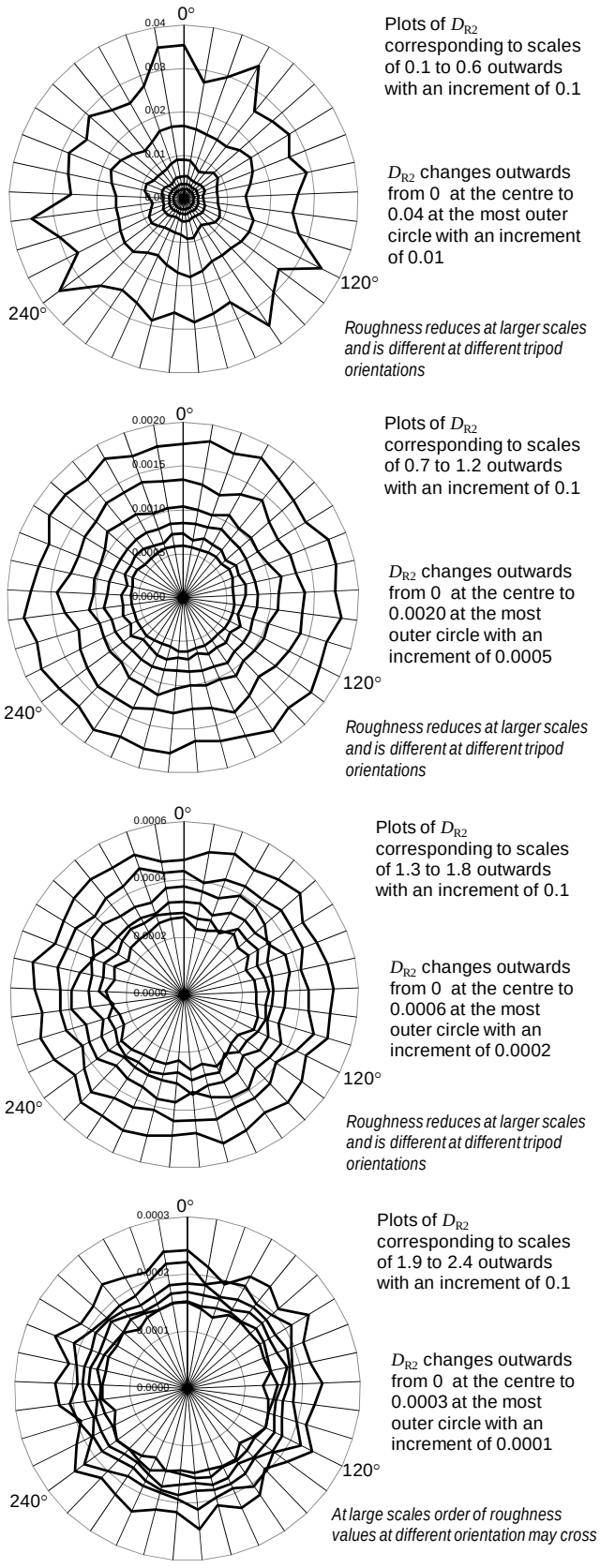

Figure 5.24 Rose diagram of D_{R2} for the synthetic surface at different orientations and scales.

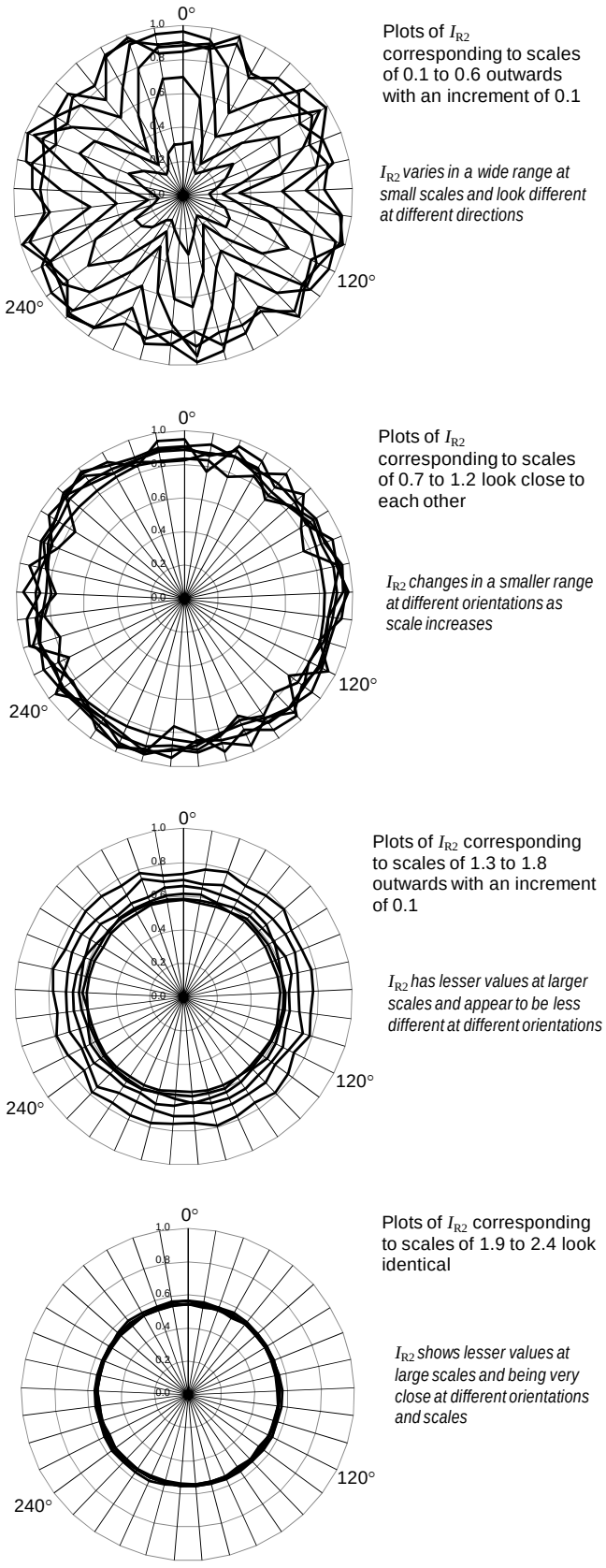

Figure 5.25 Rose diagram of I_{R2} for the synthetic surface at different orientations and scales.

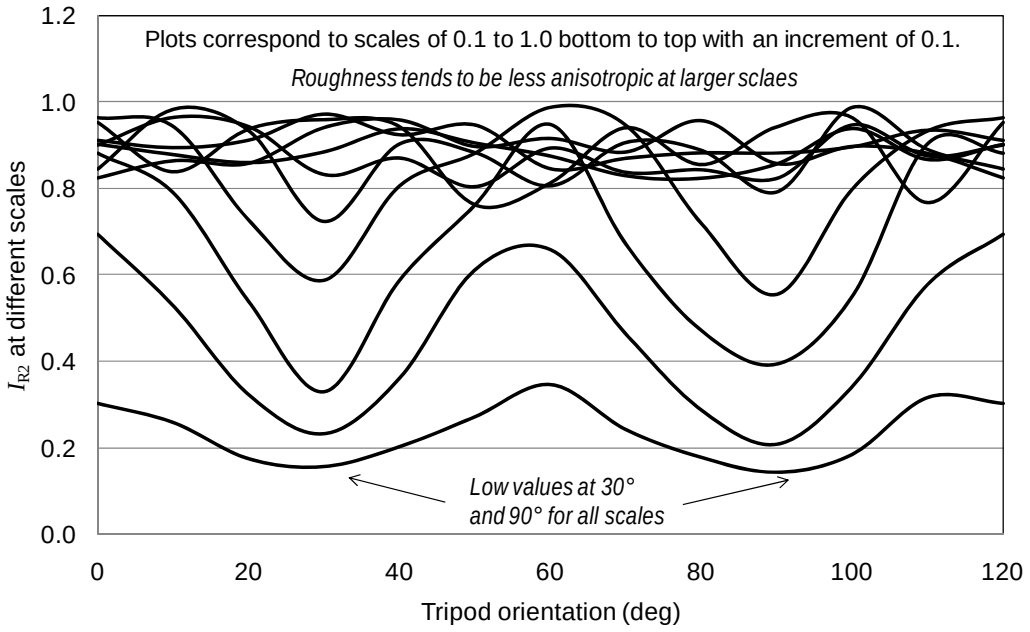

Figure 5.26 I_{R2} calculated for the synthetic surface at different orientations and scales.

5.5 Simulation of five generated surfaces

The results of fluid flow simulations and roughness analysis presented for the statistically generated fracture surface in the previous section indicated the potential correlation between fracture morphology and its fluid flow behaviour. It was also seen how D_{R2} analysis can reveal useful information about surface geometrical properties.

For comparison purposes, five statistically generated surfaces are used for both fluid flow and roughness analysis in this section. The statistical parameters of all these surfaces are identical except the correlation distance which is varied. Also, a constant seed number was used in generation of these surfaces. The idea is to investigate dependency of surface height distribution at different correlation lengths.

Figure 5.27 shows the wall geometry of five generated surfaces (GS1 to GS5). These surfaces were generated with a preferred roughness direction along 45°. This allows for validation of fluid flow and roughness analysis results. These surfaces have an equal length and width of 20 cm but data corresponding to 10 cm of this surface was selected for directional fluid flow analysis, as explained in the previous section. The height distribution for these surfaces is between 0 and 0.2 cm and the correlation lengths used here are 0.01, 1.0, 3.0, 5.0 and 10.0 cm, for surfaces GS1 to GS5, respectively. The fracture flow channels were created by replicating each surface and shifting the surface vertically with a displacement equal to the channel opening. The fracture opening at zero shear offset (i.e. mate channel geometry) is 0.11 cm.

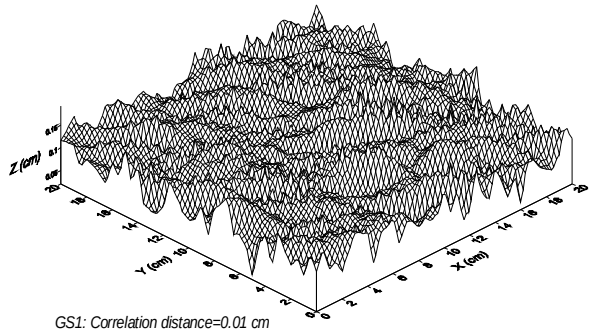

GS1: Correlation distance=0.01 cm

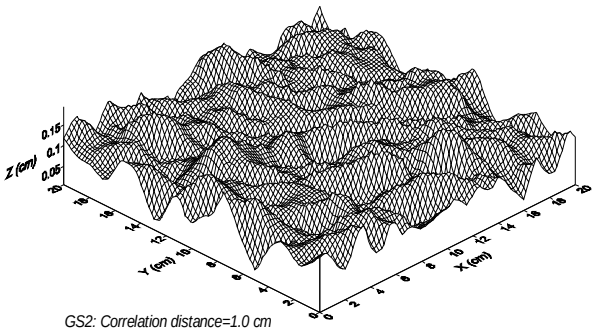

GS2: Correlation distance=1.0 cm

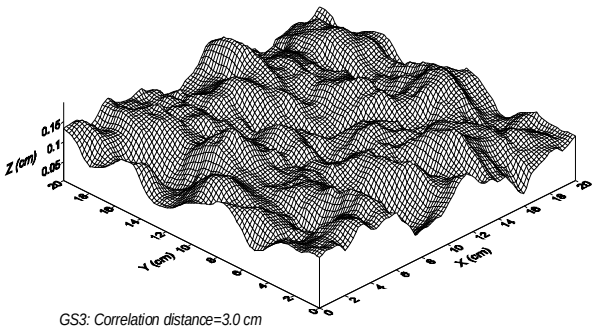

GS3: Correlation distance=3.0 cm

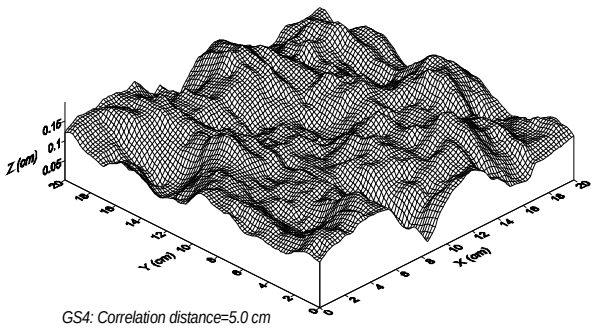

GS4: Correlation distance=5.0 cm

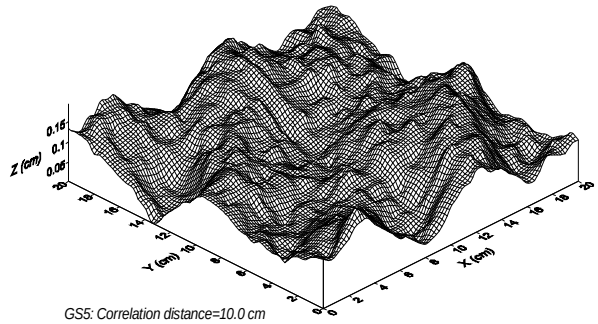

GS5: Correlation distance=10.0 cm

Figure 5.27 Geometry of 5 generated surfaces used for fluid flow simulations.

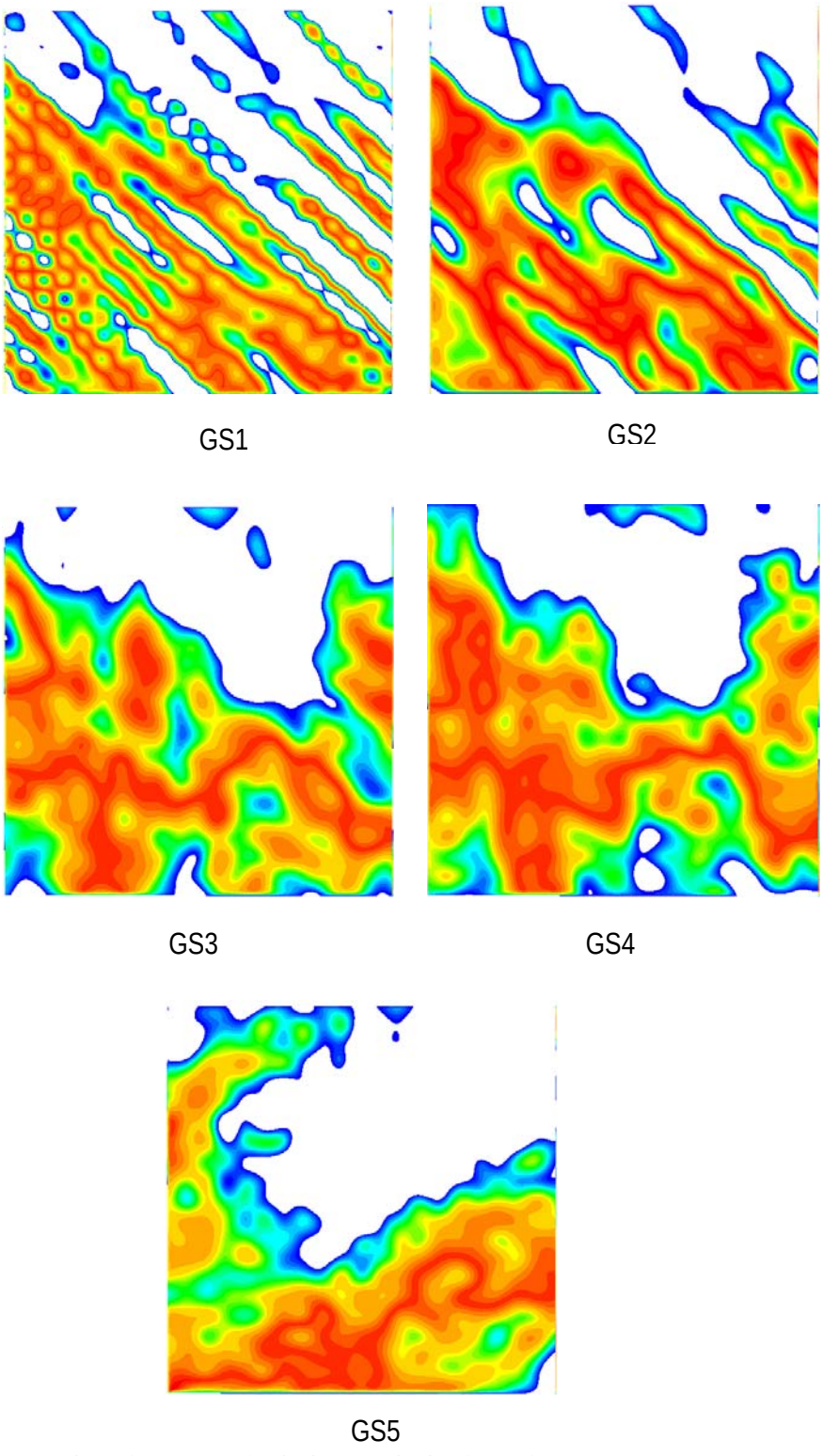

Figure 5.28 Top view of contours of velocity magnitudes for surfaces GS1 to GS5.

Figure 5.28 shows, as examples, the contours of velocity magnitudes for GS1 to GS5 along a *Z* plane when fluid is travelling from left to right along the *X* direction. The white coloured areas in this figure show those locations where the plane does not intersect the fracture surface. From this figure it can be seen that as correlation distance

increases from GS1 to GS5, the surface asperities have a larger intersection area with the *Z* plane indicating a lesser deviation of height distribution, or smoother surfaces.

In Figure 5.29, the values of pressure drops when the fluid is flowing along different directions have been compared for GS1 to GS5. The results of this figure indicate different behaviours depending on the flow direction: this is the anisotropy in the fluid flow response, as discussed earlier. Also, it is seen that pressure drop reduces as correlation distance increases from 0.01 cm to 10.0 cm. This is due to the fact that at larger correlation distances, the fluctuation in height distributions reduces and the surface appears to have bumpiness with a larger wavelength. This corresponds to surface waviness or tortuosity, as a result of which the length of the surface subjected to the fluid flow reduces and this causes less of a pressure drop as observed in Figure 5.29. Another interesting point shown by this figure is that the largest pressure drop happens at an orientation of 45°. This is related to the fact that in generation of these surfaces, as mentioned before, the preferred direction was set to 45°: the results obtained here allow confirmation of a correlation between surface geometrical properties and fluid flow responses.

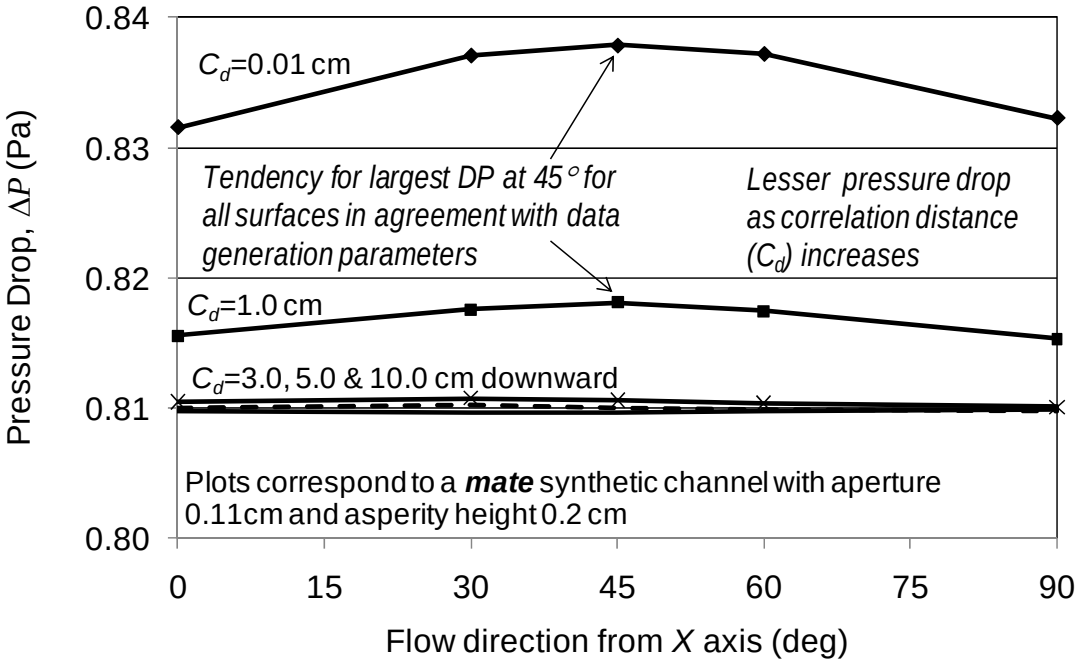

Figure 5.29 Anisotropy in pressure drops of synthetic surfaces GS1 to GS5.

The results presented here demonstrate the potential impact of shear slippage of natural fractures or existing faults and lager scale fractures in a hydrocarbon reservoir on production rate as a result of depletion. After fracture reactivation, as was observed from the given results above, the fracture aperture may change and this could potentially

increase the area open to fluid flow. This concept can be used as an enhancement technique, in particular, in fractured reservoirs: depletion from one area of the reservoir may change the aperture of nearby fractures within the next zone of production. This requires further detailed analysis incorporating the magnitude and direction of in-situ stresses with respect to taking the fracture planes into account.

Similar to the synthetic surface analysed in the previous section, here D_{R2} and I_{R2} values corresponding to surfaces GS1 to GS5 are calculated at different scales and orientations. As an example, Figure 5.30 shows the results of D_{R2} for surfaces GS1 to GS4 (corresponding to correlation lengths of CL=0.01 to 5.0 cm). From this figure it can be seen that roughness shows a larger variation at a lesser correlation length but this becomes less significant at smaller scales and in this case, the results are very close for correlation lengths of less than 3.0 cm. In Figure 5.31, I_{R2} changes for these surfaces are shown, which reveal interesting information about the geometry of these surfaces. Clear reduction for I_{R2} at all scales for GS1 and GS2 at 45° is an indication of surface periodicity along this direction. At larger correlation distances (i.e. surfaces GS3 to GS5), surface periodicity becomes less visible due to larger surface waviness and the tripod size cannot capture this for the given size of the surfaces. At these larger correlation distances, I_{R2} appears to be anisotropic (changing between 0.4 and 0.6) but it is similar along different orientations.

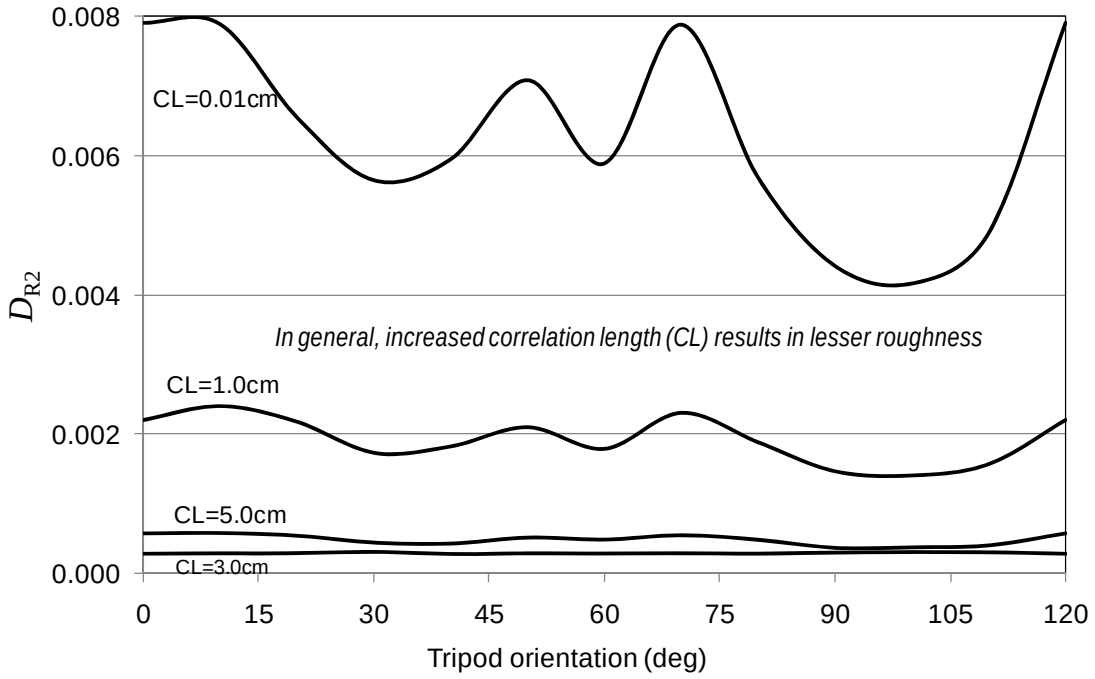

Figure 5.30 Roughness values calculated for surfaces GS1 to GS4.

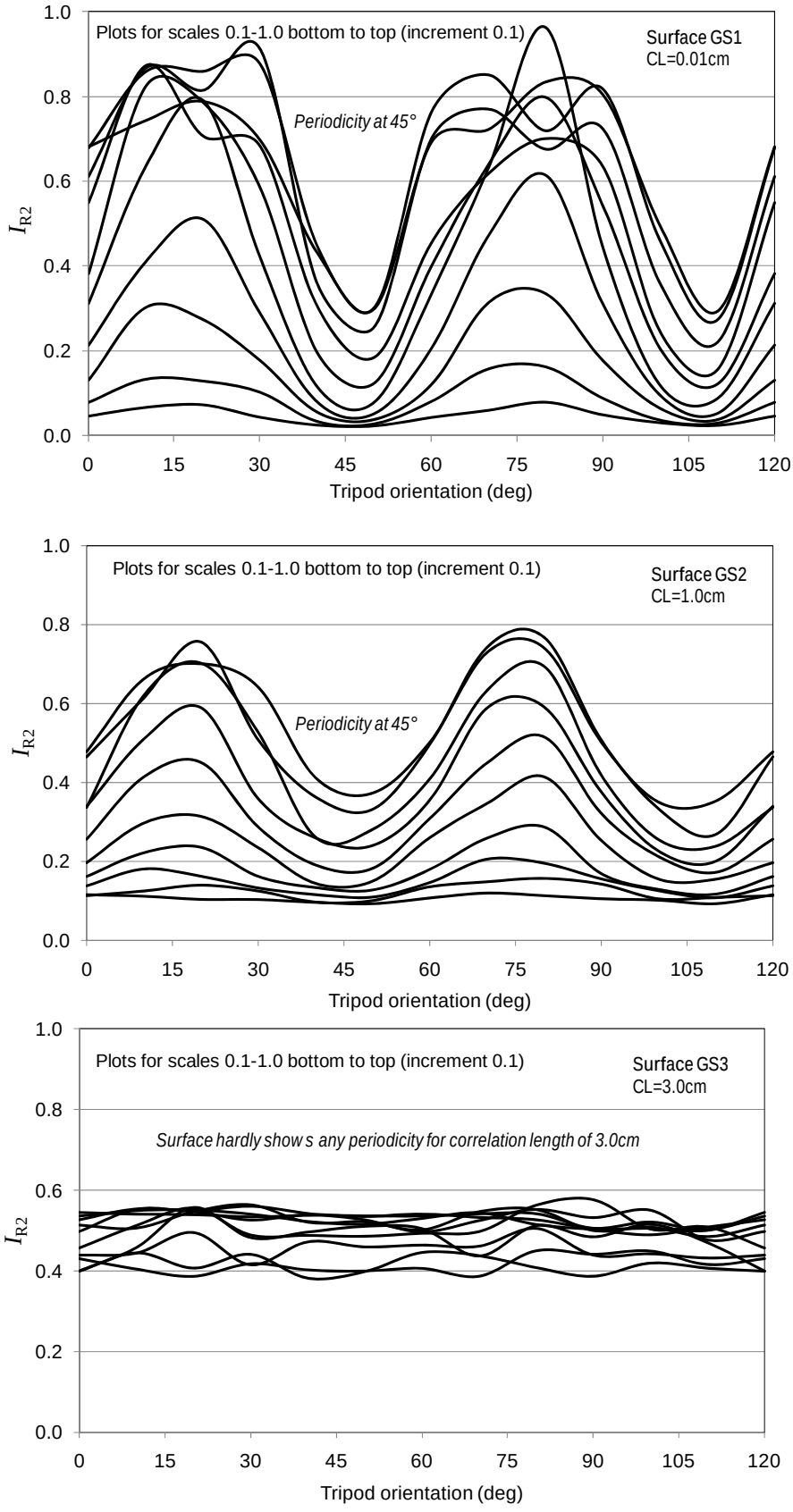

Figure 5.31 Isotropy parameter, I_{R2}, calculated for surfaces GS1 to GS3.

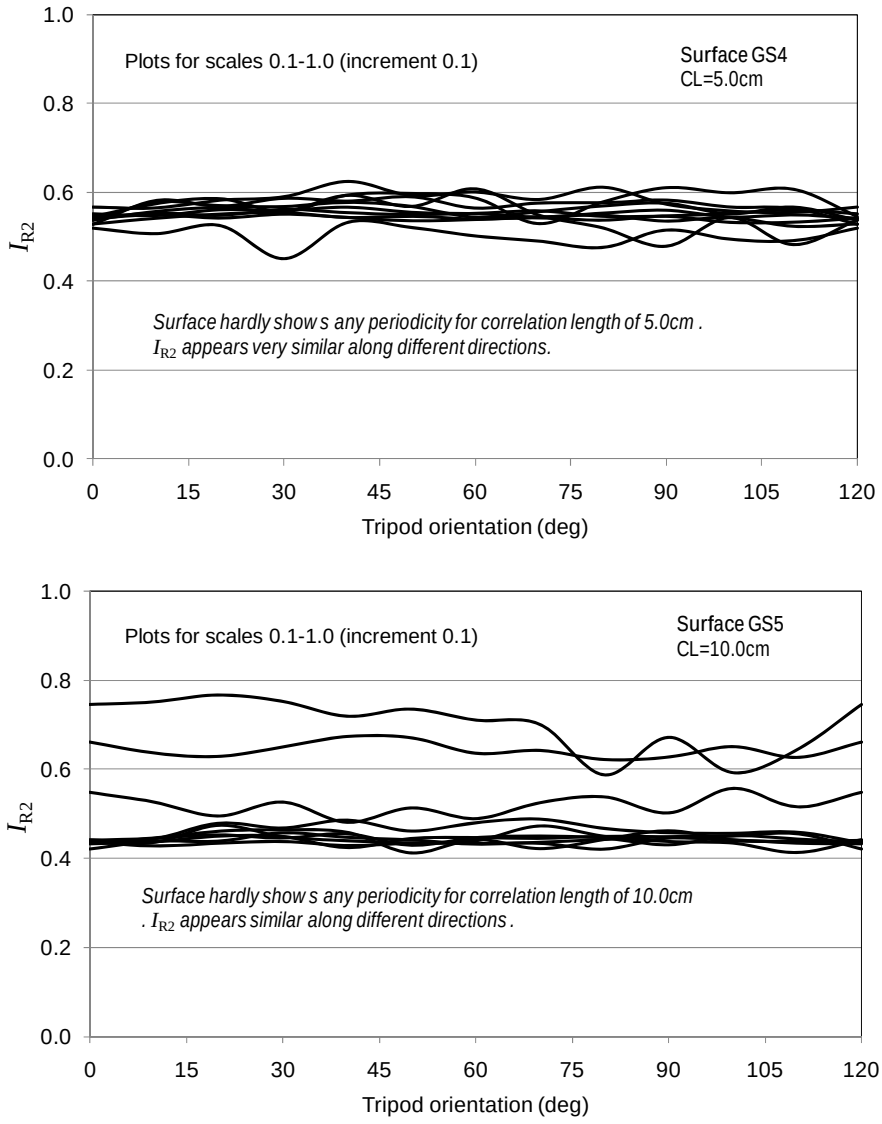

Figure 5.31 (cont'd) Isotropy parameter, I_{R2}, calculated for surfaces GS4 and GS5.

As an example, Figure 5.32 shows the rose diagrams corresponding to surfaces GS1 and GS2 (corresponding to correlation distances of 0.01 cm and 1.0 cm, respectively), which details surface anisotropy along 45° and a lesser dispersion for I_{R2} for surface GS2.

In comparing these results with the fluid flow response of these surfaces (Figure 5.29), it can be clearly seen that surface geometrical properties and fluid flow response of a surface are correlated. As correlation length increases, i.e. lesser surface roughness, pressure drops as the surface reduces. Further investigation is required to obtain numerical correlations between pressure drop and surface roughness parameters (i.e. D_{R2} and I_{R2}).

In the next section, the results of similar analyses will be presented for a real rock surface.

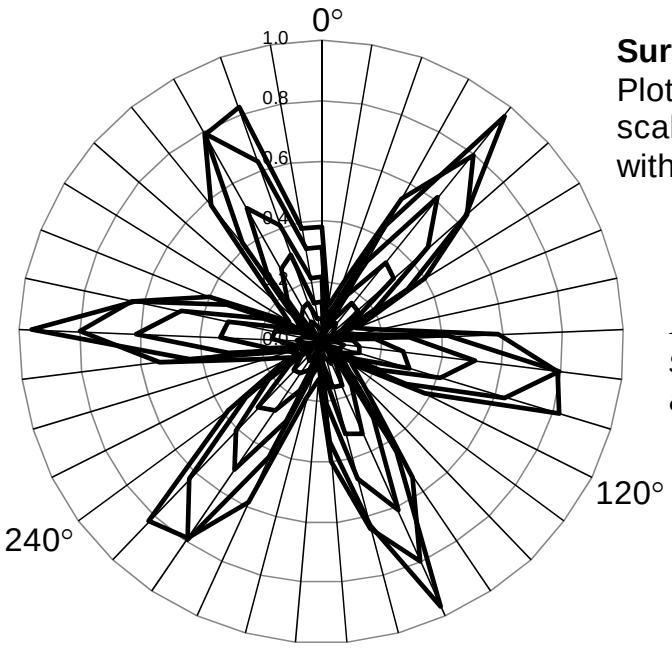

Surface GS1: CL=0.01cm
Plots of I_{R2} corresponding to scales of 0.1 to 0.6 outwards with an increment of 0.1

I_{R2} varies in a wide range at small scales and look different at different directions

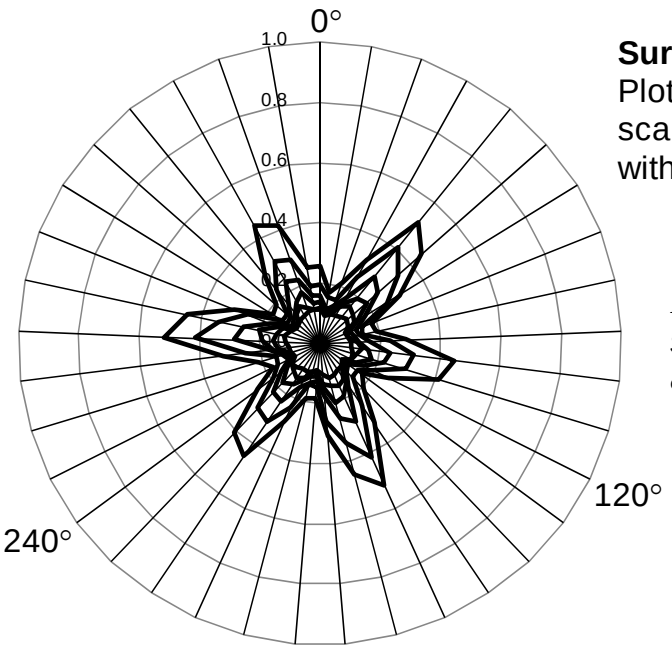

Surface GS2: CL=1.0cm
Plots of I_{R2} corresponding to scales of 0.1 to 0.6 outwards with an increment of 0.1

I_{R2} varies in a wide range at small scales and look different at different directions

Figure 5.32 Rose diagram of isotropy parameter corresponding to surfaces GS1(top) and GS2.

5.6 An example of a rock fracture analysis

In this section, the results of fluid flow simulation as well as roughness analysis corresponding to a real rock like fracture will be presented. Similar to the discussions given for corrugated and random flow channels in the two previous sections, the effect of surface roughness, anisotropy in flow response and shear offset will be studied here.

The real like rock fracture was used elsewhere for fracture shear studies in the lab (Asadi, 2010). The small and large roughness of this surface along the *X* axis direction has made this sample suitable for shear tests in opposite directions. The mortar sample replicates the geometry of a real fracture. Figure 5.33 shows different views of the rock block. Figure 5.34 presents the wireframe view of one side of this fracture whose digital elevations were extracted using digital photogrammetry. The sample has a length and width of 18 cm and 11 cm with its asperities changing between 0.0 and 0.3 cm. The periodic nature of the surface along the *X* axis direction is visible from this figure.

Fluid flow simulations were carried out using FLUENT for this fracture surface, where the flow channel was composed of two identical surfaces with an aperture of 0.11 cm. In Figure 5.35, the contours of total pressure and velocity magnitudes are shown for this fracture. It can be seen that due to the geometry of the surface, pressure and velocity are changing in a relatively wide range at different points.

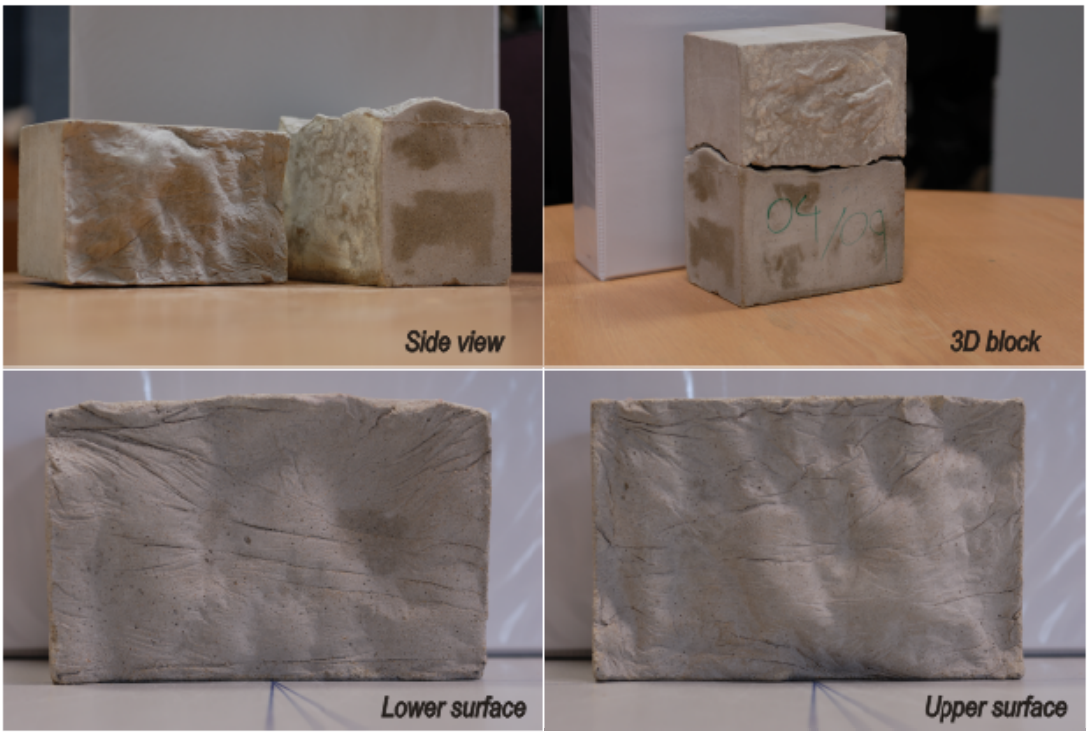

Figure 5.33 Artificial real like fracture made of mortar, used for shear tests in the lab (Asadi, 2010).

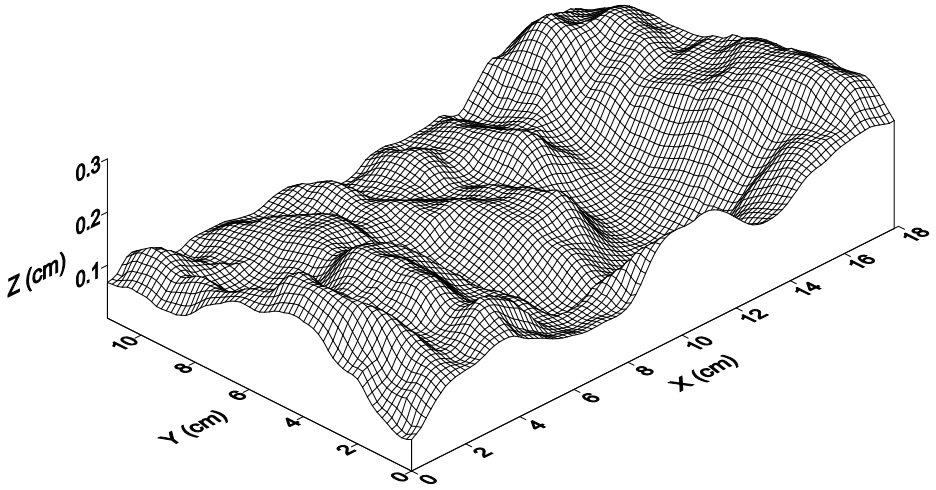

Figure 5.34 Geometry of lower wall of real like fracture used for fluid flow and roughness analysis.

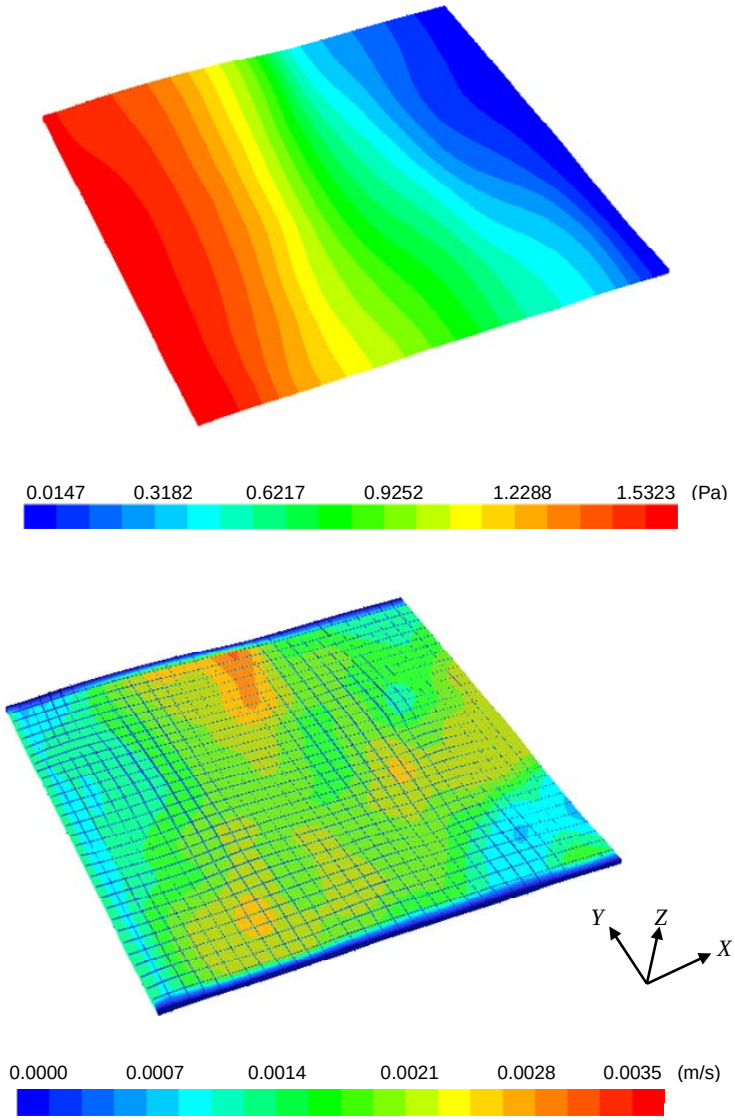

Figure 5.35 Contours of total pressure (Top) and velocity magnitude for real like fracture.

In order to perform directional fluid flow simulations similar to the synthetic surfaces analysed in the two previous sections, data within a square located at the centre of the surface was extracted. The side of the square used for this surface was 6 cm, due to the shorter length of the sample in the *Y* axis direction. Although a large number of data from the surface may be discarded using this approach, the results are expected to show the directional dependency of the fluid flow in the centre part of this surface. The results of such a study are presented in Figure 5.36. From this figure, it can be seen that the pressure drop reduces as the fluid flow direction changes from the *X* to *Y* axis: this is in agreement with the periodic nature of the surface along the *X* axis direction, as the surface tends to have a larger real length along this direction.

The results of D_{R2} analysis of the entire surface along different directions are shown in Figure 5.37. In this figure, the results presented for tripod sizes of 1.0 to 6.0 cm indicate a reduction of surface roughness at larger scales. At all scales, tendency of the surface to display more roughness above tripod orientations of 60° is apparent. Similar results are shown in a rose diagram plot in Figure 5.38.

Figure 5.39 presents the results of I_{R2} for this surface, which reveal valuable information about geometrical properties of the surface. As expected, the surface shows the largest anisotropy in its roughness close to a 0° or 120° direction, i.e. the direction of maximum roughness (see Figure 5.14 for comparison with a corrugated plane). Roughness increases as orientation of tripod deviates from zero and as can be seen from Figure 5.39, I_{R2} shows a large increase at an orientation of between 35° and 50° at different scales. This indicates that surface roughness appears to be isotropic along this tripod orientation. Considering the periodic nature of the surface along the *X* axis (i.e. 0°), such a behaviour can be justified. This can be better understood when the results are compared with Figure 5.14 for a corrugated plane. From this figure, $I_{R2} = 0$ for the corrugated plane at 0° and 60°, with its maximum occurring in between depending on the tripod size. This is because of the identical tripod sampling at these two orientations for a corrugated plane. For real surfaces where tripod sampling is identical for orientations of 0° and 120°, maximum I_{R2} will occur between these two orientations if the surface is periodic.

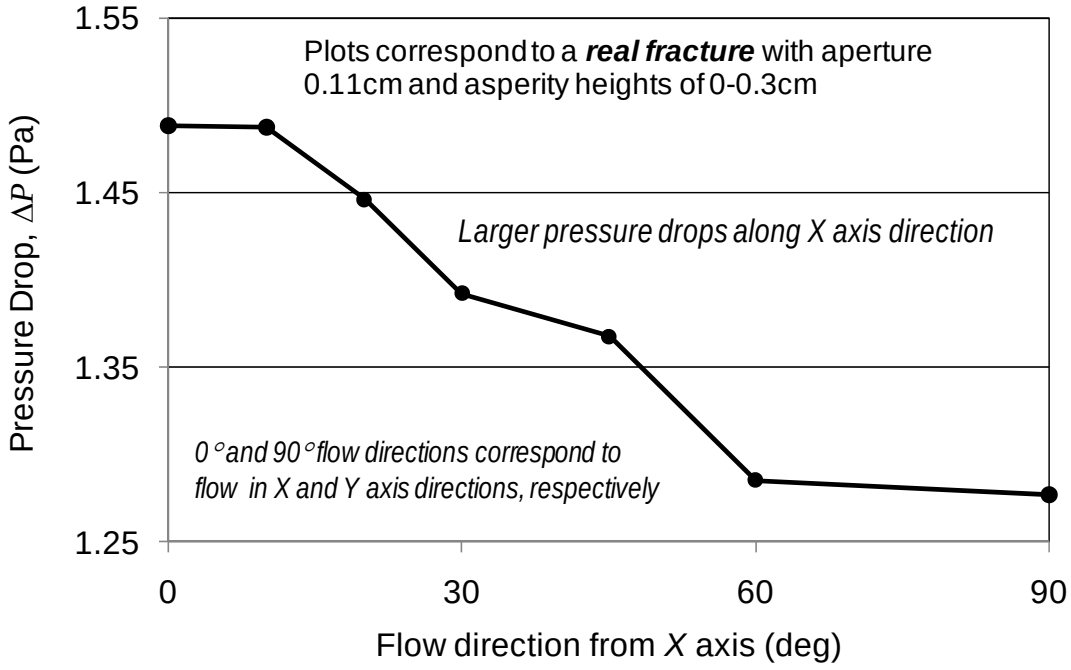

Figure 5.36 Directional fluid flow analysis for real rock fracture fluid flow analysis.

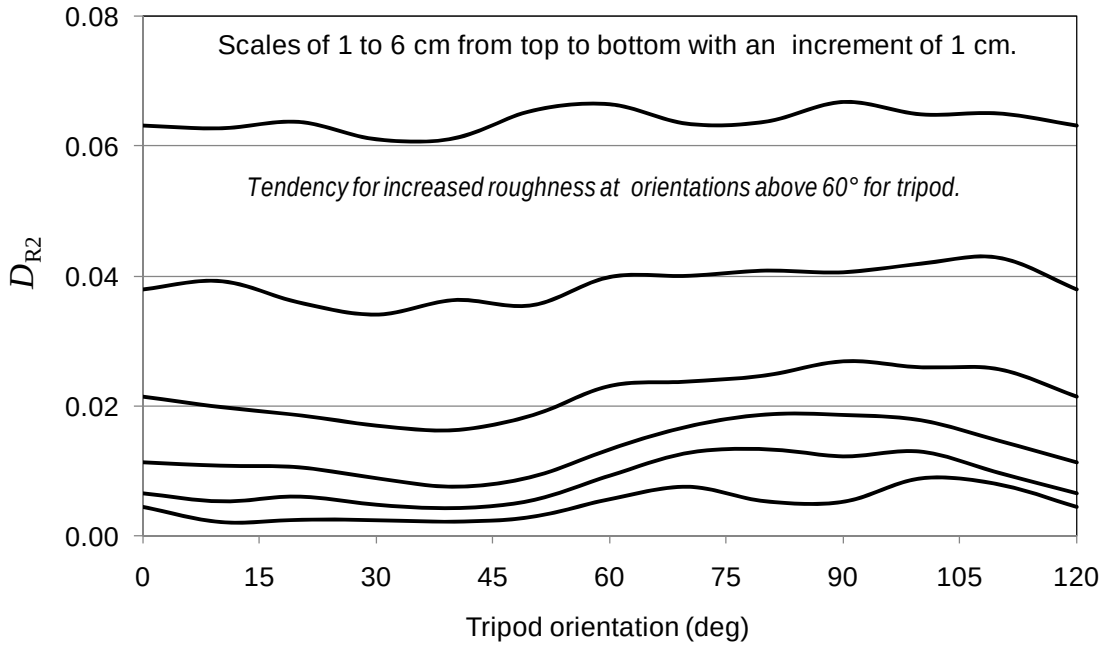

Figure 5.37 D_{R2} analysis of rock fracture.

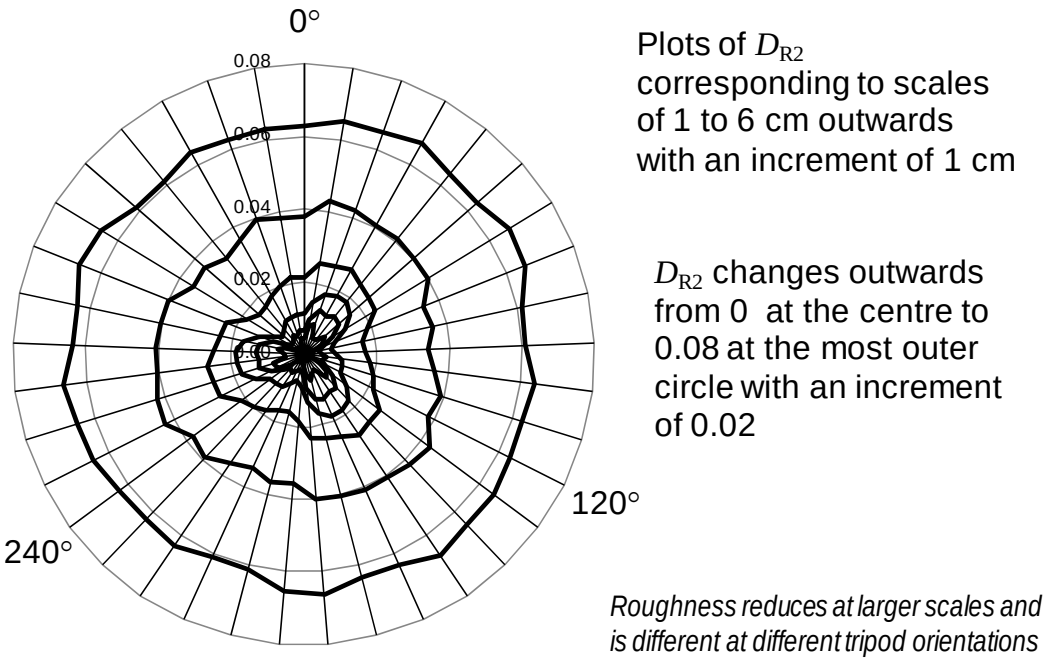

Figure 5.38 Rose diagram of D_{R2} for rock fracture.

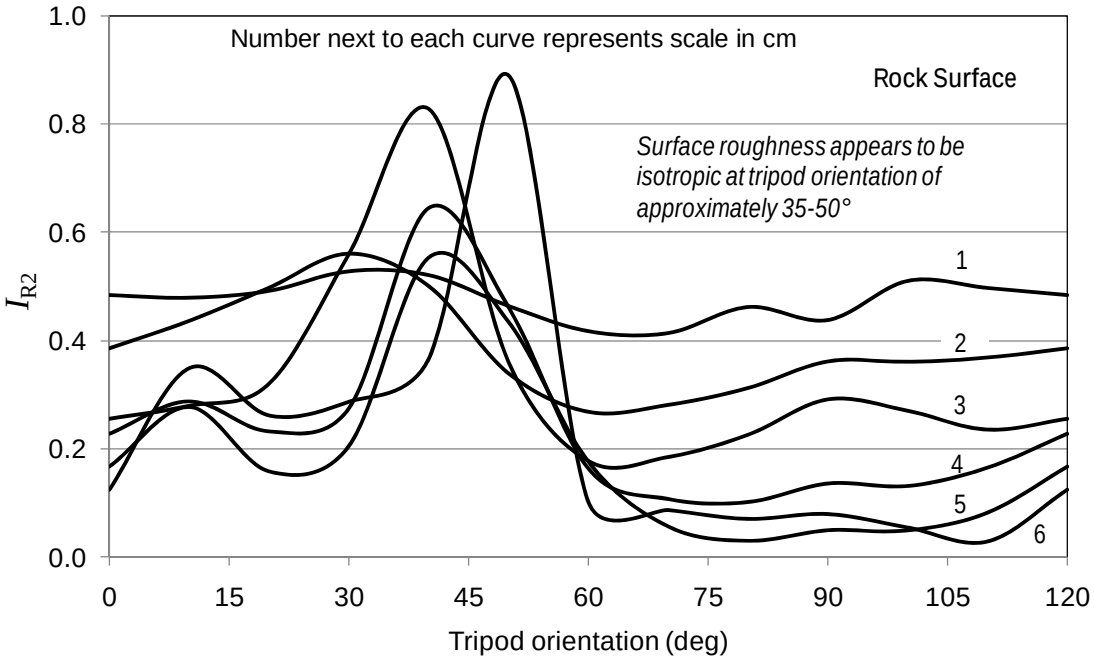

Figure 5.39 I_{R2} analysis of rock fracture.

Considering the correlations between fracture roughness and its shear behavior, it would be interesting to present the results of shear tests for this surface. Figure 5.40 shows the sample view after shearing of the upper block along the lower block to the left at two different stages with an increased normal stress of 2.5 MPa at the second stage.

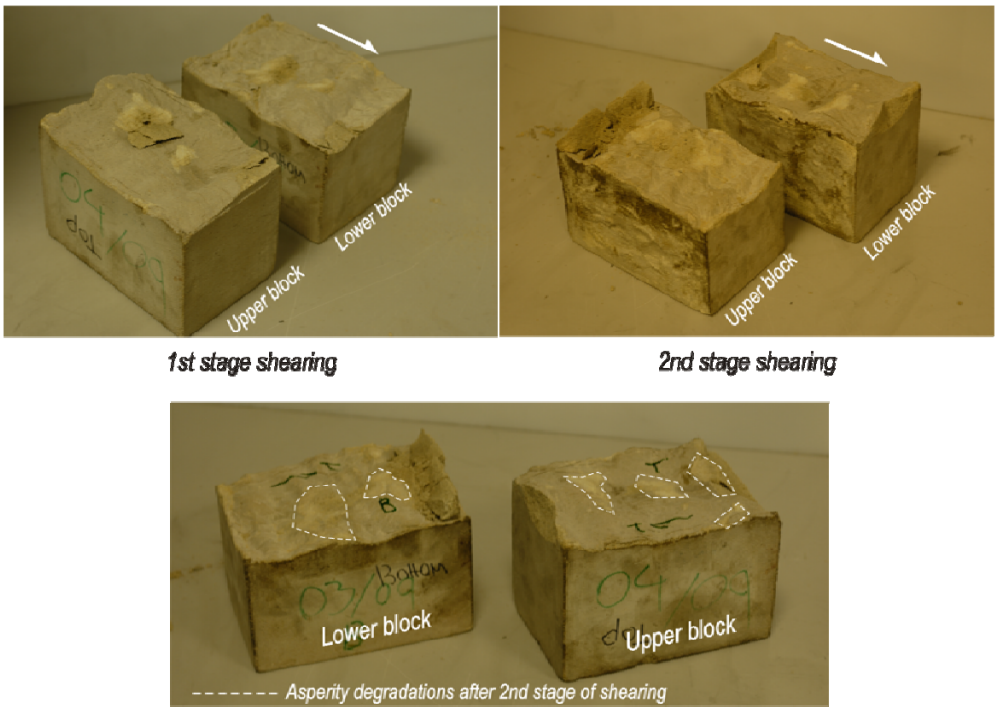

Figure 5.40 View of rock fracture after shear experiment in the lab: 2.5 MPa normal stress and at two shearing cycles (Asadi, 2010).

In this figure, the asperity degradations on both the upper and lower blocks are marked on the lower plot. These locations correspond to the areas of the two blocks which come into contact in the first instance when shearing occurs. This corresponds to a velocity magnitude of zero if the fluid travels inside this fracture. Figure 5.41 shows the plot of shear stress versus shear displacement where the maximum shear strength of about 4.8 MPa is obtained after approximately 0.50 cm of shear offset (Asadi, 2010).

For comparison purposes, the upper wall of the fracture surface was sheared towards the left with a shear displacement of 0.50 cm and fluid flow simulations of the surface were performed. In Figure 5.42, the results of velocity magnitude are shown from which the positions on the surface (where the velocity reduces to close to zero) can be identified. These locations are marked in this figure and as can be seen, these are very close to the locations along the fracture surface where asperity degradations occurred. These results, demonstrate how the hydromechanical behaviour of a fracture surface may be related to its geometrical properties. Of course, establishing valid correlations requires further investigation of this topic, which is not the objective of this thesis.

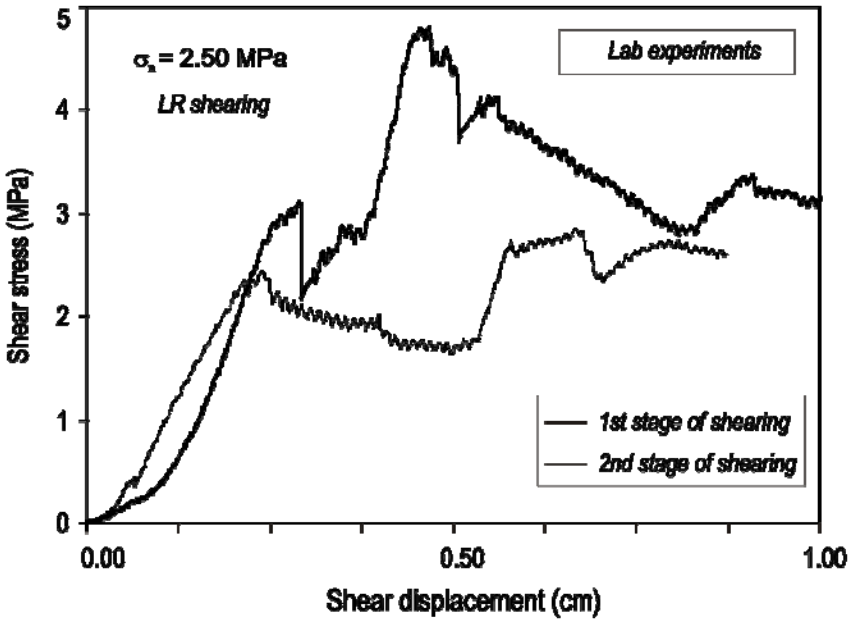

Figure 5.41 Shear stress versus shear displacement at 2.5 MPa normal stress for rock like block (Asadi, 2010).

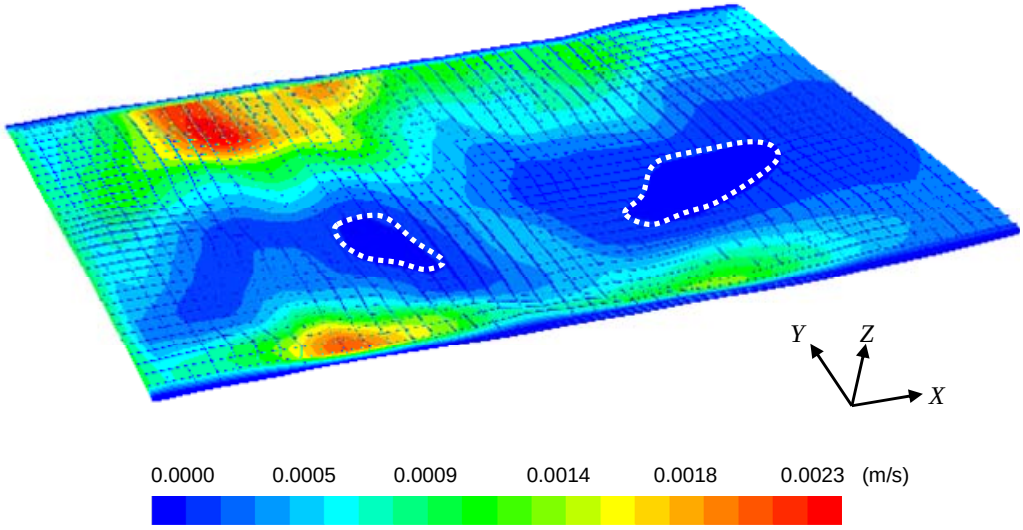

Figure 5.42 Location of zero velocities for the fracture surface after applying shear offset.

5.7 Summary

This chapter presented the results of 3D numerical simulations of fluid flow in rough fractures. The Riemannian roughness and isotropy parameters (D_{R2} and I_{R2}) were also calculated for these surfaces. The results for a corrugated plane indicated how geometrical properties (in particular periodicity) of the surface could be extracted from roughness analysis and how this corresponded to the fluid response of the surface. It was also shown how significant changes in fracture fluid flow behavior could result from shearing of the two walls. These concepts were studied further by analysing a

synthetically generated surface. Analysis of five synthetic surfaces where only correlation distances were increased in generation of these surfaces also revealed how larger correlation lengths lead to lesser surface roughness, but larger waviness and tortuosity. This also corresponded to less pressure drops for the surface. A similar analysis was performed for a rock like fracture surface with a preferred orientation for its roughness and again correlations between fracture geometry and its flow responses were found. In addition, the results of the lab shearing test of this surface analysed elsewhere was presented for comparison purposes. The location of asperity degradations of the surface was very similar to points where velocity magnitude of the surface after shearing tended to zero. This demonstrated the correlation of surface geometrical parameters and its hydromechanical behavior.

6 Summary, conclusions and recommendations

In this thesis, the effect of surface roughness on the fluid flow response of rock fractures was investigated. Numerical simulations using FLUENT were performed in both 2D and 3D and various conclusions were drawn.

A detailed summary and conclusions made from this study are presented in Sections 6.1 to 6.4 with Section 6.5 outlining some of the future studies recommended as a continuation of this work.

6.1 Analytical models

- Analytical calculations of channels with synthetic sinusoidal profile geometries showed that changing the relative wall roughness could result in a changing of the mean aperture: the mean aperture increased as relative roughness became larger.
- The 1D Riemannian dispersion parameter (D_{R1}) proposed by Rasouli and Harrison (2010), was used to investigate correlations between geometrical properties and the hydraulic response of 2D flow channels.
- The plot of D_{R1}versus hydraulic aperture of sinusoidal profiles demonstrated a close agreement with the work conducted by Zimmerman *et al.*, (1991), and indicated the potential applications of D_{R1} in encapsulating profile geometrical properties in hydraulic response of the flow channel.
- The results of analytical solutions for synthetic geometries indicated that the hydraulic aperture was relatively higher for symmetric triangular profile than that of corresponding sinusoidal profiles. This showed the importance of slight profile geometry changes on fluid flow behaviour.

6.2 2D Numerical simulations

- Simulation results of symmetric triangular mate profiles using FLUENT showed that profiles with a different number of asperities but similar total lengths exhibit similar fluid flow responses.

- From the simulations of triangular profiles, it was observed that the hydraulic aperture was equivalent to the opening for different mate fluid channels, as expected.
- For non-mate channels with an increased number of asperities, but the same total length (i.e. lesser profile asperity height), pressure drop increased if the maximum opening was not fixed. It was found that in profiles with an increased number of asperities, fluid faced a more reduced throat size along the channel. This reduced width is the reason for larger pressure drops for a higher number of asperities.
- Increased velocity in non-mate channel geometries resulted in lesser channel wall length being subjected to the fluid, however, the hydraulic aperture of the fracture reduced at the same time. As the effect of the hydraulic aperture was dominant compared to profile length, the pressure drop tended to increase.
- Simulation results showed that as asperity height or profile roughness increased, pressure drop reduced in non-mate profiles, which is due to a wider area for fluid to pass through the channel.
- Based on the analytical analysis of a unit hydraulic cell (UHC), which was performed to investigate the effect of changes in channel geometry on hydraulic behaviour, the hydraulic aperture showed an increasing trend as the channel walls deviated from each other.
- The results also indicated that hydraulic aperture increased as the UHC inlet opening became larger, however, it approached the mechanical aperture when minimum aperture became very large. The results were found to be independent of the size of the top or bottom wall (or say, asperity height) and were only dependent upon the ratio of the minimum to maximum aperture. However, the analytical equations developed here did not consider the flow properties but only looked at the geometry of the UHC.
- The plot of hydraulic aperture versus upper wall orientation for different UHCs, with two walls having different orientations, exhibited parabolic trends.
- FLUENT simulations of UHCs with different wall orientations confirmed the analytical solutions developed. This demonstrated the developed analytical formulae could be used with reasonable accuracy for the purpose of studying real rock fractures, assuming that a real fracture is a combination of several discrete UHCs.

- Using multi-variable regression techniques and FLUENT simulations, the relationship between hydraulic aperture of the UHC as a function of inlet opening and the angle between UHC walls was developed. A very close agreement with less than 10% error was obtained between the results from developed correlations and the simulation of randomly generated profiles. This demonstrated the applicability of the developed correlation for a good estimation of pressure drop in a 2D channel.

6.3 JRC flow channels

- JRC flow channels were developed for fluid flow simulation purposes in order to derive correlations between hydraulic properties and average JRC value of the fracture. Each JRC channel is a combination of two JRC profiles. Accordingly, it can be imagined that different flow channels with different geometries could have a similar averaged roughness value (or JRC). Also, by changing the position of the top and bottom walls of a fracture, this could lead to different fracture geometries and thus different flow responses (while averaged roughness is identical in both cases).
- The analysis of combined JRC profiles resulted in a more generalised correlation between averaged JRC_a and roughness parameter D_{R1}. By having D_{R1} for a real rock fracture, this correlation could be used to estimate average JRC_a. The results indicated how wide the range of JRC_a could be depending on which combination of JRC profiles were presented at the top and bottom wall of the fracture.
- From an analysis of JRC flow channels, various correlations between channel geometrical and hydraulic properties were developed. In order to only investigate the roughness effect, the minimum closure distance for the channels was kept constant. The results showed how pressure drop reduced as average JRC_a increased and this corresponded to an increase in fracture mechanical and hydraulic apertures.
- In comparing the results obtained for nine real fractures from developed correlations and direct simulation using FLUENT software, the applicability of proposed formulae was demonstrated to a large extent.

6.4 3D simulations

- 3D numerical simulations of fluid flow in rough fractures and calculations of the Riemannian roughness and isotropy parameters (D_{R2} and I_{R2}) were performed for synthetic and rock fracture surfaces. The results demonstrated the existence of orientation between fracture geometrical parameters and its fluid flow behaviour.
- The results for a corrugated plane indicated how geometrical properties (in particular periodicity) of the surface may be extracted from a roughness analysis and how this corresponded to fluid response of the surface.
- The analysis of a generated fracture surface indicated that larger asperity height distribution (i.e. roughness) resulted in higher pressure drops. Also, the fracture fluid flow response was found to be directionally dependent when fluid travelled along different directions. These results were found to be in agreement with the surface geometrical parameters extracted from surface roughness and anisotropy analysis (i.e. D_{R2} and I_{R2} calculations for the surface).
- Shear displacement of the corrugated plane as well as the analysed synthetic fracture was showed to have a significant impact on fluid flow behaviour of the surface.
- An analysis of five synthetic surfaces, where only correlation distances were increased in generation to these surfaces, also revealed how larger correlation lengths lead to larger waviness and tortuosity. This corresponded to lesser pressure drops for the surface.
- Analysis of a rock like fracture surface also revealed correlations between fracture geometry and its flow responses.
- Comparing the results of flow analysis of the rock like fracture with lab shearing test results, which were available from another study, indicated that the location of asperity degradations of the surface was very similar to points where the velocity magnitude of the surface after shearing tends to zero. This demonstrated the correlation of surface geometrical parameters and its hydromechanical behavior.

6.5 Recommendations for Future work

The results presented in this thesis indicated how surface morphological parameters could be potentially used to estimate fracture hydraulic behaviour. The Riemannian roughness parameters were found to be robust tools in revealing useful

information about surface geometrical properties. However, further investigation is required in terms of analysing several other surfaces with more complicated geometries to obtain a better idea about the link between geometry and the hydraulic behaviour of real fractures.

In an analysis performed in this study, the effect of asperity failure was not considered. The in-situ stresses could significantly influence aperture, which in turn changed the hydraulic behaviour of the fracture. Therefore, continuing research is needed to examine the stress effect with fluid flow response.

The analysis presented here was based on the assumption of laminar flow and water as the fluid. For the purpose of this study this assumption was appropriate, although one could study the effect of turbulent flow (which is more likely to be the case near a wellbore) and use two or three phase fluid in the analysis. This is indeed another interesting line for future research.

The preliminary results presented here for a rock like fracture indicated the potential correlation between asperity degradation and fluid behaviour. Further research is suggested along this line to couple the shearing mechanism of fractures with their fluid flow behaviour. This concept is to some extent related to the effect of in-situ stresses, as dependent on the magnitude of normal stress acting perpendicular to the plane of the fracture, the failure mechanism of the fracture may change from sliding to asperity failure and then failure of the intact rock. Each mechanism has a different influence on fluid behaviour of the fracture.

References

Asadi, M.S., 2010, Experimental and Numerical study of progressive shear behaviour of single rough fractures [PhD dissertation thesis]: Perth, Curtin University of Technology.

Bahrami, H., Siavoshi, J., and Bahraie, R., 2008, Estimating Fracture Permeability and Shape Factor by Use of Image Log Data in Welltest Analysis, SPE Asia Pacific Oil & Gas Conference and Exhibition: Perth,Australia.

Barton, N., 1982, Modelling rock joint behavior from in situ block tests: implications for nuclear waste repository design: ONWI-308, Columbus, OH, p. 101.

Barton, N., Bandis, S., and Bakhtar, K., 1985, Strength, deformation and conductivity coupling of rock joints: International Journal of Rock Mechanics and Mining Sciences & Geomechanics Abstracts, v. 22, p. 121-140.

Barton, N., and Choubey, V., 1977, The shear strength of rock joints in theory and practice: Rock Mechanics and Rock Engineering, v. 10, p. 1-54.

Barton, N., and de Quadros, E.F., 1997, Joint aperture and roughness in the prediction of flow and groutability of rock masses: International Journal of Rock Mechanics and Mining Sciences, v. 34, p. 252.e1-252.e14.

Barton, N.R., 1971, A relationship between joint roughness and joint shear strength, Int. Symp. on rock mech: Nancy.

Barton, N.R., 1991, A relationship between joint roughness and joint shear strength, Int. Symp. on rock mech,Nancy.

Bear, J., 1988, Dynamics of fluids in porous media: New York, Dover publication.

Belem T., Homand-Etienne F., and M., S., 2000, Measurement of large scale roughness of rock planes by means of prolilograph and geological compass: Rock Mech Rock Eng v. 4, p. 217-242.

Brady, B.H.G., and Brown, E.T., 2004, Rock mechanics: for underground mining: Dordrecht ; London, Kluwer Academic Publishers, 3rd edition.

Brown, S.R., 1987, Fluid Flow Through Rock Joints: The Effect of Surface Roughness: J. Geophys. Res., v. 92, p. 1337-1347.

Brown, S.R., 1989, Transport of Fluid and Electric Current Through a Single Fracture: J. Geophys. Res., v. 94, p. 9429-9438.

Brown, S.R., Stockman, H.W., and Reeves, S.J., 1995, Applicability of the Reynolds Equation for modeling fluid flow between rough surfaces: Geophys. Res. Lett., v. 22, p. 2537-2540.

Constantinescu, V.N., 1995, Laminar viscous flow: New York, Springer.

Crandall, D., Ahmadi, G., and Smith, D., 2010a, Computational Modeling of Fluid Flow through a Fracture in Permeable Rock: Transport in Porous Media, v. 84, p. 493-510.

Crandall, D., Bromhal, G., and Karpyn, Z.T., 2010b, Numerical simulations examining the relationship between wall-roughness and fluid flow in rock fractures: International Journal of Rock Mechanics and Mining Sciences, v. 47, p. 784-796.

Dagnall, H., 1980, Exploring surface texture, Rank Taylor Hobson.

Elsworth, D., and Goodman, R.E., 1986, Characterization of rock fissure hydraulic conductivity using idealized wall roughness profiles: International Journal of Rock Mechanics and Mining Sciences & Geomechanics Abstracts, v. 23, p. 233-243.

Enru, L., 2005, Effects of fracture aperture and roughness on hydraulic and mechanical properties of rocks: implication of seismic characterization of fractured reservoirs: Journal of Geophysics and Engineering, v. 2, p. 38.

Fecker , E., and Rengers, N., 1971, Measurement of large scale roughness of rock planes by means of prolilograph and geological compass, 1st Int Symp Rock Mech Nancy, France p. 1-18.

Federico, V.D., 1998, Non-Newtonian Flow in a Variable Aperture Fracture: Transport in Porous Media, v. 30, p. 75-86.

Fluent Inc., 2005, FLUENT 6.3 User's Guide.

Garcia, N., 1984, Monte Carlo calculation for electromagnetic-wave scattering from random rough surfaces: Physical review letters, v. 52, p. 1798.

Ge, S., 1997, A governing equation for fluid flow in rough fractures: Water Resour. Res., v. 33, p. 53-61.

Giacomini, A., Buzzi, O., Ferrero, A.M., Migliazza, M., and Giani, G.P., 2008, Numerical study of flow anisotropy within a single natural rock joint: International Journal of Rock Mechanics and Mining Sciences, v. 45, p. 47-58.

Hosseinian, A., Rasouli, V., and Bahrami, H., 2010b, Analytical and numerical analysis of fluid flow through rough natural fracture profiles, 44th US Rock Mechanics Symposium and 5th U.S.-Canada Rock Mechanics Symposium: Salt Lake City, UT.

Hosseinian, A., Rasouli, V., and Utikar, R., 2010a, Fluid flow response of JRC exemplar profiles, European Rock Symposium (EUROCK 2010): Switzerland: Lausanne, Taylor & Francis Group.

Jaeger, J.C., Cook, N.G.W., and Zimmerman, R.W., 2007, Fundamentals of Rock Mechanics (4th Edition), John Wiley & Sons.

Jing, L., 2003, A review of techniques, advances and outstanding issues in numerical modelling for rock mechanics and rock engineering: International Journal of Rock Mechanics and Mining Sciences, v. 40, p. 283-353.

Kleinstreuer, C., 1997, Engineering fluid dynamics: an interdisciplinary systems approach, Cambrdige University Press.

Koyama, T., Li, B., Jiang, Y., and Jing, L., 2009, Numerical modelling of fluid flow tests in a rock fracture with a special algorithm for contact areas: Computers and Geotechnics, v. 36, p. 291-303.

Koyama, T., Neretnieks, I., and Jing, L., 2008, A numerical study on differences in using Navier-Stokes and Reynolds equations for modeling the fluid flow and particle transport in single rock fractures with shear: International Journal of Rock Mechanics and Mining Sciences, v. 45, p. 1082-1101.

Kristinof, R., Ranjith, P., and Choi, S., 2010, Finite element simulation of fluid flow in fractured rock media: Environmental Earth Sciences, v. 60, p. 765-773.

Kulatilake, P.H.S.W., 2008, Quantification of aperture and relations between aperture, normal stress and fluid flow for natural single rock fractures: Geotechnical and geological engineering, v. 26, p. 269.

Letalleur, N., Plouraboue, F., and Prat, M., 2002, Average Flow Model of Rough Surface Lubrication: Flow Factors for Sinusoidal Surfaces: Journal of Tribology, v. 124, p. 539-546.

Liu, H., and Sterling, R., 1990, Statistical description of the surface roughness of rock joints, The 31th US Symp. Rock Mech.

Lomize, G.M., 1951, Water flow through jointed rock: Rock mechanics, p. 127 (in Russian).

Louis, C., 1969, A Study of Ground Water Flow in Jointed Rock and Its Influence on the Stability of Rock Masses: London, Imperial College,Rock Mechanics Report No. 10.

Maday, C.J., 2002, The Foundation of the Sommerfeld Transformation: Journal of Tribology, v. 124, p. 645-646.

Nazridoust, K., Ahmadi, G., and Smith, D.H., 2006, A new friction factor correlation for laminar, single-phase flows through rock fractures: Journal of Hydrology, v. 329, p. 315-328.

Nemoto, K., Watanabe, N., Hirano, N., and Tsuchiya, N., 2009, Direct measurement of contact area and stress dependence of anisotropic flow through rock fracture with heterogeneous aperture distribution: Earth and Planetary Science Letters, v. 281, p. 81-87.

Neuzil, C.E., and Tracy, J.V., 1981, Flow through fractures: Water Resour. Res., v. 17, p. 191-199.

Olsson, R., and Barton, N., 2001, An improved model for hydromechanical coupling during shearing of rock joints: International Journal of Rock Mechanics and Mining Sciences, v. 38, p. 317-329.

Oron, A.P., and Berkowitz, B., 1998, Flow in rock fractures: The local cubic law assumption reexamined: Water Resour. Res., v. 34, p. 2811-2825.

Patir, N., and Cheng, H.S., 1978, An average flow model for determining effects of three dimensional roughness on partial hydrodynamic lubrication: J Lubr Tech, v. 100, p. 12-17.

Petchsingto, T., and KARPYN, Z.T., 2009, Deterministic Modeling of Fluid Flow through a CT-scanned Fracture Using Computational Fluid Dynamics: Energy sources. Part A , Recovery, utilization, and environmental effects, v. 31, p. 897.

Rasouli, V., 2002, Application of Riemannian Multivariate Statistics to the Analysis of Rock Fracture Surface Roughness [PhD dissertation thesis]: London, Imperial college.

Rasouli, V., and Harrison, J.P., 2000, Scale effect, anisotropy and directionality of discontinuity surface roughness, ISRM Int. Symp. Eurock 2000: Aachen, Germany, p. 751-756.

Rasouli, V., and Harrison, J.P., 2001, Is the observational method of roughness determination trustworthy? , Proc. ISRM Int. Symp. Eurock 2001: Espoo, Finland. , p. 277-282. .

Rasouli, V., and Harrison, J.P., 2004, A comparison of linear profiling an in-plane method for the analysis of rock surface geomtery, Regional ISRM Sinorock2004 Symposium: China, p. 377-378.

Rasouli, V., and Harrison, J.P., 2010, Assessment of rock fracture surface roughness using Riemannian statistics of linear profiles: International Journal of Rock Mechanics and Mining Sciences, v. 47, p. 940-948.

Renshaw, C.E., 1995, On the relationship between mechanical and hydraulic apertures in rough-walled fractures: J. Geophys. Res., v. 100, p. 24629-24636.

Sarifzadeh, M., Javadi, M., and Shahriar, K., 2009, Effect of surface roughness on velocity fields through rock fractures, in Vrkljan, I., ed., Regional Symposium of ISRM, Proced EUROCK2009: Dubrovnik, Croatia, Taylor & Francis group p. 351-356.

Sarkar, S., 2002, Fluid Flow Simulation in Fractured Reservoirs, *in* Earth Resources Laboratory, M.I.o.T., ed.: Cambridge

Sarkar, S., Toks¨oz, M.N. , and Burn, D.R., 2004, Fluid Flow Modelling in Fractures, *in* Laboratory, E.R., ed.: Cambridge.

Scesi, L., and Gattinoni, P., 2007, Roughness control on hydraulic conductivity in fractured rocks: Hydrogeology Journal, v. 15, p. 201-211.

Schmittbuhl, J., Steyer, A., Jouniaux, L., and Toussaint, R., 2008, Fracture morphology and viscous transport: International Journal of Rock Mechanics and Mining Sciences, v. 45, p. 422-430.

Sisavath, S., Al-Yaaruby, A., Pain, C.C., and Zimmerman, R.W., 2003, A Simple Model for Deviations from the Cubic Law for a Fracture Undergoing Dilation or Closure: Pure and Applied Geophysics, v. 160, p. 1009-1022.

Thomas, T.R., 1999, Rough Surfaces (Second Edition), Imperial College Press.

Thompson, M.E., and Brown, S.R., 1991, The Effect of Anisotropic Surface Roughness on Flow and Transport in Fractures: J. Geophys. Res., v. 96, p. 21923-21932.

Tsang, Y.W., 1984, The Effect of Tortuosity on Fluid Flow Through a Single Fracture: Water Resour. Res., v. 20, p. 1209-1215.

Tsang, Y.W., and Whiterspoon, P.A., 1983, The dependence of fracture mechanical and fluid flow properties of fracture roughness and smaple size: Geophysical Research, v. 88, p. 2359-2366.

Tse, R., and Cruden, D.M., 1979, Estimating joint roughness coefficients: International journal of rock mechanics and mining sciences & geomechanics abstracts, v. 16, p. 303-307.

Watanabe, N., Hirano, N., and Tsuchiya, N., 2008, Determination of aperture structure and fluid flow in a rock fracture by high-resolution numerical modeling on the basis of a flow-through experiment under confining pressure: Water Resour. Res., v. 44, p. W06412.

Witherspoon, P.A., Wang, J.S.Y., Iwai, K., and Gale, J.E., 1980, Validity of Cubic Law for fluid flow in a deformable rock fracture: Water Resour. Res., v. 16, p. 1016-1024.

Yeo, I., and Ge, S., 2005, Applicable range of the Reynolds equation for fluid flow in a rock fracture: Geosciences Journal, v. 9, p. 347-352.

Yeo, I.W., de Freitas, M.H., and Zimmerman, R.W., 1998, Effect of shear displacement on the aperture and permeability of a rock fracture: International Journal of Rock Mechanics and Mining Sciences, v. 35, p. 1051-1070.

Zimmerman, R.W., and Bodvarsson, G.S., 1996, Hydraulic conductivity of rock fractures: Transport in Porous Media, v. 23, p. 1-30.

Zimmerman, R.W., Kumar, S., and Bodvarsson, G. S., 1991, Lubrication theory analysis of the permeability of rough-walled fractures: International Journal of Rock Mechanics and Mining Sciences & Geomechanics Abstracts, v. 28, p. 325-331.

zimmerman, R.W., and Yeo, In-Wook, 2000, Fluid Flow in Rock Fractures: From the Navier-Stokes Equation to the Cubic Law: Geophysical Monograph, v. 122, p. 213-224.